Ice height change in East Antarctica derived from satellite laser altimetry.

Janosch Fabian Hoffmann

November 2016

A thesis submitted for the degree of Doctor of Philosophy at

The Australian National University

I declare that the material contained in this thesis is entirely my own work except where due and accurate acknowledgement of another source has been made.

_____

_____

Janosch Fabian Hoffmann, 15th of November, 2016

Acknowledgements

My sincerest gratitude and esteem goes to my supervisor, Paul Tregoning, who was willing to take a chance on me and my project. Thank you Paul for your patience and believing in my work when I didn't. I would like to thank the whole geodesy group at the Research School of Earth Sciences. Special mention goes to Evan Gowan for always giving great advice and help on a never-ending list of programming problems. My programming knowledge would not be what it is today without your help. I would like to thank Herb McQueen for his help with Terrawulf and always being willing to fix problems as they arose. Thanks goes to Anthony Purcell for his sage advice concerning all things mathematical. Thank you Sherryl Kluver for tireless help with the administration of my program.

I would like to thank Christopher Watson, Reed Burgette and the AAD for giving the opportunity be part of a research expedition to Antarctica. I would also like to thank both Gier Moholdt and Stefan Ligtenberg for being so forthcoming about their methodologies.

Many heartfelt thanks goes to my family, Frauke, Annika, Wolle, Peter, Ruth, Ann and Tanja, lots of love. Thanks Geoff for always being my willing proofreader and career councilor, I am not sure how I would have finished this without you. My wholehearted gratitude and love goes to my partner Rebekah Plueckhahn and our baby boy Sascha, for their unending support and patience. I would like to dedicate my thesis to my grandmother Christiane Hoffmann, who passed away while I was working on my PhD. Your love and support will never be forgotten.

Abstract

In the last two decades, satellite altimetry has given the scientific community an unprecedented amount of data, which has substantially increased our understanding of the rate of change of ice surface height (dH/dt) over glaciated regions. This can be attributed to better spatial and temporal coverage of polar regions and the increased accuracy of laser and radar satellite altimeters. This accuracy is dependent on minimising errors and reducing the uncertainties of estimates of dH/dt, which are derived from ice height measurements. There are a number of different factors that contribute to the overall uncertainty budget. In this thesis, an alternative method to crossover and along-track analysis is proposed and is applied to (ICESat) height measurements. A new method of estimating surface slope at crossovers is presented and used in conjunction with the newly proposed along-track method. Particular emphasis is placed on the formal propagation of interpolation uncertainty and surface topography bias, which is often given little attention in the literature. The proposed methods are tested using a number of simulated datasets for Enderby Land and surrounds in Antarctica. The simulated datasets are derived from ICESat data, with different levels of spatially correlated noise applied to each, dependent on regionally specific ice velocities. Both the error (the difference between simulated and estimated dH/dt) and the uncertainty (a function of the interpolation distance and surface slope) are derived. It was found that the formally propagated uncertainty made a good approximation of the error and both the crossover and along-track methods were found to have the lowest uncertainty and error when using Green's function spline interpolation. The errors and uncertainties due to interpolation were an order of magnitude smaller than those obtained from the slope correction method. The overall uncertainty was found to be approximately 50% of the ICESat

single-shot uncertainty budget, showing the relative importance of including these often overlooked contributors in the final uncertainty budget of ice height rate estimates from altimetry data. The proposed methods were then applied to actual ICESat data over part of East Antarctica, including Enderby, Kemp, MacRobertson and part of Dronning Maud Lands. The dH/dt results for the study site generally showed an increase in the rate of change of ice surface height. Although most of the study site was gaining height, there were some regions with negative dH/dt estimates, such as directly behind the grounding line of the Amery Ice Shelf. These negative rates tend to have little impact on the overall estimates of dH/dt, as they are localised to very small regions. The positive rate of height change in the interior was found to be statistically significant, especially near Dronning Maud Land. The uncertainties calculated for this study do not include the ICESat single-shot uncertainty budget, as the focus of the study was the uncertainty contributions of interpolation and surface slope bias. The combination of all of these uncertainties would decrease the significance of the inland signal, however the large number of positive dH/dt estimates found in the interior does suggest that the ice height surface is increasing for this region, implying a positive mass balance change may be occurring in the interior of East Antarctica.

Contents

List of Figures

List of Tables

Nomenclature

DEM:	Digital Elevation Model
dH/dt:	The change in ice height over time
DID:	Dynamic Ice Discharge
dM/dt:	The change in ice mass over time
dV/dt:	The change in ice volume over time
ESL:	Eustatic Sea Level
ESLR:	Equivalent Sea Level Rise
GIA:	Glacial Isostatic Adjustment
GLAS:	Geo-science Laser Altimeter
GMSL:	Global Mean Sea Level
GPS:	Global Positioning System
GRACE:	Gravity and Climate Experiment satellite
ICESat:	Ice, Cloud and land height Satellite
IMBIE:	Ice sheet Mass Balance Inter-comparison Exercise
LGM:	Last Glacial Maximum
MBM:	Mass-Budget Method
RSL:	Relative Sea Level

SMB: Surface Mass Balance

TIN: Triangulated Irregular Network

w.e.: millimetres of water equivalent

Chapter 1

Introduction

Earth surface systems are highly sensitive to changes in climate. Land-born ice (i.e. ice sheets and glaciers) in particular is responding much faster and more strongly to changes in global temperatures than previously anticipated (Alley et al., 2005; Truffer and Fahnestock, 2007). Even a small redistribution of ice from the land to the oceans could lead to sizable increases in future sea-level rise. Present-day redistribution is most evident in regions with mid-latitude and tropical mountain glaciers where strong losses are being observed (Bamber and Payne, 2004; Vaughan et al., 2013). This trend is also being observed on the Greenland, West Antarctic Ice Sheets and to a lesser extent in East Antarctica. However, due to their size and complexity, the true magnitude of this loss is more difficult to determine.

Accordingly, the rapid response of some sections of the ice sheets to present-day climate change - and the uncertainty as to how large these changes are - limits the ability to forecast ice sheet contributions to future sea level (Solomon, 2007). The observation of ice sheet dynamics and their mass exchange with the oceans, as well as understanding the mechanisms that dictate these processes, is crucial in establishing the ice sheets' existing and future contributions to sea level and the uncertainties associated with these.

Over the last two decades, a large amount of research has been targeted at quantifying changes in both ice sheet/glacier dynamics and the rate of ice loss/gain. However, until recently, these estimates have been smaller than their corresponding uncertainties and the 5th IPCC report (Vaughan et al., 2013) highlights that there

are still significant deviations in the rate of loss estimates for the Greenland and Antarctic Ice Sheets. A recent international collaboration of polar scientists called the Ice sheet Mass Balance Inter-comparison Exercise (IMBIE), has attempted to reconcile these differences (Shepherd et al., 2012). They combined estimates from a number of different methods used to calculate ice mass balance. The study shows how much our understanding of ice sheets and glaciers has advanced, but also highlights the need to improve the methods used in estimating changes in ice height and mass.

The motivation behind this research is to help to improve methods used to estimate ice height change and to contribute to the understanding of how fast the Earth's climate system is responding to climate change. More specifically I want to help decrease the uncertainty as to how the ice sheets are reacting to current climate change, so we are able to better understand how they will respond in the future.

This thesis consists of 6 chapters and will be presented in the following order: Chapter 1 describes the current scientific understanding and methods used to estimate sea level rise and ice sheet mass change. Chapter 2 covers the Ice, Cloud, and land height Satellite (ICESat) mission which had the specifically designed Geoscience Laser Altimeter (GLAS) on-board to primarily measure the height changes of ice sheets. Chapter 3 describes the different analysis techniques and interpolation methods used to estimate height from ICESat data. In Chapter 4, I present my unique method of analysing ICESat data to acquire rates of ice height change. I create simulated ICESat datasets to show the accuracy of my method relative to that of previous methods. In Chapter 5, I implement my method to estimate height and mass changes using actual ICESat data and discuss the results. Chapter 6 includes a summary of my findings and concluding remarks.

1.1 Sea level rise

Global eustatic sea level has risen since the last glacial maximum (LGM) (30–19 thousand years before present (kyr BP), Lambeck et al., 2002). There is still some debate as to the amount, however the general consensus is that it has risen between

120 to 130 m, which equates to between ~6 to 10 mm a^{-1} over the entire period (Church et al., 2001; Jansen et al., 2007; Gehrels, 2010) (Figure 1.1). Global sea level rates were relatively small just after the end of the LGM. These rates increased rapidly to an average ~10 mm a^{-1} between ~15 and 6 kyr BP (Church et al., 2001). Around ~7 to 6 kyr BP the global sea level stabilised and the rate went down to approximately 0.5 mm a^{-1} (Gehrels, 2010). The timing of the stabilisation is poorly constrained and some studies suggest much more recent stabilisation dates, between 3 to 2 kyr BP (Church et al., 2001).

This disagreement in dates is largely caused by the variation in sea level estimates at the different sites used in each of the studies (Gehrels, 2010). Furthermore, the Barbados sea-level history (Figure 1.1, blue data points & red line), which is used in many studies (i.e. AR4 & 5) to constrain the LGM and the stabilisation date, is suggested by a number of authors to be significantly influenced by glacial isostatic adjustment (GIA) and therefore suspect (Gehrels, 2010).

GIA is defined as the slow uplift or subsidence of the Earth's crust due to the removal or adding of ice load during a glacial cycle, which in turn can affect a regional rise or fall in the ocean, ice or land surface height (Denton and Hughes, 2002). In more detail, for the past ~700,000 years, the Earth's climate has been defined by ~100,000-year oscillation between interglacial and glacial conditions. These changes in climatic conditions lead to the movement of water and ice over the Earth's surface and acts as a load upon the lithosphere.

The Earth's surface deforms in response to this load and during the glacial period, decreasing temperatures lead to the growth of ice-sheets at the poles under which the earth subsides. As these ice-sheets melt during the inter-glacial period, the load is removed and the earth rebounds. This deformation of the Earth's surface is isostatic, which means the lithosphere is in constant motion attempting to reach a state of equilibrium. A full explanation of GIA can be found in Peltier (2001).

With these uncertainties in mind, Gehrels (2010) states that the onset of modern rates of sea-level rise did not occur at the same time or uniformly across the globe. Nonetheless, sea level rates stabilised around the middle of the Holocene

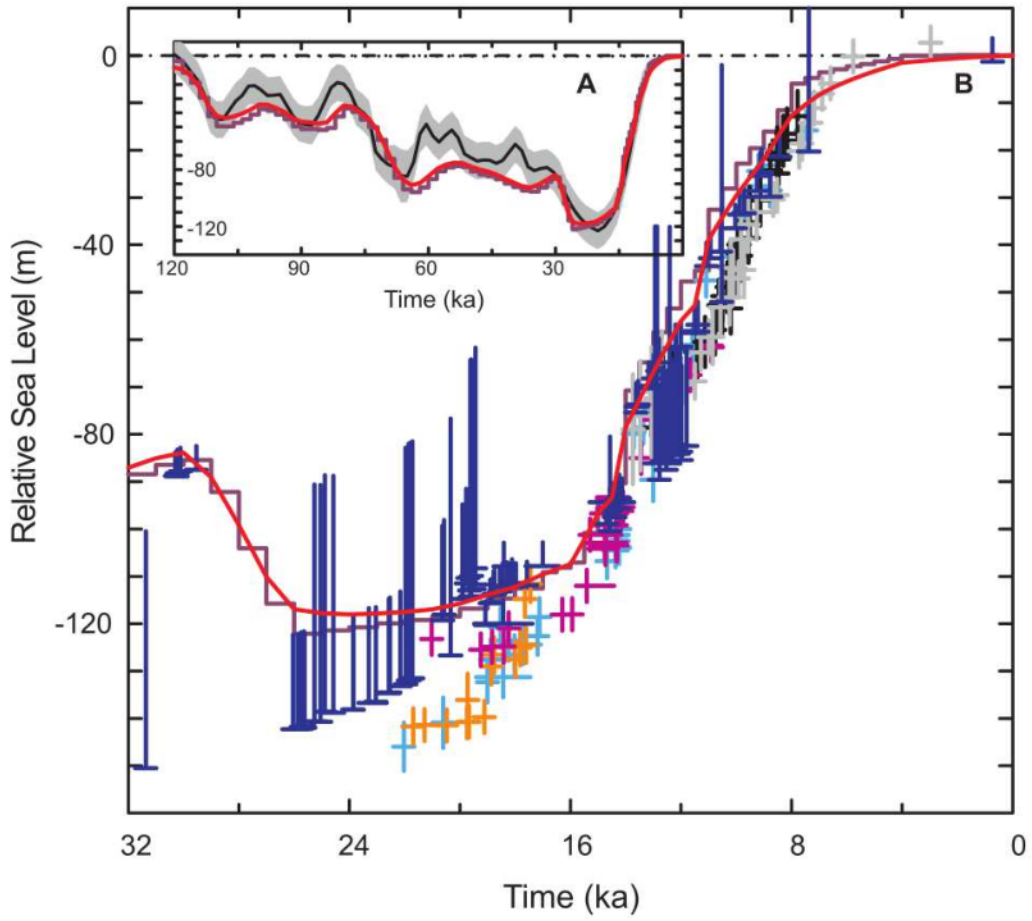

Figure 1.1: A) The ice-equivalent eustatic sea level (ESL) curve over the last glacial-interglacial cycle from analysis of Waelbroeck et al. (2002). The black line represents the median estimate over time and the grey bar defines the estimate of error. The red line represents the ICE-5G (VM2) model prediction of relative sea level (RSL) rise for the island of Barbados in the Caribbean Sea, for both Figures (A) and (B). The ICE-5G prediction of ice-equivalent ESL rise is depicted as a step-continuous brown line for both Figures (A) and (B). The two curves are similar, suggesting that for this location the model is a good approximation of the ESL history. The blue points denote individual coral-based estimates of RSL. The associated error bars are dependent upon the coral species. Shorter error bars are derived from the *Acropora palmata* species. These provide the tightest constraints upon RSL as this species is found to live within ~5 m of modern sea level. RSL Estimates with intermediate sized error bars (20 m length) are obtained from the coral *Montastrea annularis*. While RSL estimates with the longest error bars (<20 m length) are derived from a number of species that are found over a wide range of depths. Coloured crosses denote the ice-equivalent ESL reconstruction of (Lambeck and Chappell, 2001) for Barbados (cyan), Tahiti (grey), Huon (black), Bonaparte Gulf (orange) and Sunda Shelf (magenta). Taken from Jansen et al. (2007).

and, over the last 3,000 years, the average rate of sea level rise has been between 0.1 to 0.2 mm a^{-1} (Church et al., 2001). Sea level is thought to have not changed significantly since 3 kyr BP and it wasn't until the late 19th century that sea levels started to rise again (Church et al., 2001).

Sea level was found to be increasing by 1.7 $\pm$ 0.2 mm a^{-1} from 1900 to 2009, using tide gauge observations (Church and White, 2011) and 2.1 $\pm$ 0.2 mm a^{-1} from 1972 to 2008, using observations from a combination of tide gauges and satellite altimetry (Church et al., 2011) (Figure 1.2a, Table 1.1). From 1993 to 2008 the rate of sea level rise has increased to 2.61 $\pm$ 0.55 mm a^{-1} using tide gauge observations (Figure 1.2a, Table 1.1) and 3.22 $\pm$ 0.41 mm a^{-1} using both tide gauge and satellite altimetry observations (Figure 1.2b, Table 1.1). Although sea level rise has increased and the rate appears to be accelerating, the acceleration is not statistically significant as there is great variation in sea level from 1993 to 2008 (Church et al., 2011; Church and White, 2011). Nonetheless, there has been a significant acceleration in the rate of sea level rise, when the rate has been calculated from 1880 (0.009 $\pm$ 0.003 mm a^{-2}) and also from 1900 to 2009 (0.009 $\pm$ 0.004 mm a^{-2}) (Church and White, 2006) (Figure 1.3).

The sea level rates from 1972 to 2008, and 1993 to 2008 are further broken down by Church et al. (2011) in Table 1.1 and graphically represented in Figure 1.2. For the 1972 to 2008 period the largest contributions to sea level rise are, in order of amount, thermal expansion and the melting of glaciers and ice sheets. The combined Antarctica and Greenland Ice Sheet contribution was smaller than either of the other two contributors. Accordingly, as the overall rate of sea level rise increased for the 1993 to 2008 period, each of the contributions also went up (Church et al., 2011) (Table 1.1). During this time period, the contribution from glaciers and ice sheets increased significantly and, while the thermal expansion rate did increase, the amount was much smaller (Table 1.1). The importance of the Antarctic and Greenland contribution also increased and, as global mean temperatures rise, this contribution is likely to increase (Church et al., 2011; Shepherd et al., 2012).

When all the contributions are combined and compared to the tide gauge and/or

satellite altimetry estimates of sea level rise they are of the same magnitude and are in general agreement (Figure 1.2b). Data prior to 1972 is shown in Figure 1.2 but not used in the estimates, as a drop in sea level in the 1960s is poorly understood (Church et al., 2011). This is likely due to poor data coverage which is unable to adequately resolve the response to and the recovery from the 1963 volcanic eruption of Mount Agung (Church et al., 2011). This eruption may have led to a fall in sea level, due to changes in climate, which is unrepresentative of the general positive trend.

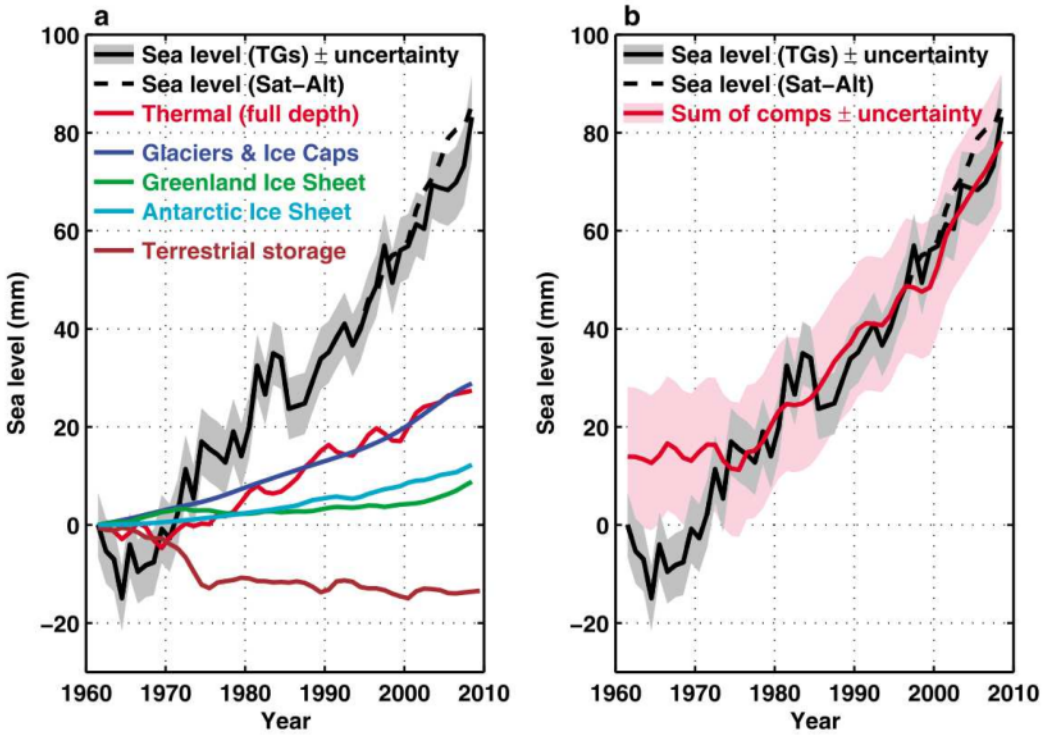

Figure 1.2: Global sea level (1961-2008). (a) The solid black line represents sea level observed using coastal and island tide gauges. The grey bar indicates estimated uncertainty. Sea level observed using TOPEX/ Poseidon/ Jason1 & 2 satellite altimeter data is pictured as a dashed black line. Sea level for this period is shown broken down into its separate contributing components (b) The sum of components in contrast to the overall estimate. The pink shading denotes the uncertainty for the sum of components. Taken from Church et al. (2011).

It is clear that sea level is rising and will continue to do so for the foreseeable future. The role of ice sheets will continue to grow in importance with regards to estimating sea level rise. It is therefore imperative that we increase our understanding of the World's ice sheets and how they will respond to current and future climate change. In the next section I will discuss the general characteristics of these ice sheets.

1.2 Characteristics of the World's largest ice sheets

The World's ice sheets hold enough water to increase average sea level by ∼66 m if it were to all melt (Solomon, 2007; Bamber et al., 2013; Fretwell et al., 2013). This estimate was calculated using only ice on bedrock (grounded ice), as ice floating on the ocean does not contribute to sea level rise. From here on when I use the term

Table 1.1: Global sea level and its contributing components. All rates are linear and in mm a^{-1}. Associated errors are given as one standard deviation estimates. Two estimates of total sea level are presented; from reconstructed tidegauge data (t.g.) and from combining reconstructed tide-gauge and altimeter data from 1993 onwards (t.g. + sat). Each total is given for two different time periods. Component estimates given separately and associated uncertainties obtained from various sources, see Church et al. (2011). Bold numbers indicate sum of other rows, as indicated in first column. Taken from Church et al. (2011)

Component	1972 → 2008	1993 → 2008
Total s.l. (t.g. only)	**1.83 ± 0.18**[b]	**2.61 ± 0.55**
Total s.l. (t.g. + sat)	**2.10 ± 0.16**	**3.22 ± 0.41**
Shallow thermal (0–700m)	0.63 ± 0.09	0.71 ± 0.31
Deep thermal (700–3000m)	0.07 ± 0.10	0.07 ± 0.10
Abyssal thermal (3000m-bottom)	0.10 ± 0.06	0.10 ± 0.06
Total thermal (full depth)	**0.80 ± 0.15**	**0.88 ± 0.33**
Glaciers & Ice Caps	0.67 ± 0.03	0.99 ± 0.04
Greenland Ice Sheet	0.12 ± 0.17	0.31 ± 0.17
Antarctic Ice Sheet	0.30 ± 0.20	0.43 ± 0.20
Land ice (G&IC, GIS, AIS)	**1.09 ± 0.26**	**1.73 ± 0.27**
Thermal (full depth) + Land ice	**1.89 ± 0.30**	**2.61 ± 0.42**
Dam retention	−0.44 ± 0.15	−0.30 ± 0.15
Groundwater depletion	0.26 ± 0.07	0.35 ± 0.07
Natural terrestrial storage	0.07 ± 0.10	−0.14 ± 0.10
Total terrestrial storage	**−0.11 ± 0.19**	**−0.08 ± 0.19**
Total mass contributions	**0.98 ± 0.33**	**1.66 ± 0.33**
Total thermal + Mass	**1.78 ± 0.36**	**2.54 ± 0.46**
Residual (t.g. only)	**0.05 ± 0.40**	**0.08 ± 0.72**
Residual (t.g. + sat)	**0.32 ± 0.39**	**0.69 ± 0.62**

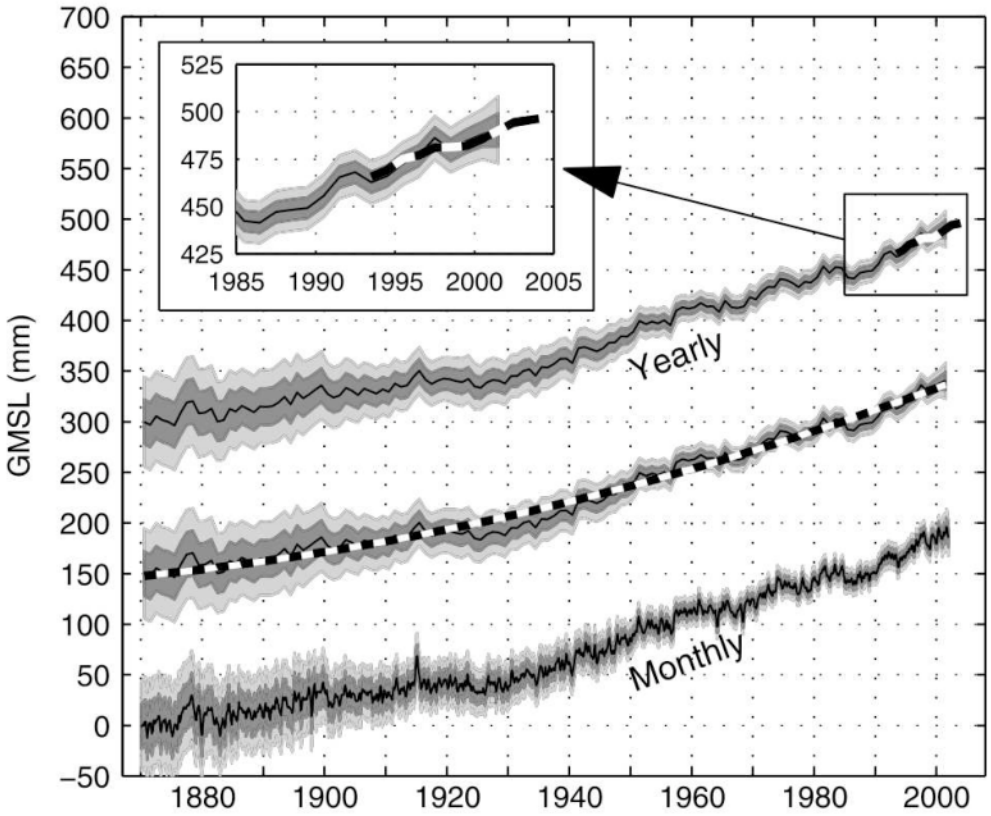

Figure 1.3: Global mean sea level (GMSL) according to the reconstruction for January 1870 to December 2001. Monthly GMSL denoted by the bottom line. The yearly GMSL with the quadratic fit (black and white line) offset by 150 mm represented by the middle line. The top line, again offset by a further 150 mm, represents the yearly GMSL with satellite altimeter data superimposed. The dark and light shading denote one and two standard deviation errors, respectively. Taken from Church and White (2006).

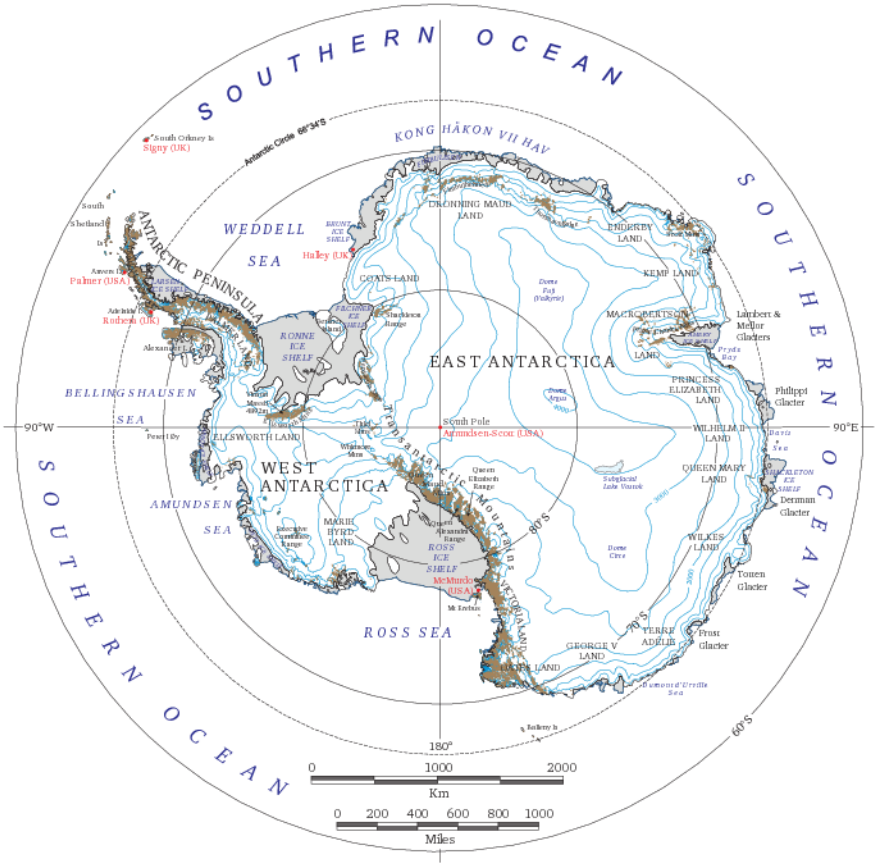

Figure 1.4: A map of Antarctica. The Antarctic Ice Sheet is the largest in the world. It can split up into the East and West Antarctic Ice Sheets. Each has its own unique bedrock topography and climate, which effects the way these ice sheets respond to climate change. Taken from http://lima.nasa.gov/pdf/A3_overview.pdf

"ice sheets" I am referring to grounded ice, unless otherwise noted. The main two ice sheets are the Antarctic and Greenland Ice Sheets.

The Antarctic Ice Sheet is the largest body of land ice in the world, with a volume of 26.92 * 10^6 km^3, and covers 98% of the continent (Fretwell et al., 2013). Its mean ice thickness, excluding ice shelves, is ~2 km, and is at its thickest in the Astrolab sub-glacial basin, where it is 4897 m from the bedrock to the surface (Fretwell et al., 2013). Approximately 88% of all land ice is found in Antarctica, which would raise global sea level by 58.3 m if completely melted. The Antarctic continent is broadly divided into two regions, East and West Antarctica (Figure 1.4). Each region has its own unique bedrock topography and climate, which affects how their corresponding ice sheets respond to changing climate.

The East Antarctic Ice sheet is mainly above sea level, making up ~81% of total grounded ice mass found in Antarctica. This equates to 53.3 m of equivalent sea

level rise (ESLR), making it the largest potential contributor to sea level (Fretwell et al., 2013). The majority of the ice is locked in the interior of the continent, which is also where the ice sheet is at its thickest. Surface slope is negligible, as most of the interior is flat (Fretwell et al., 2013). Consequently, ice flow rates (velocities), which are a function of slope and ice thickness, are slow (Bamber et al., 2001). The coastal margins have a more variable bedrock topography with higher slopes. Nevertheless the ice velocities are generally lower than in West Antarctica and Greenland, as the slopes are lower and much of the ice sheet is buttressed by ice shelves with slow flow rates (Bamber et al., 2001). There are notable exceptions to this general trend, such as the Totten Glacier, which is showing signs of acceleration (Pritchard et al., 2009). Although most of the ice is above sea level, ∼36% (or 19.2 m ESLR) of the ice is below sea level, making it more susceptible to marine incursion in the event of large scale deterioration of ice shelves along the coast (Figure 1.5) (Fretwell et al., 2013).

The West Antarctic Ice Sheet, which also includes the Antarctic Peninsula, is much smaller than its eastern counterpart, holding ∼7% of the Antarctic ice mass (4.3 m and 0.2 m ESLR, respectively). In contrast to East Antarctica, a large amount of ice is held in the ice shelves which cover large areas of West Antarctica. The ice sheet topography for this region is defined by a bedrock of steep valleys, which leads to higher surface slopes and consequently higher ice velocities. As the ice sheet passes the grounding line and turns into ice shelves, its velocity continues to remain high. Grounded ice below sea level makes up ∼79% (3.4 m ESLR) and ∼50% (0.1 m ESLR) of the total ice mass for the West Antarctic Ice Sheet and the Peninsula, respectively (Figure 1.5) (Fretwell et al., 2013). As most of the ice is below sea level and protected by the large ice shelves which buttress the land ice, the ice sheet is far more vulnerable to future marine incursions as global mean temperature rises. Recent evidence suggests that marine instabilities are occurring in West Antarctica and will continue to increase (Joughin et al., 2014; Rignot et al., 2014).

Greenland has the second largest ice sheet, which covers roughly 80% of the

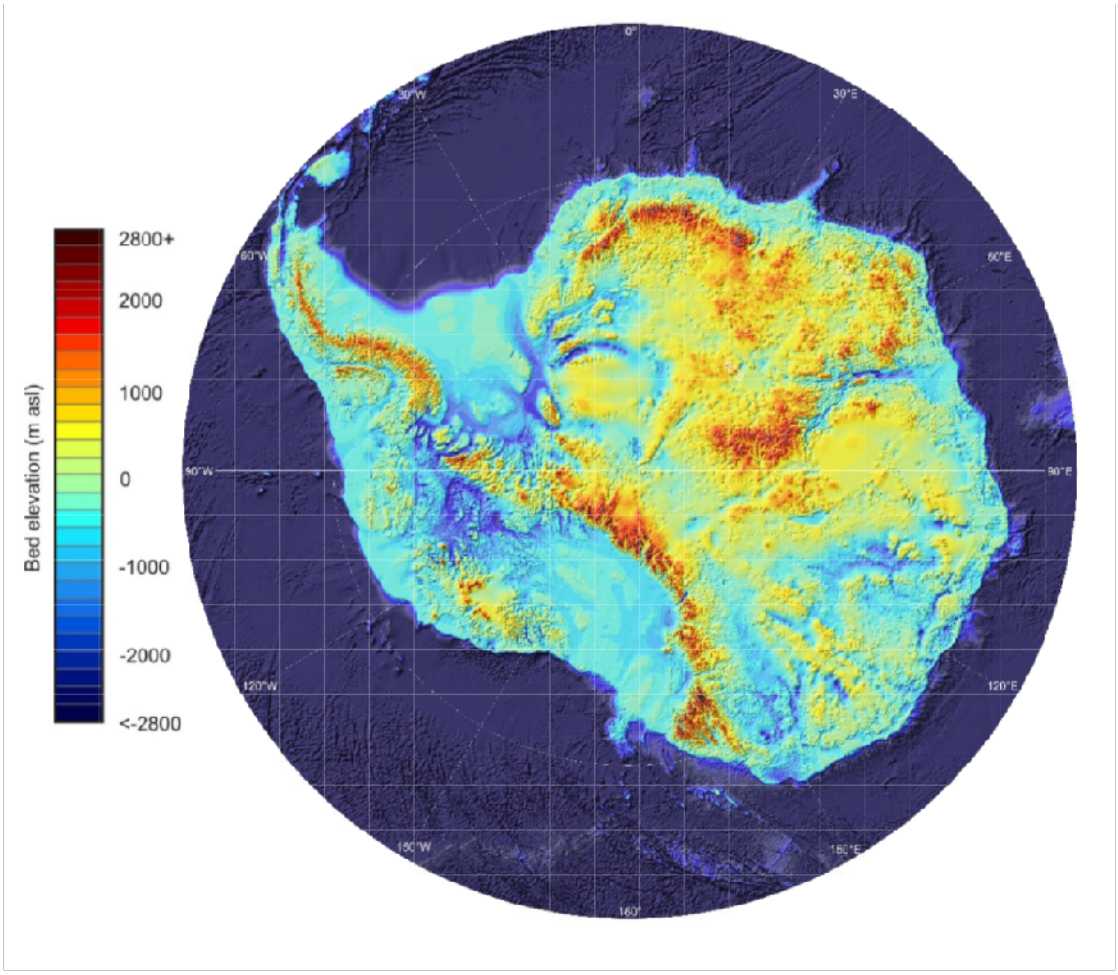

Figure 1.5: A map of the bedrock elevation of Antarctica. The majority of the continent is above sea level. ∼36% of East Antarctica and ∼79% of West Antarctica are below sea level. These areas are more susceptible to changes in climate. Taken from Fretwell et al. (2013).

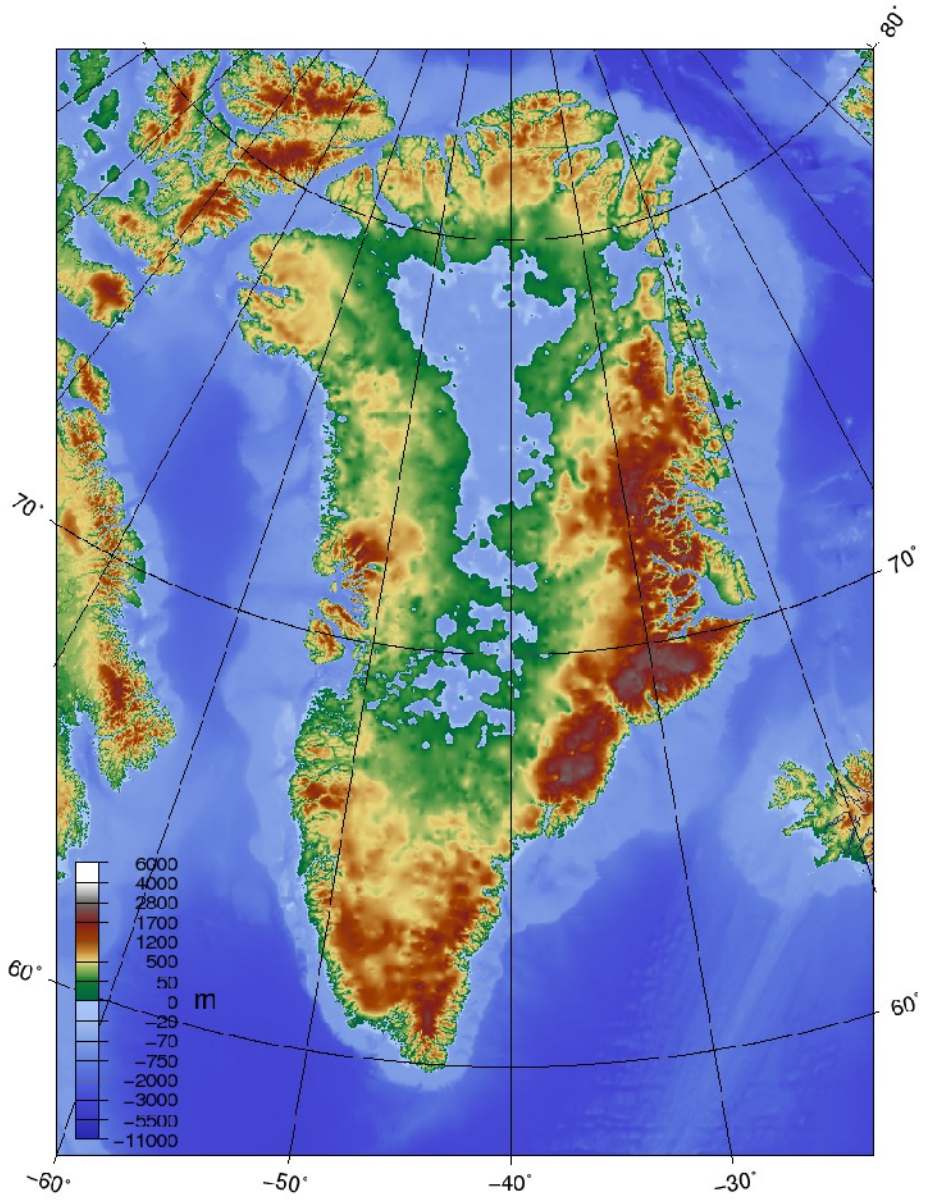

Figure 1.6: A map of the Greenland bedrock. The majority of the land is above sea level with ∼22% below sea level. Taken from Bamber et al. (2013).

island with a volume of 2.96 * 10^6 km^3 (Bamber et al., 2013). It holds ∼11% of the world's ice (7.36 m ESLR) and ∼22% (1.62 m ESLR) of this grounded ice is below sea level (Figure 1.6) (Bamber et al., 2013). Most of the ice is terrestrial and its broad front does not reach the coast. Instead the ice sheet is pushed into steep valleys, which form glaciers that interface directly with the ocean. This makes them far more susceptible to change in sea temperature, as there is no ice shelf to help mitigate the ice velocity and melt. The last 1% (∼0.65 ESLR) of Earth's ice mass is found in glaciers and ice caps, snow on land and permafrost (Solomon, 2007).

It is clear that the Earth's ice sheets are in constant flux and very dynamic

environments that, depending on their geography, will respond differently to climate change. Evidence of this can be found in geological records, which illustrate that prehistoric ice sheets of similar size to their present day counterparts have rapidly lost ice, causing increases in sea level of up to ∼12 m in less than 500 radiocarbon years (Fairbanks, 1989). Although presently it is difficult to determine whether such a collapse is imminent or likely, even a small increase in sea level contribution of all or some of the ice sheets would have a great effect on future sea level rise (Monaghan et al., 2006). Needless to say any change in either sea level or climate would have socio-political implications on a global scale (Stern, 2007).

It is therefore extremely important that we are able to determine how much the ice sheets are contributing to sea level rise. To accomplish this we must obtain the "mass balance" of each of the ice sheets. The mass balance of an ice sheet is the difference between the total snow accumulation input and the total loss through melting, ablation, or ice shelf calving. When an ice sheet's total accumulation equals the total losses it is thought to be in equilibrium. However if either the input or the output exceeds the other, the mass balance can be become either positive or negative, respectively. If an ice sheet mass balance has become negative it will start to contribute to sea level rise. In the next two sections I will discuss, firstly, the current methods used to calculate the ice sheet mass balance, and secondly the current mass balance estimates for the Antarctic and Greenland Ice Sheets.

1.3 Methods for estimating height and mass balance change

Currently, three different observation techniques are being employed to estimate height and mass balance change over the Antarctic and Greenland Ice Sheets: satellite gravimetry, the mass-budget method and satellite altimetry. With the help these methods, the understanding of ice sheet dynamics and mass exchange is greatly increased. However, these methods have a number of limitations which must be addressed when making any long term mass balance predictions. I will only briefly

outline and discuss satellite gravimetry and the mass-budget method as they are not the focus of my study. I give a more in-depth account of satellite altimetry and discuss the ICESat mission in more detail in Chapter 2.

1.3.1 Satellite Gravimetry

The Gravity and Climate Experiment (GRACE) satellite mission is the only dedicated satellite mission that is measuring the Earth's temporal gravity field. There have been two other satellite gravimetry missions in the past, the Challenging Minisatellite Payload (CHAMP) and the Gravity Field and Steady-State Ocean Circulation Explorer (GOCE). Of the three missions, GRACE has the longest life span and it has been used extensively for estimating mass changes in polar regions. The mission measurements are taken by precisely monitoring the separation of a pair of satellites that travel ∼200 km apart and have virtually the same orbit (Tapley et al., 2004). Changes in ice sheet mass are large enough to affect the orbits of the satellites and can therefore be measured by GRACE.

GRACE-based mass balance estimates of Antarctica are generally derived from 10-day to monthly spherical-harmonic gravity fields, depending on the study (Ramillien et al., 2006; Velicogna and Wahr, 2006). The spatial resolution is dependent on the Stokes coefficients degree (l) and order (m) and the greater these values the higher the spatial resolution. A spherical harmonic model of degree 120 has a spatial resolution of ∼150 km; however most studies tend only to use solutions with a maximum degree of 50 or 60, as beyond this point the estimates for the coefficients are dominated by noise rather than signal (Ramillien et al., 2006; Velicogna and Wahr, 2006). This does, however, lead to lower spatial resolutions varying between ∼400 km to ∼600 km depending on the study.

Even when using solutions with a maximum degree of 60 and below, a destriping filter must be applied to remove north-south stripes that are present in the GRACE data, which would otherwise contaminate the gravity signal (Chen et al., 2006). These filters are effective in removing the striping, however, there remains a need to apply a spatial averaging filter, which can range from simple isotropic Gaussian fil-

ters to more sophisticated anisotropic filters (Klees et al., 2008). This application of filters to remove systematic errors can lead to the gravity signal being contaminated or removed.

The GRACE gravity field is an integral of mass of the atmosphere, oceans, uplift, subsidence and water on the land in the form of aquifers, rivers, lakes etc. Consequently, if there is mass variation occurring it can not be determined directly from GRACE alone which of the above sources is causing the change (Wahr et al., 2006). It is up to the user of the data to find an independent way of separating the contributions to the overall mass change. This separation of mass components can lead to errors in the estimates.

There are three main categories that errors can fall into. The first group of errors are associated with the models the user applies to the data to separate the contributions of the atmosphere, oceans, land etc. In the case of Antarctica, GIA is the most important error, as it is poorly constrained for this region, which has a very large impact on the final estimates of mass change. The second is errors associated with satellite itself which include: gravity and orbit estimation, atmospheric drag, solar and Earth radiation pressure, oscillator and system noise (Kim and Tapley, 2002). The last group of errors is associated with the forcing models used to estimate the background gravity field including: mean earth gravity, solid, ocean, pole tides, non-tidal ocean and atmosphere, lune-solar & planetary (3rd body) perturbations etc. (Tapley et al., 2005).

1.3.2 Mass-budget method

The mass-budget method (MBM) or or flux component method estimates the difference between the sum of all the mass inputs (precipitation in the form of snow-fall) and the sum of all outputs (sublimation, melt-water run-off and ice breaking off into the ocean) (Rignot et al., 2008; Allison et al., 2009; van den Broeke et al., 2009). Mass-budgets can be calculated for the whole continent or on a regional scale, for instance drainage basins (Rignot et al., 2011b).

To obtain an accurate estimation of mass input, a sound understanding of snow

accumulation is needed. Snow accumulation can vary both spatially and temporally and consequently needs to be constrained by observations or models. Classically, snow accumulation is measured using in situ methods. Direct measurements can be taken by installing marker poles that are checked regularly. These, however, only give short temporal data sets (Forsberg et al., 2000). Longer snow accumulation records can be obtained by digging and interpreting ice cores and snow pits. Both these methods are problematic in that they are sparsely distributed and it would not be feasible to measure large parts of Antarctica in this way.

Consequently, other methods are required to fill in the large areas between survey sites. Arthern et al. (2006) used satellite based microwave readings of temperature and surface micro structure, which are both correlated to snow accumulation, to interpolate between the direct measurement survey sites.

With the advent of high resolution regional atmospheric circulation models, snowfall patterns have been modelled over ice sheets and have found to be in general agreement with the in situ measurements (van de Berg et al., 2006; Rignot et al., 2008; Lenaerts et al., 2012). There are uncertainties associated with each of these models which need to be included in the final uncertainty budget.

Mass output is generally measured at the point where ice is discharged across the grounding line of an ice sheet. This discharge is quantified by measuring the speed of ice flow and the thickness of the column of moving ice (Allison et al., 2009). Recently, these mass output estimates have greatly improved by using a combination of interferometric synthetic aperture radar (InSAR) (Shepherd and Wingham, 2007; Joughin et al., 2010; van den Broeke et al., 2011; Rignot et al., 2011b) and improved ice thickness data (Bamber et al., 2013; Fretwell et al., 2013).

Although the estimates of ice velocity have greatly improved, uncertainties still remain. For instance, ice velocity varies with depth and InSAR is only able to sense the ice velocity of the surface. Consequently an average ice velocity is used to compensate for this. This contributes to error in the estimates using this approach, as the average velocity of the discharged ice column is often less than the surface velocity (Allison et al., 2009).

Table 1.2: A list of current and past satellite mission with radar or laser altimeters on-board.

Satellite	Operational date	Latitudinal extent
Seasat	June - October 1978	+75
Geosat	March 1985 - December 1989	±72
ERS-1	July 1991 - March 2000	±81.5
ERS-2	April 1995 - September 2011	±81.5
TOPEX/POSEIDON	August 1992 - January 2006	±66
Jason-1	December 2001 - July 2013	±66.15
Jason-2	June 2008 - still operational	±66.15
Envisat	March 2002 - May 2012	±81.5
ICESat	January 2003 - February 2010	±86
CryoSat-2	April 2010 - still operational	±88

1.3.3 Satellite altimetry

Satellite altimetry has been in use since 1978 with the launch of Seasat, a radar altimeter. Since then, there have been a series of radar altimetry satellites (Geodetic Satellite (Geosat), TOPEX/POSEIDON, the remote sensing satellites (ERS-1 & ERS-2), Jason-1 & Jason-2, Environmental Satellite (Envisat) and CryoSat-2) all with similar mission objectives to measure ocean and/or land/ice surface height (1.2). It was only with the launch of the Ice, Cloud and land height Satellite (ICESat), that the first laser altimeter became operational. It was also the first satellite with the primary mission objective to sense changes in the height of the major ice sheets.

All these satellite altimetry missions measure surface height (either land, ice or sea) by firstly determining the location of the satellite by precision orbit determination. This is generally accomplished by using a combination of the GPS tracking system and satellite laser ranging between the satellite and the International Laser Ranging Service station network (Schutz et al., 2005). With this, the altitude of the satellite altimeter can be determined (Figure 1.7). This is accomplished by measuring the time it takes for the pulse to leave the satellite, reflect off the surface of the Earth and return to the satellite. More specifically:

$$\triangle t = t_R - t_T \tag{1.1}$$

where $\triangle t$ is the pulse trip time and t_T is the pulse transmit time and t_R is the pulse receive time (Kolensky, 2012). The scalar range, ρ (the distance from the satellite to the Earth) is:

$$\rho = \frac{c\triangle t}{2} \tag{1.2}$$

where c is the speed of light (Kolensky, 2012), ρ can also be defined as the altitude of the satellite (Nguyen, 2006). The range must be corrected for tropospheric delays, atmospheric delays, solid Earth and ocean tides. We now have the altimeter measurement ρ , which combined with the precision attitude determination $\mathbf{u}$ gives us the vector $\mathbf{H}$:

$$\mathbf{H} = \rho\mathbf{u} \tag{1.3}$$

To obtain the surface height, $\mathbf{R}_{\text{spot}}$, we require the position of the satellite with regards to the Earth's centre of mass (Kolensky, 2012) (Figure 1.7). This is denoted as geocentric position vector, $\mathbf{R}$, and is acquired from precision orbit determination, this is discussed later in Chapter 2 (Kolensky, 2012). Therefore to obtain the height of the surface with regards to the centre of the Earth, $\mathbf{R}_{\text{spot}}$:

$$\mathbf{R}_{\text{spot}} = \mathbf{R} + \mathbf{H} \tag{1.4}$$

The accuracy of the height estimate, $\mathbf{R}_{\text{spot}}$, is dependent on a number of factors, including, satellite orbit determination, pointing errors and attitude determination, atmospheric delay and scatter, forward scattering and saturation (Kedar et al., 2003; Csatho et al., 2005; Fricker et al., 2005; Luthcke et al., 2005; Brenner et al., 2007). Each of these contributes to the single shot error budget of the satellite mission.

Geophysical processes must also be accounted for when estimating surface height. These include GIA, solid earth tide, ocean tide loading, geo-centre motion, pole tide, firn densification and ice density (Ivins and James, 2005; Helsen et al., 2008; Ligtenberg et al., 2011). If not accounted for, each of these could be interpreted as changes in height. Significant effort is required to correct for these processes before

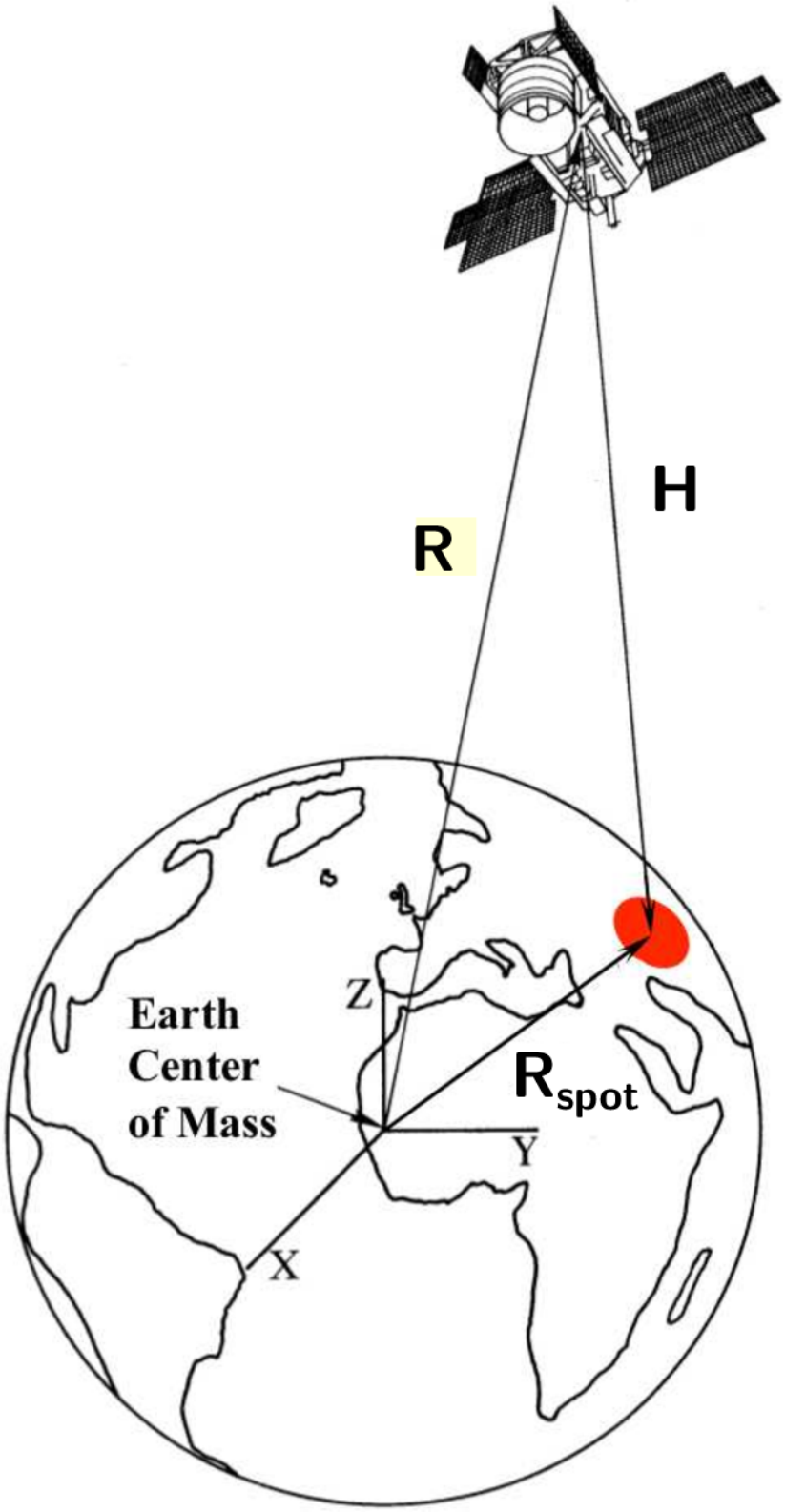

Figure 1.7: Surface height determination, denoted as $\mathbf{R}_{\text{spot}}$. The surface height is acquired by adding the vectors $\mathbf{R}$ and $\mathbf{H}$. $\mathbf{R}$ is the position of the satellite with regards to the Earth's centre of mass. $\mathbf{H}$ refers to the altitude of the satellite. Figure taken from (Schutz and Zwally, 2008) and modified.

data products are released.

The accuracy of surface height measurements is also dependent on the surface properties of the measured point. Lacroix et al. (2007) found that radar altimeters are sensitive to dielectric and penetration properties of the measured medium (i.e. snow and ice). Consequently the surface height measurements can be biased due to the internal structure of the sensed medium. Laser altimeters are less sensitive to the measured medium as the signals are directly reflected off the surface. There is also a negative consequence of this as the signal can get saturated. I discuss this later in Chapter 2.

Nonetheless, all satellite altimeters are affected by surface topography. In general terms, the flatter and smoother a surface, with regards to the footprint size, the more accurate the return; conversely, a steeper, rougher or undulating surface will lead to an inferior return (Davis and Moore, 1993). Ice sheets are characterised by generally having an even surface in their interior and steep undulating surfaces around their margins (Partington et al., 1989). Drainage basins and channels bisect the interior and the margin, adding further variability. Most of the variability occurs around the margins, where these drainage basins interface directly with the ocean (Rignot, 2006). Consequently, those regions which are most important in terms of understanding ice sheet dynamics and height/mass changes are also the regions where the altimetry measurements are the least accurate.

1.4 Ice sheet mass balance

1.4.1 Antarctica mass balance estimates

The overall mass balance estimate for Antarctica ranges from -69 to -147 Gt a^{-1}, with an associated uncertainty ranging from 5 to 80 Gt a^{-1} (Table 1.3) (Wu et al., 2010; Shi et al., 2011; King et al., 2012; Shepherd et al., 2012; Sasgen et al., 2013; Velicogna and Wahr, 2013). Much of the variation in the estimates can be attributed to either the dataset (ICESat, GRACE, MBM) or the GIA model used. Table 1.3 presents some of the most recent mass balance estimates for Antarctica, using the methods described in Section 1.3. In contrast to Greenland, where the mass balance

Table 1.3: Recent mass balance estimates for Antarctica. Some studies only made an estimate for the whole Antarctic continent available. * Includes the Antarctic Peninsula. N/A denotes no dM/dt estimate available.

Study	Method	Time span	EAIS mass estimate (Gt a^{-1})	WAIS mass estimate* (Gt a^{-1})	AIS mass estimate (Gt a^{-1})
Sasgen et al. (2013)	GRACE (AGE1b)	2003 - 2012	26 ± 13	140 ± 19	114 ± 23
Velicogna and Wahr (2013)	GRACE (IJ05_R2)	2003 - 2012	N/A	N/A	–83 ± 49
	GRACE (ICE5G)		N/A	N/A	–147 ± 80
King et al. (2012)	GRACE	2002 - 2010	60 ± 13	-118 ± 9	-69 ± 18
Shepherd et al. (2012)	Combined	2000 - 2011	26 ± 36	-114 ± 34	-87 ± 43
Shi et al. (2011)	ICESat	2003 - 2008	N/A	N/A	-73 ± 5
Wu et al. (2010)	GRACE + GPS	2002 - 2009	23 ± 29	64 ± 32	-87 ± 61

signal is affected by both surface mass balance (SMB) change and dynamic ice discharge to an equal extent, most Antarctica mass balance changes are due to dynamic ice discharge (Vaughan et al., 2013). There are some anomalous SMB signals in East Antarctica as well as higher than previously estimated accumulation along the coastal margin (van Ommen and Morgan, 2010; Boening et al., 2012; Shepherd et al., 2012). However these regional signals do not have a significant effect on the overall mass balance of Antarctica (Vaughan et al., 2013).

These estimates are affected by the three regionally distinct mass balance signals of West Antarctica, East Antarctica and the Antarctic Peninsula. It is well documented that West Antarctica and the Antarctic Peninsula are undergoing large negative mass balance changes (Chen et al., 2006; Shepherd and Wingham, 2007; Rignot et al., 2008; Shepherd et al., 2012; Vaughan et al., 2013; Velicogna and Wahr, 2013), however, the overall contribution that Antarctica makes to global sea-level rise is still uncertain (Shepherd and Wingham, 2007; Shepherd et al., 2012). This is due mainly to the large uncertainty about the state of the East Antarctica Ice

Sheet. This uncertainty is a result of poorly constrained geophysical models that underpin the East Antarctic Ice Sheet dynamics. This is due to a number of factors including; size, topographic complexity of the bedrock, isolation and GIA (Peltier, 2004; Ivins and James, 2005; Chen et al., 2006; Shepherd and Wingham, 2007). All of these factors must be taken into account when computing any measurements of height or mass change. Furthermore, the interior of East Antarctica is very large, so even though the mass signals are generally small, their combined contribution can be large. The uncertainties associated with these estimates when integrated over this large area are also substantial; often larger than the estimate.

Nonetheless, over the past three decades remote sensing has allowed scientists to start to solve the puzzle of the Antarctic Ice Sheet. The general consensus presently is that the West Antarctic Ice Sheet is losing mass in the range of -64 to -140 Gt a^{-1} with associated uncertainties ranging from 9 to 34 Gt a^{-1} (Table 1.3 (Wu et al., 2010; Shi et al., 2011; King et al., 2012; Shepherd et al., 2012; Sasgen et al., 2013; Velicogna and Wahr, 2013). There is less agreement in the case of East Antarctica, with mass estimates ranging from slightly positive to negative. The most recent studies suggest that East Antarctica is gaining mass (King et al., 2012; Shepherd et al., 2012; Sasgen et al., 2013), with estimates ranging from -23 to 60 Gt a^{-1}, with associated uncertainties ranging from 13 to 36 Gt a^{-1} (Table 1.3 (Wu et al., 2010; Shi et al., 2011; King et al., 2012; Shepherd et al., 2012; Sasgen et al., 2013; Velicogna and Wahr, 2013).

Many of the uncertainty estimates for East Antarctica are larger than the mass estimates, which puts the significance of these results in question (Shepherd et al., 2012). This ambiguous mass balance range for East Antarctica suggests that larger quantities of observations with better accuracies are needed, on an ice sheet scale but more importantly on a regional scale. It is at the regional scale that the first signs of change are generally found, for instance, glaciers grounded on or under sea level are more susceptible to climate variability and are often the initial indicators of future large mass balance changes (Davis et al., 2005).

Negative mass balances are being observed on a regional scale throughout the

Antarctic Ice Sheet. For instance Rignot et al. (2008), using radar interferometry, found that in West Antarctica there were widespread losses along the Bellingshausen and Amundsen seas increasing the regional ice sheet loss by 59% in 10 years and reaching 132 $\pm$ 60 Gt a^{-1} in 2006. This is similar to the more recent King et al. (2012) GRACE estimate of -108 $\pm$ 8 Gt a^{-1} (2002 - 2010). The largest losses in this region occurred in the Pine Island and Thwaites Glacier basins, -24 $\pm$ 7 and -54 $\pm$ 5 Gt a^{-1}, respectively (King et al., 2012). These estimates are in good agreement with other mass balance and ice loss studies (Rignot et al., 2008; Pritchard et al., 2009, 2012; Sasgen et al., 2013).

On the Antarctic Peninsula, mass loss has increased by 140% from 25 $\pm$ 45 Gt a^{-1} in 1996 to 60 $\pm$ 46 Gt a^{-1} in 2006 (Rignot et al., 2008). This increase is not so pronounced in other recent studies, -20 $\pm$ 14 Gt a^{-1} (Shepherd et al., 2012) (reconciled method) and -26 $\pm$ 3 Gt a^{-1} (Sasgen et al., 2013) (GRACE), but is still substantial. The main mass losses were concentrated around the Larsen A & B Ice Shelves and outlet glaciers and are caused by present and past glacial acceleration.

Although the overall East Antarctic mass balance estimate tends to be positive for most studies, there are basins where loss is occurring. Most notable are the Denman & Phillipi glacier basins and the Totten & Frost glacier basins in Wilkes Land, which are both losing mass of -11 $\pm$ 24 and -9 $\pm$ 43 Gt a^{-1}, respectively (Rignot et al., 2008). The uncertainties for these glacier basin estimates are large, due to the firn depth correction and snow accumulation error. More recent GRACE and ENVISAT studies have found substantial losses for the whole Wilkes Land region (Flament and Rémy, 2012; King et al., 2012; Sasgen et al., 2013). Sasgen et al. (2013) and King et al. (2012) obtained a similar results using GRACE data, but with a smaller uncertainties of -13 $\pm$ 2 Gt a^{-1} and -9 $\pm$ 4 Gt a^{-1}, respectively.

1.4.2 Greenland mass balance estimates

Unlike Antarctica, the mass loss signal for Greenland is very clear, with most estimates being much larger than their associated uncertainties (Wouters et al., 2008; van den Broeke et al., 2009; Schrama and Wouters, 2011; Sørensen et al., 2011;

Table 1.4: Recent mass balance estimates for Greenland. All studies are using only mainland data and do not include nearby islands. MBM stands for Mass Balance Method.

Study	Method	Time span	Mass estimate (Gt a^{-1})
Siemes et al. (2013)	GRACE	2003 - 2008	-165 ± 15
Ewert et al. (2012)	ICESat	2003 - 2008	-185 ± 28
	GRACE	2002 - 2009	-191 ± 21
Shepherd et al. (2012)	Combined	2000 - 2011	-211 ± 37
Sasgen et al. (2012)	GRACE	2002 - 2011	-240 ± 18
	MBM	2002 - 2011	-244 ± 53
	ICESat	2003 - 2009	-245 ± 28
Sørensen et al. (2011)	ICESat	2003 - 2008	-191 ± 23
Schrama and Wouters (2011)	MBM	2003 - 2010	-201 ± 20
Zwally et al. (2011a)	ICESat	2003 - 2007	-171 ± 4
Pritchard et al. (2010)	GRACE	2003 - 2009	-195 ± 30
van den Broeke et al. (2009)	MBM & GRACE	2003 - 2008	-237 ± 20

Zwally et al., 2011a; Shepherd et al., 2012; Siemes et al., 2013). Table 1.4 shows a collection of rates of mass change for a number of recent studies that estimated mass balance, using one of the three methods described in Section 1.3. The mass change estimate ranges from -165 to -245 Gt a^{-1} with the associated uncertainty ranging from 4 to 53 Gt a^{-1}.

The mass loss in Greenland can approximately be attributed to one half surface mass balance (SMB) loss (i.e. runoff) and one half to dynamic ice discharge (DID) over the grounding-line (van den Broeke et al., 2009; Sasgen et al., 2012). However, the relative importance of either SMB or DID varies substantially on a basin scale (Pritchard et al., 2009; van den Broeke et al., 2009; Pritchard et al., 2010; Sasgen et al., 2012; Vaughan et al., 2013).

The largest mass losses occurred in the south-west and south-east between 2002 and 2011. There is variation in the data range depending on the dataset used, for instance the ICESat temporal coverage spans from 2003 to 2009. The losses due to SMB and DID in these two regions were both substantial (Pritchard et al., 2010; Sasgen et al., 2012; Siemes et al., 2013). However, the mass loss in the south-east (ranging from -83 to -126 Gt a^{-1} with an error of range of 13 to 29 Gt a^{-1}) was to a greater extent attributed to DID (Pritchard et al., 2010; Zwally et al., 2011a;

Sasgen et al., 2012; Siemes et al., 2013). The rate estimates for the south-east are a combination of basins D and C, (Sasgen et al., 2013), other studies have approximately similar basins. By contrast, the mass loss in the south-west was due more to changes in SMB. The mass loss estimates for this region ranged from -28 to -69 Gt a^{-1} with an error of 7 to 13 Gt a^{-1} (Pritchard et al., 2010; Zwally et al., 2011a; Sasgen et al., 2012; Siemes et al., 2013). Zwally et al. (2011a) obtained a positive mass estimate of 20 Gt a^{-1} for the region above 2000 m altitude, suggesting that accumulation was occurring.

In the north and north-east of Greenland, the losses of between -15 to -32 Gt a^{-1} with an error of range of 4 to 10 Gt a^{-1}(combined A and B basins, (Sasgen et al., 2012), other studies have approximately similar basins) are almost entirely due to surface melt (SMB) (Pritchard et al., 2010; Sasgen et al., 2012; Siemes et al., 2013). The mass loss rates are lower than in the south where DID is the major source of mass loss (Sasgen et al., 2012). This is attributed to snow accumulation in the interior of Northern Greenland which has increased the SMB. This is not enough, however, to offset the overall mass loss.

Interestingly, Siemes et al. (2013) estimated a slight increase in mass of 4 ± 5 Gt a^{-1} for north-east Greenland (basin G2, Siemes et al. (2013), other studies have approximately similar basins) for the years 2003 to 2008. The uncertainty is larger than the estimate, so this estimate is not statistically significant. They attributed this to the years 2005 to 2006, where they estimated a statistically significant mass increase of 24 ± 6 Gt a^{-1}, which may have been caused by the increased accumulation mentioned above. The rest of the years all have negative mass estimates, which decreased the mass gain for that region. Zwally et al. (2011a) obtained a similar mass increase result of 16 Gt a^{-1} for the combined basins. Most of this mass gain occurred above 2000 m with a gain of 18 Gt a^{-1}. While -2 Gt a^{-1} of ice were lost from below 2000 m, no uncertainties were presented in their study. Again this shows that accumulation was occurring in the interior of Northern Greenland.

The north-west is similar to other northern regions of Greenland in that $\sim$75% of the mass loss is from SMB. However $\sim$25% of the loss is due to DID which is not the

case for the rest of Northern Greenland (Sasgen et al., 2012). Mass loss rates range from -30 to -58 Gt a^{-1} with an error range of 3 to 7 Gt a^{-1} (Pritchard et al., 2010; Zwally et al., 2011a; Sasgen et al., 2012; Siemes et al., 2013). Again Zwally et al. (2011a) found a positive rate of 5 Gt a^{-1} above 2000 m. Even though there appears to be accumulation occurring over much of the interior of Greenland, it is surpassed by the SMB and DID loss along the coast at less than 2000 m. In contrast to this general trend, Flade Isblink (81.4 N, 15.1 W) and Storstrømmen (77.1 N, 22.6 W) outlet glaciers are gaining mass. It is thought that as these glaciers originate in the interior, the positive signal may be caused by processes occurring inland (Pritchard et al., 2010; Sørensen et al., 2011).

1.5 Summary

Our understanding of mass balance in Antarctica and Greenland has increased dramatically over the past two decades. The IMBIE project shows us that, in general, all the methods of estimating mass balance are in agreement, especially in West Antarctica and Greenland (Shepherd et al., 2012). By combining the mass balance estimates from different methods, we can obtain a level of certainty that has not previously been possible. The IMBIE project also highlights the need for a longer reconciled time series, which can be achieved through future missions that are designed to measure changes in ice mass.

Chapter 2

The Ice, Cloud and land height Satellite (ICESat) - An overview of the mission and data analysis techniques

2.1 ICESat Mission overview

ICESat was launched on 13 January 2003 as part of NASA's Earth Science program within NASA's Earth Observing System (EOS) group. Its primary objective was to estimate present day ice height changes, to an accuracy of less than 1.5 cm a^{-1} (spatially averaged over 100 x 100 km sections on ice sheets), from which the mass balance of the ice sheets could be determined. This would help in the understanding of the associations between polar climate and ice height/mass changes, with a strong focus on the present and future contributions of the ice sheets to global sea level rise (Zwally et al., 2002; Schutz et al., 2005).

ICESat had further scientific goals which included: the measurement of the vertical structure of clouds and aerosols, and cloud heights; the sensing of land topography and vegetation canopy heights and finally the measurements of sea ice roughness, sea ice thickness, ocean surface heights, and surface reflectivity (Zwally et al., 2002).

Table 2.1: ICESat campaigns. The average days in operation were ∼33 days. Lasers were turned on either two or three times per year. Campaign 1A had an 8 day cycle for validation purposes. Data from Zwally et al. (2011b).

Start Date	End Date	Days in Operation	Laser Identifier
2003-Feb-20	2003-Mar-29	38	1A
2003-Sep-25	2003-Nov-19	55	2A
2004-Feb-17	2004-Mar-21	34	2B
2004-May-18	2004-Jun-21	35	2C
2004-Oct-03	2004-Nov-08	37	3A
2005-Feb-17	2005-Mar-24	36	3B
2005-May-20	2005-Jun-23	35	3C
2005-Oct-21	2005-Nov-24	35	3D
2006-Feb-22	2006-Mar-28	34	3E
2006-May-24	2006-Jun-26	33	3F
2006-Oct-25	2006-Nov-27	34	3G
2007-Mar-12	2007-Apr-14	34	3H
2007-Oct-02	2007-Nov-05	37	3I
2008-Feb-17	2008-Mar-21	34	3J
2008-Oct-04	2008-Oct-19	16	3K
2008-Nov-25	2008-Dec-17	23	2D
2009-Mar-09	2009-Apr-11	34	2E
2009-Sep-30	2009-Oct-11	12	2F

ICESat had three lasers on-board, which were supposed to provide uninterrupted annual coverage of the polar regions. However, there was a failure in a pump diode array of Laser 1 and, in order to extend the mission's life and maximise the scientific return, it was decided to modify the operation plan (Abshire et al., 2005). This would reduce the likelihood of the same failure occurring in the other two lasers. Initially a 183-day repeat cycle orbit was planned, this was changed to a 91-day repeat cycle with a ∼33 day sub-repeat cycle (a single laser campaign) where the lasers were turned on three times per year to maximise seasonal coverage (Schutz et al., 2005). This limited the temporal resolution of the ICESat data, meaning there were less data points available from which to estimate dH/dt.

Laser 3 failed on the 19th of October 2008 and it was decided to run Laser 2 using only the weak beam. The mission ended on the 11th of October 2009. ICESat had a planned 3 year mission life span with a 5 year goal. The actual mission life span was 7 years, although the data collected was temporally more sporadic and the measurement density was diminished due the earlier failures (Table 2.1). NASA

plans to launch ICESat-2 in 2017 as a follow-on to the ICESat mission.

2.1.1 Instrument description

ICESat flew ∼600 km above the Earth's surface in a near circular orbit. This was a compromise between the need to have a low orbit to reduce instrument power use and a higher orbit to extend the orbit lifetime and hence the duration of the mission (Schutz, 2001; Zwally et al., 2002). Based on the need to cover the West Antarctic ice streams and the desire to optimise the crossover geometry, the inclination was chosen to be 94°, which resulted in latitudinal coverage to 86° north and south of the equator (Schutz, 2001). This produced a cross-track spacing of ∼29 km in the latitudinal direction and ∼2.5 km in the longitudinal direction at a latitude of 85° and ∼340 km and ∼30 km, respectively, at the equator (Nguyen, 2006). As the crossover spacing decreased from the equator to the poles, the density of crossovers increased and Nguyen (2006) found ∼ 70, 150, 485 and 11,340 crossovers in an average 100 x 100 km^2 area centered at the latitudes -70.5°, -75.5°, -80.5°, -85.5°, respectively.

The Geoscience Laser Altimeter System (GLAS) was the primary instrument on board ICESat and is still the only satellite laser altimeter to have been in operation over the ice sheets. GLAS had three lasers on-board, each was run consecutively. These lasers emitted a 1064 nm (infrared) pulse that measured surface height and dense cloud and a 532 nm pulse which measured the vertical distribution of clouds and aerosols (Zwally et al., 2002; Schutz et al., 2005) (Figure 2.1).

Apart from GLAS, ICESat's optical bench also included a stellar and attitude reference system, a laser reference camera, power supplies, on-board computer, receiver telescope and detector, and an instrument star tracker and gyros to determine the orientation of the optical bench (Schutz et al., 2005) (Figure 2.2). Also, on-board ICESat was a Global Positioning System (GPS) receiver which was used in precise orbit determination (Schutz et al., 2005).

The GLAS footprint is approximately 65m in diameter and each footprint is separated by 172 m in an along-track direction (Figure 2.1). For comparison, the

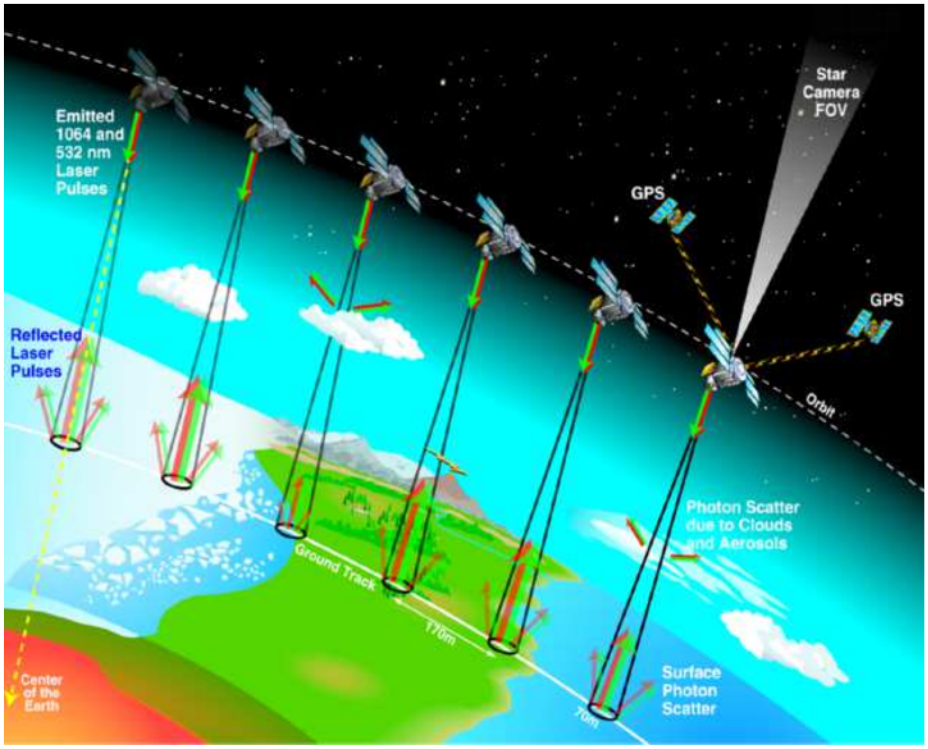

Figure 2.1: ICESat using the GLAS instrument measures the distance between it and surface, clouds and atmospheric aerosols using 2 different laser pulses (1064 nm (infrared) and 532 nm (green)). The position of the satellite is tracked via GPS and its orientation is determined by a star camera. Figure is taken from ICESat brochure (Zwally and Schuman, 2002).

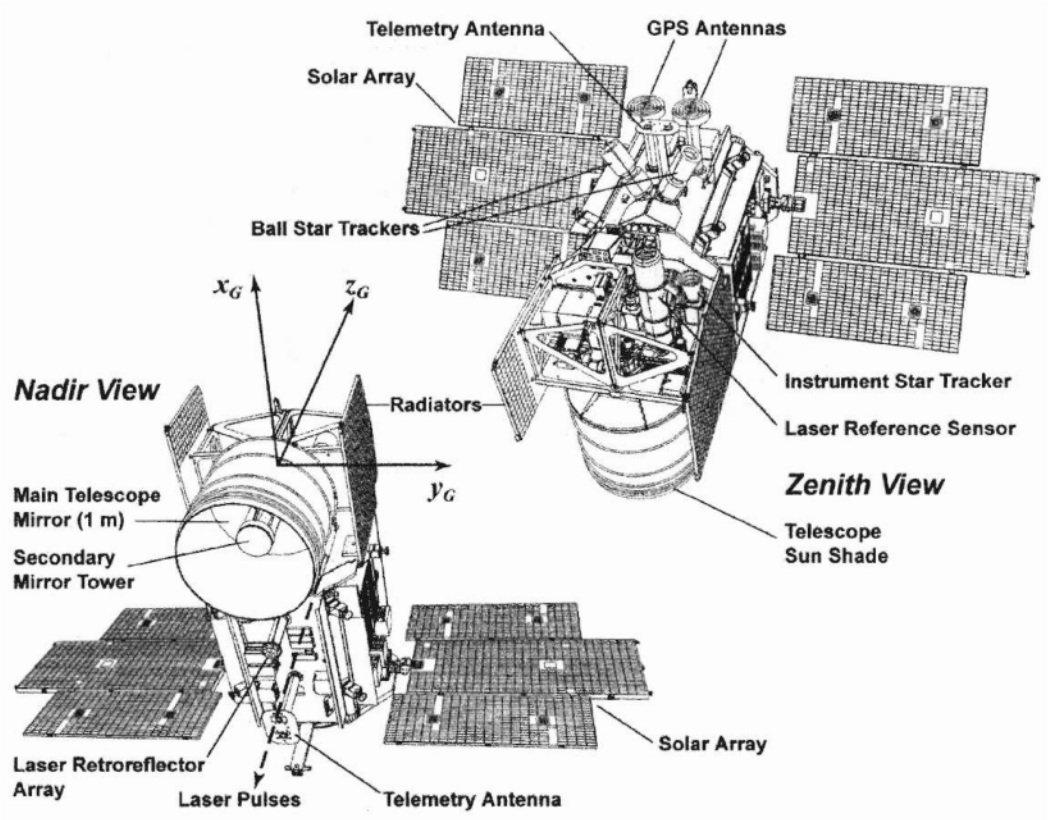

Figure 2.2: ICESat nadir (Earth-facing) and zenith views. Figure is taken from (Schutz et al., 2005).

radar altimeters, ERS-1 & -2 have footprints of 2-10 km in diameter, depending on the slope of the terrain, and are separated by ∼330 m in an along-track direction (Bamber and Gomez-Dans, 2005; Legresy et al., 2005). This equates to a true spatial resolution of close to 1 km (dependent largely on latitude) for the GLAS system compared to the ERS-1 & -2 radar altimeter, which produces height estimates that are typically correlated over distances of about 4 km on ice sheet terrain (Bamber and Gomez-Dans, 2005).

2.1.2 The GLAS waveform

In Section 1.3.3, I discussed in general terms how height measurements are obtained from a satellite altimeter. I will now discuss how this applies to the GLAS instrument. The GLAS laser emits a 1064 nm pulse, which illuminates a spot on the Earth's surface. This transmitted pulse is digitized, at a rate of 1 GHz, as it leaves the instrument. The transmitted pulse has a distribution which is approximately Gaussian (Figure 2.3) (Zwally et al., 2002).

As the laser pulse returns back to the satellite it is captured by a receiver telescope (1 m diameter), which passes the pulse to the analog detector (Zwally et al., 2002; Abshire et al., 2005). The detector takes the pulse and digitizes it at the same rate as the transmitted pulse. The return pulse can have multiple peaks and it is the last peak that is received which is used in the range calculation (Zwally et al., 2002). Both the digitized transmitted and returned pulses are stored and sent to the ground for processing.

Under ideal conditions this return pulse will have a similar distribution to that of the transmitted pulse. In reality, this is often not the case and the accuracy and quality of the return is affected by a number of different factors which I discuss in the next sections. In order to account for variation in the return pulse shape (Figure 2.3), it is modelled using the following equation:

$$w(t) = e + \sum_{m=1}^{Np} A_m \exp\left[\frac{(t - t_m)^2}{2\sigma_m^2}\right] \tag{2.1}$$

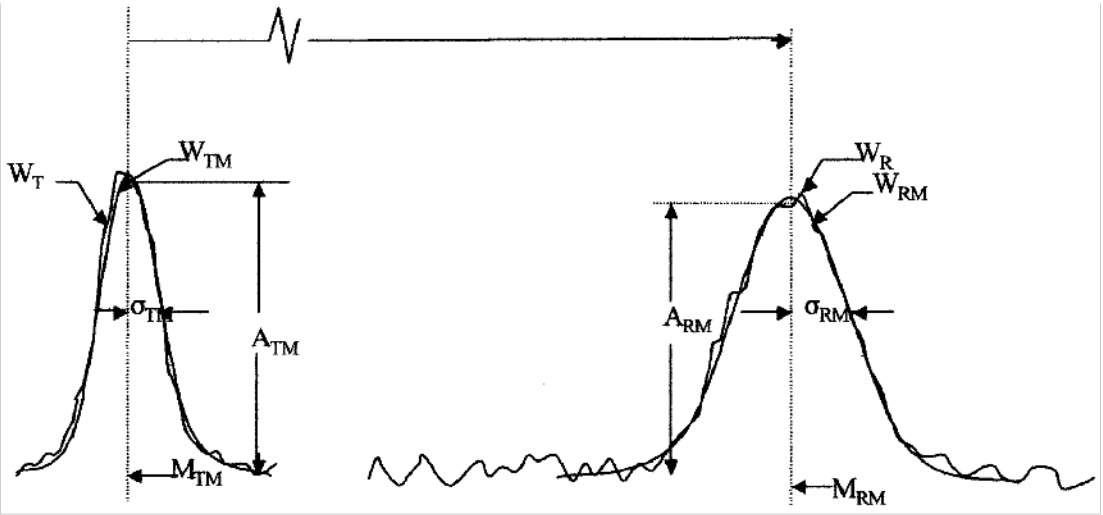

Figure 2.3: A representation of the the transmitted and returned waveform with a fitted waveform. W denotes the entire pulse (both transmitted and returned) or fitted waveform. The subscripts T and R denote the transmitted and returned pulse respectively, while the subscript M refers to the Gaussian model fitted to the entire pulse W . M denotes the mid-point of the waveform and σ is standard deviation of the waveform. A denotes the amplitude of the fitted waveform. Taken from Zwally et al. (2002).

where e is the bias or noise, Np is the number of peaks present in the returned waveform (the maximum number being six), A_m is the amplitude, t_m is the peak position and σ_m is the standard deviation of the mth Gaussian peak (Zwally et al., 2002).

This model is fitted to the return pulse using a non-linear least squares fitting procedure to compute the model parameter in the above equation (Zwally et al., 2002). The range is determined by calculating the time between the centroid of the transmitted pulse (M_{TM} , Figure 2.3) and the centre of the Gaussian fitted waveform to the last peak of the return pulse (M_{RM} , Figure 2.3). The accuracy of the GLAS range determination is affected by a number of factors are discussed below.

2.1.3 GLAS accuracy

There are a number of sources of error associated with the GLAS instrument (Table 2.2). Zwally et al. (2002) estimated a pre-launch error budget of 13.8 cm for the mission. Fricker et al. (2005) created a GPS-derived digital height model (DEM) of the Salar de Uyuni, the world's largest salt flat, and compared the ICESat results to the DEM. They estimated under optimal conditions that the single-shot error bud-

Table 2.2: Pre-launch estimates of GLAS Single-shot Error Budget. Table is taken from Zwally et al. (2002). **Updated error estimates and RSS in parentheses**.

Error Source	Error Limit (cm)
Precision orbit determination	5 (1-2, Schutz and Zwally (2008))
Precision attitude determination	7.5 (5, Schutz et al. (2005))
Atmospheric delay	2
Atmospheric forward scattering	2
Other (tides, etc.)	1
RSS (total)	13.8 **(6.2)**

get for the GLAS instrument was 2 cm with a precision of less than 3 cm. The main contributors to the error budget are precision orbit determination, precision attitude & pointing determination, atmospheric delay, saturation correction and atmospheric forward scattering (Schutz and Zwally, 2008).

2.1.3.1 Orbit determination

The orbit of ICESat is monitored using a GPS tracking system. On board ICESat is a laser retro-reflector array, which supports Satellite Laser Ranging (SLR) between the satellite and the International Laser Ranging Service station network (Schutz et al., 2005) (Figure 2.2). This secondary tracking system is not used in the precision orbit determination, but is purposefully held back to validate the GPS locational data (Zwally et al., 2002; Schutz et al., 2005). Using SLR it has been determined that the orbit determination has an error of 1-2 cm, which is an improvement on the pre-launch 5 cm estimate (Zwally et al., 2002; Schutz et al., 2005).

2.1.3.2 Precision attitude and pointing determination

Satellite laser altimetry has the advantage over radar altimetry that it has a smaller surface footprint and the laser reflections are restricted to a small surface layer (Abshire et al., 2005). Consequently, ICESat is able to observe accurately any sudden changes in slope, minimising its impact on the single-shot error budget. Radar altimetry height accuracy is shaped largely by the slope-induced error, due to the larger footprints (Abshire et al., 2005; Brenner et al., 2007).

However, the small footprint of the GLAS instrument can amplify some associ-

ated errors, the most significant being errors in the pointing determination (Nguyen, 2006). In order to obtain the exact position of the laser footprint, the angular orientation (precision attitude determination) of the optical bench and the direction of the outward facing laser (pointing determination) must be well understood in the context of an external reference frame (Sirota et al., 2005). The precision attitude determination for the GLAS instrument is calculated using a set of gyroscopes and an instrument star tracker which has an 8° field of view and is able to observe up to six stars (Sirota et al., 2005). With this attitude information, the pointing determination can be estimated to within ∼2 arc-seconds which equates to ∼5 cm of vertical error per arc-second per degree of total slope (Schutz and Zwally, 2008).

2.1.3.3 Atmospheric forward scattering and delay

When the GLAS laser pulses come into contact with cloud cover, the performance of the signal can be degraded or the signal can be lost completely (Fricker et al., 2005). This degradation is due to the forward scatter of the transmitted photons, which occurs before the pulse reaches the surface (Spinhirne et al., 2005). The scattered photons are reintegrated into the returning path of the non-scattered photons if they are within one degree of the pulse vector's trajectory and, therefore, still in the GLAS field-of-view (Zwally et al., 2002; Nguyen, 2006). This results in a delay of the return pulse to the detector and produces a broadening of the main peak and an elongation of the tail in the echo waveform (Fricker et al., 2005; Nguyen, 2006). This can lead to return pulse waveforms which are biased toward longer ranges, which leads to lower height estimates (Schutz et al., 2005).

The error associated with both the delay and forward scatter of the return pulse is 2 cm, respectively (Zwally et al., 2002). When clouds are extremely thick the pulse does not reach the Earth's surface and instead measures the height of the cloud cover. This is not a problem with previous satellite altimeters such as ERS-1 & -2 or ENVISAT that use a radar pulse instead of a laser pulse, as they are able to penetrate cloud cover (Herzfeld et al., 2008).

2.1.3.4 Saturation

The saturation of the ICESat pulse generally occurs over bright smooth flat surfaces (Fricker et al., 2005), such as the interior of the Antarctic and Greenland Ice Sheets (Brenner et al., 2007). The GLAS 1064 nm laser is susceptible to detector saturation when a high energy pulse is returned, as the receiver's automatic gain control is unable to adjust below its preset lower limit (Fricker et al., 2005). Energy levels were found to be four times higher than the expected pre-launch values for Antarctica, when pulse returns from full strength lasers at the start of each laser campaign were assessed (Nguyen, 2006).

These saturated return pulses have distorted waveforms, and, when ICESat's standard Gaussian fitting process is applied to this data, it becomes biased toward longer ranges, which leads to lower height estimates (Fricker et al., 2005; Schutz et al., 2005; Brenner et al., 2007). The saturation errors are generally a few centimetres but can reach up to 1.5 metres in some cases (Brenner et al., 2007; Pritchard et al., 2009).

Saturation can be corrected for and pulse returns with exceptionally high saturation can be removed altogether (Fricker et al., 2005). Using their saturation correction technique, Fricker et al. (2005) showed that they were able to significantly decrease the bias associated with saturation. All ICESat data releases after this study have been corrected for saturation and the accuracy improves with each release.

2.1.4 Summary

The ICESat mission has given the scientific community an extremely useful dataset of ice height measurements spanning 2003 to 2009. The mission was able to meet its scientific objectives and the collected data has helped in improving our understanding of the Antarctic and Greenland ice sheets and their potential contribution to sea level rise. Our understanding of the errors involved in obtaining ice height measurements from the GLAS instrument has improved over the course of the mission as well as knowledge of how to mitigate these sources of error where ever possible. In the

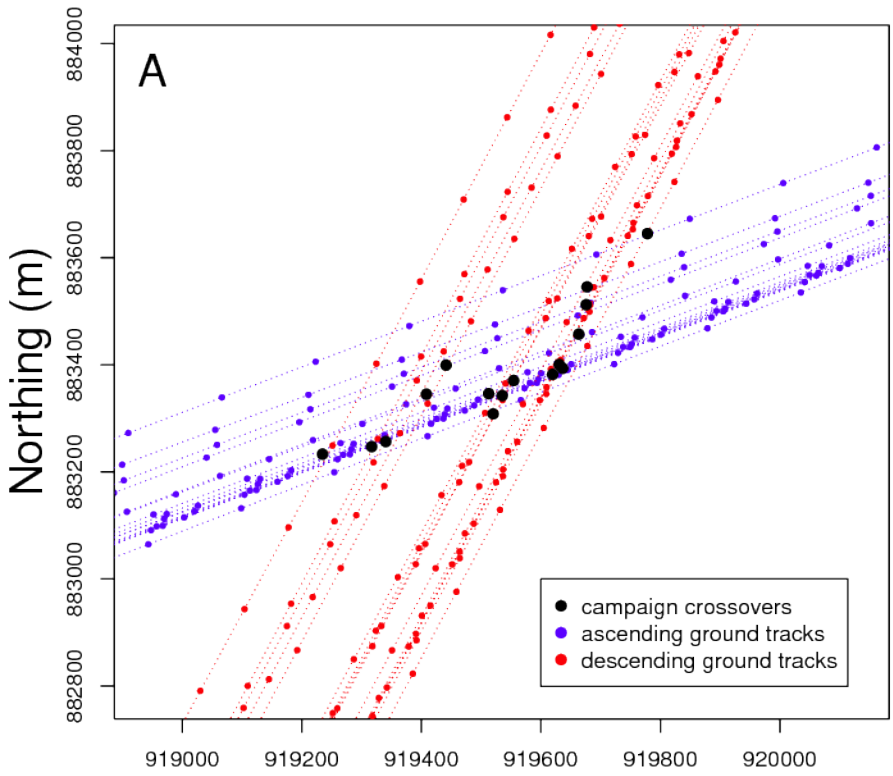

Figure 2.4: A typical ICESat crossover region (2003-2009), each repeat-track is offset slightly from previous tracks. The blue lines indicate the ascending repeat-tracks, while the red lines show the descending repeat tracks. The black circles are the locations of the campaign crossovers.

next section I discuss how ICESat data has been used by the scientific community to derive rates of ice height change.

2.2 ICESat analysis techniques

The primary purpose of ICESat was to observe changes in height over time, it is therefore imperative that a measurement taken at one location can be compared to later measurements in the same location. With this in mind, an orbit was chosen to maximise the number of times the satellite's orbit intersects with previous orbital paths, specifically over the poles. The orbit creates a latticework of non-exact repeat ground-tracks (repeat-tracks) where, at regular intervals, an ascending and descending repeat-track intersect each other, known as a crossover (Figure 2.4).

These crossovers can occur up to three times per year over a single location. Over the whole ICESat operational period (October 2003 to March 2009), a pair of intersecting repeat-tracks could have as many as 21 campaign crossovers (Figure 2.4).

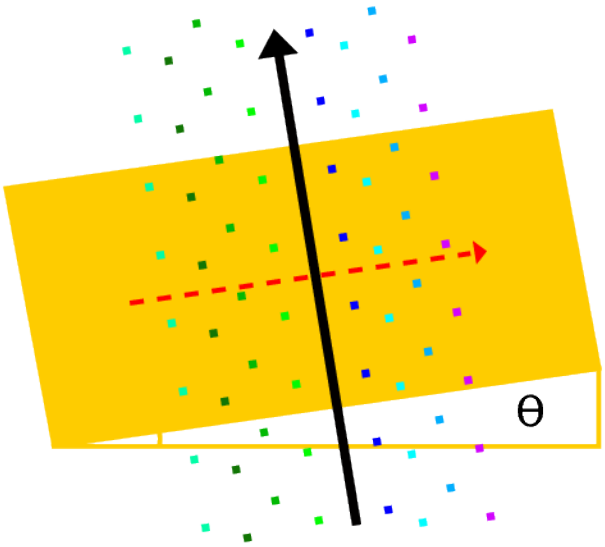

Figure 2.5: A stylised representation of a ground-track segment with a surface slope. The black line represents the reference track, pointing in an along-track direction. Coloured lines illustrate the repeat-tracks. The yellow box represents the across-track slope and θ is the angle of the across-track slope. The dashed red line indicates direction of increasing slope.

In reality, the number of campaign crossovers varied annually from one to three.

Ideally, each repeat-track would lie in exactly the same location as the previous repeat-track, and crossovers would always occur in the same location. This, however, was not the case for ICESat. Due to the error in the precision attitude and pointing determination of the satellite, the position of the repeat-track height measurements and crossover locations could be offset by tens to hundreds of metres between different laser campaigns (Figures 2.4 and 2.5) (Zwally et al., 2005).

In order to reconcile the repeat-track geometry, previous studies have used a number of different methods to obtain dH/dt estimates from offset along-track height measurements (e.g. Smith et al., 2005; Zwally et al., 2005; Brenner et al., 2007; Slobbe et al., 2008; Gunter et al., 2009; Pritchard et al., 2009; Smith et al., 2009; Moholdt et al., 2010; Shi et al., 2011; Sørensen et al., 2011; Zwally et al., 2011a). Each method has a different way of managing the effects of repeat-track geometry on estimates of dH/dt. Various assumptions are made for these methods to be valid, which leads to uncertainty of the accuracy of the dH/dt estimates. The uncertainty of each step in the method, is not always formally propagated into the final estimate of dH/dt uncertainty (e.g. Pritchard et al., 2009; Sørensen et al., 2011) and I will

discuss this later in greater detail.

Generally, rates of height change on large ice sheets are small; however, due to their area, even a small uncertainty in the estimate of dH/dt can lead to significant uncertainties in mass balance changes (dM/dt). For example, a 5 mm/yr height rate uncertainty over a section of East Antarctica ($3 * 10^6$ km^2, ~20% of Antarctica), would introduce an uncertainty in dM/dt of ~13.75 Gt/yr (assuming an ice density of 917 kg/m^3), larger than many annual mass balance estimates for the whole of East Antarctica. This value is an over-estimation, as it is a constant rate offset (bias). In reality errors in height rate estimates vary, partly minimising the overall effect of the error. On the other hand, an inter-campaign bias (which has been found for ICESat data, Siegfried et al. (2011)) would manifest itself as such a constant rate bias; therefore it is important to correct for such effects (Borsa et al., 2013).

This demonstrates that a small uncertainty over a large area can have large repercussions on the statistical significance placed on a final dH/dt or dM/dt estimate. It is therefore important that we understand the uncertainty contributions on estimates of dH/dt due to repeat-track geometry.

As each repeat-track is offset in position, it is important to differentiate between the accumulation, ablation of ice/firn, sub-glacial lake runoff, on an annual and seasonal basis and the spatially changing surface slope. A rate of change estimated using non-overlapping height measurements will most likely include a height change component that is due to surface slope rather than to ice gain or loss. Not accounting for this contaminates the dH/dt estimate with a cross-track slope bias.

Assume that we have a reference track that is running in an along-track direction with four repeat-tracks lying parallel on either side of the reference track (Figure 2.5), separated by 25 m from the next repeat-track. The outer most repeat-tracks would be ~112.5 m away from the reference track. Now, assume that the surface topography below the repeat-tracks is a plane with a surface slope of 0.05° (3′) increasing perpendicular to the reference track in a left to right direction (represented as θ in Figure 2.5). This simple scenario would introduce a cross-track difference in height of ~19.6 cm between the two most distant repeat-tracks and, if a rate of change

were to be estimated using these height differences, one would obtain a rate caused by change of surface topography rather than a dH/dt related to temporal ice height variations. This is an idealised example as repeat-tracks are never this symmetrical and sometimes overlap.

Nonetheless the example highlights that for a dH/dt estimate to represent the "true" temporal change in ice height, the cross-track surface slope must be removed. Furthermore, the uncertainty of surface slope should be propagated into the final dH/dt uncertainty in order to properly represent the accuracy of the rate estimate.

I will now discuss the analysis techniques reported in the literature to deal with offset ICESat repeat-tracks. They can be broadly split into two categories: crossover analysis and along-track analysis.

2.2.1 Crossover Analysis

Crossovers are ideal locations for estimating dH/dt rates, as they occur at regular time intervals and relatively close together. The impact of cross-track slopes on height rate estimates is considerably reduced using crossovers, as the intersecting repeat-tracks are not parallel, which is the case for along-track repeat-tracks (Gunter et al., 2009). The along-track slope of each of the intersecting repeat-tracks is known and can be taken into account when estimating height change.

The first step in crossover analysis is to identify the position of each campaign crossover, being the point where an ascending and a descending repeat-track intersect from the same laser campaign (Figure 2.4). There are a number of different methods to determine the position of the campaign crossover. The method of Brenner et al. (2007) estimates the campaign crossover positions by fitting a polynomial to each ascending and descending repeat-track and calculating where they intersect. The location is further refined by taking a subset of the intersecting repeat-tracks close to the first estimate and refitting the polynomials. If there are no valid height measurements within 170 m of the crossover, it is discarded. Gunter et al. (2009) used cubic spline interpolation on all data points within ∼400 m (up to 10 valid points) of the campaign crossover to refine the position.

As these repeat-tracks intersect at regular time intervals and at nearly the same location, the change in height (dH/dt) can be estimated for the crossover region (the region which includes all the campaign crossovers) using interpolation (Figure 2.4) (Zwally et al., 2005; Smith et al., 2005; Brenner et al., 2007; Gunter et al., 2009; Moholdt et al., 2010). The height is estimated at the campaign crossover for both the ascending and descending repeat-tracks. This is achieved by the along-track interpolation of the closest height measurements to the campaign crossover position. Zwally and Brenner (2001); Smith et al. (2005); Zwally et al. (2005); Brenner et al. (2007) etc. linearly interpolate two height measurements on each side of the campaign crossover location for both the ascending and descending repeat-tracks. The two heights are differenced by removing the later campaign height estimate from the earlier estimate (∼33-day time period) (Brenner et al., 2007). This difference is a estimate dH of the crossover region rather than an absolute height value. These height differences are then converted to dH/dt by using crossover times linearly interpolated from each ascending and descending repeat-track (Gunter et al., 2009).

Gunter et al. (2009) used clusters of inter-campaign crossovers, that is, ascending and descending repeat-tracks from different laser campaigns. They determined the height at the crossover via cubic-spline interpolation of data within 0.25 seconds (up to 10 valid points) of the inter-campaign crossover time. They compute the height differences for all of these inter-campaign crossovers and obtain a dH/dt for the crossover region. Moholdt et al. (2010) picked inter-campaign crossovers from similar seasons with a temporal separation of 3 to 4 years, to estimate the average dH/dt for 2003–2008, using linear interpolation. They also differenced seasonally distinct inter-campaign crossovers to obtain seasonal height changes.

Schenk and Csatho (2012) proposed a method to estimate both the dH/dt and surface slope at crossovers. They do this by fitting third-order polynomials to all the height measurements of each of the ground-tracks, resulting in up to 200 equations per crossover. Using a least-square approach, they simultaneously solve these equations for the height and surface slope parameters, where the square distance between the actual height measurements and the estimated surface becomes the minimum

(Schenk and Csatho, 2012). The uncertainty of the least-squares fitting procedure is also formally propagated using a simple stochastic model, which assumes that all the height measurements are uncorrelated and of the same precision. This method is also applied along-track, which I will discuss in the next section.

The drawback of all the methods, except for Schenk and Csatho (2012), is the assumption that the height change signal is constant over the crossover region. This may be the case in regions of little precipitation, such as the Antarctic interior (Van Der Veen et al., 1998; Yi et al., 2005; Van Der Veen et al., 2009). However, near the coast, the height change signal often varies across the crossover region (Van Der Veen et al., 1998; Yi et al., 2005; Van Der Veen et al., 2009). Therefore, if the position of a campaign crossover varies, it can potentially measure a different height change signal to past or future laser campaigns. If these variations are not taken into account they will induce height differences which will bias dH/dt estimates. Van Der Veen et al. (2009) found height variation (standard deviation) of 8 cm for most of the 500 m laser altimeter segments over Greenland. Near the coastal margins they found higher height variations between 0.3 and 0.5 m, this is in general agreement with my height variability findings (see Figure 3.3b).

A further limitation of crossover analysis is that it only makes use of a small portion of the available data and much of the along track data is left unused. Due to the orbit chosen for ICESat, the number of crossovers varies greatly with latitude. The number of crossovers increases from $\sim$ 70, 150, 485 and 11,340 over an average 100 x 100 km^2 area centered at the latitudes -70.5°, -75.5°, -80.5°, -85.5°, respectively (Nguyen, 2006). Consequently crossover analysis is far more effective at estimating dH/dt near the poles than closer to the equator. This is problematic near the coastal margins of Antarctica and Southern Greenland, where due to the repeat-track geometry, there are far fewer crossovers than at higher latitudes.

2.2.2 Along-track Analysis

In contrast to crossover analysis, along-track analysis utilises all the along-track data available, giving it a much higher spatial coverage. The along-track analysis method can only make use of the height data from one repeat-track per campaign

(∼33 days). Therefore the along-track method must be able to reconcile the varying position of the height measurements over time.

There are a number of different along-track methods used in the analysis of ICESat data. The most popular method is to break the ground-track into small 500 - 700 m along-track segments, which typically cover between 3 to 4 data points per laser campaign (Howat et al., 2008; Smith et al., 2009; Moholdt et al., 2010; Sørensen et al., 2011; Zwally et al., 2011a; Ewert et al., 2012). These methods then generally parameterise the secular trend (dH/dt), the seasonal signal and the underlying surface topography, which are all solved for simultaneously using some form of regression applied to a mathematical model specific to the study (Howat et al., 2008; Smith et al., 2009; Moholdt et al., 2010; Sørensen et al., 2011; Zwally et al., 2011a; Ewert et al., 2012).

Howat et al. (2008), Smith et al. (2009) and Moholdt et al. (2010) used a least-squares regression technique that fits rectangular planes to the ICESat repeat track segments to obtain a dH/dt, while Zwally et al. (2011a) first interpolated the along-track height measurements to an equally spaced (172 m) reference track. For each reference point, they then solved by least squares for the seasonal signal and height at that point as well as the underlying surface topography. The other studies solve for the above parameters at a single point on the segment.

The seasonal component is generally obtained by solving a set of trigonometric functions, whose makeup is highly dependent on the study (Howat et al., 2008; Smith et al., 2009; Moholdt et al., 2010; Ewert et al., 2012). As ICESat had a very inconsistent temporal coverage (operational 2-3 times a year), due to early laser failure, parameters associated with seasonal signals have high uncertainties (Ewert et al., 2012). Consequently, most studies include a seasonal model to separate the annual variation signal from the linear dH/dt (Ewert et al., 2012). In the case of Zwally et al. (2011a) these seasonal and inter-annual variations are ignored, as they assumed that departures from linearity are retained in the residuals and can be analysed later if necessary.

Lastly, the surface slope component is estimated and removed using a number

of different methods presented in the literature. Sørensen et al. (2011) present two unique slope bias removal methods. In their first method, they created a reference surface for each along-track segment and then obtain the height of the reference surface for the ICESat measurement location. This height is then removed from the ICESat height to correct for slope.

Two ICESat laser campaigns were picked, based on the following criteria: firstly, the two laser campaigns had to be separated by one year, to minimise the effect of seasonal signals and the actual difference in height between the laser campaigns. Secondly, the laser campaigns were chosen to have the greatest spatial coverage to best represent the surface slope (Sørensen et al., 2011). The height, cross-track and along-track slope were estimated by applying a least squares fit to the two laser campaigns. Sørensen et al. (2011) noted that this method was sensitive to seasonal changes and actual height changes between the two laser campaigns. Consequently this method of slope correction could introduce a bias into the dH/dt when there are significant changes in ice height, since a component of the height signal may be removed.

The second method of Sørensen et al. (2011) is similar to the methods presented by Howat et al. (2008) and Smith et al. (2009). A linear regression is estimated from both along-track, cross-track surface slope and the topography underlying the height changes, while Ewert et al. (2012) approximate the underlying topography to account for any existing topography-induced height differences between measurements by fitting a biquadratic surface polynomial.

Both Sørensen et al. (2011) and Ewert et al. (2012) noted that, for the dH/dt to be separated from the local ice surface topography, it is important that the repeat-tracks are ordered so that the temporal behaviour is not correlated with the cross-track surface slope. For instance, assume that the first repeat-track is acquired, and then every subsequent repeat-track is positioned so it is adjacent to the previous repeat-track and so on. If the dH/dt is positive and increasing linearly with time, it would be very difficult to separate it from the similarly linear cross-track slope as they would be strongly correlated. All methods that model local topography using

some form of repeat-track analysis, which includes all methods presented above, are susceptible to this.

More generally, the use of combination of parameters that are not independent will lead to a strong correlation and the inability to separate the secular dH/dt from the seasonal signal and the surface topography. The uncertainties of each of these components are often not published or formally propagated into the final uncertainty budget. For instance Sørensen et al. (2011) stated that they do not propagate their uncertainties from any of the separate components and assumed that the along-track segment is small enough that the error on the measurements is constant. The variances obtain from the regression analysis are used as a measure of uncertainty and the goodness of fit (Sørensen et al., 2011).

Schenk and Csatho (2012), as mentioned earlier, estimate the surface shape at crossovers, which they then linearly interpolated along-track, using the two closest crossovers. They apply the same method as described in Section 2.2.1 to the along-track data, but introduce the interpolated surface shape parameters into the least squares procedure as additional pseudo observation equations. This allows them to separate the surface topography from the secular dH/dt trend. This method assumes that surface slope is constant over the crossover site, and, more importantly that the surface slope does not vary greatly between crossovers. This may be the case in the interior of Antarctica, but is not true for the margins of ice-sheets where surface slope varies greatly. Schenk and Csatho (2012) do however formally propagate the surface slope uncertainties into their final uncertainty budget, which is not the case for many of the other methods described in this section.

There are other along-track analysis methods that do not require the estimation of a linear trend. Pritchard et al. (2009) used triangulated irregular networks (TINs) to estimate the change in height of small segments along ICESat ground-tracks. They created triangular surfaces using three points from previous repeat-tracks and linearly interpolating to a point in the current repeat-track. Consequently, one interpolated point is always compared to an actual height measurement. As the satellite was only operational three times a year, it was only possible to estimate

height change in 1.5 to 4 year intervals. This method sacrifices temporal resolution in favour of higher spatial resolution as it requires four repeat-tracks to estimate the dH/dt at a signal point.

Pritchard et al. (2009) dealt with surface slope bias by assuming that the triangular surfaces created were planar and therefore triangular interpolation accounts for both the cross-track and along-track surface slope. The problem with this assumption is that the three points in the triangle are measurements taken at different times of the year, so it is unclear whether these changes in height are due to surface slope, seasonal signal or actual variations in ice height that may have occurred between laser campaigns. Pritchard et al. (2009) do not estimate the uncertainty of their method; instead they publish a "detection threshold" value, which includes ICESat instrument and surface mass balance uncertainties.

Slobbe et al. (2008) used overlapping footprints and differenced the two heights to acquire a dH/dt. They used ICESat data from 2003 to 2007, so dH/dt time intervals range from ∼1 month to 4 years, depending on the relative time between repeat-tracks. This negates the need to solve a least squares regression or interpolate, removing the added uncertainty. However, this comes at the cost of spatial resolution, as a large amount of the data is excluded.

As the centre points of the overlapping footprints do not generally overlap, Slobbe et al. (2008) must correct for a underlying topography bias. They used an external DEM published by DiMarzio et al. (2007b) to obtain the slope at a given point and subtracted the DEM height from the ICESat height measurement. The DEM was created by placing a 1 km regular grid over the height data of the first seven ICESat laser campaigns. The height at each node was estimated by fitting a biquadratic surface to the closest height measurements in a radius surrounding the grid node (DiMarzio et al., 2007b). The DEM grid-nodes generally do not overlap the ground-track nodes, so the DEM height was interpolated to the ground-track section.

This method is simple and efficient, however, it is problematic due to the nature of the DEM. As the DEM was itself derived from a series of ICESat laser campaigns,

it is built on the assumption that there are no height changes during this time, which may not be the case. If the surface height changed significantly during this time, it would be absorbed into the DEM. Consequently, using this DEM to correct for slope could lead either to the under- or over-estimation or complete removal of actual height change signals. Furthermore, the height uncertainties and the linear interpolation uncertainties are not propagated into the final height estimate and, therefore, their contributions are ignored in the final dH/dt estimate uncertainty.

Lastly, Ewert et al. (2012) analysed the use of DEMs to correct for slope. A 1 km^2 and 500 m^2 DEM exists for Greenland and Antarctica, respectively (DiMarzio et al., 2007a,b). They concluded that no DEM with a high enough resolution exists for Greenland (and by extension Antarctica) as, according to sampling theorem, the DiMarzio et al. (2007a,b) DEMs could not include topographical features smaller than 2 km and 1 km, respectively for Greenland and Antarctica. They state that the DiMarzio et al. (2007a) DEM and others like it are not suitable for the purposes of surface slope correction in relation to along-track analysis. Slobbe et al. (2008) propagated the uncertainties of the observed height differences that they obtained from the overlapping footprints. However, they did not do the same for the surface slope correction, which should include both the DEM and interpolation uncertainty.

2.3 Chapter Summary

The ICESat ice height dataset has given us an unprecedented look at the way ice-sheets respond to climate change, however it is not without its deficiencies (errors) as demonstrated in Section 2.1.3. These errors must be addressed and quantified, so we are able to give a level of confidence as to how reliable our estimates are. I show in Section 2.2 that the scientific community has offered many novel solutions to try to mitigate these inherent errors. Nonetheless some errors, such as slope, can not be truly accounted for, due to the nature of the ICESat data. Each study tries to address these errors by making certain assumptions which, if not true, will invalidate the study's method. In having many different methods of deriving ice height changes from ICESat, we are able to help mitigate this problem. In this thesis I

propose one such method, which also makes certain assumptions, but will hopefully increase our overall understanding of the ice height changes and how they are best derived from ICESat data.

Chapter 3

The effect of interpolation and surface topography on rates of ice height change in East Antarctica derived from satellite laser altimetry - a simulation study

3.1 Introduction

Estimates of the rate of change of ice height (dH/dt) over large spatial regions have only become possible since the advent of remote sensing in the form of satellite altimetry. There have been a number of radar altimetry missions including Geosat, TOPEX/POSEIDON, ERS-1 & ERS-2, Jason-1 & Jason-2, ENVISAT and CryoSat-2, which have been used to estimate dH/dt. ICESat is the first laser altimeter satellite and its primary goal was to estimate present day ice height changes (Zwally et al., 2002), which has led to much more accurate and precise estimates of local, regional and continental dH/dt for both Antarctica and Greenland (Zwally et al., 2005; Howat et al., 2008; Slobbe et al., 2008; Gunter et al., 2009; Pritchard et al., 2009; Shi et al., 2011; Sørensen et al., 2011; Zwally et al., 2011a; Ewert et al.,

2012).

There are number of errors and biases that influence the accuracy of the ICESat dH/dt estimates, which I have discussed in detail in the previous chapter. These include precision orbit determination (Zwally et al., 2002; Schutz et al., 2005), precision attitude and pointing determination (Abshire et al., 2005; Sirota et al., 2005; Schutz and Zwally, 2008), atmospheric delay and forward scattering (Schutz et al., 2005; Spinhirne et al., 2005), saturation (Fricker et al., 2005), instrument bias (Borsa et al., 2013), limited temporal resolution due to instrument failure (Abshire et al., 2005), ground-track geometry and surface topography bias (Schenk and Csatho, 2012). Of these factors, ground-track geometry and surface topography bias are often discussed as a contributor to uncertainty, however there is no clear consensus on how to deal with errors induced by surface slope (Howat et al., 2008; Slobbe et al., 2008; Pritchard et al., 2009; Smith et al., 2009; Moholdt et al., 2010; Sørensen et al., 2011; Zwally et al., 2011a; Ewert et al., 2012; Schenk and Csatho, 2012). Moreover these methods do not always include slope bias uncertainty in the final uncertainty budget of height change estimates (e.g. Slobbe et al., 2008; Sørensen et al., 2011; Pritchard et al., 2009).

In this chapter I present a new method for estimating dH/dt and slope at crossovers as well as along-track. The first section of this chapter describes a simulation study where I created simulated surfaces, from which I created simulated datasets of ICESat height estimates with different levels of height variability. These datasets allowed me to test the standard form of crossover analysis, as well as to assess my own method. I also test my own along-track analysis method using the simulated datasets. I summarise my crossover and along-track analysis methods in the second section of the chapter and present my new method of estimating surface slope at the crossovers, applying this to my along-track dH/dt estimates. I then use my simulated surfaces to test the accuracy of the crossover and along-track analysis with each interpolation method. Lastly, I present my results on which crossover/along-track and interpolation method is most accurate and present the contribution of each of these different methods to the error/uncertainty of the dH/dt

estimates. I also discuss the contribution of surface slope bias to along-track analysis uncertainties. This work will contribute to the better understanding of the magnitude of the uncertainties coming from the type of analysis method, interpolation and slope correction .

3.2 Methods

In this section I discuss how I created simulated surfaces and datasets, on which I tested my interpolation analysis methods. I then present my unique crossover and along-track methods of interpolating altimetry data to generate dH/dt estimates. Lastly I discuss the interpolation methods that I use.

3.2.1 Generating simulated surfaces and datasets

A ~2 million km^2 section of Antarctica was chosen to simulate surface heights along ICESat ground-tracks, encompassing Enderby, Kemp and part of MacRobertsons Land in East Antarctica. This includes the Scott, Napier and Princes Charles Mountain Ranges, the Amery Ice Shelf, a section of coastline and the interior. Having these features as part of the simulated surfaces allowed me to test the ability of each interpolation method to perform in varying topographical conditions (Figure 3.1).

The first step in the simulation was to create a realistic, but idealised surfaces on which to base the actual simulation. Using the section of Antarctica in map 3.1, surfaces were created through time using the *Surface* function of the GMT package (Wessel and Smith, 2013). *Surface* uses continuous curvature splines in tension algorithm and creates a surface-grid by solving:

$$(1 - T_i)\nabla^2(\nabla^2 z) - T_i\nabla^2 z = 0 \tag{3.1}$$

where T_i is a tension factor between 0 and 1 (the i subscript indicates internal tension), z is the height of the measurement, and ∇ indicates the Laplacian operator. Wessel and Smith (2013) found that a tension of 0.25 worked best for potential field

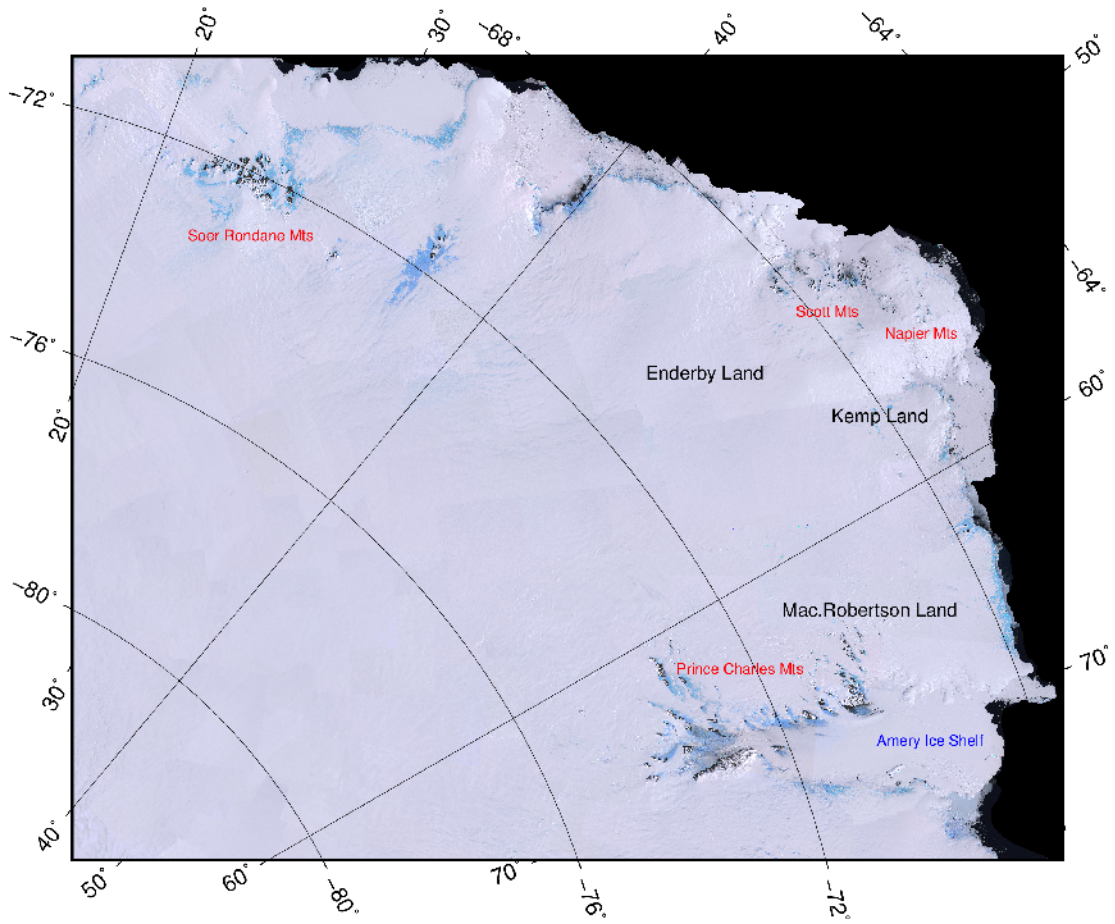

Figure 3.1: The study site, showing regions (black text), mountain ranges (red text) and ice shelves (blue text).

data, while a tension of 0.35 worked best for steeper topographical data. I used a tension factor of 0.35 as the goal of the first step was not to capture all the height variability found in ICESat height data, but to create surfaces that realistically represent the topography (i.e. surface shape and slope) of the study site. I found this choice minimised sudden unrealistic changes in height, which are generally uncommon on the flat ice surfaces of Antarctica. The surfaces obtained from the *Surface* function were therefore smoother than the actual ICESat data. Surfaces were created using the ICESat height measurements of each∼33-day laser campaign, from October 2003 to March 2009. This interval ensures that seasonal variations are included in the final simulated datasets.

I used a grid spacing of 10m for the surface grid files, which was the computational limit for my study. This grid spacing provides a data resolution well below the 172m spacing between ICESat data points and allows for accurate replication of height variability when data points are close by.

The above method essentially removed a lot of the surface height variability (SHV) found in actual ICESat data due to the smoothing of the spline interpolation. To make the surfaces more realistic, I added spatially correlated noise to selected height measurements. I will now discuss how the spatially correlated noise was created, followed by my selection criteria for height measurements.

The study site was split into 1 km^2 sections and, if the section had more than 30 data points, the section was used. The mean height was calculated for each campaign and the data was normalised by removing the campaign mean from all height measurements for the given campaign. The campaign data were combined and binned to create a histogram. A least squares non-linear fit was applied to the histogram values to create a model of the SHV for that section, using a combination of a Gaussian, linear and quadratic function with three terms:

$$f(x) = \alpha_0 exp\left(-\frac{(x-b)^2}{2c^2}\right) + \alpha_1 + \alpha_2 x + \alpha_3 x^2 \tag{3.2}$$

where α_0 is the height, b is the centre and c is the width (standard deviation) of the Gaussian function. α_1 is the constant term, α_2 is the linear term and α_3 is the

quadratic term. The combination of functions that is utilised was determined by calculating a reduced chi-square goodness-of-fit statistic and using the function with the smallest value. Figure 3.2 shows the SHV of two sections, one in the interior and the other on the coast. As expected, the interior section has a smaller range than the coastal section.

Now that I am able to simulate SHV across the study site, I created three simulated ICESat surfaces, known as the low (LSHV), medium (MSHV) and high (HSHV) surfaces. I applied different levels of noise, depending on ice velocities using the following selection criteria: LSHV - noise was only applied to grid nodes with ice velocities greater than 100 m/yr, MSHV - greater than 50 m/yr and HSHV - greater than 10 m/yr. The approximate velocities for each grid node were obtained from the MEaSUREs InSAR-Based Antarctica Ice Velocity Map provided by Rignot et al. (2011a). If a grid node fell within one of the above selection criteria a height offset was applied to that node, which was randomly sampled from the locations corresponding SHV distribution.

In order to determine which simulated surface best represents the actual ICESat data, the mean, standard deviation and SHV range were calculated at each crossover (500 m radius around the crossover) and in 1 km^2 sections along-track. This was done both for the actual ICESat heights and simulated data (Figures 3.3 and 3.4). The difference in the mean height between the actual ICESat data and the MSHV dataset, across the whole study area, was found to be insignificant (t-test, actual $\mu = 0.973$, MSHV: $\mu = 0.962$, $p = 0.32$). The difference in mean height of the LSHV and HSHV datasets, when compare to the actual ICESat data mean height, were both significant (t-test, actual $\mu = 0.973$, LSHV: $\mu = 0.821$, $p = 0.043$ & HSHV: $\mu = 1.088$, $p = 0.037$). Thus, the MSHV dataset best represents the actual SHV across the study area and the LSHV and HSHV dataset results can be viewed as best and worst case scenarios.

One of the interpolation methods I tested, the Green's function spline interpolation is also a spline fitting technique. It can therefore be argued that this is not an independent test since my simulated data was created using a spline method

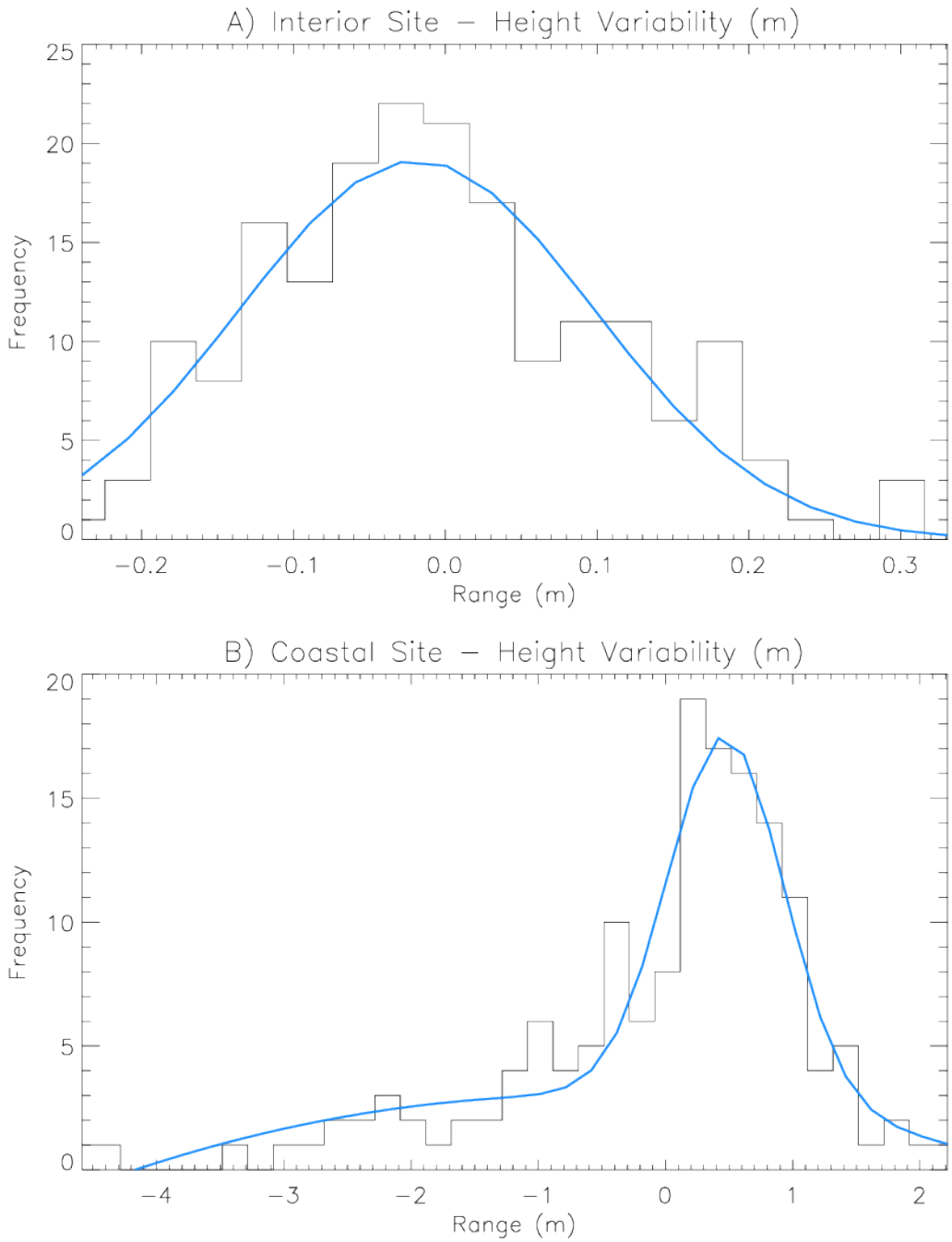

Figure 3.2: Surface height variability (SHV) range for 1 km^2 sections of actual ICESat data. A) the range for a site in the interior. B) the range for a coastal site. The blue line denotes the best-fit distribution function.

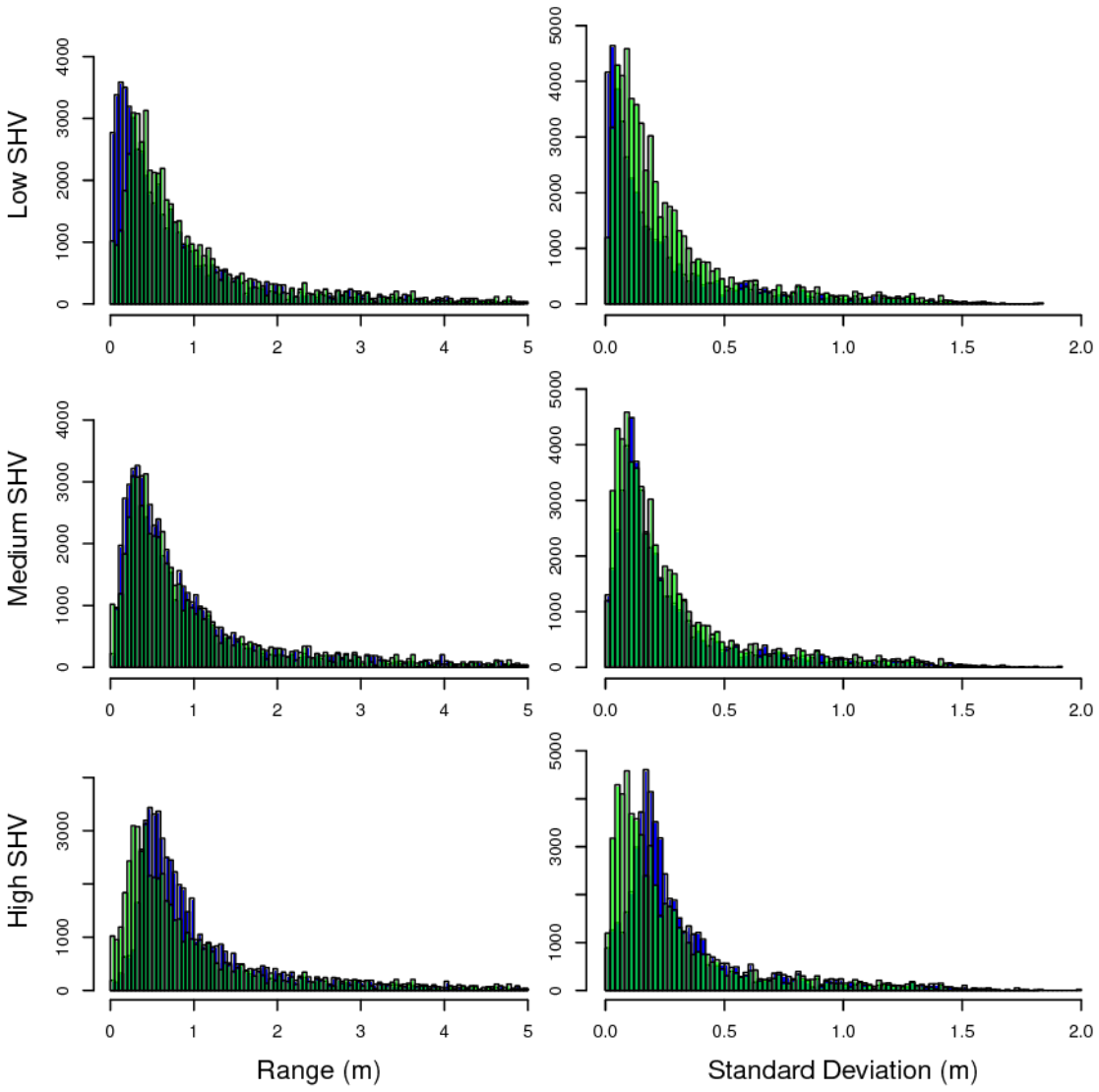

Figure 3.3: Histograms of the SHV range and standard deviation of actual heights (green) and simulated heights (blue) across the study site.

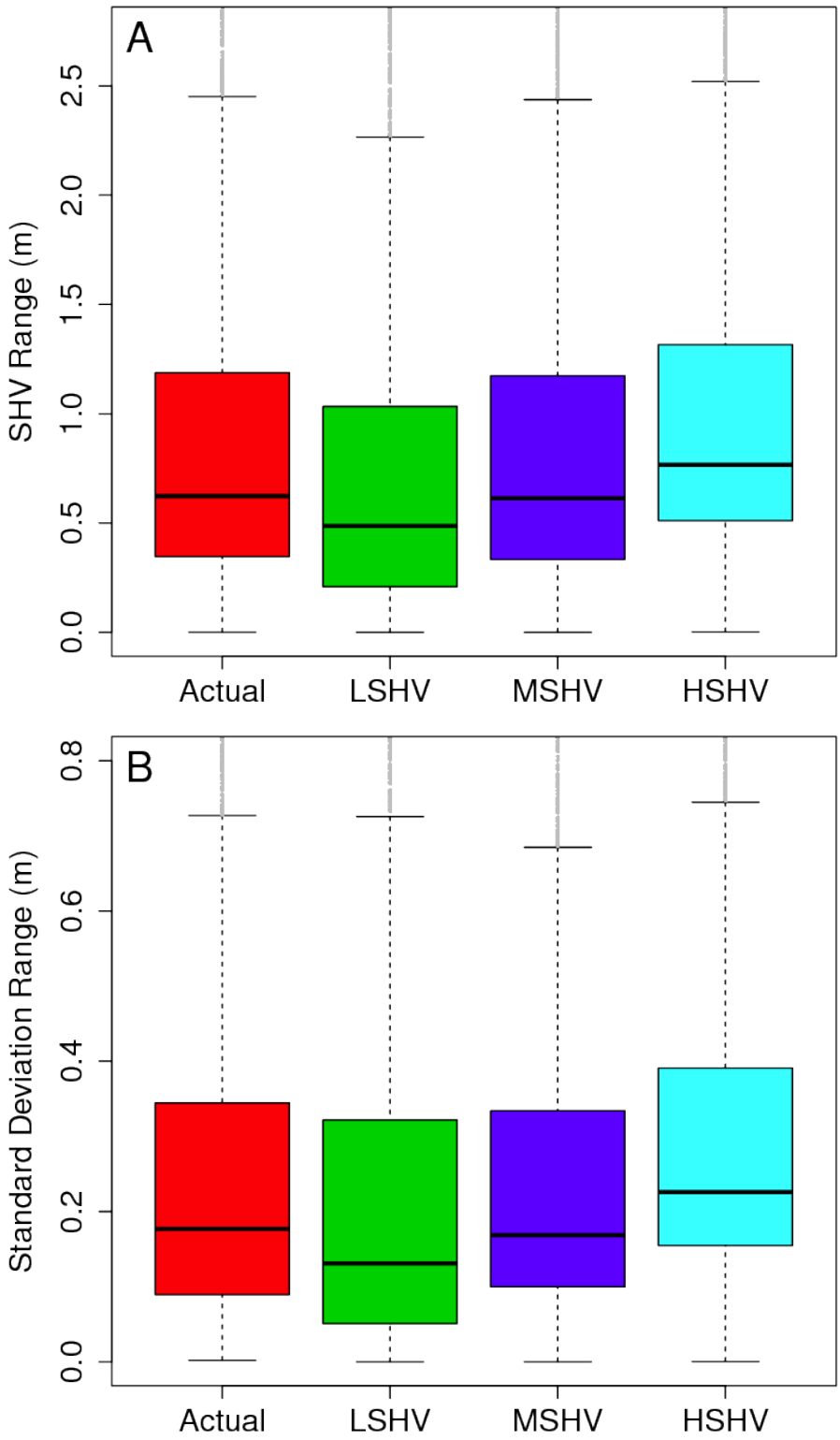

Figure 3.4: Box-plots showing the A) SHV range and B) standard deviation of heights across the study site for actual ICESat heights and three simulated surfaces.

and therefore the Green's function spline interpolation might be expected to produce results similar to the continuous curvature splines in tension algorithm. To test for this possible correlation, I also created surfaces using a inverse distance nearest-neighbour algorithm.

I found that the Green's function spline interpolation performed similarly, regardless of whether it was applied to the spline or nearest-neighbour derived surfaces (Figure 3.5a), and the differences in the final height estimates were not significant (t-test, Green's function spline: $\mu = 1.372 * 10^{-5}$, nearest-neighbour: $\mu = 3.427693 * 10^{-4}$, $p = 0.5257$). Conversely, when I applied the nearest-neighbour interpolation to the nearest-neighbour derived surface, it performed better than on the spline surface (Figure 3.5b) and the heights were significantly different (t-test, Green's function spline: $\mu = 0.00215$, nearest-neighbour: $\mu = 0.00476$, $p = 3.525 * 10^{-3}$). This correlation was not apparent for any of the other interpolation methods. I chose to use the spline-derived surfaces as they tended to represent actual topographic data better than the nearest neighbour surfaces, which was prone to sudden changes in height. The above surfaces were then sampled using actual ICESat locations, creating the LSHV, MSHV and HSHV simulated observational datasets, which will be used later to test my new crossover and along-track methods.

I will be using a number of terms in later sections that I will now clarify to avoid confusion. The term "simulated" will now always refer to the above surfaces and derived ICESat datasets, rather than actual ICESat heights. The term "estimated" will refer to the results obtained from my analysis techniques when applied to the simulated dataset. I will be comparing simulated results derived directly from the surfaces and estimated results, the difference between these two results will be referred to as the "error". In other words, the error is the difference between the "true" results from the simulated surfaces and the estimated results from my analysis techniques. Lastly, when I use the term "uncertainty", I am referring to the standard deviation (σ) that was calculated using my analysis techniques applied to simulated data. Ideally the uncertainty estimate will be as close to the magnitude of the error as possible, as this will give more confidence in my analysis techniques when applied

to actual ICESat data.

3.2.2 Gridded approach to crossover analysis

Rather than comparing height estimates from campaign crossovers that are offset in position from campaign to campaign, such as in the standard campaign crossover method (e.g. Brenner et al., 2007), in my new approach, I choose to define a grid that geographically spans the locations of all the campaign crossovers of any given pair of intersecting non-exact repeat ground-tracks (known from now on as repeat-tracks). I then estimate the height at each of the grid nodes. My gridded approach is designed to allow the location of the repeat-tracks to vary across the crossover region, while estimating the height for the whole crossover region. I will now describe the method in detail:

1. The simulated ICESat data is divided into ascending and descending repeat-tracks. Each of these "mission" ground-tracks (mission-tracks) includes all the repeat-tracks which are offset in position and generally do not overlap. Each pair of ascending and descending repeat-track has its own campaign crossover (Figure 3.6a).

2. To find the centre of the crossover region (mission crossover), I fit a polynomial to both the ascending and descending mission tracks in 25 km increments. The point where the two polynomials intersect is the mission crossover location. The position is further refined by only using data points within a 1 km radius of the first estimate of the mission crossover location. A linear polynomial is refitted to the subsets of both the ascending and descending mission tracks. The point where the linear polynomials intersect is the refined mission crossover location (Figure 3.6b).

3. The mission crossover location becomes the central node of the grid, defined as the mission grid. I tested a number of different grid sizes and found that a 25-node, 400 m x 200 m grid with a grid spacing of 100 m and 50 m, respectively, is the optimal size (Figure 3.8). This was large enough to allow for the spatial variability of the campaign crossovers but not so large that grid nodes have no close data points from which to interpolate their height (Figure 3.7a). I found that the mission grid covers all the campaign crossovers in 94% of cases, however at some crossovers this

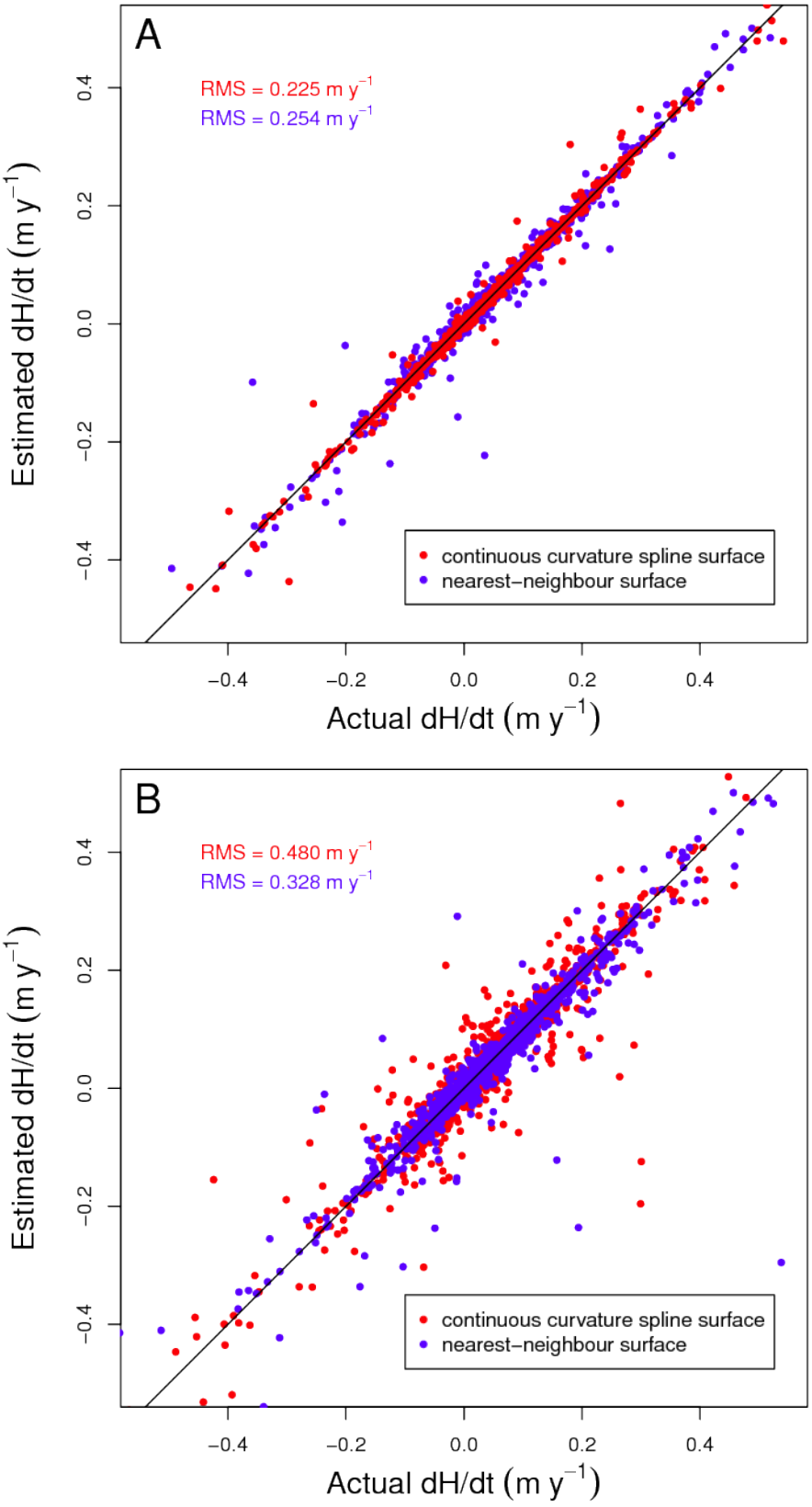

Figure 3.5: The impact of interpolation type on simulated data creation. A) Green's function spline interpolation. B) Nearest-neighbour interpolation.

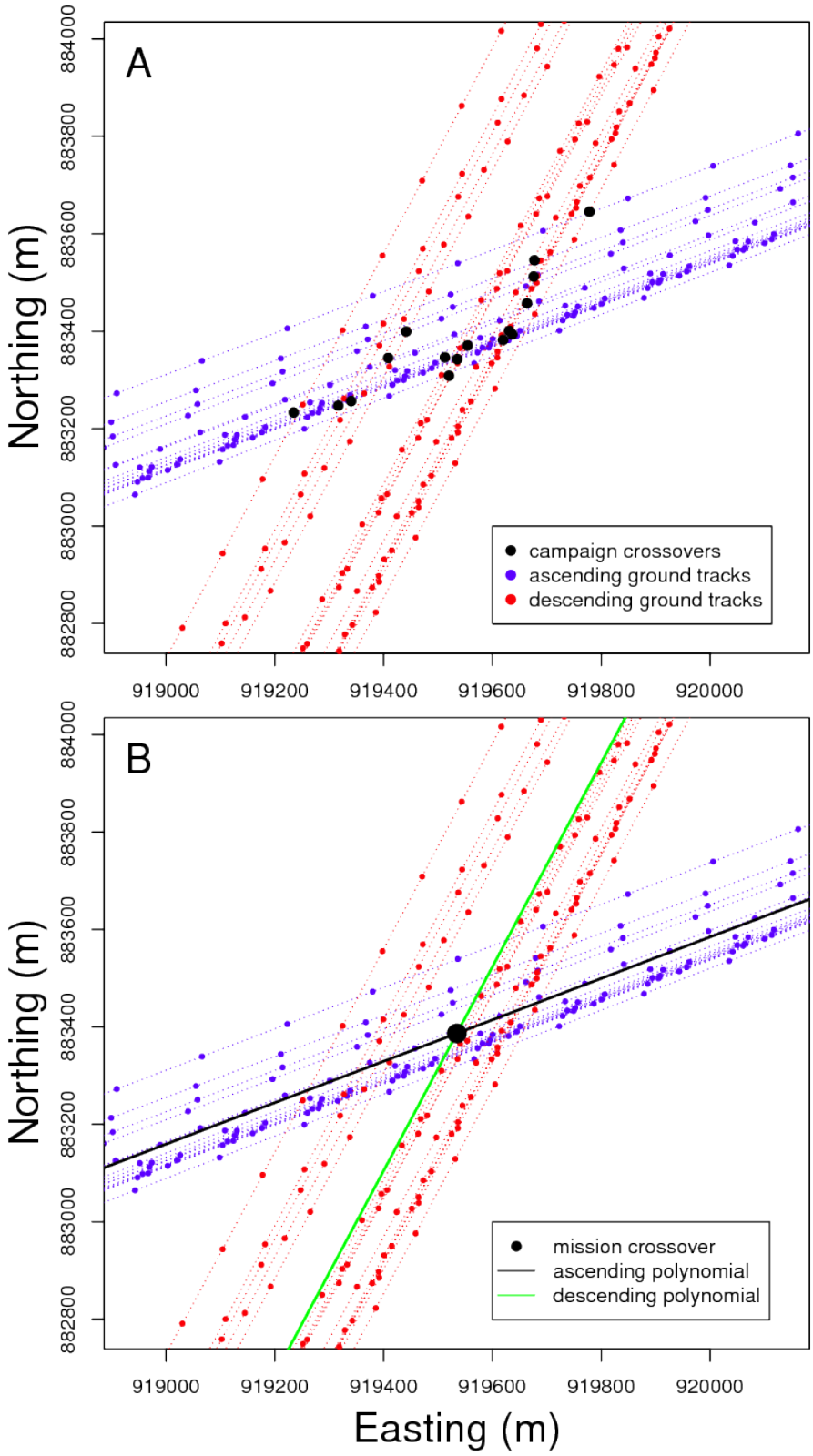

Figure 3.6: Determining the campaign and mission crossovers. A) This figure illustrates the campaign crossover locations (in black) of all the ascending (blue) and descending (red) repeat-tracks. B) I fit a polynomial line to both the the ascending (blue) and descending (red) repeat-tracks, the point where the intersect is known as the mission crossover.

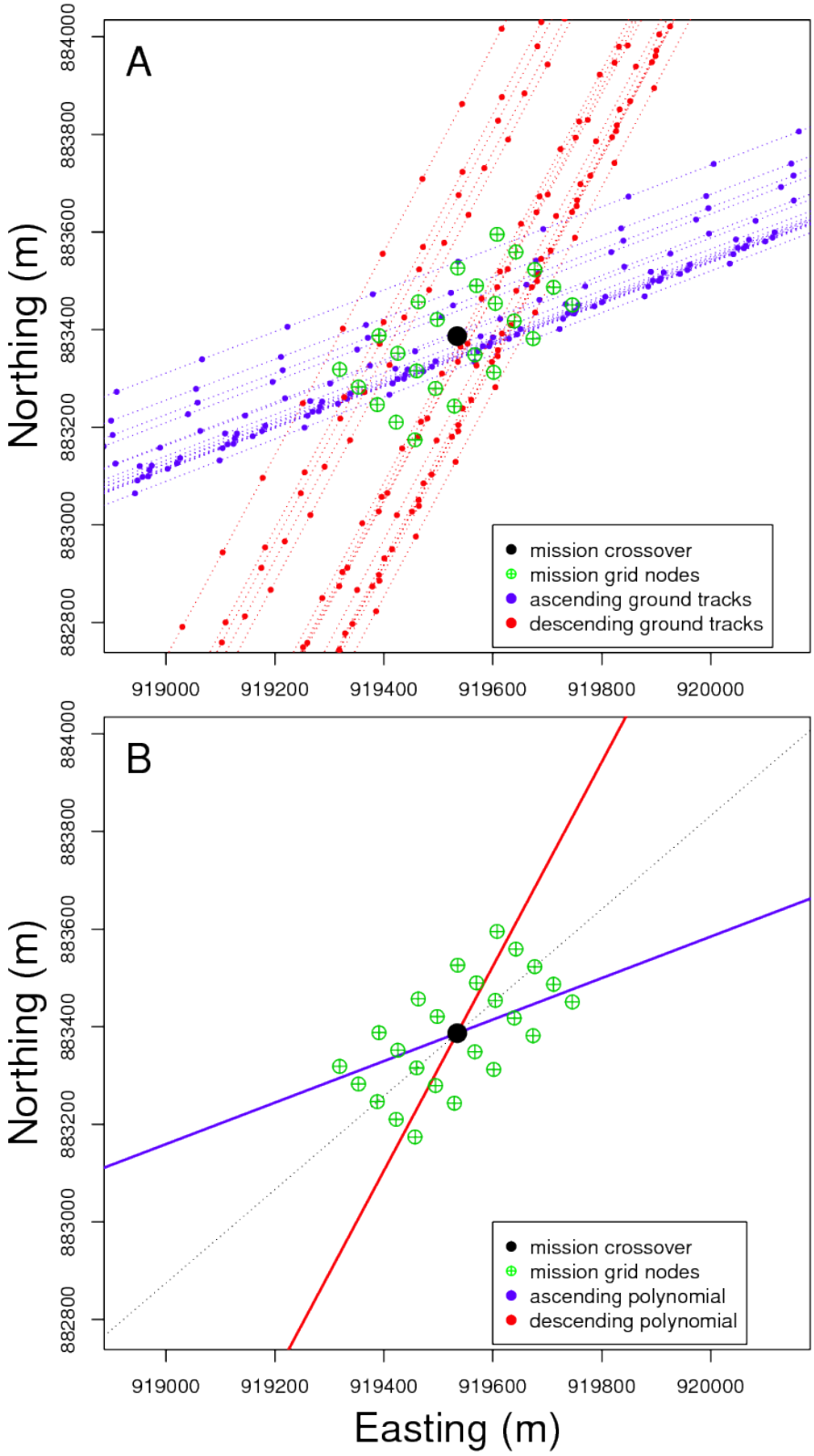

Figure 3.7: Determining the location and orientation of the mission grid. A) The 25 node grid is placed over the mission crossover, making it the central node of the grid. B) The orientation of the mission grid is determined by firstly identifying the short sides of intersecting mission-tracks. The angles are halved for both sides and the line which runs along this angle and intersects the mission crossover, denotes the orientation of the mission grid.

is not the case. I will show an example below.

4. The orientation of the mission grid is determined by the angles created by intersecting mission tracks. The long axis of the grid is determined by running a line which bisects the two short sides of the intersecting mission tracks, while passing through the mission crossover (Figure 3.7b).

5. I used all height data points of each repeat-track that makes up the campaign crossover, within a 500 m radius (interpolation zone) to interpolate the height of each grid node. I assumed that no significant accumulation or ablation has occurred, during the time interval between the ascending and descending repeat-tracks.

6. I also calculated an uncertainty for each grid node height estimate, which is determined by the variance of all height measurements in the interpolation zone and weighting them using an inverse-distance algorithm:

$$w_i = \frac{1}{1 + (3d_i/sr)^2},\ i = 1, N \tag{3.3}$$

where w is the weighting and d is the distance between the grid node and the height measurement, sr denotes the search radius, which is set to 500 m. Therefore, grid node heights that depend upon height measurements further away will have a higher uncertainty.

7. A dH/dt is estimated for each of the 25 grid nodes by computing a weighted least-squares regression to the time series of heights of each of the interpolated grid nodes. The uncertainties are used as weights and, therefore, points that are not close to ICESat measurements will have little effect on the dH/dt estimate. These uncertainties are propagated into the uncertainty of each grid node dH/dt.

Figure 3.9a presents one such time series. The height estimate of the central node for 2003.83, shown in blue, is well constrained as seen in Figure 3.9b. The ascending and descending campaign repeat-track meet in the middle of the mission grid, minimising the distance between the grid nodes and the actual height measurements. In the case of the central node, a ICESat height measurement is nearly directly below it and therefore the uncertainty is low. My choice of grid size aimed to maximise this situation to minimise the need for interpolation.

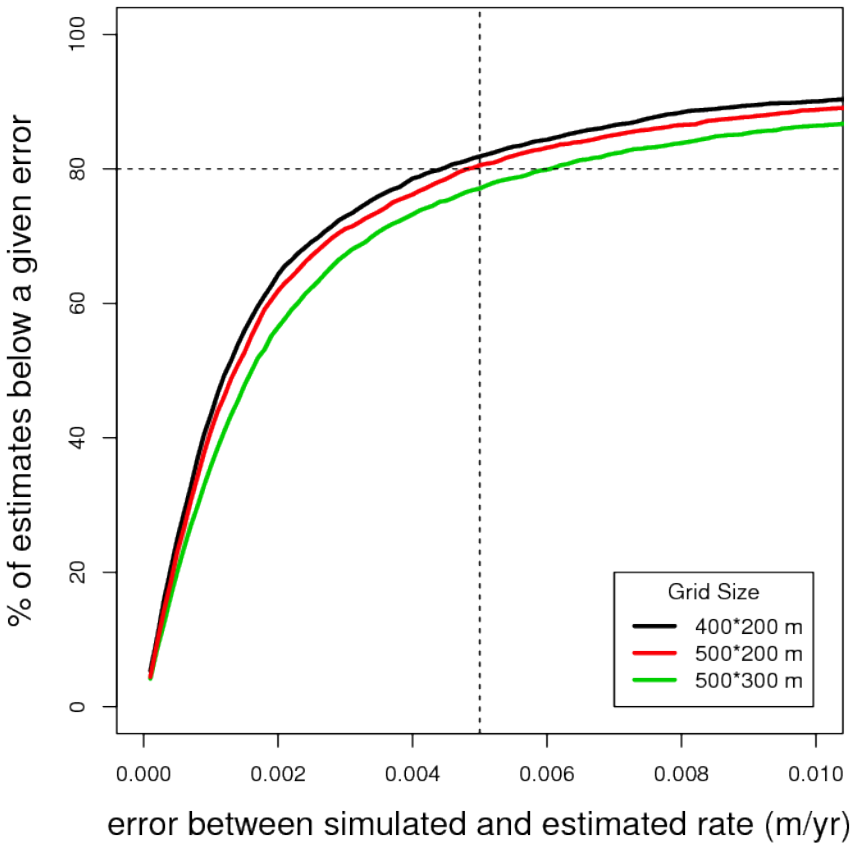

Figure 3.8: Percentage of estimates below a given rate error (difference between the estimated value and the simulated value) when comparing different grid sizes. The results presented are from the MSHV surface.

As mentioned earlier, some campaign crossovers fall outside of the mission grid, as is this case for the 2008.83 height estimate (green arrow, Figure 3.9c). The central node is far away from the actual campaign crossover or any ICESat height measurements and, consequently, the uncertainty for this estimate is high.

A weighted mean of the 25 grid node rates is calculated, yielding a mean dH/dt for each crossover region. Grid nodes far from repeat-tracks will have high uncertainties and, therefore, contribute very little to mean rate. The weightings used are a combination of the RMS of the least squares regression and propagated uncertainties from the height estimates. A mean uncertainty is also estimated. The advantage of this approach is that heights can be estimated at the same locations over time, allowing to accurately estimate rates of height change for the crossover region, while accommodating different levels of accuracy because of varying repeat-track geometry.

I repeated this method, each time using a different interpolation technique: nearest-neighbour interpolation (see Lu and Wong, 2008), Delaunay triangulation with linear interpolation (see Shewchuk, 1996), ordinary kriging (see Journel and Huijbregts, 1978; Olea, 1999) and Green's function spline interpolation (see Wessel, 2009), to interpolate the grid nodes heights. These interpolation methods are discussed in more detail in Section 3.3 and the results of my gridded crossover method can be found in Section 3.4.2.

This method has a useful by-product: a Digital height Model (DEM) generated from the interpolated grid nodes for each ∼33-day laser campaign, from which the cross-track slope can be estimated. The method I used to create these DEMs is described below.

3.2.3 Estimating surface slope correction from crossover DEMs

As the location of my mission grid is static, grid nodes lend themselves well to creating a localised DEM of the crossover region. To estimate the surface slope and aspect at each crossover region, I derived a reference DEM by choosing the laser campaign covering the largest area and having the lowest dH/dt uncertainties, and estimated a height for each grid node using only data from the given laser campaign. I used a 3 x 3 point moving window to calculate the finite differential, where the central node is the point on the surface $z = f(x, y)$ and its slope (S) and aspect (A) are defined as a function of the gradients at x and y.

$$S = arctan\sqrt{f_x^2 + f_y^2} \tag{3.4}$$

$$A = 270^\circ + arctan\left(\frac{f_y}{f_x}\right) - 90^\circ\frac{f_x}{|f_x|}, \tag{3.5}$$

where f_x and f_y are the cross-track and along-track components (Zhou and Liu, 2004). There are several popular algorithms used for calculating f_x and f_y, differing in which grid nodes are used and the weightings applied. I chose to use the second-order finite-difference algorithm as it was found to perform best using high resolution DEMs (Jones, 1998), although my own tests found little difference between this and

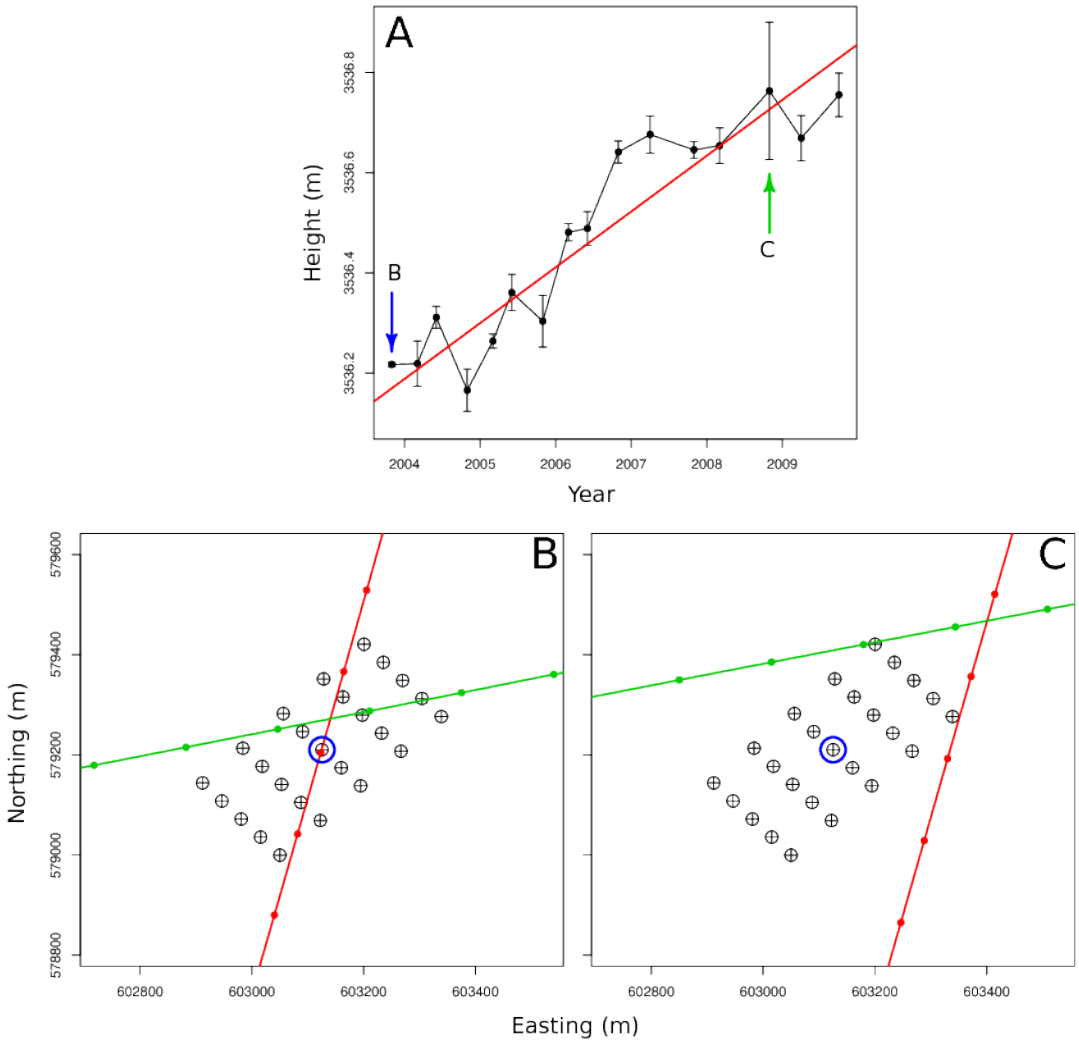

Figure 3.9: A) A time series of one grid node from a mission grid. The central node of the mission grid is used as an example, which happens to also be the location of the mission crossover (denoted by the blue circle in figure B and figure C). The blue arrow points to a well constrained point in 2003.83, which is presented in figure B, while the green arrow points to a badly constrained point in 2008.83, shown in figure C. B) An ascending (green) and descending (red) repeat-track for the 2003.83 campaign (campaign 2A). The mission grid is well positioned and a ICESat measurement is directly below the central grid node, therefore the uncertainty of the interpolated height is low. C) An ascending (green) and descending (red) repeat-track for the 2008.83 campaign (campaign 2D). No ICESat measurements are close to the central node and therefore the interpolated height in this case has a higher uncertainty and will contribute less to the mean rate estimate.

the accuracy of the other five gradient algorithms presented by Zhou and Liu (2004). The f_x and f_y for second-order finite-difference algorithm are denoted as:

$$f_x = (z_8 - z_2)/2g,\ f_y = (z_6 - z_4)/2g \tag{3.6}$$

where z denotes the grid nodes used and g is the grid resolution. Zhou and Liu (2004) found that, when grid resolution is low, the choice of algorithm becomes less important. I chose a grid resolution of 100 m, which Zhou and Liu (2004) deemed to be low resolution.

As this method requires nine grid nodes (3x3 grid window) to estimate the surface slope and aspect, only the surface slopes of the central nine grid nodes in my 25-node crossover grids could be determined (Figure 3.10). I then took the weighted mean of these nine estimates to derive a mean surface slope, aspect and uncertainty for each crossover region. An uncertainty for each slope estimate was calculated by adding the uncertainties of the two height estimates used in each slope estimate. Therefore, heights that are not well constrained have less effect on the overall estimate of surface slope for the crossover region.

3.2.4 Gridded approach to along-track analysis and slope correction

In this section I present a new method of estimating dH/dt along-track, incorporating my surface slope estimates at crossovers to provide the cross-track surface slope corrections for along-track segments between the crossovers. I superimposed a 500 m x 300 m grid (24 nodes), with a grid spacing of 100 m, over segments of along-track data for each ~33-day laser campaign and then estimated the height at each grid node for each laser campaign, using the Green's function spline interpolation method, which I found to be the most accurate (section 3.4.1). I used the same gridded method to estimate dH/dt for each along-track segment, as presented in section 3.2.2. The only differences between my crossover and along-track methods are the number of nodes, the size of the grid and the use of only one repeat-track for the interpolation in the along-track method, instead of two in the crossover method.

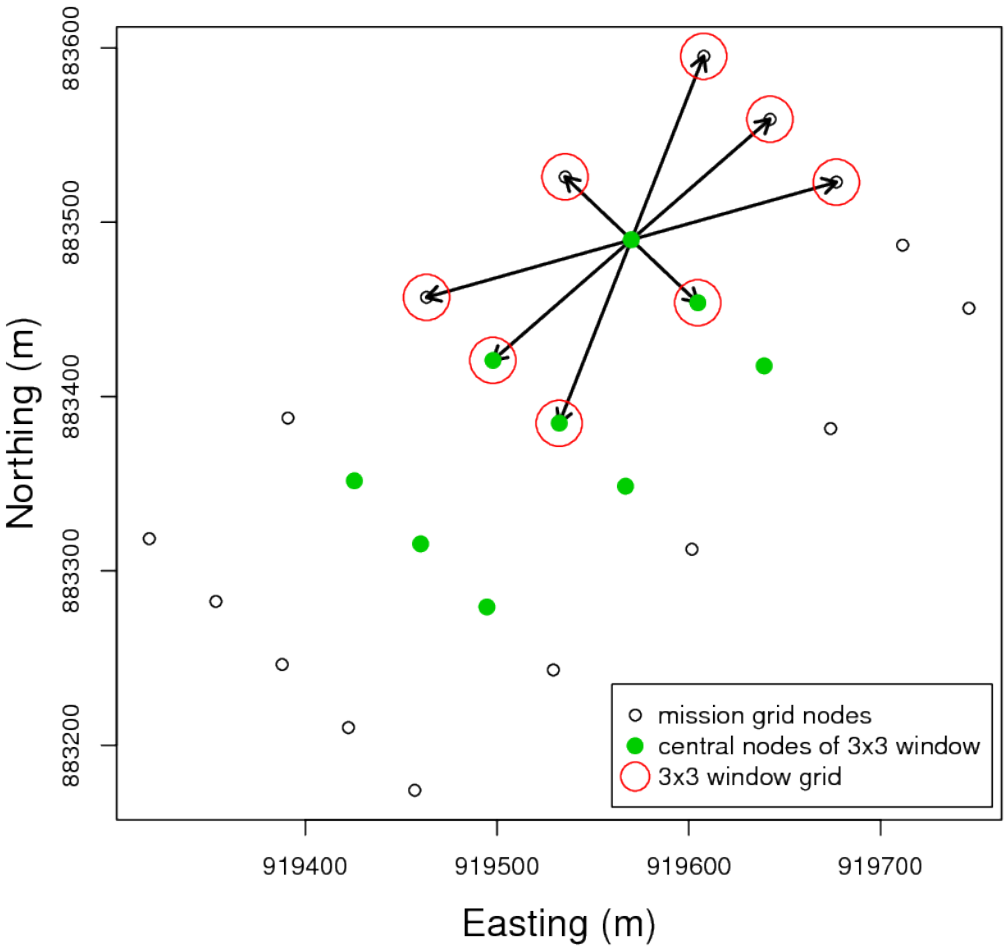

Figure 3.10: A visual representation of slope estimation using a 3x3 grid window (solid green circles) on a 25-node mission grid (black circles). The eight outer nodes (red circles) are required to estimate the slope and aspect of the central node (solid green circle). This scheme only allows for a slope estimation of the inner nine nodes.

In order to correct for surface slope along-track, I applied a two step process. Firstly, I linearly interpolated the cross-track slope to each along-track segment using my cross-track slope values derived from the DEMs at the two closest crossovers. The uncertainty of the surface slope estimate is also propagated to the interpolated slope. This uncertainty increases as a exponential function of distance from the crossover positions. That is, the uncertainty increases as the grid's position is further from the crossover:

$$\hat{\sigma} = \sigma_{int} * exp\left(\frac{d}{g/2}\right) \tag{3.7}$$

where $\hat{\sigma}$ is the estimated uncertainty for the along-track segment. σ_{int} is the linearly interpolated uncertainty from the two closest crossovers, d is the distance from the closest crossover and g is the distance between the two closest crossovers. I chose this function as it best represented the simulated error distribution over the study site (Figure 3.16).

As the resolution of the first method is low, especially near coastal regions where few crossovers are present, I also estimated surface slope along-track using the method presented by Ewert et al. (2012). I fitted the following biquadratic function to all the along-track data in the segment to approximate the local ice surface topography:

$$\triangle S_i = a_0 + a_1 x_i + a_2 y_i + a_3 x_i^2 + a_4 x_i y_i + a_5 y_i^2 + a_6 x_i^2 y_i + a_7 x_i y_i^2 + a_8 x_i^2 y_i^2 \tag{3.8}$$

where i is the counter (i = 1, 2, 3, . . ., N). N denotes the number of height measurements within the along-track segment. x and y are the location of the height measurement. This polynomial is used to account for the height differences due to surface topography between the individual height measurements (Ewert et al., 2012). As mentioned earlier, this method is susceptible to track constellation correlation (Sørensen et al., 2011; Ewert et al., 2012). I tested for this correlation and, if present, the surface slope estimate was removed and I used the interpolated surface slope

value from the crossovers.

I also compared all along-track surface slope estimates to the crossover interpolated estimates and, if they were in agreement (1-sigma), the along-track estimate was used. If there was agreement, I was confident that the across-track surface slope signal had been separated from the dH/dt signal. If this is not the case, I compared the along-track surface slope estimate with the two along-track estimates before and after (∼1 km in either direction) . If there was no along-track constellation correlation and the estimates were in agreement (1-sigma), I used the along-track derived estimate. Otherwise I used the interpolated crossover estimate. This combination of methods increases the surface slope correction resolution, which is low when using only crossovers, while maintaining a higher accuracy than just using the along-track data. I define this as the combined surface slope correction method.

This is repeated segment by segment along all of the ground-tracks. The slope uncertainties were propagated into the height estimates, which in turn are propagated into the final dH/dt for each segment. The results of my along-track method are shown in Section 3.4.3. The accuracy of my slope correction method is discussed in Section 3.4.1.

This method is similar to that of Schenk and Csatho (2012), who also linearly interpolate their surface slope parameters along-track. They, as well as other along-track plane-fitting methods (e.g. Howat et al., 2008; Smith et al., 2009; Moholdt et al., 2010; Sørensen et al., 2011; Zwally et al., 2011a; Ewert et al., 2012), assume that surface shape does not change over 1 km scales. My method does not make this assumption and allows the surface shape to vary, which is the case near the margins of the ice-sheets, where the most change is occurring.

3.3 Interpolation methods

In this section I discuss four different interpolation methods that have been used in the literature to interpolate between measurements of height (Brenner et al., 2007; Gunter et al., 2009; Pritchard et al., 2009); being Nearest-neighbour interpolation, Delaunay triangulation with linear interpolation, Geo-statistical analysis: Ordinary

Kriging and Green's function spline interpolation. I discuss each method's strengths and weaknesses, to give the reader a good theoretical foundation of the interpolation method used in this study.

3.3.1 Nearest-neighbour interpolation

The nearest-neighbour interpolation is the simplest and fastest method used to interpolate regular and irregular positioned points. There are many different ways of implementing this method and, for this study, an inverse-distance weighting algorithm was used. The distances are calculated between the node and all data points within a specified search radius (500 m in this study) and time interval (~33 days in this study), the closest points (10 points in this study) are used in the interpolation. Data points that are closer to the node are given greater importance and their contribution to the final estimate is therefore greater (Lu and Wong, 2008). The estimate is determined by calculating weighting factors, which are inversely related to the distance and the search radius:

$$w_i = \frac{1}{1 + (3d_i/sr)^2},\ i = 1, N \tag{3.9}$$

where d is the distance from the node and sr is the search radius. The estimated height, H^* is found from:

$$H^* = \sum_{i=1}^{n}(w_i h_i),\ i = 1, N \tag{3.10}$$

where h_i are the original height values and,

$$\sum_{i=1}^{n}(w_i) = 1 \quad and \quad w_i = f\{d_i\} \tag{3.11}$$

This is one of many inverse-distance weighting algorithms, the simplest being:

$$w_i = \frac{1}{d_i},\ i = 1, N \tag{3.12}$$

where an exponent can be added to d_i to increase the importance of points closer

to the point of interest.

The interpolation uncertainty is calculated for each grid node as a function of both the variance of the height measurements and how close they were to data points. Consequently, grid nodes that were closer to repeat-tracks were well determined and had lower uncertainties, while grid nodes far away from repeat-tracks were poorly determined and therefore had greater uncertainties. This relationship between distance and uncertainty is the same for most interpolation methods, even though their accuracy does vary as shown in Section 3.4.

There are number of disadvantages to this method. Firstly, the choice of weighting function is arbitrary and, if the properties of the underlying surface are not well understood, this can introduce ambiguities (Burrough, 1986). Secondly, the interpolation can be biased by unevenly distributed height measurements, especially when there are clusters of points (Hu, 1995). This situation leads to anisotropy where each point in the cluster will receive nearly the same weighting, creating an artificially large weight that is directionally dependent (Tomczak, 1998). Lastly, the inverse-distance weighting method by its very nature is a smoothing/averaging technique and therefore maximum and minimum values can only occur where there are actual data points (Burrough, 1986).

3.3.2 Delaunay triangulation with linear interpolation

Delaunay triangulation is one of many different triangulation techniques. Triangulation is broadly defined as the segmentation of a surface into group of triangles, where each triangle's side should be entirely shared by two contiguous triangles. The Delaunay triangulation, like other triangulation algorithms, creates a triangular mesh of planes which connects the data points inside the area of interest. What makes this algorithm unique is the way in which the triangles are created. A circle is placed over the triangle, which intersects each of the three corners of the triangle, this circle is known as a circum-circle (Figure 3.11). For a triangle to be categorised as a Delaunay triangle, it must satisfy the "empty circle property" (Shewchuk, 2002), being that no data points other than the three points that make up the triangle are

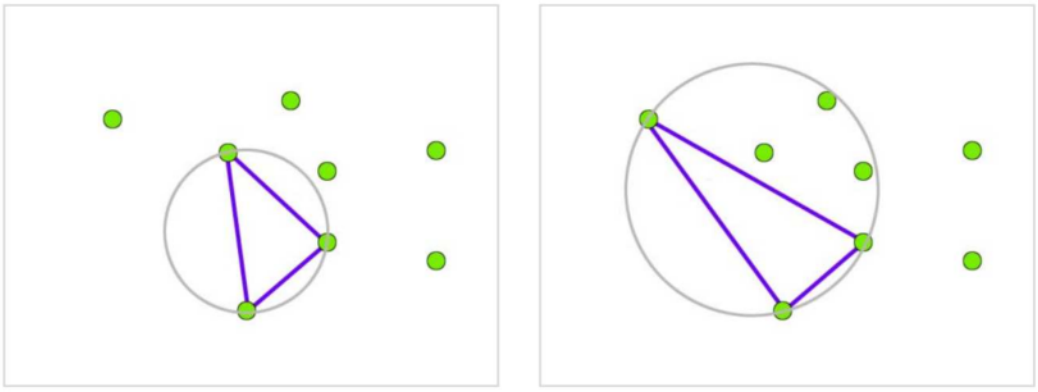

Figure 3.11: The triangle on the left is a Delaunay triangle as it has no other data points except vertices in the circum-circle and it therefore satisfies the "empty circle property". The triangle on the right is not a Delaunay triangle as there are other data points in the circum-circle.

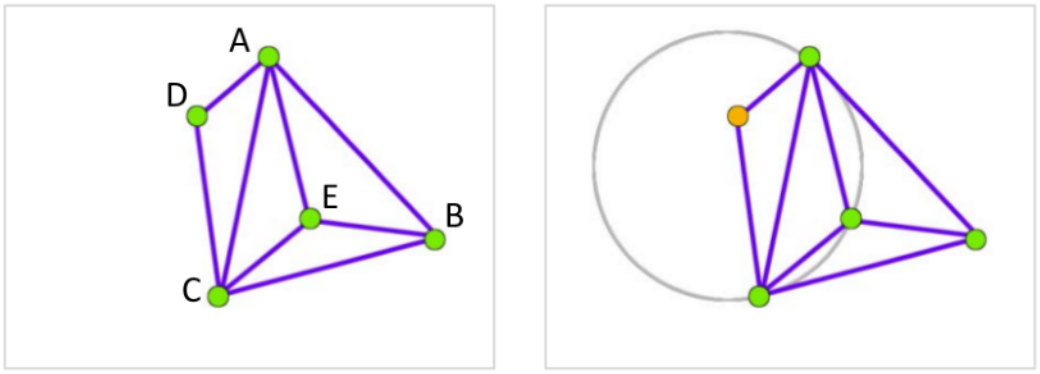

Figure 3.12: The triangular mesh on the left is not a valid Delaunay configuration, as the AEC triangle has another data point in its circum-circle as seen in the right hand figure.

allowed to be inside the circum-circle (Figure 3.11). The triangular mesh shown in Figure 3.12 is an example of an invalid configuration as the AEC triangle does not satisfy the "empty circle property" and is therefore not a Delaunay triangle. When the AC edge is flipped to DE edge a valid Delaunay triangulation is created (Figure 3.13).

There are a number of different algorithms that can yield valid networks of Delaunay triangles. The goal of these algorithms is not only to create valid networks but also to maximise the minimum angle of all the triangles to minimise the number of acute triangles in the triangular network (De Berg et al., 2008). This leads to more accurate estimates. Figures 3.12 and 3.13 show an example of the flip algorithm, it is the most simplistic and intuitive method, however it is also very slow when applied to large datasets (Shewchuk, 2002).

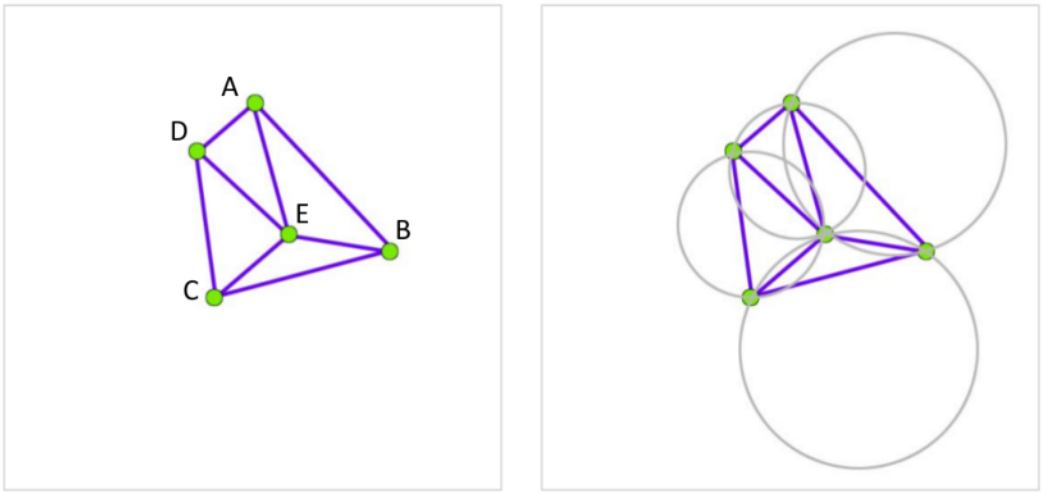

Figure 3.13: The invalid triangular configuration in Figure 3.12 is made valid by flipping the AC edge to the DE edge as seen on the left hand side. It therefore satisfies the "empty circle property" as seen on the right.

Other algorithms include the incremental (Watson, 1982), sweepline (Fortune, 1987), sweephull (Sinclair, 2010) and divide and conquer methods (Shewchuk, 1996). Each method has its strengths and weaknesses. In this study, I used the Shewchuk (1996) divide and conquer method of Delaunay triangulation, as this algorithm is the fastest and most robust of the Delaunay triangulation methods.

The advantage of using the Delaunay triangulation method is, firstly, it is an exact estimator, as the height measurements are part of the triangular surface and therefore the method honours the original data points (Hu, 1995). Secondly, as this method does not have a smoothing effect like nearest neighbour interpolation technique, it performs well over surfaces with substantial relief features. It is able to maintain the structural integrity of features such as valleys, ridge lines, peaks and troughs etc. (Hu, 1995). It is also faster at representing surfaces as it requires less points to do so than other methods (Hu, 1995).

The Delaunay triangulation method also has some disadvantages. As it is an exact estimator it can only estimate heights within the triangular mesh and cannot extrapolate outside of this domain. This can be a problem near the boundary of a dataset, where there are no triangles. Consequently, when using Delaunay triangulation to estimate heights on a regular grid, the grid must fit inside the triangular network. Furthermore, the surfaces created by Delaunay triangulation can have a jagged appearance as no smoothing occurs. This can also lead to discontinuous

slopes at the edges of triangle or outlier height points (Hu, 1995).

In this study, Delaunay triangulations are applied to all the simulated ICESat data, which creates triangulated irregular networks (TINs). TINs are long thin triangular mesh networks that follow the ICESat ground-tracks and do not form triangles between distant ground-tracks. It is important not to triangulate the regions between distant ground-tracks as this will produce long, acute triangles that do not represent the true surface properly. As mentioned earlier, estimates can only be obtained for points within a given triangle, which means Delaunay triangulation method does not work with my gridded along-track method (see chapter 4, for more details on this).

The method does work well over crossovers, where a TIN was created using data points within an 800m radius. This search radius is larger than that of the nearest-neighbour interpolation method to make sure that all points of interest are within a corresponding TINs triangle. The estimate is calculated by linearly interpolating across that triangular surface. The interpolation uncertainty is estimated for each node using the three height measurements and their distance from the estimated point.

3.3.3 Geo-statistical analysis: ordinary kriging

Geo-statistical methods for interpolation and extrapolation of irregularly spaced data are also known as kriging methods. Kriging covers a family of methods based on the principle of unbiased least-squares optimisation and is generally introduced in a probabilistic framework (Matheron, 1963; Journel and Huijbregts, 1978). It can however be viewed as a numerical interpolation technique (Herzfeld, 1992). Assumptions about degree of stationarity of the variable (in this case surface height) or an underlying trend can be included in the unbiased estimates (Hock and Jensen, 1999; Herzfeld et al., 2008).

Kriging consists of two steps: (1) an analysis of the spatial structure of the data, where experimental semi-variograms are calculated and then the variogram models are derived; (2) kriging estimation including interpolation and extrapolation.

First, an experimental semi-variogram was calculated according to:

$$\gamma\left(h\right)=\frac{1}{2n(h)}\sum_{i=1}^{n}\left[z(x_i)-z(x_i+h)\right]^2 \tag{3.13}$$

where $z(x_i)$ and $z(x_i+h)$ are the measurements at locations x_i and x_i+h respectively and $n(h)$ is the number of pairs separated by the vector h. The experimental semi-variograms are calculated by binning the variances of height measurements by their distance and then fitting an analytical variogram model. A variogram model was chosen which best explains the transition from closely neighbouring samples with a higher degree of co-variation to reduced co-variation typical of samples farther apart (Olea, 1999). There are a number of authorised variogram models available and each has its own unique function type and varies depending on the choice of parameter values. Each model has certain mathematical requirements that have to be met, so each model has it own distinctive solution(Olea, 1999).

The main variogram model used in my study is the Gaussian model:

$$\gamma(0)=0$$

$$\gamma(h)=C_0+C\{1-exp(-\frac{h^2}{a^2})\}\ when\ h>0 \tag{3.14}$$

where γ is the semi-variogram and h the distance between the two points of interest. The parameter a represents the so-called "range of influence" of the semi-variogram. C is the sill (the point at which samples are "independent" of one another), C_0 is the nugget effect, which is of little importance in this study, due to its extremely small size (Clark and Harper, 2000).

In the kriging method termed ordinary kriging, the value $z_0=z(x_0)$ at the point x_0 is estimated by:

$$z_0=\sum_{i=1}^{n}\alpha_i z_i \tag{3.15}$$

where α_i are the weighted kriging coefficients and $z_i=z(x_i)$ are the measurements at locations $x_i(i=1,...,n)$ in a neighbourhood of the point being estimated x_0.

The weighted coefficients are determined so that the estimation error has minimum variance and the estimation is unbiased, which requires the following condition to be true:

$$\sum_{i=1}^{n} \alpha_i = 1 \tag{3.16}$$

The kriging system solution is obtained using the best fitting variogram model (combination of mathematical model and parameter values) as specified earlier (For a complete derivation of the kriging method, see Cressie (1992); Olea (1999)).

If there is an inherent regional trend apparent in the data, universal kriging may be used which differs from ordinary kriging in its use of the "unbiasedness" condition (Eq. 3.8). The "unbiasedness" condition of universal kriging takes into account a locally variable trend, also called drift (Olea, 1999). Herzfeld et al. (2008) found that ordinary kriging was better suited for interpolation of altimeter data than universal kriging, because the drift modelled by a polynomial component in the higher order universal kriging methods creates artifacts in the gaps between distant ground-tracks.

The advantage of using kriging to interpolate surface height, is that the uncertainty can be estimated directly. Kriging is an optimal interpolator and therefore estimates have minimum variances and are also unbiased. The variances can also be plotted in the same fashion as that of the estimates and therefore a measure of confidence can be obtained when a specific distribution is assumed (Hu, 1995). Kriging has an extremely useful property known as declustering, where points that are in a cluster are treated as the same point and are weighted as such. This helps to minimise the effect of anisotropy, which is problematic in nearest neighbour interpolation.

The major drawback to kriging is its strong reliance on the variogram model. The choice of variogram model is guided primarily by the best least-squares fit and not the actual processes which underpin the spatial variation in the region. It is therefore often difficult to assess how well it truly represents the spatial correlation in the area of interest. By its very nature, kriging is basically a smoothing interpo-

lation technique that behaves much in the same way that a filter does (Hu, 1995). Its strength therefore lies in observing general spatial trends and minimising the likelihood of erroneous or large oscillations in surface height estimates. Conversely, it does not perform well when the data presents abrupt breaks, peaks or troughs, such as one might find in glaciers and outlet flow regions.

3.3.4 Green's function spline interpolation

One of the most popular methods to obtain height estimates involves using splines to fit a minimum curvature surface to the available data (Wessel, 2009). While effective, this method does not perform well when using data with outliers or sudden and erratic changes in height (Wessel and Bercovici, 1998). Under these conditions, the method introduces extraneous inflection points resulting in large oscillations between the data points used to constrain the surface or curve (Wessel and Bercovici, 1998). This issue can be corrected by adding tension to the surface or curve, a process called continuous curvature splines in tension (Wessel, 2009).

I used the Green's function spline interpolation method first presented by Wessel and Bercovici (1998). The method works by creating an interpolated surface from a linear combination of Green's functions at each data point in the domain. The linear combination is determined by calculating the Green's function for all distances between the estimated point and all the available data points (Wessel, 2009). The contribution of each of these Green's functions is weighted by a scale related to the data point in question and then summed to obtain the final height estimate at that point (Sandwell, 1987; Wessel, 2009).

Formally, the Green's function spline surface, $w(\mathbf{x})$, can be expressed as:

$$w(\mathbf{x}) = T(\mathbf{x}) + \sum_{j=1}^{n} \alpha_j \, g(\mathbf{x}, \mathbf{x}_j) \tag{3.17}$$

where $\mathbf{x}$ is estimated point location, $T(\mathbf{x})$ is a trend function that removes either a regional trend associated with the data or any processes that cannot be expressed with Green's functions, in the later case this is generally a constant (Wessel, 2009). g is the Green's function, $\mathbf{x}_j$ is the position of the jth data point and α_j are the

associated unknown weights (Wessel, 2009).

The α_j unknown weights are determined by evaluating Eq. 3.10 at all the data point locations $(1, n)$:

$$w(\mathbf{x}_i) = \sum_{j=1}^{n} \alpha_j \, g(\mathbf{x}_i, \mathbf{x}_j), \quad j = 1, n \tag{3.18}$$

This yielded a n by n square linear system which is solved for α_j (Wessel, 2009). The Green's function must satisfy the inhomogeneous partial differential equation (Wessel, 2009):

$$\nabla^2 \left[\nabla^2 - p^2\right] g(\mathbf{x}, \mathbf{x}^{'}) = \delta(\mathbf{x} - \mathbf{x}^{'}) \tag{3.19}$$

where ∇^2 is the Laplacian operator, δ is the Dirac Delta function, and p is the tension (Wessel, 2009). When solving Eq. 3.12, ∇^2 and δ must be expressed in the appropriate coordinate system (Cartesian for this study). This results in a different Green's functions $g(\mathbf{x}, \mathbf{x}^{'})$. As the splines are in tension it is a prerequisite of the method that derivatives higher than the curvature should exist and be continuous as well (Wessel and Bercovici, 1998; Wessel, 2009). There are a number of different Green's functions for splines in tension used in the literature. I used the Green's functions published by Wessel and Bercovici (1998) for $p > 0$:

$$g(\mathbf{x}, \mathbf{x}^{'}) = (1/p\,|\mathbf{x}|)(e^{-p|\mathbf{x}|} - 1) + 1 \tag{3.20}$$

and its gradient:

$$\left|\nabla g(\mathbf{x}, \mathbf{x}^{'})\right| = (1/p\,|\mathbf{x}|^2)[e^{-p|\mathbf{x}|} - 1(p\,|\mathbf{x}| + 1)] + 1 \tag{3.21}$$

Wessel (2009) recommends a moderate p value for topographic data and, for this study, I tested a series of p values (see section 3.2.1). It is recommended that the input is normalised before the Green's function method is applied. After the linear system has been solved, the trend (if one was present) and normalisations are recovered for the final output values (Wessel and Smith, 2013). An uncertainty is also calculated, again using the standard deviation and distances between the data

points and the estimated point.

There are a number of advantages to using the Green's function spline interpolation. Firstly, as there are no requirements for a regular input or output grid, one is free to choose the output geometry (Wessel, 2009). Secondly, the interpolation can be constrained not only by surface heights but also surface slopes, making it very flexible (Wessel and Bercovici, 1998). Lastly, the method is able to extrapolate height points outside of the data domain, making it especially useful when applied to the sparse along-track ICESat data.

The major disadvantage of this method is that, even with tension applied, numerical instabilities can occur when the ratio of the minimum point separation to the maximum point separation is large (Wessel and Bercovici, 1998). In the rare occasion that this occurs, the uncertainty is generally large as it is calculated in part using the distances between data points and the estimate point. Due to the method's versatility, it is applied to both crossover and along-track data.

3.4 Results and Discussion

I sampled my simulated surfaces using actual ICESat repeat-tracks to create three simulated ICESat height datasets, each with a different noise level. Each height measurement retained its exact location and time of measurement, only the height value was simulated. These datasets allowed me to test whether my gridded crossover approach was more accurate than the standard campaign crossover method and to determine which interpolation technique performed the best when used in conjunction with the two crossover analysis methods. I could also assess how well my gridded approach was able to estimate heights and surface slope corrections for the along-track data. Finally, I could assess how accurately I had estimated the slope at crossovers and how closely these estimates of surface slope, once interpolated along-track, resembled the cross-track surface slope at along-track segments.

3.4.1 Assessing accuracy of crossover and interpolation methods

From the simulated dataset, I first identified all the campaign and mission crossover locations. To reiterate, the mission crossover is the central location of all the campaign crossovers with a crossover region. I then determined the "true" dH/dt of the crossover region by sampling the simulated surface, and calculated dH/dt for the crossover region. For the gridded method, I sampled the surfaces using the grid nodes placed over all the campaign crossovers. I then applied the gridded crossover approach to calculate dH/dt from the simulated heights, as explained earlier in section 3.2.2. I determined the error in the approach by differencing the estimated dH/dt from the simulated dH/dt.

In the case of the standard campaign method, I sampled the heights for both the ascending and descending repeat-tracks from the simulated surfaces. These heights were interpolated to the campaign crossover location. I then differenced the heights to obtain the dH for the campaign crossover. The dH estimates were converted into dH/dt by using crossover times linearly interpolated from each ascending and descending repeat-track (Gunter et al., 2009). As the "true" dH/dt is known from the simulated surfaces, I differenced the dH/dt estimate and the simulated dH/dt to derive a measure of the error of the estimate.

The result for each method is an interpolated dH/dt estimate, a simulated dH/dt, the error (the difference between the simulated and the estimated value) and an uncertainty, for each crossover location. For the gridded crossover method, I tried four different interpolation methods; nearest-neighbour interpolation (see Lu and Wong, 2008), Delaunay triangulation with linear interpolation (see Shewchuk, 2002), Ordinary kriging (see Olea, 1999) and Green's function spline interpolation (see Wessel, 2009). For the campaign crossover method I used only linear interpolation and Green's function spline interpolation, as the other interpolation methods were unsuitable for this case.

3.4.1.1 Results: gridded approach to crossover analysis

The use of a static mission grid approach showed that the Green's function spline

interpolation method (GRID-GFSI) was the most accurate interpolation technique when used on all three surfaces (Figure 3.14). 88.7%, 84.8%, 83% of crossovers had rate error less than 5 mm/yr for the LSHV, MSHV and HSHV surfaces, respectively (I chose the maximum dH/dt target error to be 5 mm/yr as this produced a dM/dt error which was the approximate average of the dM/dt uncertainties collated by Shepherd and Wingham (2007)). Delaunay triangulation with linear interpolation using the gridded approach (GRID-DTLI) was the next best approach with 85.4%, 81.8%, 78.3% of crossovers having a rate error less than 5 mm/yr for the LSHV, MSHV and HSHV surfaces, respectively. It generally performed as well as the GRID-GFSI approach; however, when few data points were available, the triangles created were very large and the weakness of using a basic method like linear interpolation became apparent. Nearest-neighbour interpolation using the gridded approach (GRID-NNI) was outperformed by GRID-DTLI, except with the HSHV surface, where they performed equally: 76.8% and 77.7% respectively with a rate error less than 5 mm/yr.

Ordinary Kriging using the gridded approach (GRID-OK) performed least well with much larger rate errors (Figure 3.14). Ordinary Kriging uses a model of distance variability (semi-variogram) and assumes that the data is normally distributed, which works well when using larger more uniformly distributed datasets. The range of the variogram model was chosen to be 50 km. I also tried using a variogram model for the whole site and with much smaller ranges, but found that the 50 km range worked best.

The selection of a well fitted variogram model is paramount for the kriging process and requires a detailed understanding of spatial properties of the variable and the ability to visually interpret the fit of the model (Hock and Jensen, 1999; Herzfeld et al., 2008). In this study I was unable to visually inspect every variogram (as there were thousands), and therefore I relied on an automated process which fitted each variogram model to the data and found the best fit. It is clear that kriging is best suited for creating dH/dt surfaces for entire ice sheets as, by working with residuals instead of absolute values, the data can be assumed normally distributed. I found it

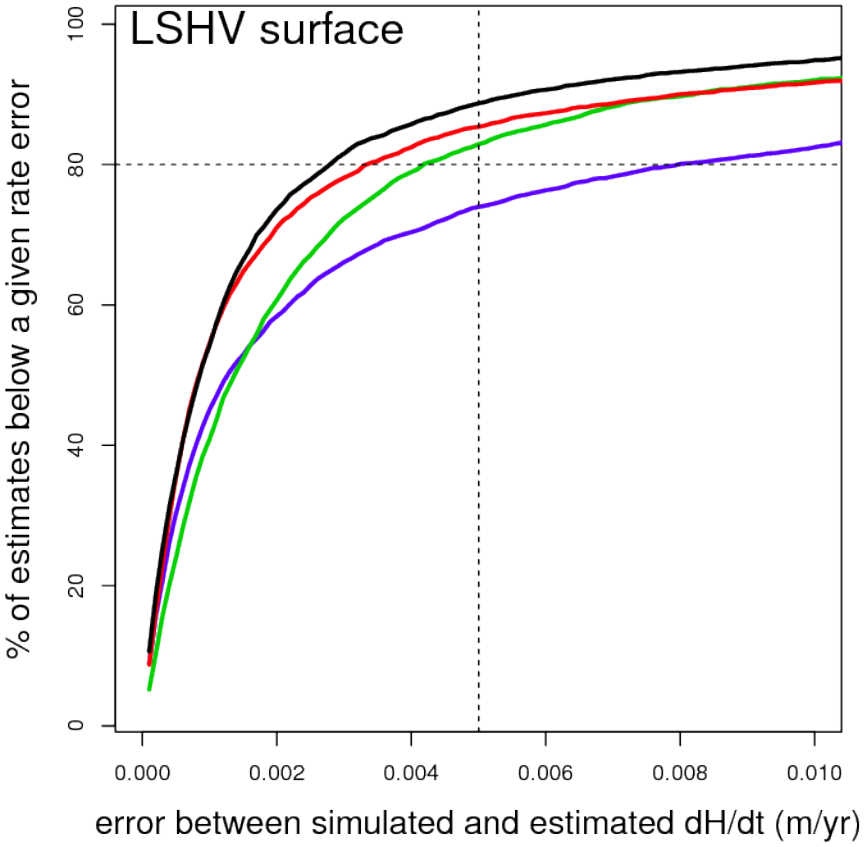
LSHV surface
% of estimates below a given rate error
0
20
40
60
80
100
0.000
0.002
0.004
0.006
0.008
0.010
error between simulated and estimated dH/dt (m/yr)

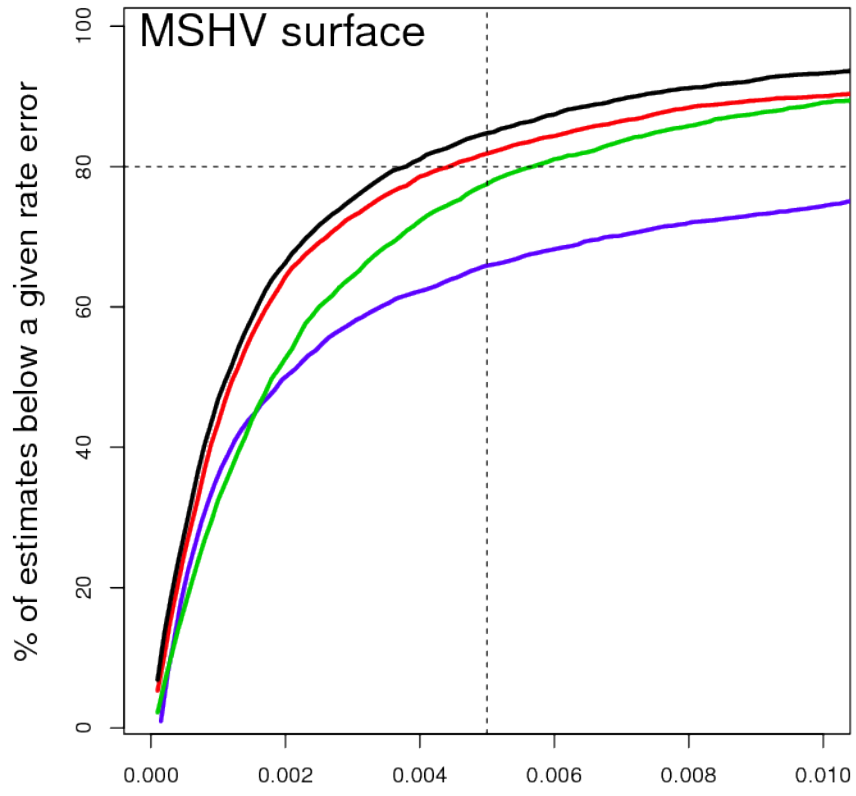
MSHV surface
% of estimates below a given rate error
0
20
40
60
80
100
0.000
0.002
0.004
0.006
0.008
0.010

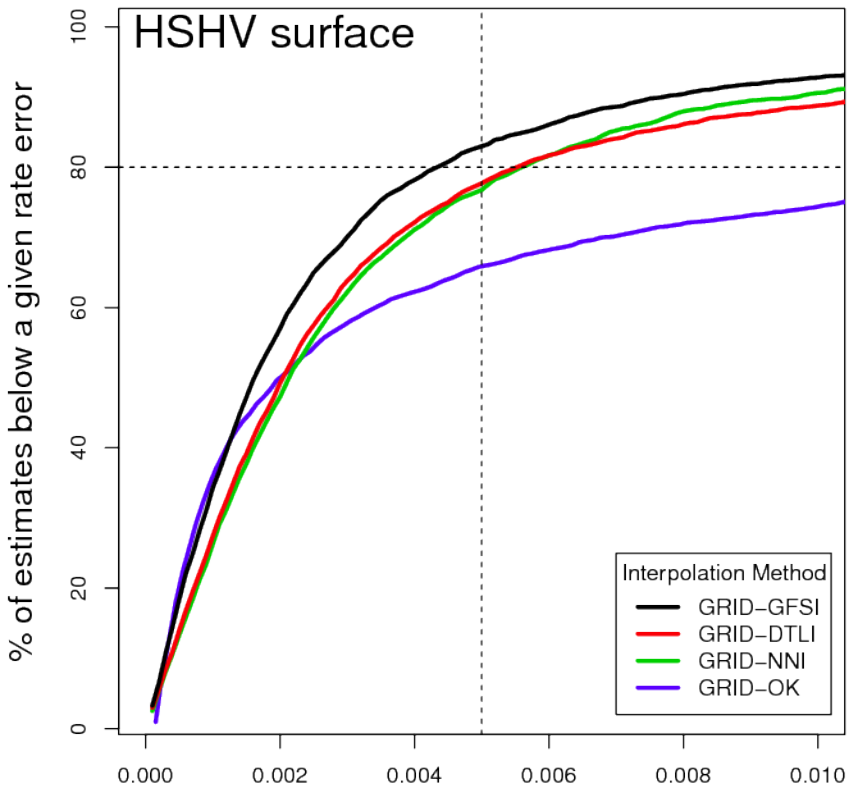

Figure 3.14: Percentage of dH/dt estimates below a given rate error when comparing gridded campaign crossover dH/dt estimates to dH/dt simulations using the LSHV, MSHV and HSHV surfaces. Four interpolation methods are applied to each surface, Green's function spline interpolation (GFSI), Delaunay triangulation with linear interpolation (DTLI), Nearest-neighbour interpolation (NNI) and Ordinary Kriging (OK).

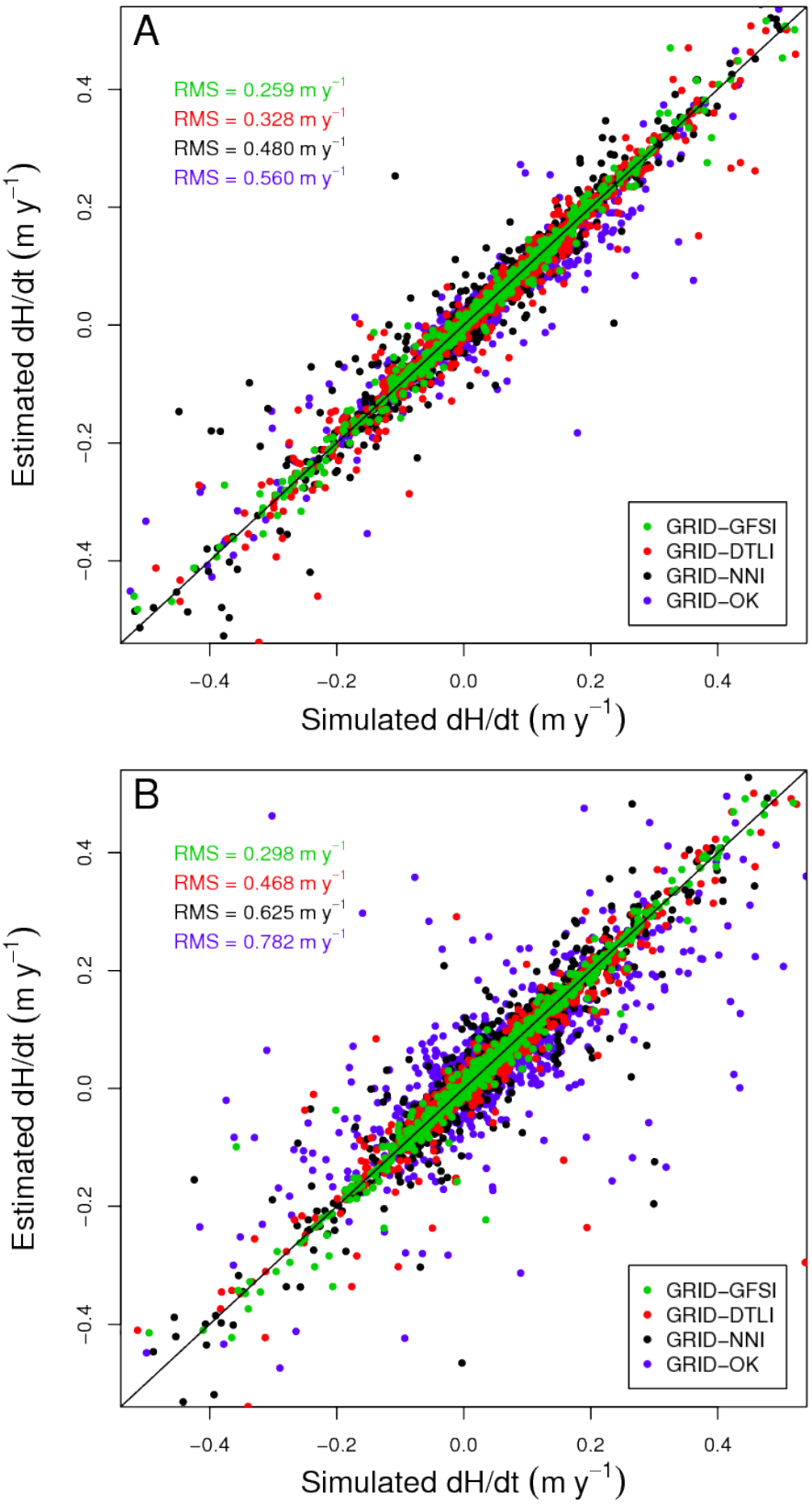
A
RMS = 0.259 m y^{-1}
RMS = 0.328 m y^{-1}
RMS = 0.480 m y^{-1}
RMS = 0.560 m y^{-1}
GRID–GFSI
GRID–DTLI
GRID–NNI
GRID–OK
Estimated dH/dt (m y^{-1})
Simulated dH/dt (m y^{-1})
−0.4
−0.2
0.0
0.2
0.4
B
RMS = 0.298 m y^{-1}
RMS = 0.468 m y^{-1}
RMS = 0.625 m y^{-1}
RMS = 0.782 m y^{-1}
GRID–GFSI
GRID–DTLI
GRID–NNI
GRID–OK
Estimated dH/dt (m y^{-1})
Simulated dH/dt (m y^{-1})

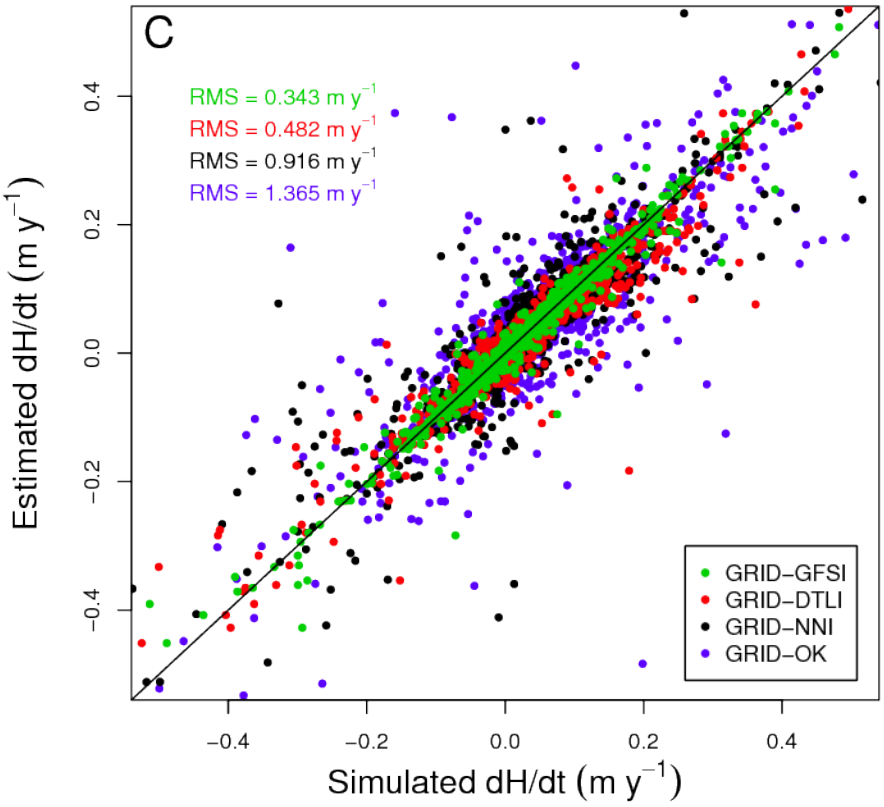

Figure 3.15: Comparison of estimated dH/dt rates, using the gridded crossover method, with regards to simulated dH/dt. A) dH/dt estimates with regards to the LSHV surface dH/dt. B) dH/dt estimates with regards to the MSHV surface dH/dt. C) dH/dt estimates with regards to the HSHV surface dH/dt. All four interpolation types where used (GRID-DTLI, -GFSI, -NNI and -OK). GRID-GFSI had the lowest RMS of all of the interpolation methods, regardless of SHV surface.

is unable to accurately estimate heights at the level of tens to hundreds of metres.

As another measure of uncertainty I looked at the linear relationship between simulated and estimated uncertainties. I calculated the RMS for interpolation methods and simulated surfaces as seen in Figure 3.15. The RMS results mirror the errors obtained when differencing the simulated dH/dt with the estimated dH/dt as shown above. GRID-GFSI had the lowest RMS values for all surfaces, followed by, in increasing order of RMS, GRID-DTLI, GRID-NNI and GRID-OK. Moholdt et al. (2010) also calculated a RMS for their crossover method, obtaining a mean uncertainty of 0.20 m y^{-1}which is similar to the RMS of 0.258 m y^{-1} obtained when I compare the GRID-GFSI method dH/dt estimates to the dH/dt's of the MSHV surface (Figure 3.15b). When comparing these results, it should be noted that Moholdt et al. (2010) obtained their RMS estimate by comparing their ICESat height estimates with glacier DEM's that had previously been obtained, as opposed to my comparison with simulated data. Furthermore, they used only used 329 crossover locations over the Svalbard archipelago, which is mountainous, while I used 3880 crossovers (an order of magnitude greater) of which a large proportion are located in the interior of East Antarctica, which is mostly flat. It is therefore questionable whether a true comparison can be made, nonetheless it is reassuring that both my and their RMS results are similar and follow a basically linear relationship.

The distribution of errors across the study site were not equal and Figure 3.16c shows that errors from the GRID-GFSI were generally low in the interior, but increased near the coastline and in the vicinity of rock outcrops and mountains. The estimated uncertainties generally follow the same trend as the errors, however, they did over-estimate the error, especially close to the coastline and rocky terrain (Figure 3.16d). Nonetheless, the similarity between the error and the uncertainty suggests that, when the gridded crossover method is applied to simulated height data, the estimated uncertainties represent well the actual level of interpolation error.

3.4.1.2 Results: campaign crossover analysis

The campaign crossover method at first glance appears to perform as well as my gridded approach in replicating the dH/dts of the simulated data (Figure 3.17a).

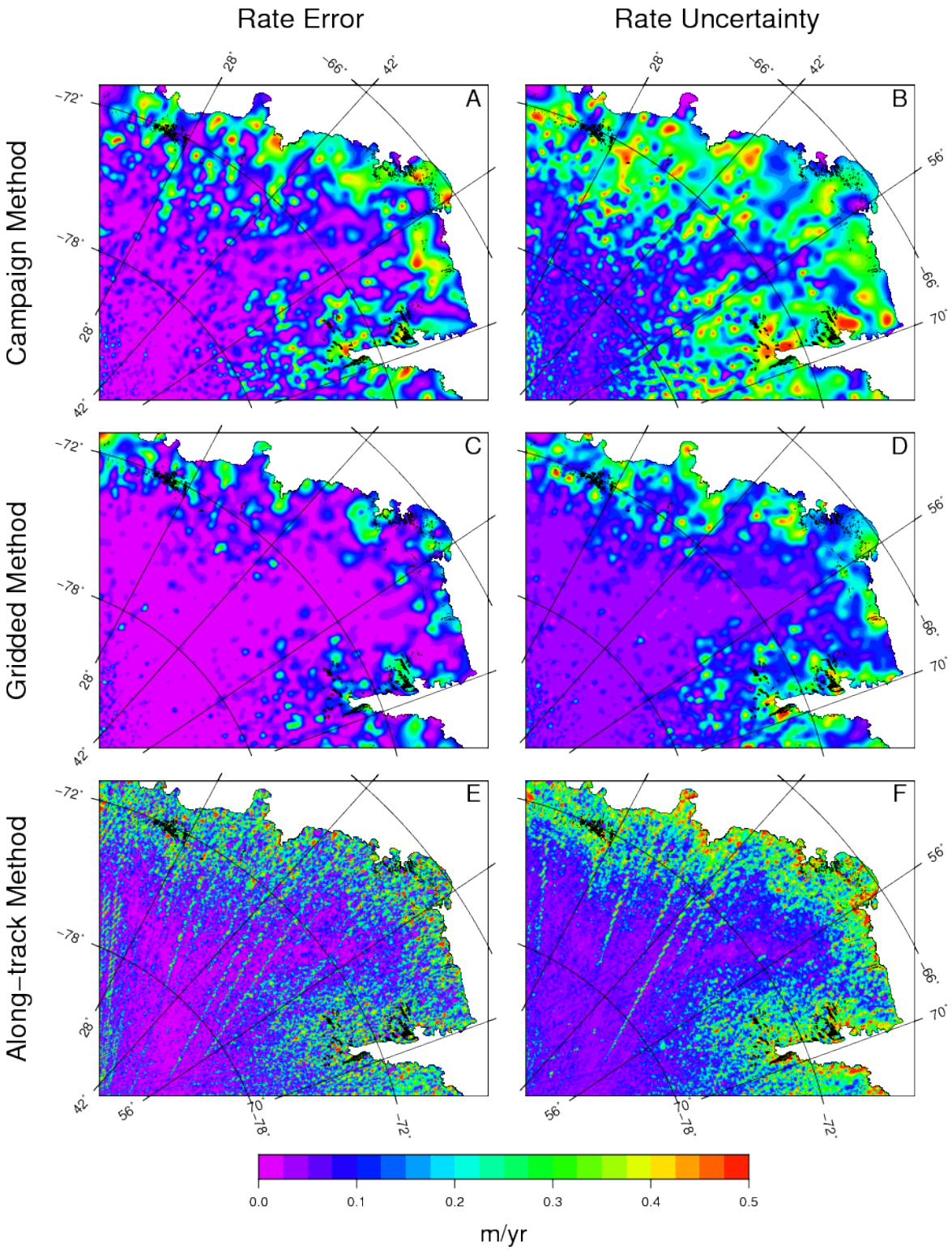

Figure 3.16: The distribution of interpolation errors and uncertainties for the standard campaign crossover method (A, B), gridded crossover method (C, D) and gridded along-track method (E, F). Green's function spline interpolation used.

Green's function spline interpolation (CC_CC-GFSI) was more accurate than linear interpolation (CC_CC-LI) when applied to the LSHV and MSHV surfaces. Using CC_CC-GFSI on the MSHV surface resulted in 95.2% of crossovers having a rate error (the error in estimating dH/dt) less than 5mm/yr, while 85.7% of crossovers had a rate error of less than 5mm/yr when using CC_CC-LI on the same surface. Both methods performed equally when applied to the high variability surface, with CC_CC-GFSI and CC_CC-LI approaches having 47.1% and 46.2% of rates with errors less than 5mm/yr, respectively.

There is, however, one concern which puts these results into a different light. As mentioned earlier, the campaign crossover positions are not fixed. Therefore, even though the estimate of dH is very accurate at the campaign crossovers, the overall estimate of dH takes place at a different location each time. To assess the effect that changing location has on dH/dt, I compared these results to the simulated dH/dt for the crossover region. The rate error between the dH/dts estimated using the campaign method and the simulated dH/dts was large (Figure 3.17b). The CC_GRID-GFSI approach only has 60.7% of crossovers with a rate error less than 5mm/yr, when using the MSHV surface. This example shows that dH/dt can and does vary spatially across crossover regions (the area that includes all the campaign crossovers) and, consequently, this has a considerable effect on estimating rates of change of height. This comparison highlights the weakness of the campaign crossovers method's assumption that height change signals do not vary greatly in the crossover region.

The campaign method errors, as presented in Figure 3.17a, are much larger than those of the gridded crossover method. The errors still follow the basic pattern of the gridded crossover method, with lower errors in the interior and greater errors close to the coast and rocky terrain. However, larger errors are far more prevalent, extending further inland than with the gridded crossover method. The uncertainties generally over-estimate the errors and there are some large inconsistencies between the two statistics (Figure 3.16b). The most obvious difference is found along the northern coast of Enderby Land, where the errors are at times larger than the uncertainties

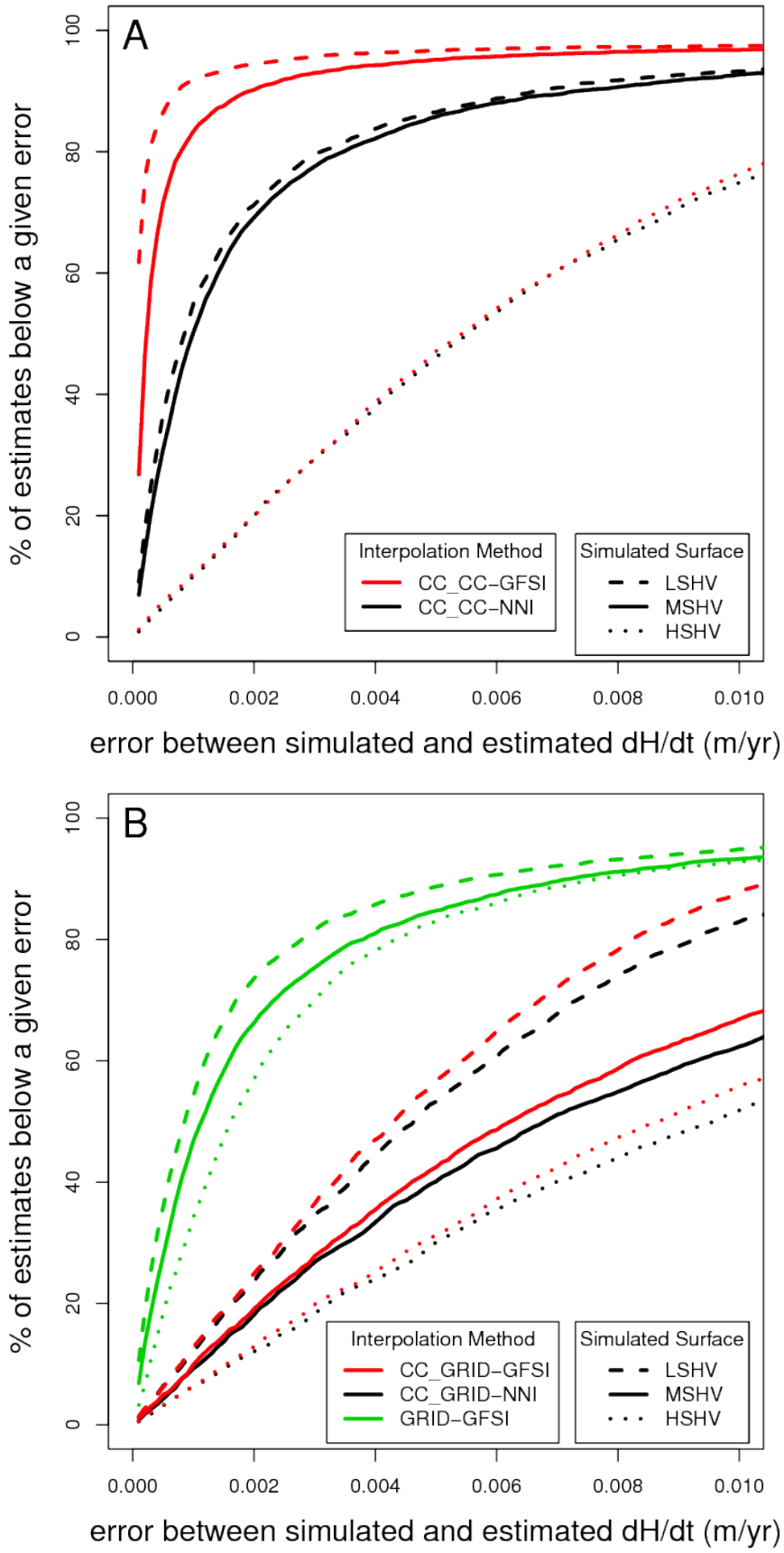

Figure 3.17: Percentage of estimates below a given rate error when comparing a) standard campaign crossover dH/dt estimates with standard campaign crossover dH/dt simulations b) standard campaign crossover dH/dt estimates with gridded crossover dH/dt simulations.

(Figure 3.16a).

3.4.2 Assessing accuracy of surface slope estimates at gridded crossovers and along-track

To obtain the most accurate estimates of surface slope I used DEMs derived from the GRID-GFSI method as it was found to perform the best as seen in Section 3.2.2. The differences between the estimated surface slopes at crossovers, calculated for simulated surfaces and estimates from the GRID-GFSI method, were generally small with ∼82.7% of surface slope differences well below 0.01° and the mean surface slope difference being 0.012° (Figure 3.18a). This amounts to only a ∼1.7 cm height error over 100 m, which gives confidence that the surface slope and aspect could be accurately estimated, in most cases, directly from the observations at crossovers. The slope differences were generally smaller in the interior (∼93.4% $< 0.005°$, mean: 0.0024°), where surface slopes were lower and greater around the margins (∼75.3% $< 0.01°$, mean: 0.026°), where slopes were larger (Figure 3.18b).

Figure 3.19a shows an example where the difference in surface slope between the interpolated data and simulated data is very small. In the case of high spatial height variability, there is also large variability in the surface slope and aspect, leading to larger surface slope differences across the crossover, and the mean surface slope does not represent the variations in surface slope occurring at the crossover (Figure 3.19b). The height errors in these cases, as a result of surface slope over 100 m, were ∼1.2 mm (Figure 3.19a) and ∼143.4 mm (Figure 3.19b), respectively.

I also calculated the RMS between simulated and estimated slopes for both the GRID-GFSI and AT-GFSI methods (Figure 3.20). The linear relationship between the simulated and estimated slopes is clear, with an RMS of 0.542° and 0.948° when using the GRID-GFSI and AT-GFSI methods, respectively. These RMS result are similar to those of Moholdt et al. (2010), who obtained a 0.58° and 1.24° for their crossover and along-track methods, respectively.

Height errors as a result of crossover surface slope were found to be small over most of the study region when using the GRID-GFSI method (Figure 3.21a). Errors were smaller in the interior and larger along the coast and on rocky terrain. The

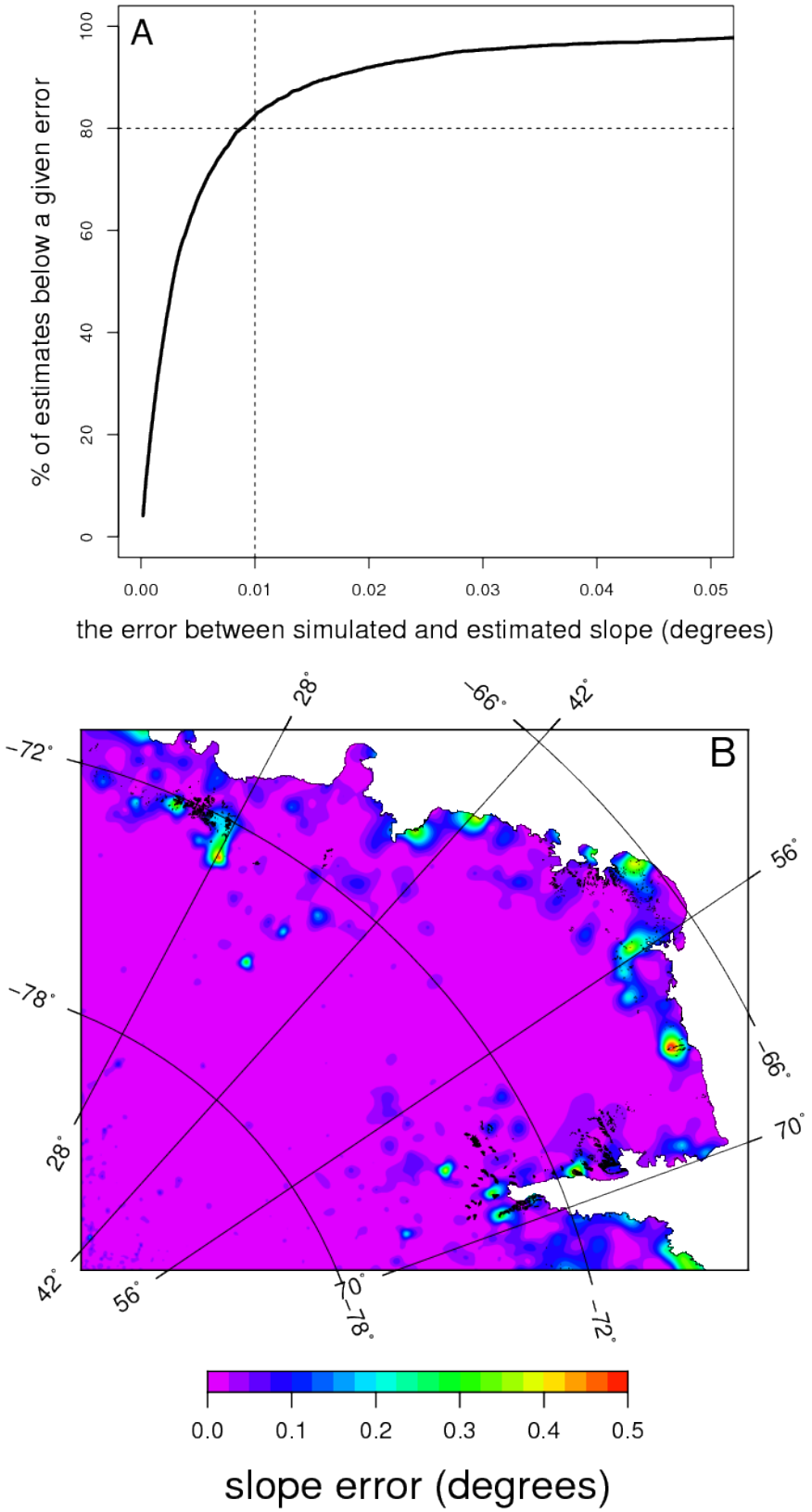

Figure 3.18: a) Surface slope difference (error) between estimated and simulated surface slope. b) Spatial distribution of the surface slope error.

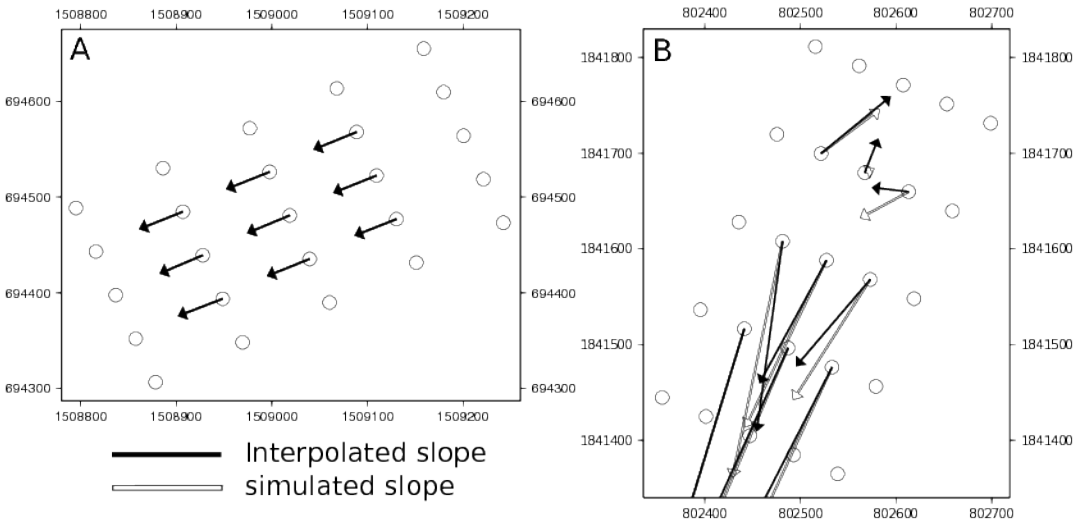

Figure 3.19: a) a crossover where difference between the estimated and simulated surface slope is small b) a crossover where difference between the estimated and simulated surface slope is large.

associated uncertainties were in general agreement with the errors, however, the uncertainties tended to overestimate the errors (Figure 3.21b).

To determine how well I can derive cross-track surface slope for along-track segments, I calculated the cross-track surface slope at each along-track observation point using the combined surface slope correction method described in Sections 3.2.3 and 3.2.4. I then calculated the error (the difference between my combined method and simulated cross-track surface slopes) in cross-track surface slope at each along-track grid node, and the height error introduced by the surface slope error over a distance of 100 m (Figure 3.22a). This distance is the approximate average distance between the centre of all the repeat-tracks and the outermost repeat-tracks. It is therefore a measure of the likely maximum height error due to cross-track surface slope, as many repeat-tracks were much closer than 100 m to the centre of the along-track segment.

As the height errors introduced by changes in surface slope are unknown when using actual ICESat data, a robust estimate of the error is required. I found that the height uncertainties derived from my cross-track surface slope uncertainties were the same magnitude as the height errors, and therefore a good approximation of the "true" height errors derived from my cross-track surface slope errors (Figure 3.22a). There is, however, some spatial divergence between the error and the uncertainty

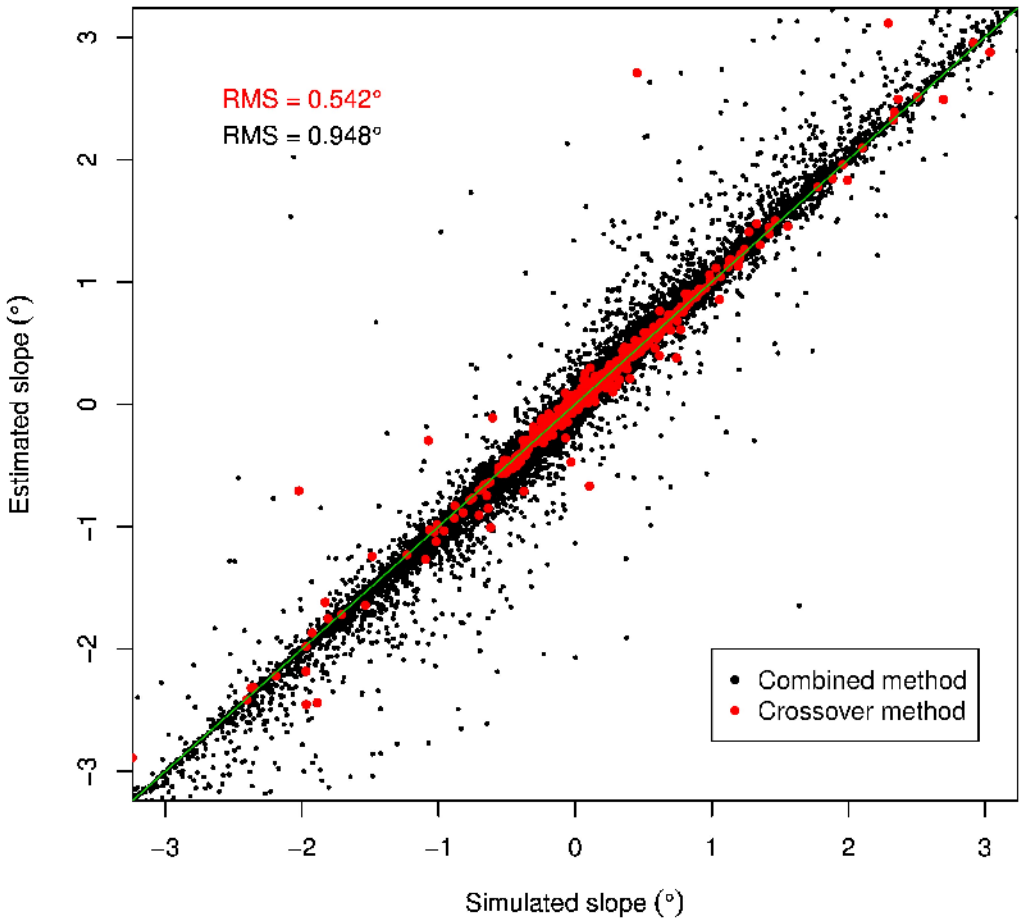

Figure 3.20: Comparison of estimated slope with regards to simulated slope. Slopes where calculated using both the GRID-GFSI (red dots) and AT-GFSI (black dots) methods. The GRID-GFSI RMS of 0.542° is smaller than the AT-GFSI RMS of 0.948°.

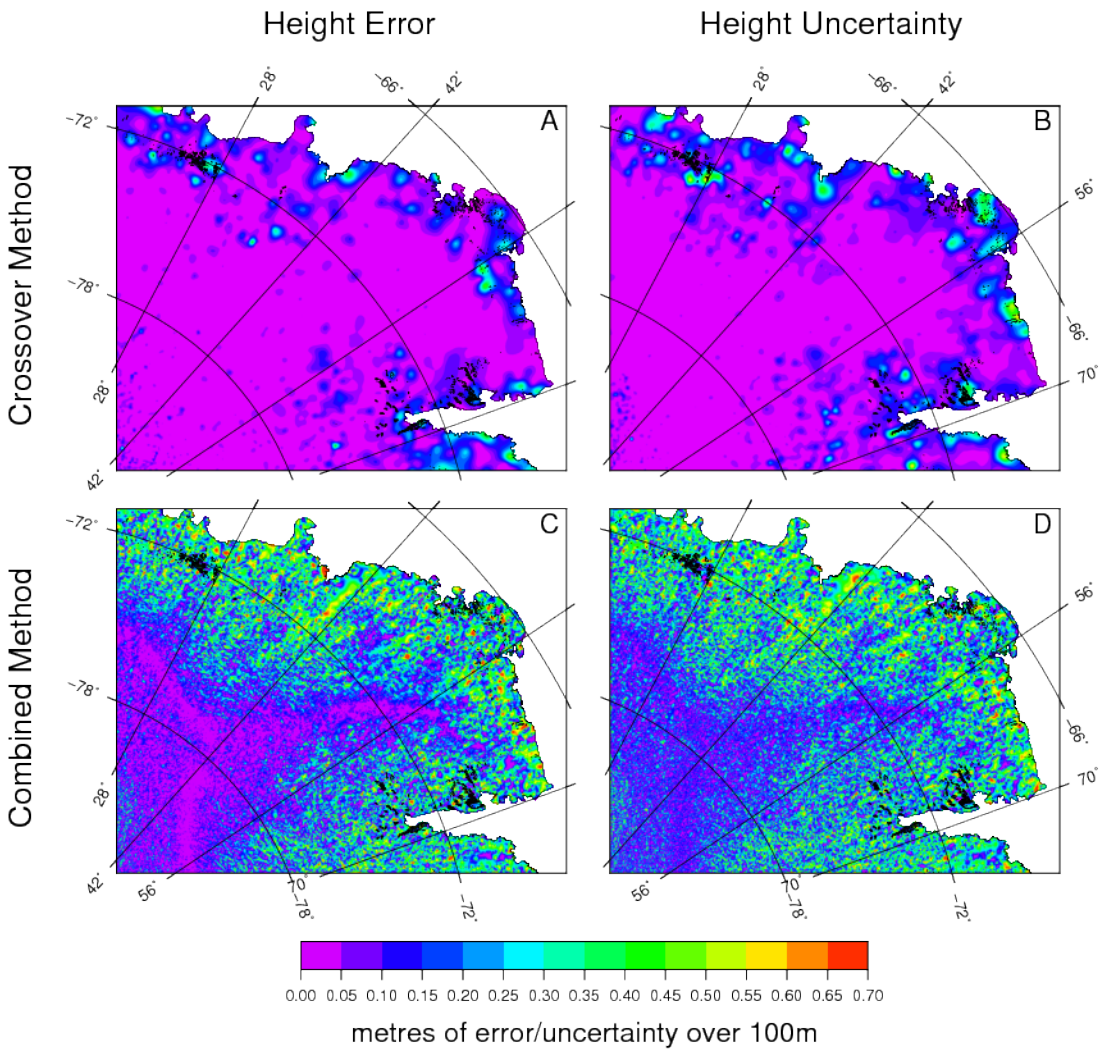

Figure 3.21: The distribution of height errors and uncertainties due to slope variability. All height errors and uncertainties are calculated 100 m away from the centre of the crossover or along-track segment.

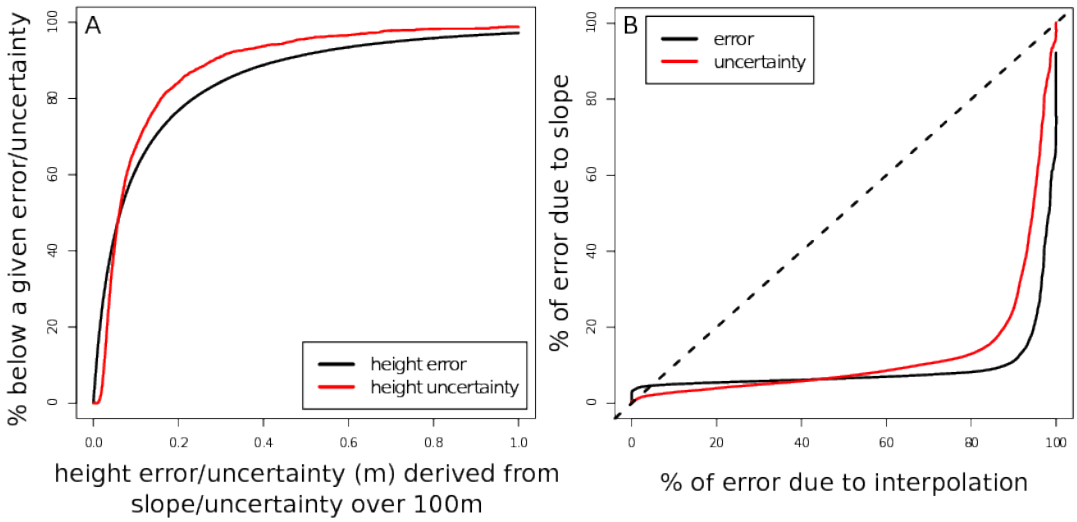

Figure 3.22: a) Percentage of along-track segments below a given height error derived from the surface slope error over 100 m. b) Ratio of height error/ uncertainty due surface slope and interpolation.

across the study site (Figures 3.21c and 3.21d). This difference can be attributed to the interpolation of surface slope between two crossover points, where the uncertainty is a function of the distance between these points. Consequently, when the interpolated crossover surface slope estimates are used, the uncertainty increases along-track as the estimations move further away from the crossovers, with a maximum at the midpoint of the two crossovers (Figure 3.21d). The error does not adhere directly to this spatial relationship, although surface slope errors are generally smaller closer to crossover locations, where there are more height measurements present.

I propagated the height errors due to cross-track surface slope and interpolation into the dH/dt estimates and found that the dH/dt errors introduced due to cross-track surface slope error were an order of magnitude larger than those introduced by interpolation. Figure 3.22b presents this relationship as a ratio of the percentage of errors, binned into 5 mm/yr increments. This is reflected in the ∼10.1 cm mean dH/dt error due to surface slope, which is far greater than the ∼9.3 mm mean dH/dt error due to interpolation. This confirms that height errors due to cross-track surface slope can introduce a considerable amount of error into the final estimate of dH/dt for each along-track segment. Figure 3.23 shows the distribution of slope error and uncertainty. The uncertainty generally overestimates the true error and uncertainties are generally higher near the coast. This is not surprising, as my combined slope method has be tuned to increase uncertainty exponentially as we move further away from crossovers. Near the coast, crossover density is low thus increasing the distance between the crossovers, which in turn increases the uncertainty. It is clear that slope correction uncertainty is considerable and needs to be fully propagated into the final uncertainty estimates in satellite altimetry studies.

3.4.3 Assessing accuracy of the gridded along-track method.

To test the accuracy of my along-track Green's function spline interpolation method (AT-GFSI), I calculated the dH/dt using the simulated surface for each segment. The difference between the estimated and simulated dH/dt quantifies the estimate of rate error for each along-track segment. All the height estimates

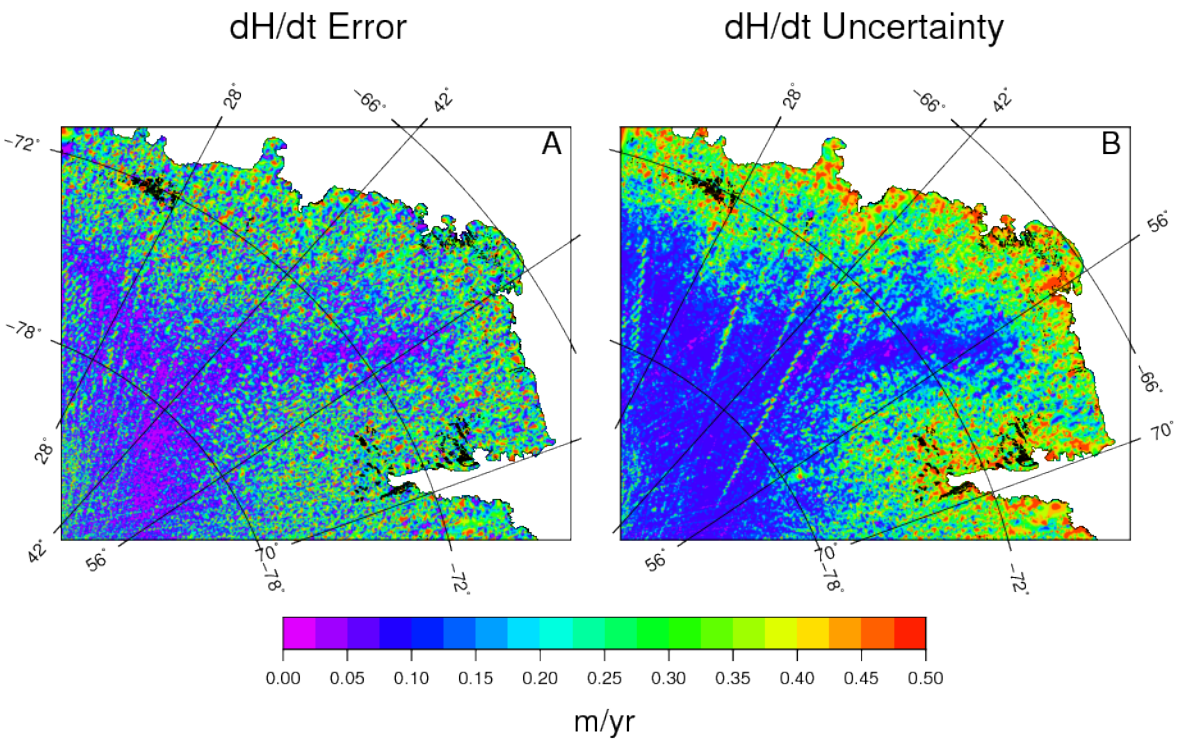

Figure 3.23: The distribution of dH/dt a) errors and b) uncertainties due to surface slope variability.

were corrected for surface slope, using my approach described in Section 3.2.4. As expected, the results of the AT-GFSI method were less accurate than the gridded crossover estimates and I found that only 57% of along-track segments had a rate error of less than 5 mm/yr, whereas 84.8% of gridded crossovers had a rate error of less than 5 mm/yr (Figure 3.24a).

This difference in accuracy is not surprising as the crossovers have two repeat-tracks intersecting each other, which improves the interpolation accuracy. Furthermore the need for crossover surface slope correction adds another level of complexity to the along-track analysis, which is not the case for crossovers. I confirmed this by comparing the rate errors derived in crossover regions using both intersecting repeat-tracks and then using single repeat-tracks. The difference is considerable: when only one repeat-track was used to estimate the dH/dt, ~62% of rate errors were less than 5 mm/yr, compared to 84.8% when both repeat-tracks were used (Figure 3.24b). Clearly, having two intersecting repeat-tracks improves the accuracy of the dH/dt estimates in crossover regions.

The RMS estimates for the along-track method, were 1.424 m $y^{-1}$and 6.732 m y^{-1}, for the AT-GFSI and AT-NNI methods, respectively (Figure 3.25). The AT-GFSI

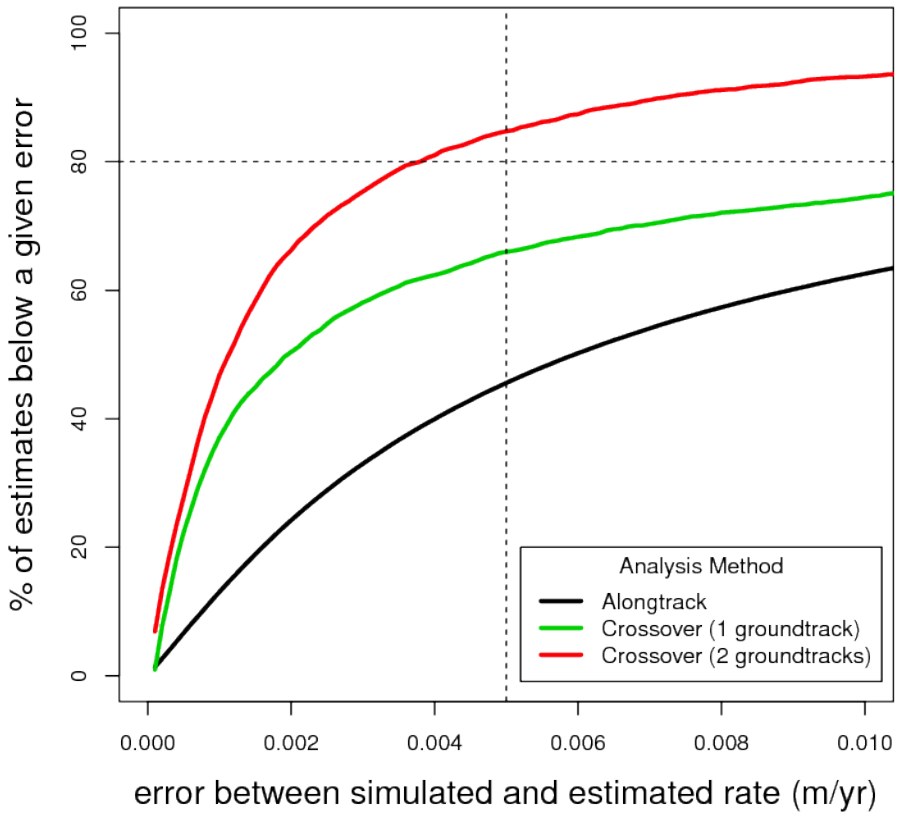

Figure 3.24: Percentage of estimates below a given rate error when comparing a) along-track and gridded crossover dH/dts with dH/dt simulations b) gridded crossover dH/dts estimated from one and two repeat-tracks.

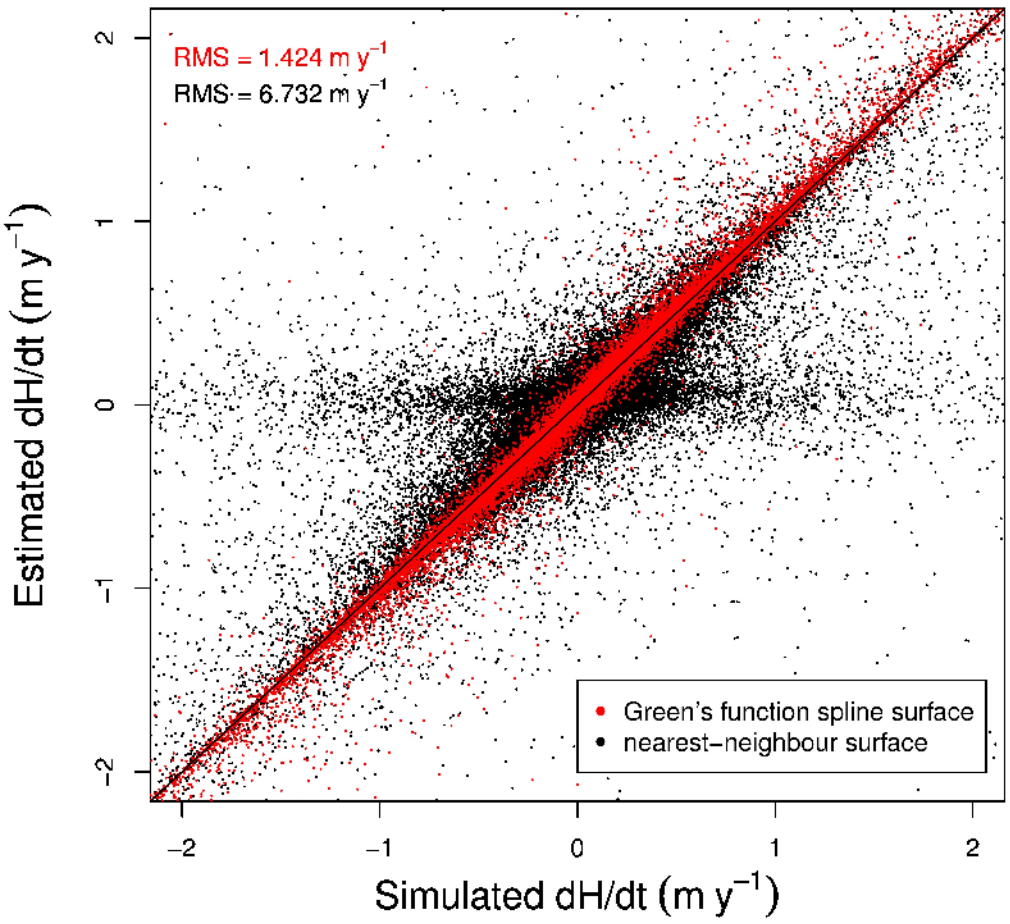

Figure 3.25: Comparison of estimated dH/dt rates with regards to simulated dH/dt. Rates where calculated using both the AT-GFSI (red dots) and AT-NNI (black dots) methods. The AT-GFSI RMS of 1.424 m y^{-1} is smaller than the AT-NNI RMS of 6.732 m y^{-1}, showing the latter method to being more accurate.

results were strongly linear however there appears to by a systematic error present in the estimated dH/dt results for the AT-NNI method, which presents itself as a horizontal line passing through the zero on the y-axis of (Figure 3.25). Again the results are similar to Moholdt et al. (2010), who obtained a RMS of 1.24 m y^{-1}, however I used ∼400,000 comparisons for my analysis, while Moholdt et al. (2010) used ∼9000 points for their comparison.

The distribution of errors of the AT-GFSI method across the study site again follows the same trend, where errors are generally smaller in the interior and greater around the margins and rocky terrain (Figure 3.16e). There are some large errors present along some of the ground-tracks in the interior: the cross-track location of the repeat-track in this region were found to be further apart than in other regions. This decreases the accuracy of the interpolation (fewer data points over a greater

distance) and introduces a greater surface slope bias. The uncertainties follow a similar spatial pattern to the errors, although they again tend to overestimate the magnitude of the error (Figure 3.16f).

3.4.4 Gridded crossover versus along-track dH/dt uncertainties

Now that I had a relatively good estimator of the height error due to cross-track surface slope, I propagated the cross-track surface slope uncertainty into the final AT-GFSI dH/dt uncertainty. These uncertainties also included the previously calculated interpolation and regression uncertainties. The final weighted dH/dt uncertainty was $\sim\pm8.3$ cm/yr for the whole study site. Around the coastal margins of the site the weighted dH/dt uncertainty was much higher ($\sim\pm34.7$ cm/yr), while in the interior it was much lower ($\sim\pm2.1$ cm/yr). Approximately 90% of uncertainties were well below 10 cm/yr.

Using just the GRID-GFSI method, the final weighted dH/dt uncertainty was $\sim\pm1.7$ cm/yr for the whole study site. Again dH/dt uncertainties were greater around the margins ($\sim\pm12.5$ cm/yr) and smaller in the interior ($\sim\pm0.7$ cm/yr). The GRID-GFSI uncertainties followed the same pattern as the AT-GFSI uncertainties, however, $\sim$90% of uncertainties were well below 3 cm/yr. This results show that the gridded crossover method is more accurate than the gridded along-track method. This is not surprising as crossovers have twice the height measurements and no need for across-track slope correction. Furthermore, due to the orbit of ICESat, more crossovers occur in the centre of the Antarctic continent than along its margins. Consequently, we would expect uncertainties to be lower as less change is occurring in the interior of Antarctica. This highlights the deficiency of the gridded crossover method, in that we are most interested in what is happening along the margins as this is where most of the ice loss is occurring. Therefore, even though the gridded along-track method is not as accurate, it is still very useful and should be used in conjunction with the gridded crossover method.

3.5 Conclusions

I have tested the accuracy of my ICESat data analysis methods, the gridded crossover method and the gridded along-track method, using a simulated ICESat dataset. I found that, regardless of the analysis type and simulated surface used, the Green's function spline was the most accurate interpolation method with the lowest errors and uncertainties (Figures 3.14 and 3.24). I are not aware of this form of interpolation having been used in the estimating of ICESat dH/dt and I present it as an accurate alternative to previously used methods.

I devised a new approach to deriving height estimates at crossover regions, introducing a crossover grid of nodes on which heights are interpolated. My gridded crossover method was found to be more accurate than the standard campaign crossover method often used in previous studies (Zwally et al., 2005; Smith et al., 2005; Brenner et al., 2007; Gunter et al., 2009; Moholdt et al., 2010) (Figures 3.16 and 3.17). The static nature of the grid allowed me to estimate heights at the same location through time, which had not previously been the case. It also allowed me to estimate a DEM directly from the data without having to make any assumptions about the variation of dH/dt in the crossover region. I was able to mitigate the effect of interpolation by down-weighting height estimates that were not well constrained, which in turn minimised their contribution to the final dH/dt estimate (Figure 3.9). This allowed me to estimate slope at crossovers with some confidence.

My novel gridded crossover method is by no means ideal and suffers from the some of the deficiencies of the above methods, however it does allow me to create small DEMs at crossovers, which in turn lent themselves well to estimating surface slope. By using the crossovers as regions to verify the biquadratic along-track estimates of surface slope, I maximised the accuracy of the surface slope estimates, while minimising the inherent surface slope bias present in the ICESat data.

dH/dt estimates at crossovers were generally more accurate than rates estimated from along-track segments, where only one repeat-track is available for the interpolation/surface fitting. Nonetheless the gridded crossover method uses only a small part of the ICESat dataset, whereas the along-track methods uses all of the data,

making it a more complete method in terms of coverage. I believe my gridded crossover method is still a very useful tool as it can be used to help validate the less accurate along-track dH/dt estimates. Moholdt et al. (2010) also used their campaign crossover method for this same purpose.

Previously, the problem of cross-track surface slope has been dealt with by estimating the slope and removing it from the height estimates, using either a low resolution "independent" DEM (Slobbe et al., 2008; Sørensen et al., 2011) or some kind of surface created from close lying along-track ICESat data (Howat et al., 2008; Smith et al., 2009; Moholdt et al., 2010; Sørensen et al., 2011; Ewert et al., 2012). These approaches all suffer from the fact that there are no truly independent DEMs for Antarctica with a resolution required for slope correction. This problem is currently insurmountable and will be dealt with in upcoming missions such as ICESat-2.

The mean uncertainty budget for both the surface slope correction and interpolation correction, when using the AT-GFSI method, is $\sim\pm 8.3$ cm/yr. All other interpolation methods had much greater uncertainties. This highlights that the choice of analysis method, interpolation type and surface slope correction method can have a large effect on the overall accuracy of dH/dt, while also showing that it is important to include a measure of uncertainty that reflects these choices.

Chapter 4

Rates of ice height and mass changes in Enderby, Kemp, MacRobertson & Dronning Maud Lands and the East Antarctic interior.

4.1 Introduction

The Antarctic is currently undergoing great change due to increased global temperatures and this change is likely to increase over the coming century (Rignot et al., 2011b; Shepherd et al., 2012). The magnitude of this change is still uncertain as the data used in estimating Antarctic mass-balance changes has a relatively small temporal range that only spans the last two decades (Stocker et al., 2013). This is further compounded by the large variability of mass balance signals recorded across Antarctica.

The Western Antarctic is losing mass, with the greatest losses and accelerations occurring at Thwaites and Pine Island glacier outlets in the Bellingshausen and Amundsen seas (Pritchard et al., 2009; Rignot et al., 2011b; King et al., 2012; Shepherd et al., 2012; Sasgen et al., 2013). The Antarctic Peninsula has seen large scale mass loss from the collapse of the Larsen A & B ice shelves (Rott et al., 2002) and, even though there is evidence to suggest that precipitation has increased along

the Antarctic Peninsula (Thomas et al., 2008), it is negligible in the light of the losses (Pritchard et al., 2009).

The situation in East Antarctica is not so clear, with the overall signal being of much smaller magnitude than that of Western Antarctica. There is a small overall gain in mass across the whole ice sheet, however there are some regional differences. There is a strong positive signal in Dronning Maud and Enderby Lands, however the mass-balance of these regions is strongly shaped by inter-annual accumulation variability along the coast. Positive anomalies were found over Dronning Maud Land during 2005, 2007 and most strongly in 2009 (Shepherd et al., 2012; Sasgen et al., 2013). These anomalies are more likely due to large-scale changes in the atmospheric circulation than to any changes in the dynamics of ice flow (Sasgen et al., 2013). Although these anomalies have decreased the rate at which East Antarctica loses mass, the overall mass-balance record is too short to assess whether these anomalies are part of a greater trend (Shepherd et al., 2012).

In contrast, the mass-balance signal for George V and Wilkes Land is negative, with Totten, Cook and Oats Land outlet glaciers all showing mass loss and accelerated flow rates (Pritchard et al., 2009; Rignot et al., 2011b; King et al., 2012; Shepherd et al., 2012; Sasgen et al., 2013). Nonetheless, the overall contribution to the total ice loss of East Antarctica from these areas is small in comparison to the larger positive signal associated with East Antarctica.

The regionally significant trends present in East Antarctica, as seen in the above examples, are the result of mass signals occurring along the coastline and in the outlet glaciers. Inland East Antarctica has a smaller signal in comparison to the trends found along the coast, as precipitation generally decreases from the continental margins to the interior (Boening et al., 2012). There is evidence from satellite altimetry to suggest that the rate of ice height change is increasing in the East Antarctic interior (Horwath et al., 2012) and this has been attributed to increased precipitation (Davis et al., 2005). Furthermore some global circulation models (GCMs) predict that this will happen (Monaghan et al., 2006). However these findings are contradicted by ice core data which shows no increase in precipitation in the interior since

the 1950s (Monaghan et al., 2006). Thus, it is still unclear whether the rate of ice height change is increasing in the interior and furthermore whether this is due to increased precipitation.

A more recent study by Boening et al. (2012) analysed both GRACE and CloudSat data and found large mass increases throughout Dronning Maud Land and, to a lesser extent, Enderby Land between the years 2009-2011. These mass increases were attributed to large anomalous precipitation events that occurred in May 2009 and June 2010. These were caused by anomalous atmospheric blocking events that were induced by Rossby wave trains propagating from the tropics to the Southern Ocean (Hirasawa et al., 2000). These increased the poleward flow of moist air along the western side of the blocking high pressure system and led to a significant increase of precipitation from the ocean to the coast of Dronning Maud Land (Boening et al., 2012). This study, as well as the findings of Shepherd et al. (2012) and Sasgen et al. (2013), suggests that there has been a marked increase in ice height/mass throughout the interior of East Antarctica. Nonetheless, as the rate of change signal is very small in the interior, the uncertainties associated with estimates of mass change are generally of the same or greater magnitude than that of the estimate (Nguyen and Herring, 2005). Consequently, it is still unclear as to whether the interior of East Antarctica is gaining or losing mass.

To try and better determine the trend estimates and their associated uncertainties in the interior of East Antarctica, especially Enderby and Dronning Maud Lands, I applied my crossover and along-track method, described in Chapter 3, to analyse actual ICESat data. The ICESat mission's orbit was chosen, in part, to cover much of the East Antarctic interior. It had a latitudinal coverage down to 86°S, making it ideal for this study (Zwally et al., 2002).

4.2 Method

4.2.1 Study Site

The study site I have used encompasses approximately one fifth of East Antarctica (~2,360,065 km^2) and includes all of Enderby and Kemp Land, half of Dronning Maud Land and a section of MacRobertson Land (Figure 4.1). The purpose of the study was to test my new interpolation and surface slope correction methods rather than to obtain a mass balance estimate for the whole of Antarctica. I chose this region specifically because it included parts of the interior, areas of fast flowing ice, as well as steep coastal terrain.

This region has previously been found to have one of the largest positive mass signals in East Antarctica (Boening et al., 2012; Shepherd et al., 2012; Sasgen et al., 2013). To better compare my results to those of previous studies, I have broken up the study site into drainage basin divides, using the drainage basin divide dataset provided by Zwally et al. (2012) (one of the datasets used by the Ice sheet Mass Balance Inter-comparison Exercise (IMBIE)). The Zwally et al. (2012) dataset is in large part interchangeable with the previous drainage basin divide datasets described by Rignot et al. (2008, 2011b).

My study site covers all of the drainage basins 7, 8, 9 and covers ~19% of basin 3, ~83% of basin 6, ~74% of basin 10 and ~2% of basin 11. The study site is further broken down by ice velocity. Data points with an ice velocity of greater than 100 m a^{-1} are separated from those data points with velocities less than 100 m a^{-1} (Figure 4.2), as described by Pritchard et al. (2009). Pritchard et al. (2009) made this distinction to better detect if the rate of ice change is due to ice dynamics ($>$ 100 m a^{-1}) or due to seasonal variations in the firn pack due to accumulation or ablation ($<$ 100 m a^{-1}). They obtained their ice velocities from the Jezek (2002) digital mosaic of ice motion assembled from RADARSAT-1. I obtained ice velocities from the MEaSUREs InSAR-Based Antarctica ice velocity map provided by Rignot et al. (2011a). This dataset uses a digital mosaic of ice motion assembled from multiple satellite interferometric synthetic-aperture radar datasets (RADARSAT-1

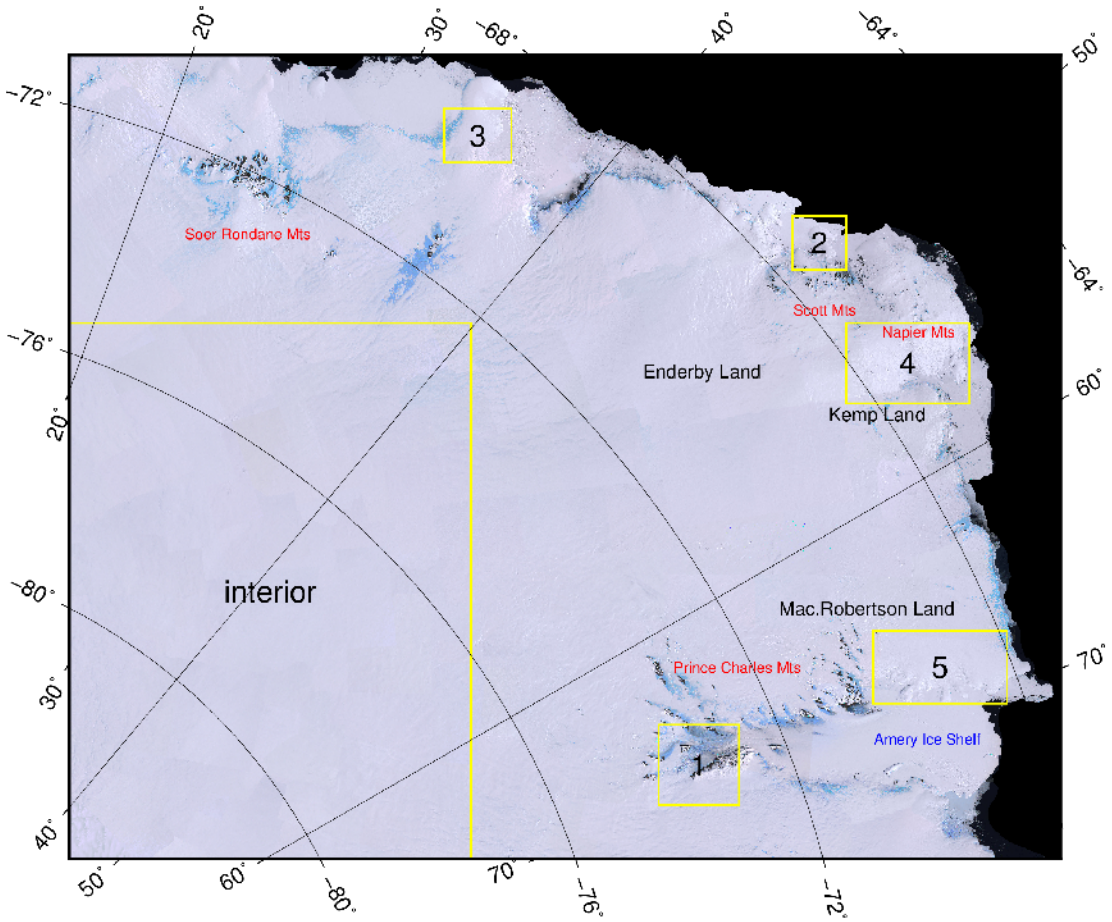

Figure 4.1: The study site: encompassing 1/5 of East Antarctica. The boxes with numbers show the location of the site looked at in detail. Regions (black text), mountain ranges (red text) and ice shelves (blue text)

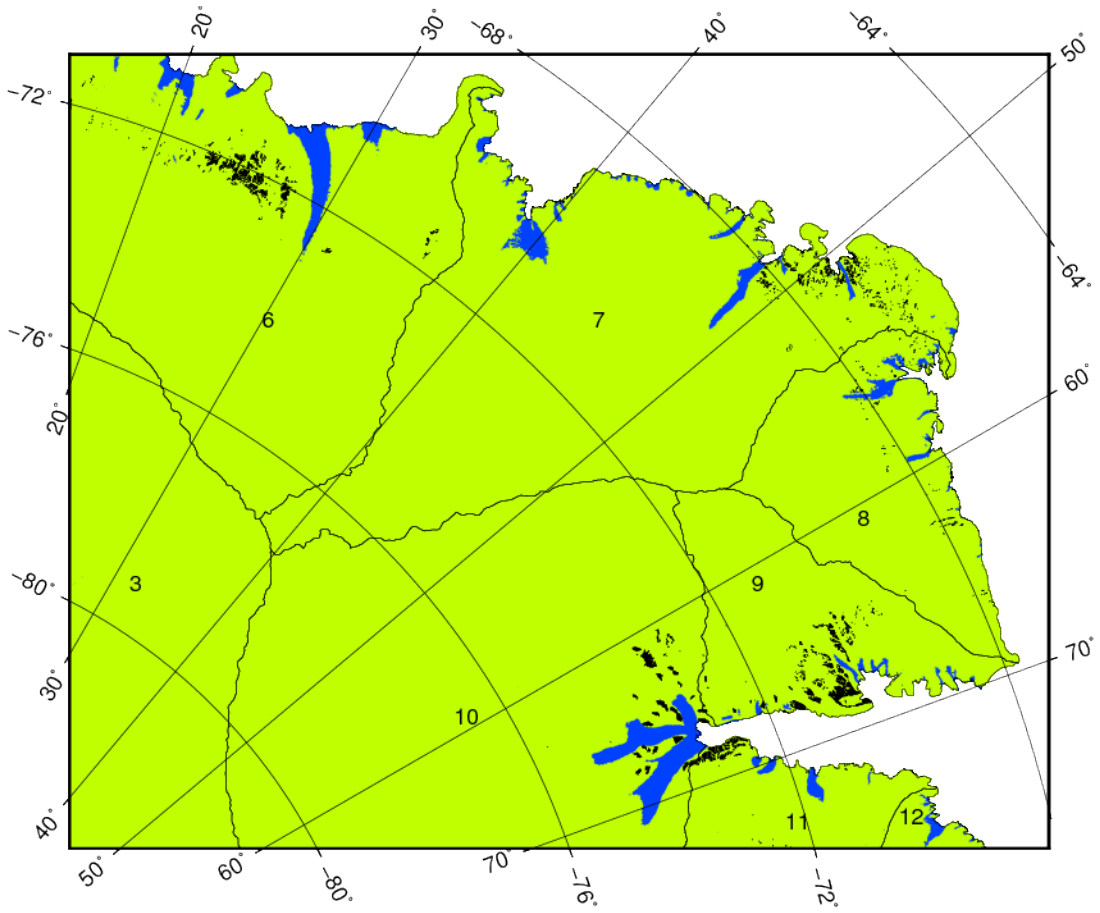

Figure 4.2: Drainage Basins and velocities. Numbers demarcate drainage basin divides after Zwally et al. (2012). Blue indicates areas with an ice velocity of greater than 100 m a^{-1}, while areas in green have an ice velocity less than 100 m a^{-1}. Ice velocities are derived from Rignot et al. (2011b).

& -2, ENVISAT, OSAP, ERS-1 & -2 etc.).

4.2.2 Processing ICESat Data

I used the ICESat GLA12 Release 633 data product, from January 2003 to November 2009, using all available campaigns. This data has been corrected for a variety of errors and biases including general instrument bias, tropospheric delays, precision orbit and altitude determination, saturation range correction etc. I have also applied an out of release correction reported by the ICESat Project Science Team in January 2013, which corrects an error in the range determination from the transmit-pulse reference point selection, known as the centroid vs. Gaussian offset. This reduces the laser campaign bias present in all ICESat data (Urban and Schutz, 2005; Gunter et al., 2009; Borsa et al., 2013). For further information about the correction see Borsa et al. (2013). The correction files were obtained from NSIDC (2013).

The ICESat data product comes with several quality flags (Zwally et al., 2011b), which I utilised to remove points with large errors. I removed all points with a gain (flag: i_gval_rcv) larger than 30 counts (Brenner et al., 2007). This 'pseudo cloud filter' was proposed by Nguyen and Herring (2005) and removes potential data points affected by cloud cover. I also used the range offset quality/use flag (i_rng_UQF) to remove any data points that potentially have issues with attitude quality or with corrections (Slobbe et al., 2008). Lastly, I removed all data points that have more than one peak in the return (flag: i_numPk), found by a Gaussian fitting procedure (Slobbe et al., 2008).

In order to minimise any other erroneous height measurements, I removed any points that are above the 3-sigma threshold relative to the Antarctic 1 km digital height model (DEM) from combined ERS-1 radar and ICESat laser satellite altimetry data created by Bamber et al. (2009). Lastly, using the rock outcrop polygon dataset (Antarctic Digital Database version 6.0), I removed any height measurements within the rock polygons, as we are interested in change in ice height and not rock. These height measurements generally have large errors associated with them due to extreme slopes.

4.2.3 Interpolation of crossover and along-track data

In my simulation study (Chapter 3), I showed the effect that the choice of interpolation has on the accuracy of the final dH/dt estimates. I found that the Green's function spline interpolation (see Wessel, 2009) had the smallest error (the difference between the simulated and estimated dH/dt) and uncertainty (1-sigma) when using both my crossover and along-track methods. Consequently, this is the main interpolation method I will apply when using actual ICESat data. I will also derive dH/dt estimates using nearest-neighbour (see Lu and Wong, 2008) and Delaunay triangulation with linear interpolation (see Shewchuk, 1996) to show the effect that using a less accurate interpolation method can have on the final result. The interpolation methods are described in detail in Chapter 3.

4.2.4 Estimating dH/dt

The method I used to estimate dH/dt is explained in detail in Chapter 3, Sections 3.2.2 and 3.2.4. In summary, I divide the ICESat data into ∼33-day laser campaigns. A 25-node grid is placed over the central point (mission crossover) of the crossover and a height is estimated for each node by interpolating the closest height measurements (the search radius and number of data points varies depending on the interpolation method used).

An uncertainty is calculated for each node using the distances between the node point and the height measurements, and the standard deviation of the data points within the search radius. Consequently, nodes that use fewer and more distant data points have a higher uncertainty on the interpolated heights. This is repeated for each laser campaign and a height change rate is estimated for each node, using weighted least squares. The interpolation uncertainty is used as the weight for the height at each laser campaign. The least squares surface slope uncertainty and the interpolation uncertainty are propagated into a final uncertainty of the height estimate at each node. The crossover dH/dt is calculated by taking the weighted mean of all 25 dH/dt estimates at each crossover.

The same method is used when processing the along-track data, except that the grid has 24 nodes and the grid position is moved along the ground-tracks in 600 m intervals. I used Green's function spline and nearest-neighbour interpolation. Delaunay triangulation with linear interpolation is not used with the gridded along-track method, as there are generally not enough triangles to cover the whole gridded region.

I filtered the dH/dt estimates, using the method described by Pritchard et al. (2009), by calculating the median over a 25 km radius of each point and removing any points ± 0.75 times the inter-quartile range. This limits further error from forward scattering and any residual error from the other sources (Pritchard et al., 2009). The added benefit of this is that it allows me to make direct comparisons between my findings and those of Pritchard et al. (2009). I rejected ∼18% of the dH/dt estimates using this method. Pritchard et al. (2009) have a second step in

their filtering process where they break Antarctica into 10 km sections and calculate the spatial mean of the previously filtered points (this typically averages several thousand points). I chose not to do this to the dH/dt results as I am interested in the changes at a local level (high resolution). I do use this method when estimating dV/dt and dM/dt which I discuss later.

4.2.5 Surface slope correction

In Chapters 2 and 3, I discussed in detail the need to correct estimates of along-track dH/dt for surface slope. Not doing so can lead to the estimated dH/dt being a measure of the change in sampling of the surface topography over time rather than a change in ice height. In Section 3.2.4 I presented a novel approach to estimating surface slope at crossovers and I used this method when analysing the real ICESat data.

In summary, I estimated the surface slope at the crossovers and then linearly interpolated them between two neighbouring crossovers to derive cross-track slopes for the along-track observations. I then also estimated the surface slope along-track using the method described in Section section 3.2.4. If the surface slope estimates are in agreement (1-sigma), I used the along-track estimate. In such cases, I am confident that my along-track estimate of surface slope is not removing any actual change in height. This scenario generally occurs when surface slopes are small, for instance in the Antarctic interior. However if the two estimates did not agree, I used the surface slope estimates at the crossovers. This often occurs in areas of larger magnitude surface slope, for instance around the coast. This increases the surface slope correction resolution, which is low when using only crossovers, while maintaining a higher accuracy than just using the along-track data.

4.2.6 Estimating dV/dt and dM/dt

As there are few studies that estimate dH/dt at a basin level, across Antarctica (e.g. Zwally et al., 2005; Pritchard et al., 2009), I felt it was important to calculate mass rate estimates (dM/dt) to establish how my results compare to other studies

who only published dM/dt basin results (e.g. King et al., 2012; Sasgen et al., 2013). Furthermore, estimates of mass balance change are extremely important as they help in our understanding of the current and future contributions of the ice sheets to sea level rise.

In order to convert the dH/dt estimates into dM/dt, I first removed a firn column signal to obtain the dH/dt that is solely due to the underlying ice column. I used the Ligtenberg et al. (2011) firn densification model (FDM), which describes all the processes that take place inside the firn column (compaction, refreezing, firn to ice transition) and at its surface (snowfall, sublimation, snow-melt) to calculate the surface height change due to these processes (Ligtenberg pers. comm., 2013). I calculated monthly mean surface heights from the FDM and obtained a firn column rate for the ICESat operational period, which I removed from the ICESat dH/dt. In this the seasonal firn column signal is removed and the dH/dt due to the underlying ice column is obtained. Consequently, if there is no change in the ice column beneath the firn column, the dH/dt from the FDM should match the ICESat dH/dt (Ligtenberg et al., 2011). It is worth noting that I compared the results of Pritchard et al. (2009) to my uncorrected dH/dt results, as they do not correct their dH/dt for firn densification.

I converted the corrected dH/dt estimates to a rate of change of volume (dV/dt) by breaking the study site into 10 km^2 sections and calculating the spatial mean of all the dH/dt estimates within each section. The change in volume is determined for each section by multiplying the area by the mean dH/dt. Lastly, I converted the estimates of dV/dt to dM/dt by multiplying the volume by the density of solid glacier ice (917 kg m^3), as this is an estimate of the solid ice column (Ligtenberg et al., 2011). This then yields a dM/dt estimate of the ice column for each 10 km^2 section.

In order to estimate dM/dt due to the mass change in the firn column, I use Lenaerts et al. (2012) surface mass balance model (SMB). The SMB model from Lenaerts et al. (2012) is complementary to the Ligtenberg et al. (2011) FDM, as the former is used as a forcing for the latter model (Ligtenberg pers. comm., 2013).

The SMBM model is derived in part from the regional atmospheric climate model RACMO2.1/ANT and it is assumed that the firn column is in equilibrium over the 32-year (1979-2010) period covered by RACMO2.1/ANT (Ligtenberg et al., 2011; Lenaerts et al., 2012). So, with this assumption in mind, mass is added to the firn column (a positive dM/dt) if the firn column accumulation is greater than average, and visa versa.

I obtained the surface mass balance (mm water equivalent (w.e.)) for each month and converted them to a mass rate (Gt a^{-1}) by multiplying the surface mass balance by the grid box area dataset provided by Ligtenberg, again breaking this into 10 km^2 sections (Ligtenberg pers. comm., 2013). I then calculated the SMB anomaly over the ICESat operational time period, yielding the dM/dt of the firn column for the same time period for each section. Lastly I added the mass change from the ice and firn columns to obtain a final dM/dt estimate for each section. I then repeated this for each of the basin divides described above.

As a side note, the conversion from dV/dt to dM/dt is an extremely complex step and it is not one of the primary goals of my thesis. The dM/dt results I obtained from the method described above are by no means comprehensive and should be viewed as such. Nonetheless, this conversion allows comparisons to other dM/dt studies (e.g. King et al., 2012; Sasgen et al., 2013). Furthermore, I do not correct my results for glacial isostatic adjustment (GIA), which is not well constrained for the Antarctic continent. Again, Pritchard et al. (2009) also do not correct for GIA, which allows for direct comparison.

4.3 Results

4.3.1 General overview of dH/dt results

In general, for my study site, the mean dH/dt signal increases over late 2003 to late 2009. Combining the along-track and crossover results, I obtained a mean dH/dt of 0.04 $\pm$ 0.036 m a^{-1} using Green's function spline interpolation (COMB-GFSI) and 0.037 $\pm$ 0.038 m a^{-1} using nearest neighbour interpolation (COMB-NNI). Using

just the crossover data, I calculated a mean dH/dt of 0.045 ± 0.016 ma^{-1} using GRID-GFSI, 0.043 ± 0.021 m a^{-1} using GRID-DTLI and, lastly, 0.045 ± 0.029 m a^{-1} using GRID-NNI.

That the crossover results are larger than the combined results is not surprising as the crossover data has a lot less coverage around the coast. Consequently a mean rate calculated using only the crossover data will be biased towards the positive interior rates where crossovers are more numerous. Conversely, the along-track data has a greater coverage near the coast, which is where the majority of negative rates are located, and therefore the mean rate will reflect this. This, in part, also explains why crossover uncertainties are lower than the combined uncertainties, as there is more variation near the coast which is not captured in the crossover data. These general findings show that using the GRID-GFSI and COMB-GFSI results yield the smallest uncertainties when applied to crossover and along-track data, respectively. This mirrors the findings of my simulation study and shows that the GFSI is the most accurate interpolation method that I have tested.

4.3.2 dH/dt estimates and associated uncertainties for the whole study site

Although the overall dH/dt rate for my study site is positive, there is variation across the region, regardless of the interpolation method used (Figures 4.3a - 4.7a). All of the high rate signals are found near the coast, however these are localised and consequently have less influence on the larger drainage basin signals. Table 4.1 shows the the mean dH/dt results and uncertainties of each drainage basin in the region. Rates are calculated for the whole drainage basin (all velocities), as well as for only points with ice velocities less than or greater than 100 m a^{-1}.

Uncertainties are estimated along with the rates. They follow a similar pattern to their associated rates, with sigma values being larger along the coast and near steep terrain, while decreasing on flat terrain mainly in the interior (Figures 4.3b - 4.7b). Uncertainties were lowest for COMB-GFSI followed by COMB-NNI methods, (Figures 4.3b & 4.4b). Uncertainties obtained using the GRID-GFSI method were

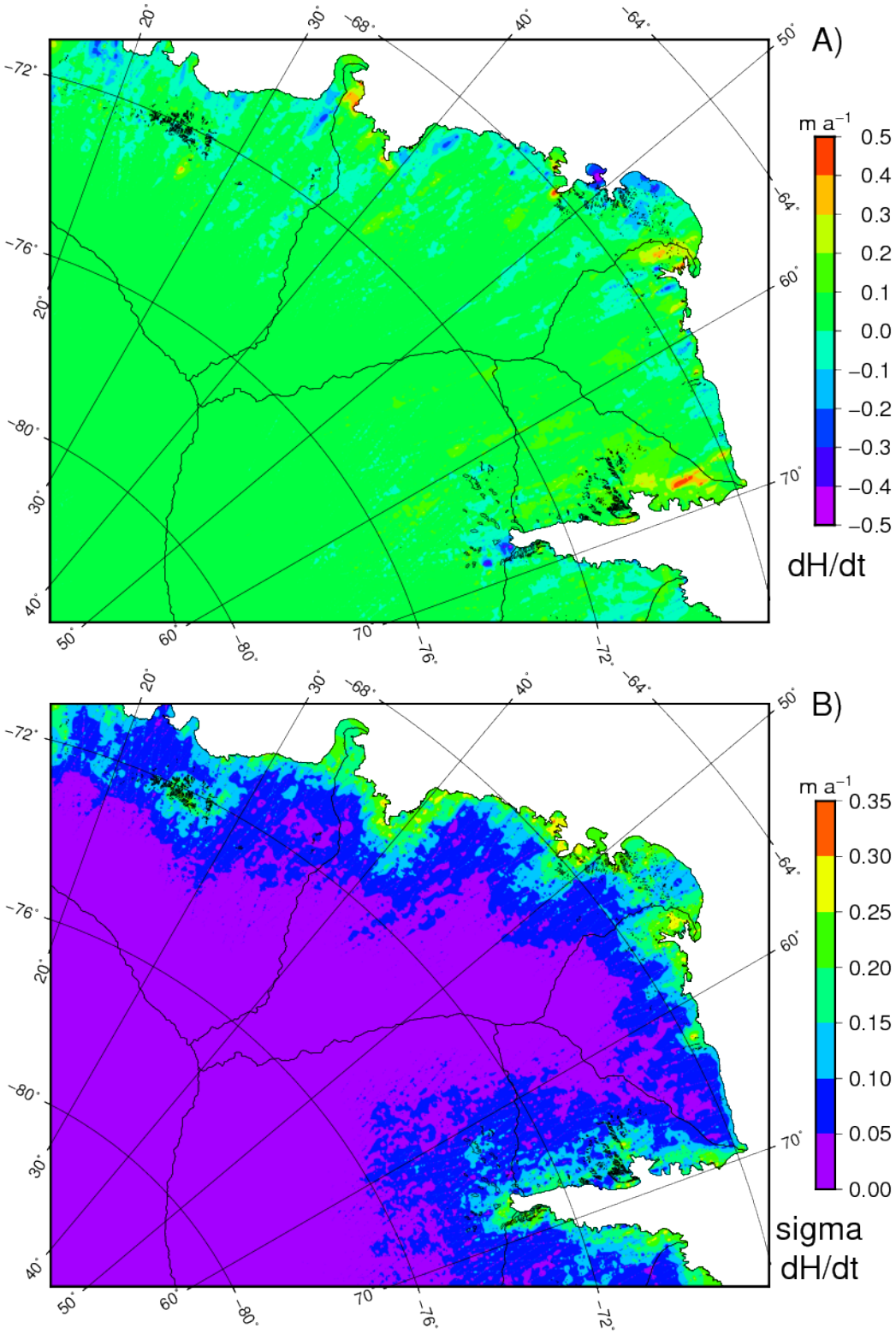

Figure 4.3: A) dH/dt estimates B) uncertainties of dH/dt estimates using the COMB-GFSI method. All measurements have been filtered, any points within a 25 km search radius that are ± 0.75 times the inter-quartile range are removed, after Pritchard et al. (2009). The largest rates and spatial variation in rates occur along the coast, while in the interior rates are smaller and more homogeneous. The majority of rates across the study site are positive, with the exception being along the coast, more specifically at the grounding zone of Amery Ice Shelf and in north-north western Enderby Land. The uncertainties are smallest in the interior, greatest along the coast and in areas of steep surface slope (i.e. mountains, rock outcrops).

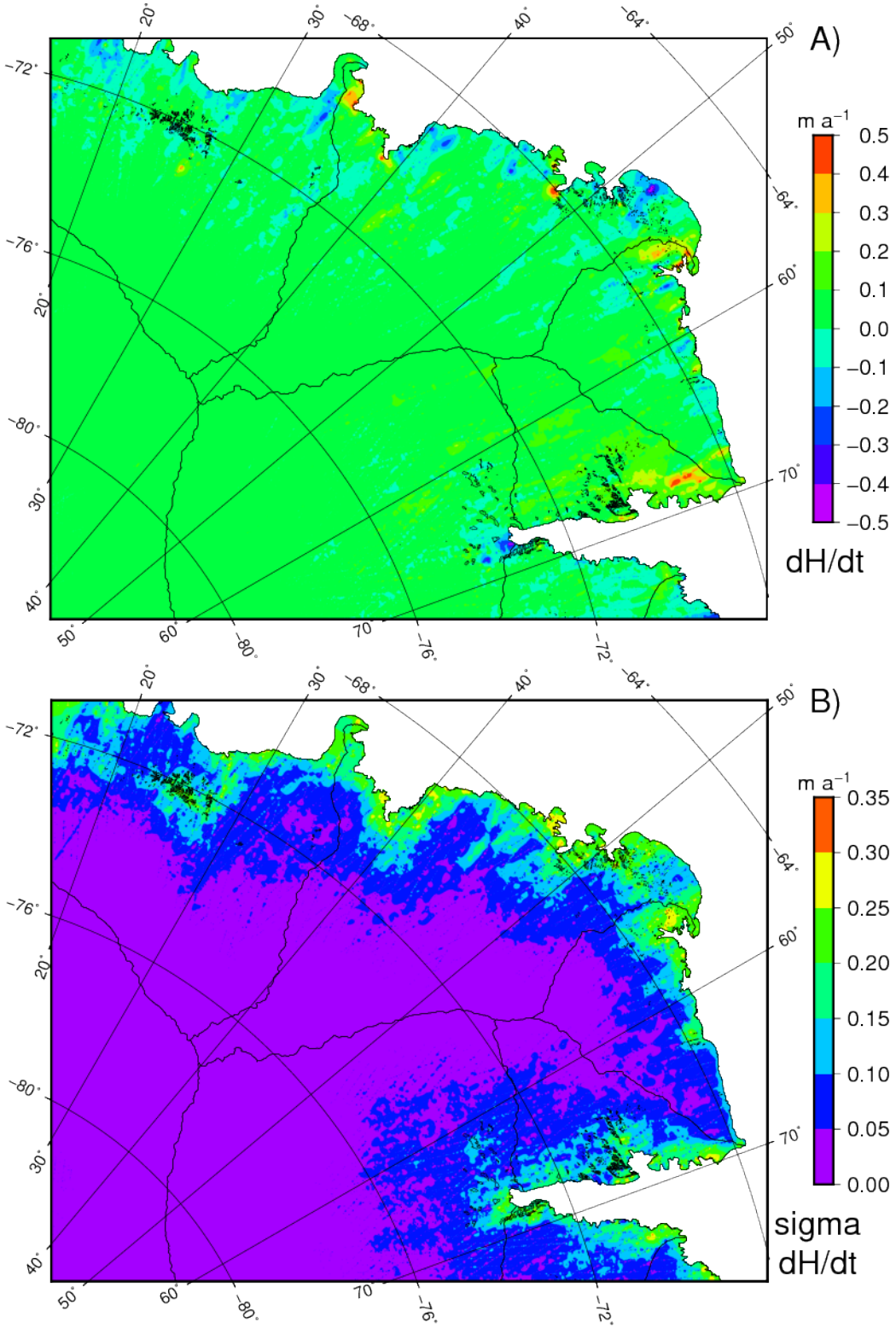

Figure 4.4: A) dH/dt estimates B) uncertainties of dH/dt estimates using the COMB-NNI method. All measurements have been filtered, after Pritchard et al. (2009). The distribution of rates are similar to the Green's function spline interpolation results, however in general the rates are slightly lower. The distribution of sigma values is similar to the COMB-GFSI results, expect that the coastal sigma signals are slightly larger.

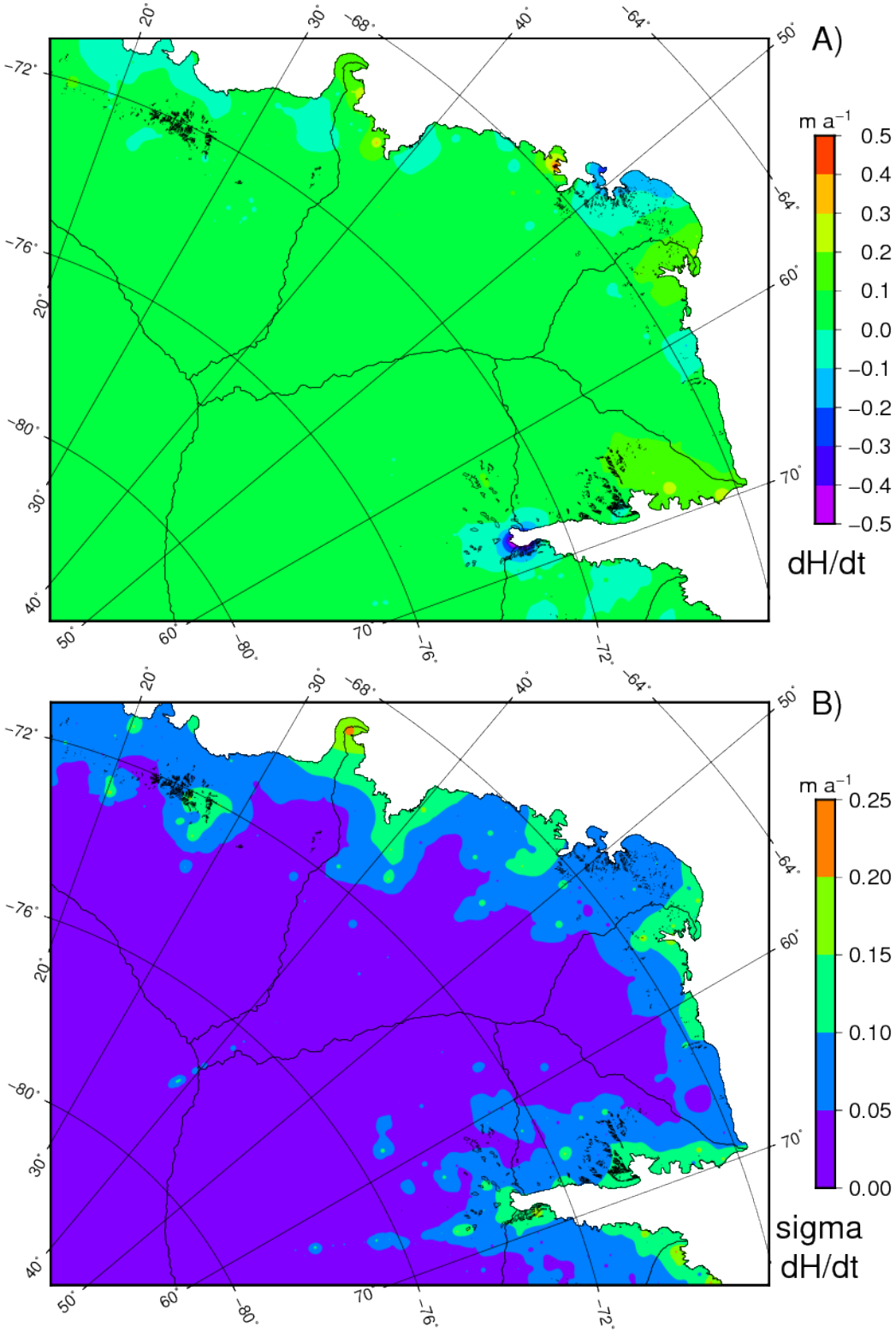

Figure 4.5: A) dH/dt estimates B) uncertainties of dH/dt estimates using the GRID-GFSI method. All measurements have been filtered, after Pritchard et al. (2009). The general distribution of rate signals is similar to the combined results, however, the resolution is much lower. The sigma values are generally lower than those of the combined data. The general distribution of signal values is similar to the combined results, however, the resolution is much lower.

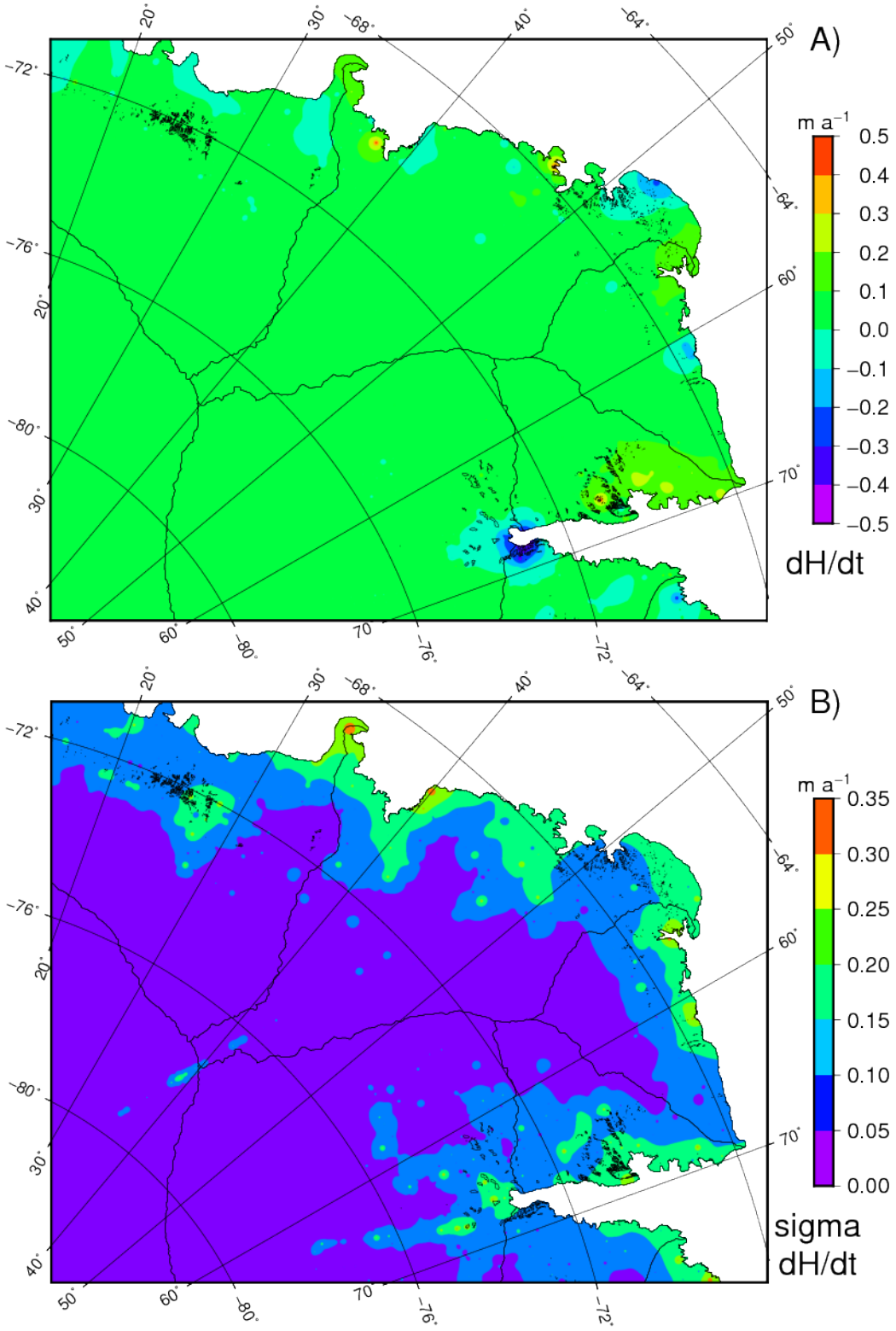

Figure 4.6: A) dH/dt estimates B) uncertainties of dH/dt estimates using the GRID-NNI. All measurements have been filtered, after Pritchard et al. (2009).

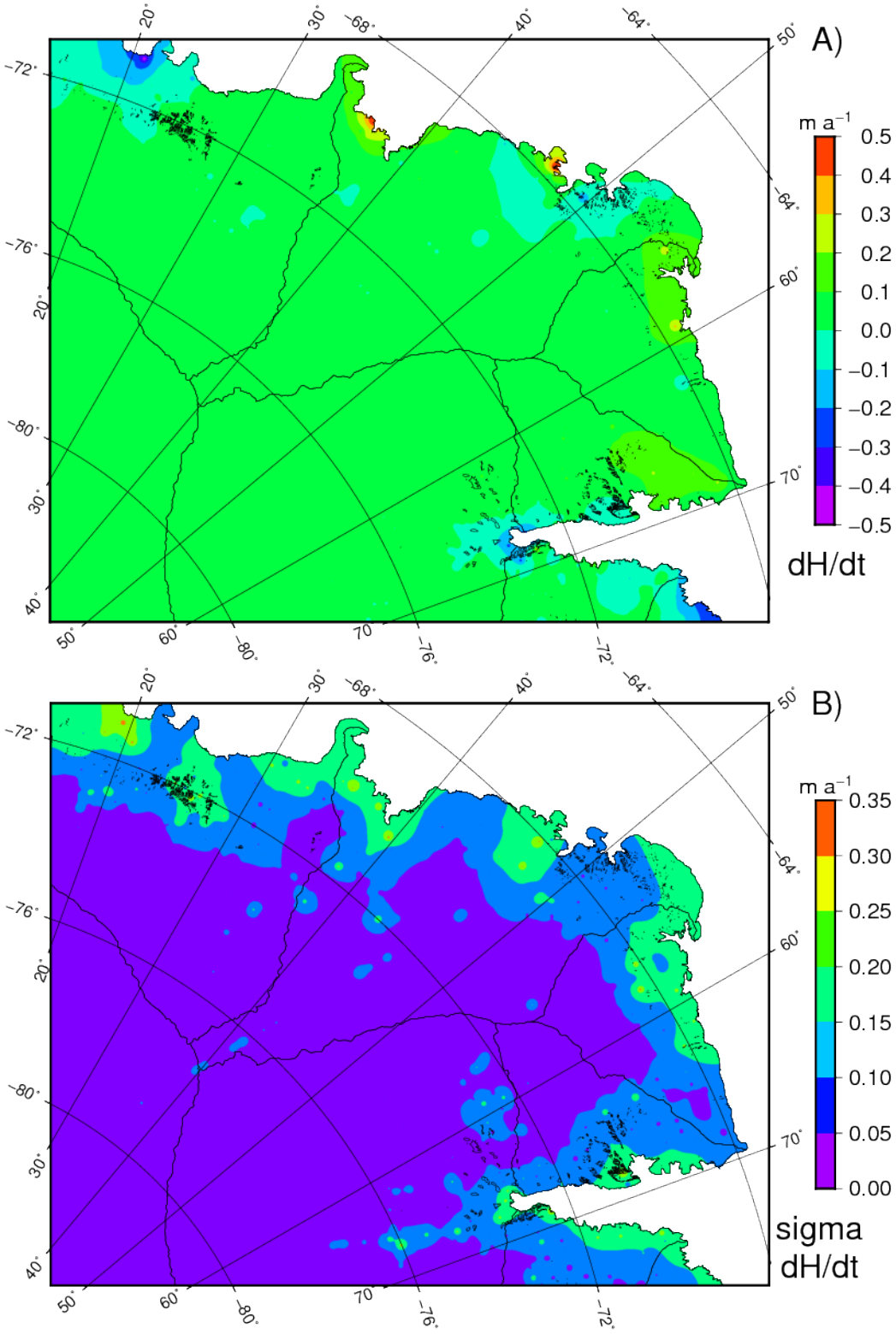

Figure 4.7: A) dH/dt estimates B) uncertainties of dH/dt estimates using the GRID-DTLI method. All measurements have been filtered, after Pritchard et al. (2009).

also the smallest when using only crossover data, followed by GRID-DTLI and lastly GRID-NNI methods (Figures 4.5b, 4.6b & 4.7b). Uncertainties derived from crossover data were generally smaller than those estimated from the combined data. This is not surprising as the crossover geometry allows for more accurate estimates of dH/dt (see Chapter 3). Furthermore, there is no need for surface slope corrections, which is necessary for the along-track method.

4.3.3 Basin-by-basin dH/dt estimates and associated uncertainties

The integrated drainage basin (all velocities) results are all positive with the exception of drainage basin 12 (location: Figure 4.2, data: Table 4.1 & Table 4.2). Drainage basins 6 and 10 both have negative rates for points with ice velocities greater than 100 m a^{-1} using either the combined or crossover data in conjunction with any of the interpolation methods (-0.025 $\pm$ 0.041 m $a^{-1}$and -0.036 $\pm$ 0.028 m a^{-1}, respectively for COMB-GFSI results and -0.018 $\pm$ 0.011 m $a^{-1}$and -0.009 $\pm$ 0.008 m a^{-1} for the GRID-GFSI results) (see Table 4.1 & Table 4.2 for more results). The uncertainty for the COMB-GFSI basin 6 estimate is larger than the rate and therefore the result is not significantly different from zero. The GRID-GFSI results for basin 6 are significant and also negative, which strengthens the validity of the COMB-GFSI estimate.

Both drainage basins have large fast flowing ice streams that have substantial glacial outlets that interface with the ocean (Figure 4.2). Drainage basin 10 includes the grounding zone of the Amery Ice Shelf, which has one of the strongest negative rate signals for the whole study site (Figures 4.3a - 4.7a). Drainage basin 6, in comparison, has a number of fast flowing ice streams, each with a negative rate signal (Figures 4.3a - 4.7a). Each of the signals is not as strong as that of drainage basin 10; however, in combination they are substantial. Even though both drainage basins have negative signals for points with ice velocities greater than 100 m a^{-1}, they are overwhelmed by the positive inland signal, which dictates the overall rate signal (Table 4.1a & b).

Table 4.1: dH/dt results (along-track and crossover combined) for the study site, using A) Green's function spline interpolation and B) nearest neighbour interpolation. Drainage Basins by Pritchard et al. (2009) and Zwally et al. (2012) are denoted by letters and numbers, respectively. dH/dt rates are also categorised according to ice velocity following Pritchard et al. (2009) method, greater than 100 m a^{-1} (ice dynamics) or less than 100 m a^{-1} (seasonal variations in the firn pack due to accumulation or ablation). Drainage basins with * denote full coverage, while other basins only have partial data coverage. NM denotes no measurements in this region with for the given velocity.

A) Green's function spline interpolation

drainage basin	ice velocity < 100 m a^{-1}		ice velocity > 100 m a^{-1}		all velocities	
	mean dH/dt	mean sigma	mean dH/dt	mean sigma	mean dH/dt	mean sigma
3	0.049	0.005	NM	NM	0.048	0.005
6	0.021	0.022	-0.025	0.041	0.02	0.023
7*	0.03	0.018	0.071	0.064	0.031	0.019
8*	0.047	0.02	0.004	0.068	0.046	0.021
9*	0.086	0.022	0.106	0.04	0.086	0.023
10	0.048	0.009	-0.036	0.028	0.046	0.009
11	0.011	0.034	0.021	0.043	0.011	0.034
12	-0.009	0.025	-0.025	0.031	-0.021	0.028
AB	0.054	0.019	0.126	0.067	0.0540	0.0196
BC	0.05	0.012	-0.012	0.031	0.0488	0.0125

B) nearest neighbour interpolation method

drainage basin	ice velocity < 100 m a^{-1}		ice velocity > 100 m a^{-1}		all velocities	
	mean dH/dt	mean sigma	mean dH/dt	mean sigma	mean dH/dt	mean sigma
3	0.049	0.006	NM	NM	0.049	0.006
6	0.002	0.034	-0.022	0.049	0.001	0.034
7*	0.03	0.021	0.064	0.067	0.031	0.022
8*	0.049	0.022	0.02	0.08	0.048	0.023
9*	0.087	0.023	0.102	0.041	0.087	0.024
10	0.048	0.009	-0.034	0.032	0.046	0.009
11	0.016	0.035	0.089	0.071	0.019	0.036
12	0.032	0.034	-0.018	0.028	0.02	0.029
AB	0.034	0.021	0.094	0.068	0.035	0.022
BC	0.052	0.013	-0.006	0.037	0.05	0.013

Table 4.2: dH/dt results (crossover data) for the study site, using A) Green's function spline interpolation and B) nearest neighbour interpolation. C) Delaunay triangulation.

A) Green's function spline interpolation

drainage basin	ice velocity < 100 m a^{-1}		ice velocity > 100 m a^{-1}		all velocities	
	mean dH/dt	mean sigma	mean dH/dt	mean sigma	mean dH/dt	mean sigma
3	0.046	0.002	NM	NM	0.046	0.002
6	0.02	0.008	-0.018	0.011	0.019	0.007
7*	0.035	0.005	-0.008	0.02	0.035	0.006
8*	0.038	0.007	0.153	0.008	0.041	0.009
9*	0.062	0.012	0.061	0.014	0.062	0.014
10	0.054	0.003	-0.009	0.008	0.053	0.003
11	-0.024	0.016	-0.024	0.018	-0.025	0.017
12	-0.124	0.012	-0.035	0.009	-0.068	0.013
AB	0.036	0.006	0.032	0.017	0.036	0.006
BC	0.051	0.005	-0.004	0.014	0.05	0.005

B) nearest neighbour interpolation method

drainage basin	ice velocity < 100 m a^{-1}		ice velocity > 100 m a^{-1}		all velocities	
	mean dH/dt	mean sigma	mean dH/dt	mean sigma	mean dH/dt	mean sigma
3	0.047	0.002	NM	NM	0.047	0.002
6	0.019	0.008	-0.008	0.011	0.018	0.007
7*	0.042	0.007	0.038	0.019	0.042	0.009
8*	0.039	0.009	0.123	0.009	0.041	0.01
9*	0.084	0.014	0.125	0.014	0.085	0.012
10	0.055	0.004	-0.003	0.01	0.054	0.004
11	0.01	0.032	-0.163	0.047	0.001	0.033
12	0.027	0.017	-0.111	0.014	-0.025	0.016
AB	0.042	0.007	0.059	0.016	0.042	0.007
BC	0.055	0.006	-0.008	0.015	0.054	0.006

C) Delaunay triangulation method

drainage basin	ice velocity < 100 m a^{-1}		ice velocity > 100 m a^{-1}		all velocities	
	mean dH/dt	mean sigma	mean dH/dt	mean sigma	mean dH/dt	mean sigma
3	0.047	0.004	NM	NM	0.047	0.004
6	0.026	0.007	-0.008	0.013	0.026	0.007
7*	0.036	0.006	0.289	0.025	0.04	0.007
8*	0.06	0.008	0.136	0.016	0.063	0.008
9*	0.026	0.01	-0.008	0.007	0.025	0.01
10	0.049	0.004	0.011	0.011	0.048	0.004
11	0.043	0.027	-0.065	0.036	0.043	0.027
12	-0.047	0.014	MN	MN	-0.047	0.013
AB	0.04	0.007	0.245	0.022	0.047	0.007
BC	0.047	0.005	-0.003	0.014	0.046	0.005

Drainage basins 7 and 8 both have strong localised negative signals. Drainage basin 7 has two such signals along the north north-western coast of Enderby Land, while drainage basin 8 has a number of weak negative signals (Table 4.1 & Table 4.2). In both cases these localised negative rates have little effect on the overall mean rate for each drainage basin, which is also reflected in the crossover results (Table 4.2). This result is similar to the findings of Pritchard et al. (2009); King et al. (2012) and Sasgen et al. (2012) who all found substantial gains in either dH/dt or dM/dt.

The section of drainage basin 3 which is located in my study site is entirely landlocked and has a positive dH/dt signal (0.048 $\pm$ 0.005 m a^{-1}, COMB-GFSI) (Table 4.1 & Table 4.2). It covers most of the interior of the study site and consequently it had no ice height measurements with ice velocities above 100 m a^{-1}. It has one of the smallest uncertainties as surface slopes are very small in this region.

Drainage basin 9 has the highest positive signal of 0.086 $\pm$ 0.023 m a^{-1} (COMB-GFSI) for the study region. The large positive dH/dt signal just inland of the coast is clearly shaping the overall signal for the whole basin. This is likely due to accumulation, which will be discussed later. The crossover dH/dt signals for this basin are very variable, however there is general agreement that the signal is positive (Table 4.2). Only 18.6% of drainage basin 11 is located in my study site. It has a small but insignificant positive signal (0.011 $\pm$ 0.034 m a^{-1}, COMB-GFSI) and the fast

flowing regions are actually gaining mass (0.021 ± 0.043 m a^{-1}, COMB-GFSI). Again the estimate is not significant, so it is difficult to determine whether this basin is losing or gaining height. The crossover data suggests that the basin may in fact be losing height (-0.024 ± 0.018 m a^{-1}, GRID-GFSI), however the density of crossovers is low in this region, which casts doubt over this result.

My study site only covers 1.6% of drainage basin 12 and a large portion of this is in a region of high ice velocities close to the coast. Consequently the drainage basin signal is completely coastal, with no impact from the interior, unlike all the other drainage basins in my study site. It is apparent that all the rates of drainage basin 12 (-0.021 ± 0.028 m a^{-1}, COMB-GFSI and -0.068 ± 0.013 m a^{-1}, GRID-GFSI) are largely influenced by the mean rates from points with ice velocities greater than 100 m a^{-1} (-0.025 ± 0.031 m a^{-1}, for COMB-GFSI and -0.35 ± 0.009 m a^{-1}, for GRID-GFSI). This is different from the other drainage basins, where the points with ice velocities less than 100 m a^{-1} are in the majority and largely dominate the signal from points with ice velocities greater than 100 m a^{-1} (Table 4.1a). The rates for the combined data are not statistically significant, which minimises the implications of the results.

This is in general agreement with the findings of Pritchard et al. (2009), who estimated a rate of -0.08 m a^{-1} for points with ice velocities greater than 100 m a^{-1} for drainage basin 12. Drainage basin 12 is approximately the same as drainage basin CC' after Pritchard et al. (2009). This comparison is limited due to the small percentage of the drainage basin in my study site. Nonetheless, Figure 2 in Pritchard et al. (2009) shows rates between 0 and -0.3 m a^{-1} for the section of the drainage basin I used, suggesting they would estimate a similar mean rate for that region.

Interestingly, the rates estimated using the nearest neighbour interpolation are only negative for points with ice velocities greater than 100 m a^{-1}, while the rate for the whole drainage basin is positive (Table 4.1b). Nearest neighbour interpolation can be insensitive to sudden changes in height, which would cause this difference. In the next section I will compare my results with those of Pritchard et al. (2009).

4.3.4 Comparison with Pritchard et al. (2009) dH/dt results

Currently, there are few other altimetry studies that have published dH/dt estimates for East Antarctica on a basin scale. Most studies only present their estimates in dM/dt and then generally for the whole of East Antarctica (Shepherd et al., 2012). Pritchard et al. (2009) is the only recent study (similar time frame) that published their dH/dt estimates from ICESat on a basin scale. Their time scale (2003 to 2007) is slightly shorter than that of my study and they do not estimate the uncertainty directly, instead they give a "detection threshold" value which is an estimate of overall uncertainty. Nonetheless this study is very similar to mine and therefore direct comparisons are valid. My study site covers two of Pritchard et al. (2009) drainage basins (A'B and BC). The A'B drainage basin approximately covers the same area as drainage basins 7 and 8 in my study and BC approximately covers drainage basins 9 and 10. There are some differences, so I recalculated the mean dH/dt for the A'B and BC drainage basins.

The results I obtained are broadly similar to those of Pritchard et al. (2009), as both obtained positive signals for basins A'B and BC. For A'B they estimated a mean rate of 0.07 m a^{-1} (detection threshold: 0.11) and for points with ice velocities less than 100 m a^{-1}, I obtained mean rate of 0.054 $\pm$ 0.019 m a^{-1} (using COMB-GFSI). For points with ice velocities greater than 100 m a^{-1} they had a mean rate of 0.15 m a^{-1} (detection threshold: 0.13), while I obtained a rate of 0.126 $\pm$ 0.067 m a^{-1} (using COMB-GFSI) (Figure 4.8 and Table 4.1). This was the largest positive rate that Pritchard et al. (2009) estimated for the whole of Antarctica. I also obtained a strong positive signal, however my rate estimate for basin A'B was smaller than that of Pritchard et al. (2009). This difference is most likely due to the surface slope correction, which led to more occurrences of small negative rates along the coast of the A'B basin.

The difference between the rate estimates for the BC basin is less pronounced. Pritchard et al. (2009) estimated a rate of 0.05 m a^{-1} (detection threshold: 0.09), while I calculated a rate of 0.05 $\pm$ 0.012 m a^{-1} for points with ice velocities less than 100 m a^{-1}. For points with ice velocities greater than 100 m a^{-1}, Pritchard et al.

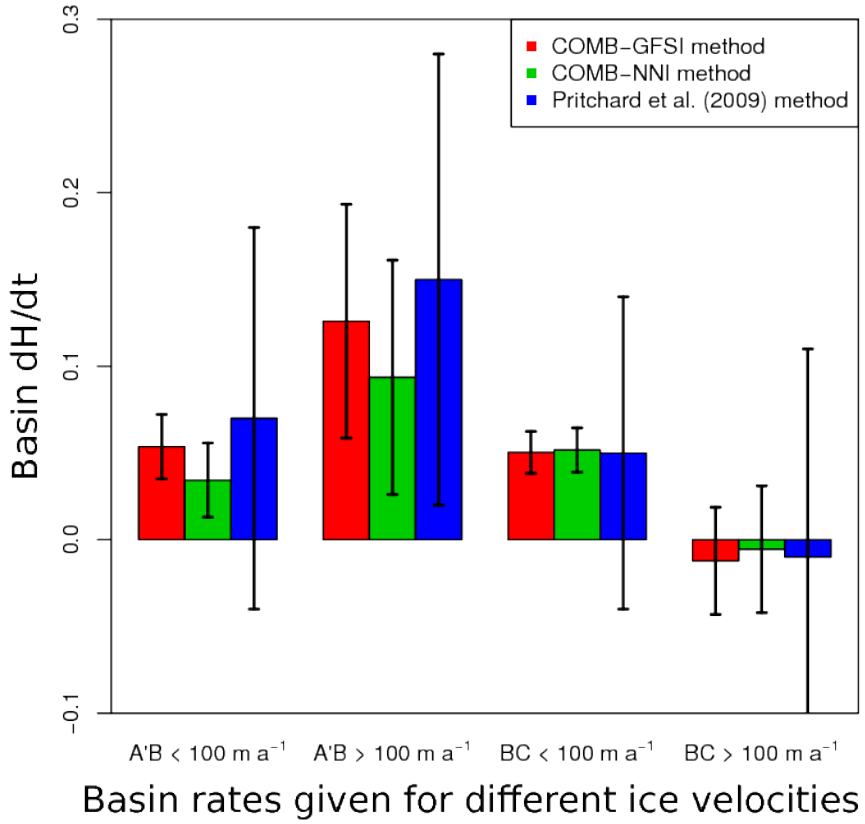

Figure 4.8: A comparison of basin dH/dt and uncertainty. Basin rates given for ice velocities less than and greater than 100 m a^{-1}. Red bar denotes Green's function spline interpolation; green bar: nearest neighbour interpolation; blue: Pritchard et al. (2009) method.

(2009) obtained a rate of -0.01 m a^{-1} (detection threshold: 0.09) and I obtained a rate of -0.012 $\pm$ 0.031 m a^{-1}(Figure 4.8 and Table 4.1). Both of these latter estimates are within 1 sigma and are not significantly different from zero, due to the large surface slopes and height variability around the Amery Ice Shelf. When the COMB-NNI results are compared to the Pritchard et al. (2009) results, they are not as close in agreement as are the COMB-GFSI results.

It is important to note that Pritchard et al. (2009) do not correct their estimates for surface slope, as they assume that the Delaunay triangulation interpolation method they use accounts for both across-track and along-track surface slope. For this to be true, the surface slope covered by the triangle must not be curved and the rate of height change between the three points of the triangle must be constant through time. These assumptions may not be valid: firstly, the surface slope of a surface can be curved, or shaped in a way that a simple triangular surface is not able to represent. Surface slope bias must be corrected for directly and the differences between my findings and those of Pritchard et al. (2009), especially in regions of high surface slope, can be explained by this difference in methodology. Secondly, rates of height change are not necessarily constant through time and can vary significantly from season to season. Therefore the points of the triangle might be seasonally biased, which would bias the linear interpolation across the triangular surface. I minimise this bias by only estimating heights from data that is collected within a $\sim$33-day laser campaign. Pritchard et al. (2009) use a range of 1.5 to 4.5 years, which does not take this bias into account. Consequently, I believe my method is more accurate as I only estimate heights from data points positioned close in time and I correct for surface slope using polynomial surfaces that are able to account for the curvature of the surface slope.

The uncertainties estimated for my study were lower (often an order of magnitude lower) than the "detection threshold" estimates given by Pritchard et al. (2009). These threshold values include 0.07 m a^{-1} measurement uncertainty across all estimates and a SMB/runoff variability uncertainty. I do not include SMB/runoff variability in my uncertainty budget, as I focused on the uncertainty of the inter-

polation and surface slope bias. Other factors that also contribute to the higher accuracy of my method are; firstly, I am using a newer release of the ICESat data, which has had a number of errors corrected, making it more accurate and with smaller uncertainties; secondly, I estimate my rates using the complete ICESat data set, while Pritchard et al. (2009) only used data up to late 2007 (which was all that was available at the time of publication).

Zwally et al. (2005) also estimated rates on a basin level for the whole of Antarctica. Their findings are different from the results of both this study and Pritchard et al. (2009). They are not directly comparable as they used ERS-1 & -2, radar altimeters that were active over Antarctica from 1992 to 2001. Consequently the time period does not overlap, making it hard to make comparisons. Furthermore, they do not publish dH/dt for each drainage basin, but instead estimate dI/dt (change in ice-thickness) for both grounded and floating ice. My and Pritchard et al. (2009) studies only estimate dH/dt for grounded ice. The grounded ice dI/dt estimates that Zwally et al. (2005) obtained for the drainage basins are generally negative but small. In their Figure 2, they presented the distribution of both dH/dt and dI/dt. The dH/dt rates appear to be more positive, but it is difficult to compare. Potentially the regional signal for my study has gone from slightly negative to positive over the two time periods, or alternatively the methods used are too different to compare.

4.3.5 dH/dt case studies: significant coastal rate signals

As mentioned earlier, all ice height rates are filtered using the method presented by Pritchard et al. (2009). This filtering process is essential to remove any data points which are erroneous or affected by large surface slopes. The consequence of this is that mean rate estimates generally become smaller. In this section I look in detail at five of the largest regional signals found in my study site, discuss the effect of filtering and try to establish why the signals are strongest in these regions.

4.3.5.1 Site 1

The first site is directly inland from the grounding line of the Amery Ice Shelf in MacRobertson Land, where the Lambert and Mellor glaciers meet (Figure 4.1 and Figure 4.9). The region is approximately ~20,000 km^2 in size and most of the region has a positive dH/dt between 0.1 and 0.2 m a^{-1}. Directly behind the grounding line is a region ~2500 km^2 in size which has a negative mean dH/dt of -0.38 ± 0.32 m a^{-1} (Figure 4.9a). Both the ascending and descending repeat-tracks return negative signals suggesting that, even if surface slope is not accounted for (which it is), the sign of the signal is clear. Furthermore, there is a crossover situated directly behind the grounding line, which has a dH/dt of -0.24 ± 0.14 m a^{-1}. This result is in agreement with Pritchard et al. (2009) (ICESat data) and Flament and Rémy (2012) (ENVISAT data), who both found losses directly behind the grounding line. Losses at the grounding line were also found at the Totten and Denman glaciers, also situated in East Antarctica, although losses there were larger than those found at the Lambert and Mellor glaciers (Figure 4.9a) (Flament and Rémy, 2012).

This region has some of the largest velocities on and around the Amery Ice Shelf, suggesting that most of the loss is due to ice flow dynamics rather than SMB of the firn. The SMB model from Lenaerts et al. (2012) reinforces this argument, as it estimates a SMB of very close to zero for this area. Consequently, all the changes are occurring in the ice column. This area is not covered by the Ligtenberg et al. (2011) FDM model and, therefore, I was not able to estimate the seasonal firn column signal, which makes it difficult to determine whether the height changes are due to firn densification or ice flow dynamics. Albeit indirectly, the location of the loss in height does suggest that ice flow dynamics are the cause of this change.

The uncertainties are greatest behind the grounding line as well as on the southern slopes (south on Figure 4.9c & d) of a large outcrop of rock and mountains (denoted as southern slopes). The larger uncertainties behind the grounding line can be attributed to the substantial surface slope uncertainties, that are due to the fast flowing nature of the region. The large uncertainties near the rock outcrops are due in part to the large snow/ice slope going from north to south. Furthermore, the

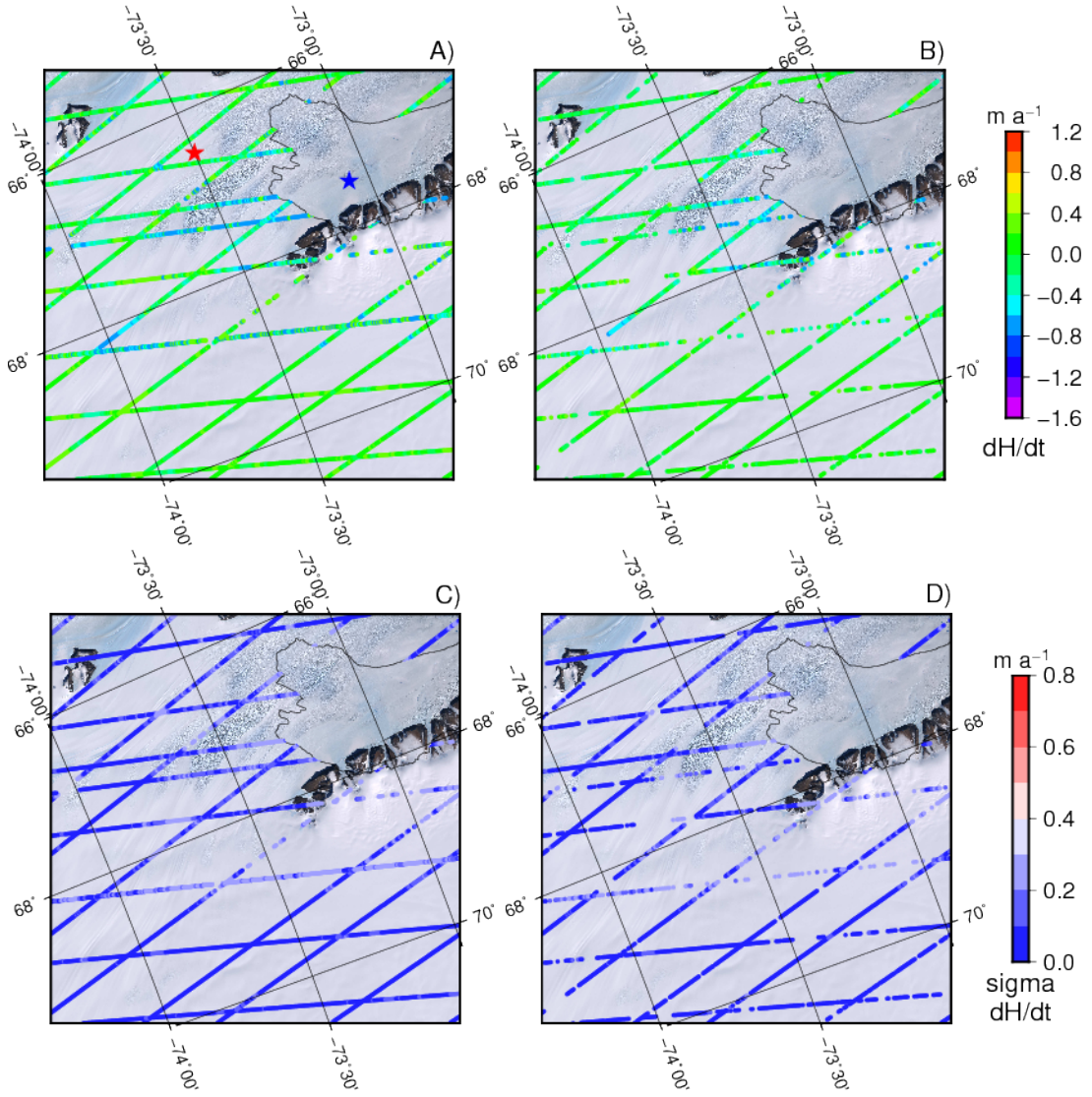

Figure 4.9: Site 1: dH/dt estimates and uncertainties A) unfiltered. B) filtered. C) unfiltered sigma. D) filtered sigma. The black line denotes the grounding line of the Amery Ice Shelf and comes from the SCAR Antarctic Digital Database. This site had some of the highest negative rates, even after the (Pritchard et al., 2009) filtering process was applied. The blue and red stars show the locations of the Lambert and Mellor Glaciers, respectively.

ICESat repeat-tracks for the ground-track located on the southern slopes are spaced further apart than usual, leading to less accurate estimates of height. Most of these points are removed by the filtering process (Figures Figure 4.9c & d). However, the filtered results (Figure 4.9b) and the unfiltered results (Figure 4.9a) still have a similar distribution, although, in the case of the filtered results, the negative signal is somewhat diminished. Consequently, the filtering process for this site has had a small effect on the regional signal.

4.3.5.2 Site 2

The second site is situated on the east coast of Enderby Land and covers an area of ~5000 km^2. It has some of the highest recorded unfiltered height losses for my study site (Figure 4.1 and Figure 4.10a). It also has some of largest uncertainties, which lessens the significance of the height loss estimates (Figure 4.10c). The temporal coverage of the ICESat dataset for this area is very sporadic due to seasonal cloud cover. Most of the dH/dt estimates are between 0 and -0.5 m a^{-1}, however there is a single ground-track in the centre of the site that has rates between -1.2 to -1.6 m a^{-1}. There are some suspect points that have rates of greater than -10 m a^{-1} and these are also the points with the greatest uncertainties. This ground-track has the lowest temporal range of data and rates are estimated using as few as 4 to 6 laser campaigns of height data over the ICESat operational period (2003 - 2009).

Figure 4.11a shows an example of a point with a low temporal range (5 points) with a rate of -1.65 $\pm$ 0.70 m a^{-1} (location: Figure 4.10a, black box). This point was not removed by the filtering process, as even though the standard deviation for each of the data points is relatively high, ranging from ~20 to 60 cm, the uncertainty estimate is still lower than the rate estimate. Many points were removed that had very high standard deviations, one such point is shown in Figure 4.11b (location: Figure 4.10a, red box). This point has a rate of -12.6 $\pm$ 6.2 m a^{-1}(5 points) and was filtered out as the rate was significantly larger than surrounding rates. The standard deviations of each interpolated point were also extremely large suggesting erroneous data points. To put this into perspective, Figure 4.11c shows a point further inland

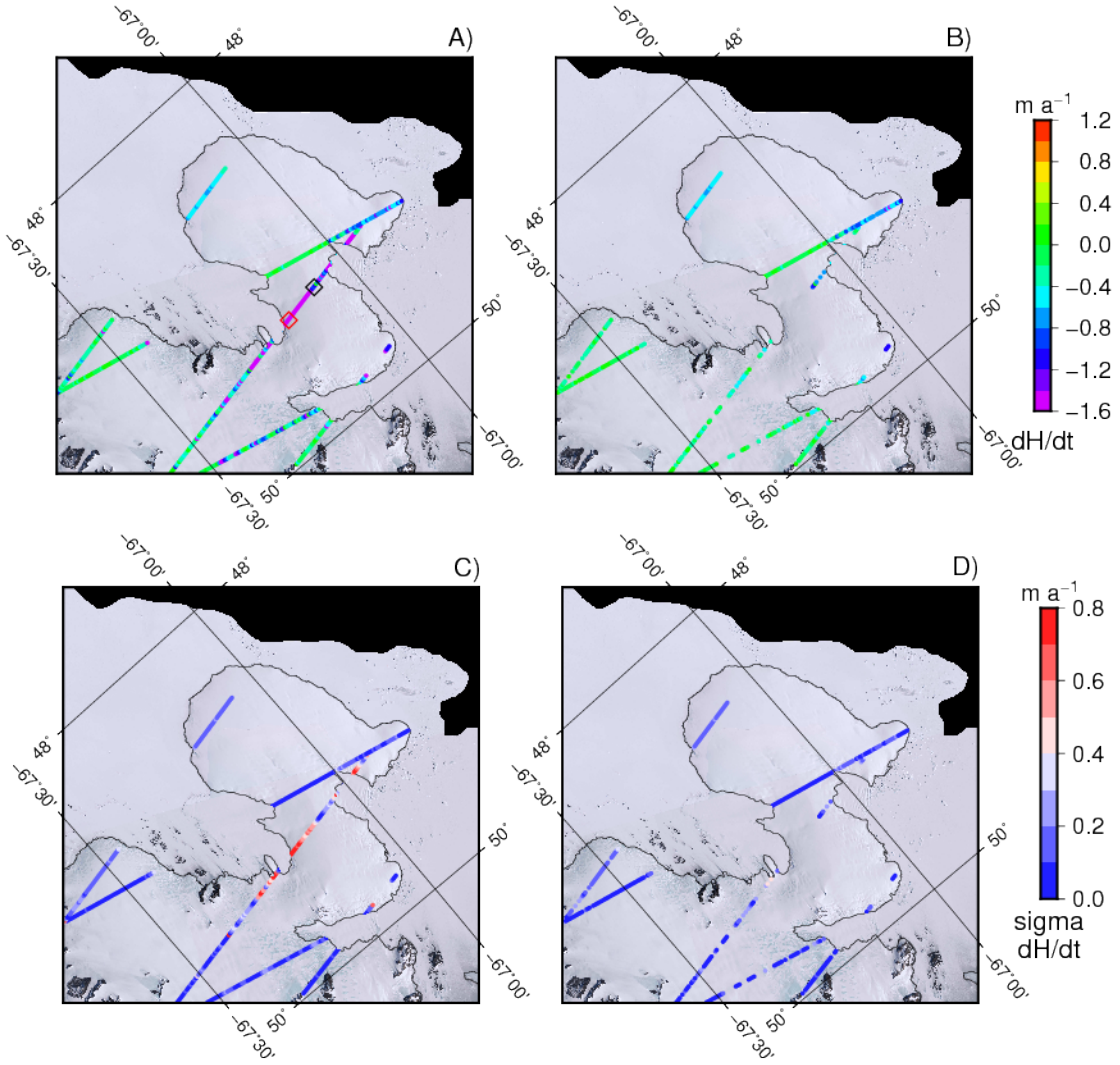

Figure 4.10: Site 2: dH/dt estimates and uncertainties A) unfiltered. B) filtered. C) unfiltered sigma. D) filtered sigma. The black line denotes the coastline. This site had some of the largest negative rate changes present in the study site. The black box shows the location of the time series in 4.11a. The red box shows the location of the time series in 4.11b. Many of these rates were filtered out using the method described by Pritchard et al. (2009).

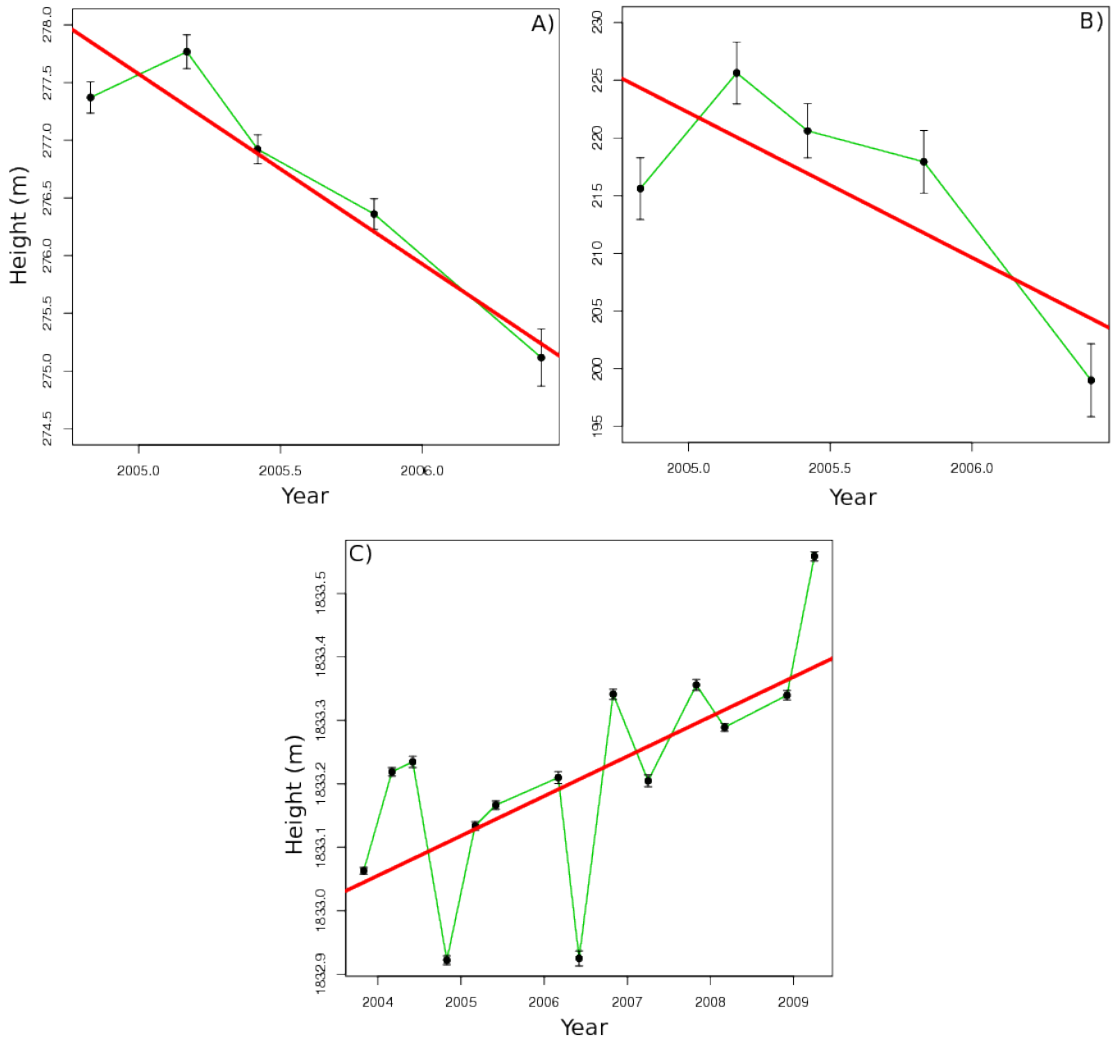

Figure 4.11: The difference between badly constrained and well constrained height estimates. A) A point near the coast with only five laser campaigns. The rate of change is -1.65 ± 0.7 m a^{-1}. This point was not filtered out. B) This point is also near the coast and in a region of high surface slope, it was filtered out as it was significantly different from surrounding points. Both A) & B) located in Site 2 (4.10). The rate of change is -12.6 ± 6.2 m a^{-1}. C) A point further inland with 14 laser campaigns and a rate of change of 0.06 ± 0.014. C) is located in the interior site (4.17).

where the temporal resolution (14 points) is much higher and, consequently, the rate has a much lower uncertainty (location: Figure 4.17). The standard deviations of interpolated heights for each laser campaign in this example range from single digit millimetre estimates to tens of millimetres.

There is a crossover close to this ground-track where the estimated dH/dt was -0.4 $\pm$ 0.05 m a^{-1}, which is more in line with the rest of the dH/dt rates for the region (Figure 4.10a, large blue box). Furthermore, the estimates from the ascending and descending repeat-tracks do vary. When the filtered data (Figure 4.10b) is compared to the unfiltered data (Figure 4.10a), the estimates are significantly different ($\sim$2-sigma, using the unfiltered sigma estimate and $\sim$4-sigma using the filtered sigma estimate). For this site the filtering process removes a significant amount of data, which in turn decreases the overall negative rate signal for the region.

The Lenaerts et al. (2012) SMB model estimates a positive rate $\sim$0.1 m a^{-1} for this region, which suggests that accumulation is occurring. This accumulation signal however is overwhelmed by the larger negative signal for the region. Again the Ligtenberg et al. (2011) FDM model does not cover this coastal area, however points further inland indicate that positive changes are occurring in the firn. Furthermore, this region is an area of slow flowing ice and therefore change in rate is most likely due to firn column ablation rather than ice dynamics.

4.3.5.3 Site 3

The third site is located on the boundary of Dronning Maud Land and Enderby Land and covers an area of $\sim$9000 km^2 (Figure 4.1). It is also directly on the border of two drainage basin divides. The western side of the site (drainage basin 7) has a positive signal ranging from 0.2 to 1.2 m a^{-1} , while the eastern side (drainage basin 6) has a negative signal ranging from 0 to -0.2 m a^{-1} (Figure 4.12). Both regions have a large range of height rate uncertainties, which again are directly related to the sporadic temporal coverage and greater than normal distance between repeat tracks of the ICESat data.

The dH/dts estimated at crossovers found on both sides of the divide are in

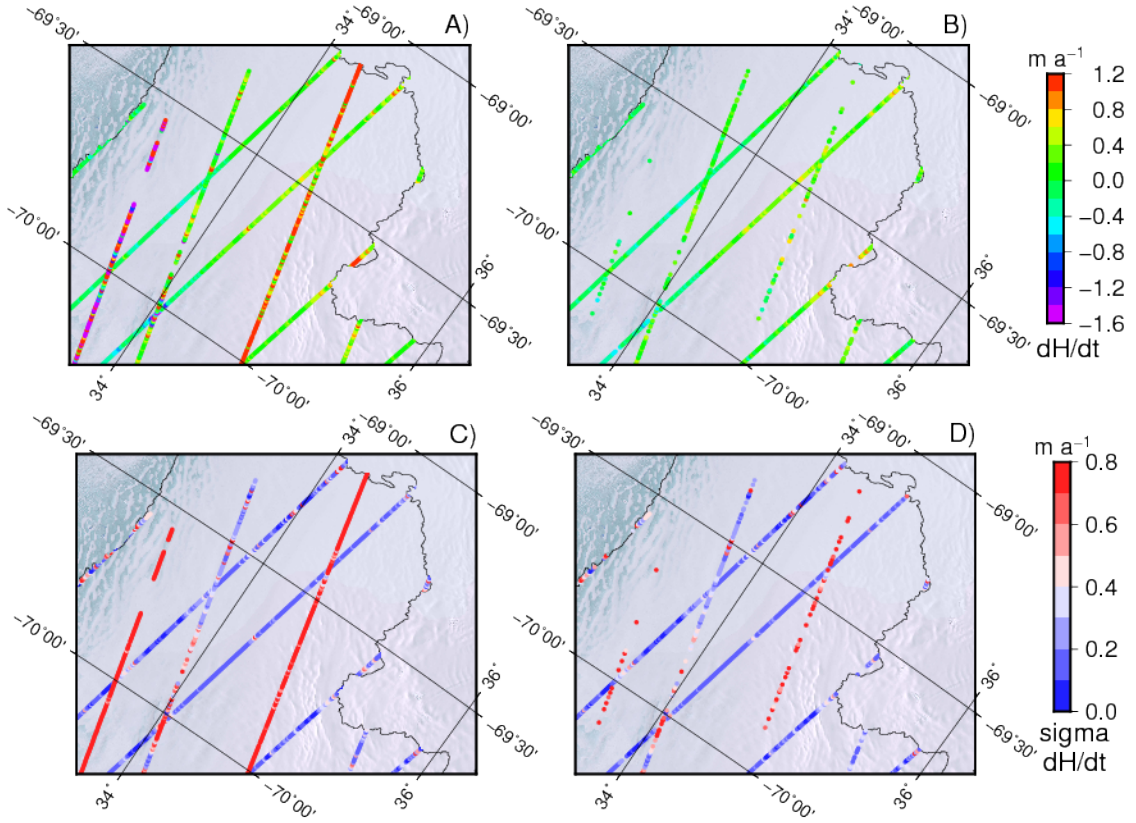

Figure 4.12: Site 3: dH/dt estimates and uncertainties A) unfiltered. B) filtered. C) unfiltered sigma. D) filtered sigma. The black line denotes the coastline. This site had areas with large positive and smaller negative rates. After filtering much of the strong signal was removed as seen in B).

general agreement with the along-track data in terms of the sign of the signal, however the dH/dt estimates at the crossovers are much smaller in both cases. In the west, dH/dt estimates at crossovers were 0.231 and 0.369 m a^{-1} respectively, while in the east they were -0.261, -0.079 and -0.037 m a^{-1} . This discrepancy is in large part due to two ground-tracks with large uncertainties, one located in the east and one in the west. When filtered rates (Figure 4.12b) are compared to unfiltered rates (Figure 4.12a), it is clear that most of the larger estimates with their large associated uncertainties are filtered out, leaving the regional mean dH/dt to be 0.68 m a^{-1} .

Converting the regional mean dH/dt to water equivalent yields an estimate of 0.43 m w.e. a^{-1} which is similar to the SMB estimate of ~0.5 m w.e. a^{-1}. As these estimates are so similar, it is very likely that most of the positive signal is due to increased accumulation.

4.3.5.4 Site 4

The fourth case study is positioned on the border of Enderby Land and Kemp Land and this region has areas of fast and slow flowing ice (Figure 4.1 and Figure 4.13, area: ~30,000 km^2). Consequently, the range of rates occurring here is very broad. In the fast flowing ice streams near the coast the rates range from -0.2 to -0.6 m a^{-1}, while further inland in the slower flowing areas rates vary from 0.2 to 1.0 m a^{-1} and uncertainties range from 0.03 to 0.7 m a^{-1} (Figure 4.14). Up on the near stationary plateau, rates are an order of magnitude smaller and are typically less than 10 mm a^{-1} .

Interestingly, all the crossover points that are found in this region have a positive dH/dt. There is one crossover which is located in a region where the along-track rates estimate losses, however this point has a slightly positive dH/dt of 0.0121 m a^{-1} . This is one of the few locations where the crossover data is insensitive to a signal that the along-track method detects. There is a lot of variation in dH/dt estimates along the coast and, consequently, when these estimates are filtered there is a considerable difference between the filtered and unfiltered results. As can be

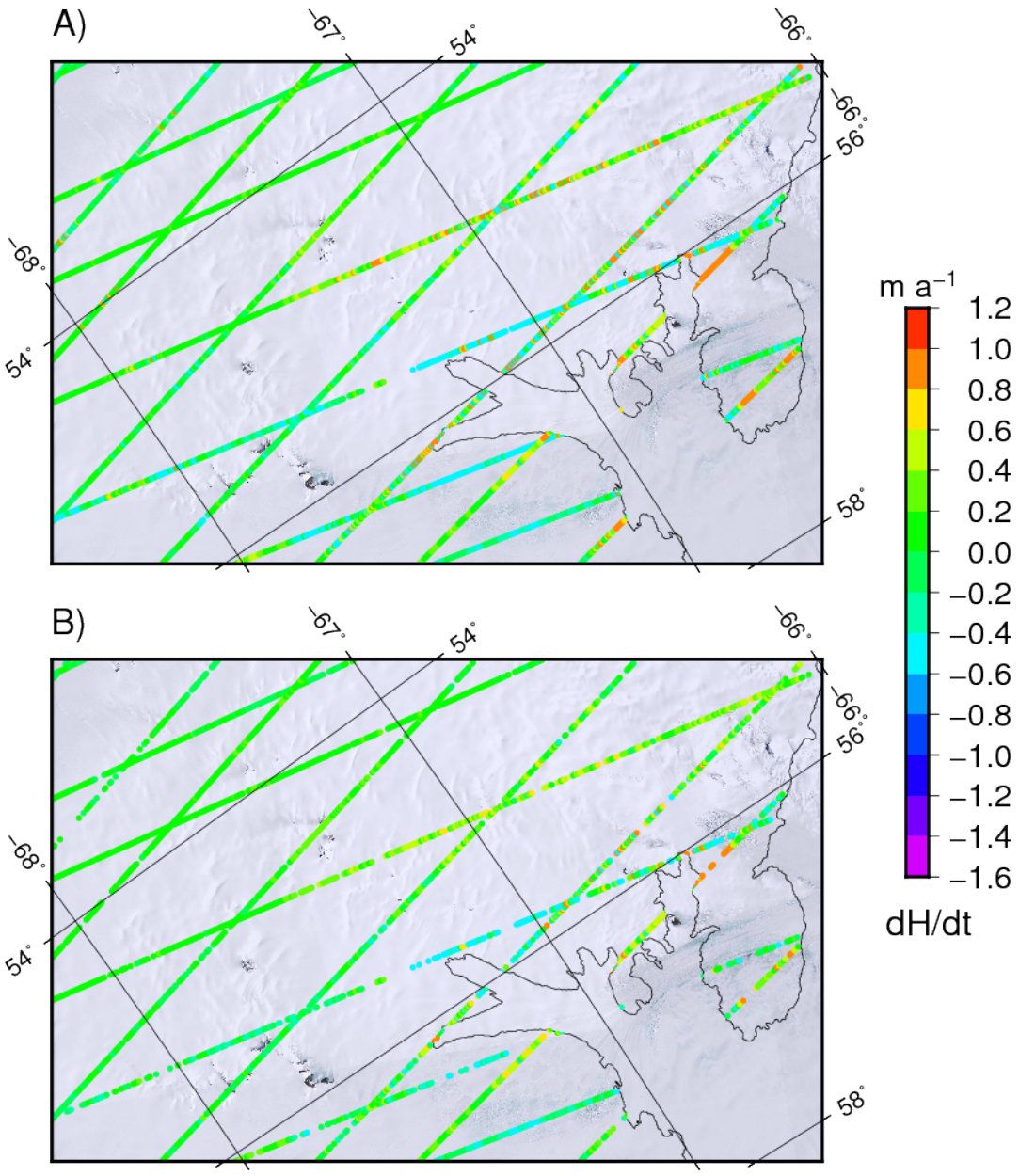

Figure 4.13: Site 4: dH/dt estimates A) unfiltered. B) filtered. The black line denotes the coastline.

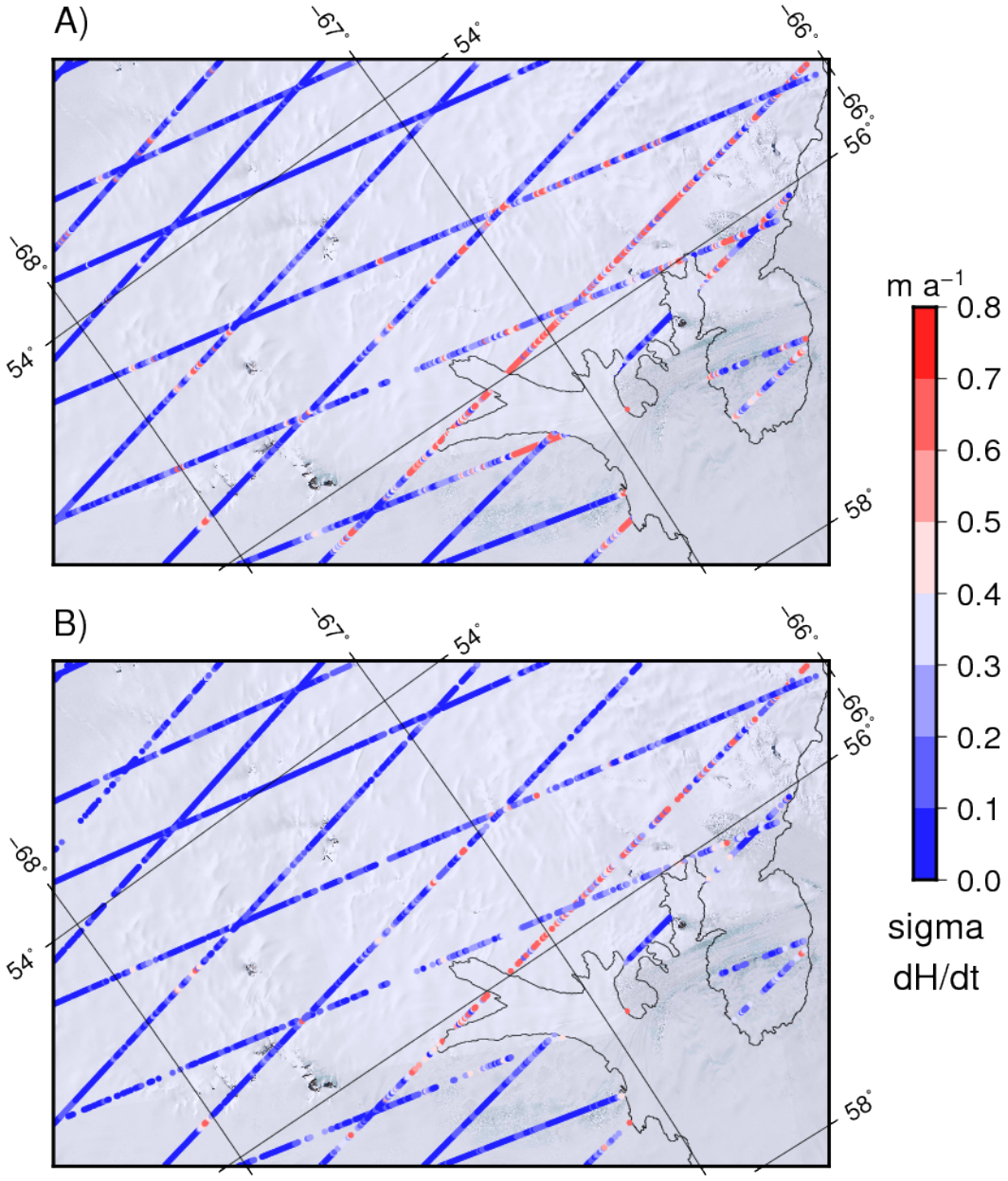

Figure 4.14: Site 4: dH/dt uncertainties. A) unfiltered sigma. B) filtered sigma. The black line denotes the coastline.

seen in Figure 4.13 the strong negative signal (unfiltered mean: -0.39) is significantly smaller (3-sigma, p=0.0012) when the dH/dt estimates are filtered (filtered mean: -0.06). Of all of the case studies, the composition of rates for this site was the most affected by the filtering process.

Using the SMB model I estimated an accumulation rate in the firn layer of ~0.4 m w.e. a^{-1} for the region, while the regional water equivalent dH/dt estimate was 0.291 m w.e. a^{-1}. This difference is likely due to the discrepancy in resolutions of the ICESat and SMB model data. ICESat, which works at a resolution as low as tens of metres, is able to detect a localised negative signal which in turn reduced the water equivalent dH/dt estimate for the region. The SMB model on the other hand has a resolution of 27 km and is unable to detect this small local signal, hence the difference in the estimates. Nonetheless the ICESat data and the SMB model are in broad agreement on a regional level and the height increase is most likely due to increased accumulation.

4.3.5.5 Site 5

The fifth case study is located in MacRobertson Land due east of the Prince Charles Mountains (Figure 4.1 and Figure 4.15, area: ~25,000 km^2). The dH/dt estimates here are predominantly positive, ranging from 0 to 0.9 m a^{-1} . The highest rates (0.6 - 0.9 m a^{-1}) are found at the centre of the site, which is made up of a combination of flat terrain and the top sections of valleys which head to the coast. Most of the rates outside of this region are lower, ranging from 0 to 0.4 m a^{-1} . The uncertainties are generally low except for along the coast where the uncertainty is often greater then the estimate (Figure 4.16). Many of these points are removed during the filtering process as can be seen in Figure 4.16b. Interestingly the uncertainties for the strong positive signal at the centre of the site are relatively small. Consequently, when the data is filtered this strong signal is still present (Figure 4.15b).

The crossover points in this region are in agreement with the along-track data. They are mostly positive and of the same magnitude as the surrounding along-track estimates. Generally, regional signals derived from crossover data are smaller, how-

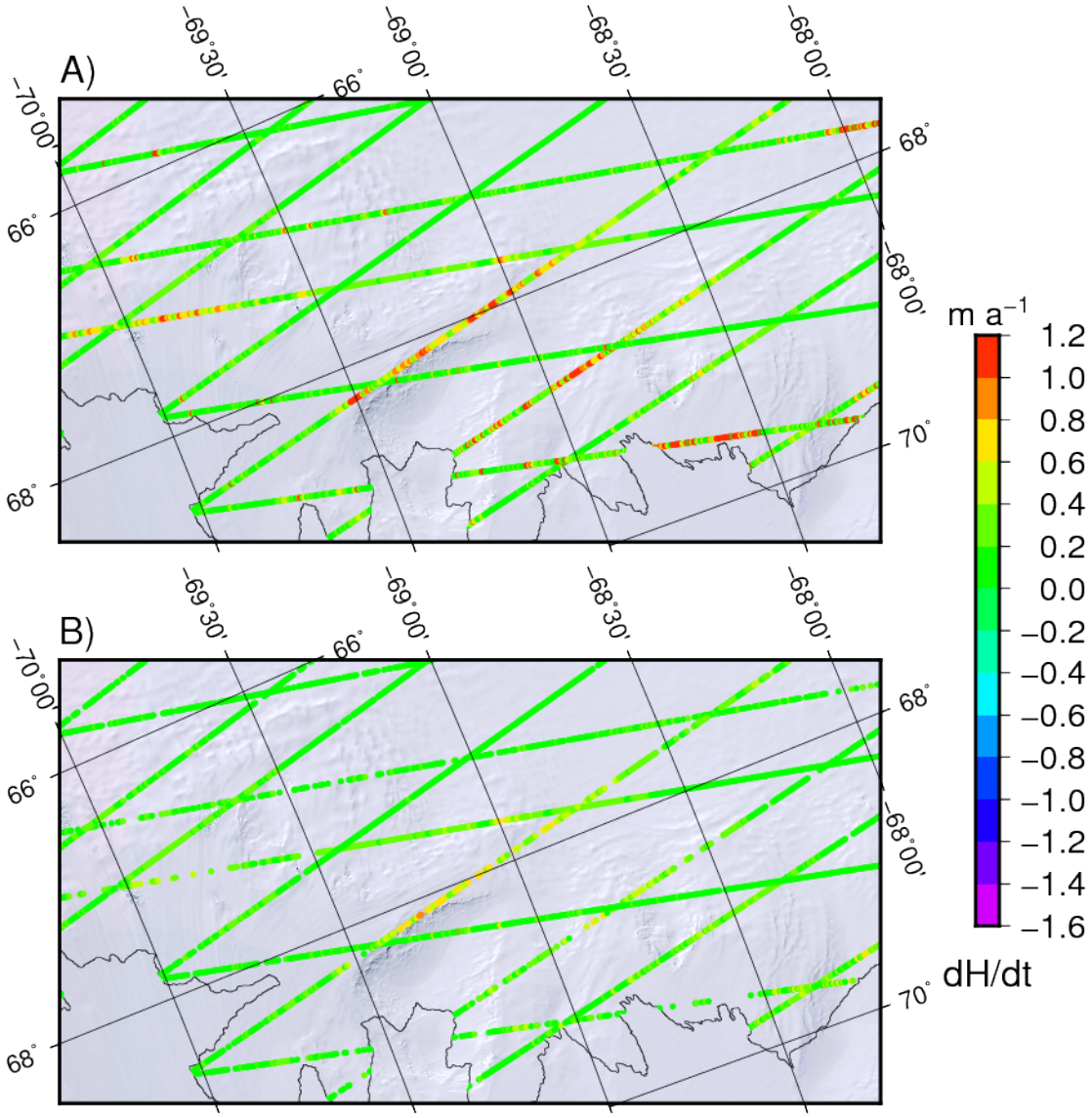

Figure 4.15: Site 5: dH/dt estimates A) unfiltered. B) filtered. The black line denotes the coastline. This site showed some large gains, which were still present after the filtering process was applied.

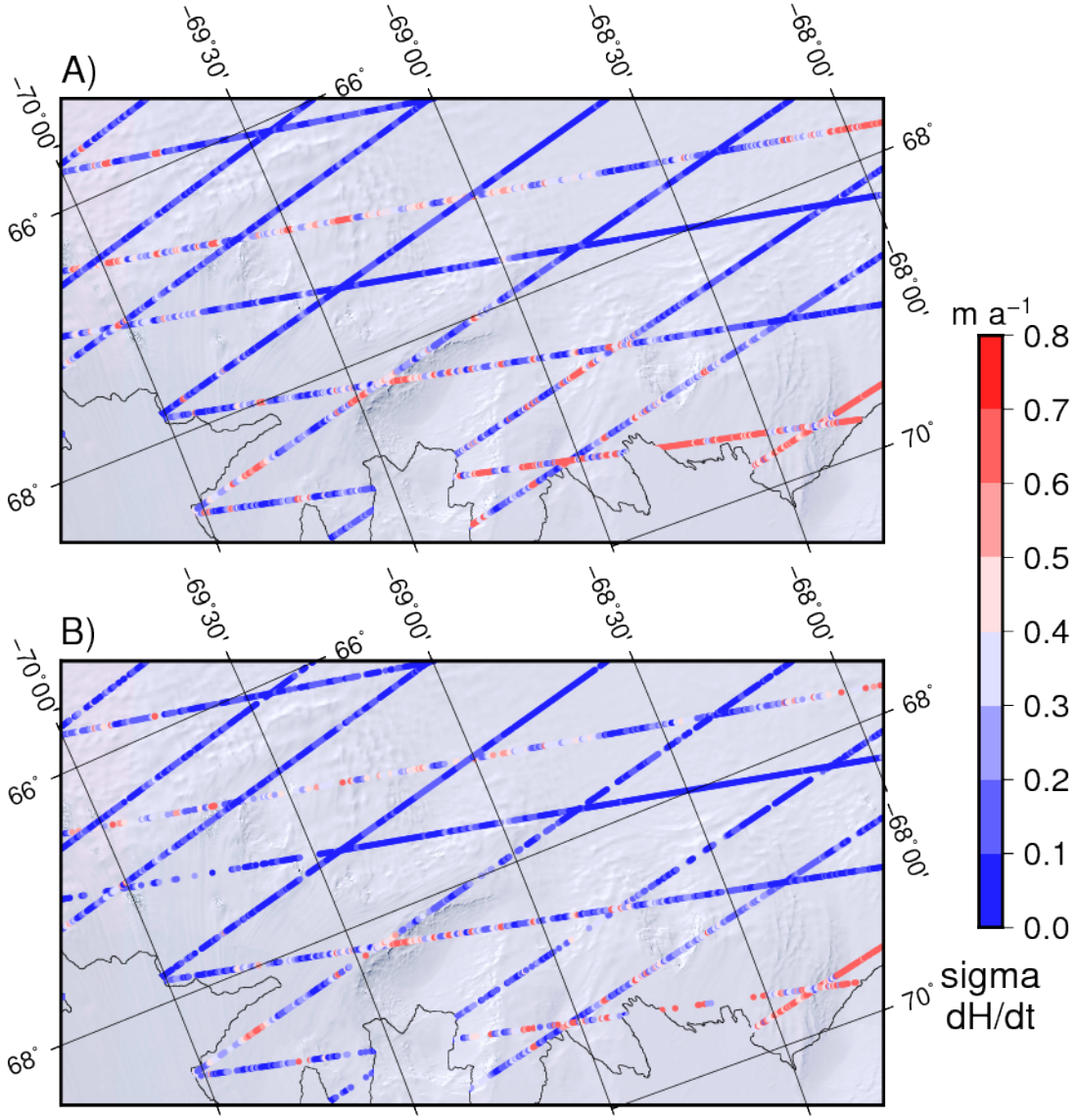

Figure 4.16: Site 5: dH/dt sigma A) unfiltered. B) filtered. The black line denotes the coastline. The filtering process removed any points near the coast with large uncertainties.

ever in this case the signal is more broadly spread (Figure 4.3). Even though this region is close to the coast and has a series of ice streams that flow into the Amery Ice Shelf, it is characterised by slow velocities, which would help in the accumulation of snow in the firn pack.

The SMB model estimates an accumulation rate in the firn layer of ~0.7 m w.e. a^{-1}, which is the highest rate estimated for all case study sites. I estimated a regional water equivalent dH/dt estimate of 0.62 ± 0.41 m w.e. a^{-1}, which is in agreement with the SMB model. This agreement is similar to that of case study site 4, in that the increased height is mostly likely due to seasonal increases in accumulation.

4.3.6 dH/dt case study: is ice height increasing in the interior?

In the previous case studies I have looked at a number of the large local rate signals that are present throughout my study site. These signals are considerably larger than the rates in the interior, as can be seen in Figures 4.3a - 4.7a, where the interior is represented as a single colour. However, if one focuses specifically on the interior, variations in the positive signal do appear, albeit of a much smaller magnitude than the coastal signals. With the previous examples I purposefully did not filter the results after Pritchard et al. (2009), to show and discuss the effect that filtering has. In the case of the interior I applied the filter as I wanted to accurately estimate the rate and its associated uncertainties, while removing outlying or erroneous data.

The region I have denoted as the "interior" is ~750000 km^2 (~1/3 of the study site, Figure 4.1) and the closest point to the coast is approximately 500 km away. Most of the region is over 1000 km from the coast. The majority of the surface slopes in this region are below 0.1 degrees and it is one of the flattest regions outside of the geographic south pole (Bamber et al., 2009) (Figure 4.21). I can therefore be confident that the region I have chosen is a good representation of the East Antarctic interior.

Previously, studies that estimated dH/dt for Antarctica generally focused on the coast and, more specifically, on West Antarctica where the greatest changes in mass

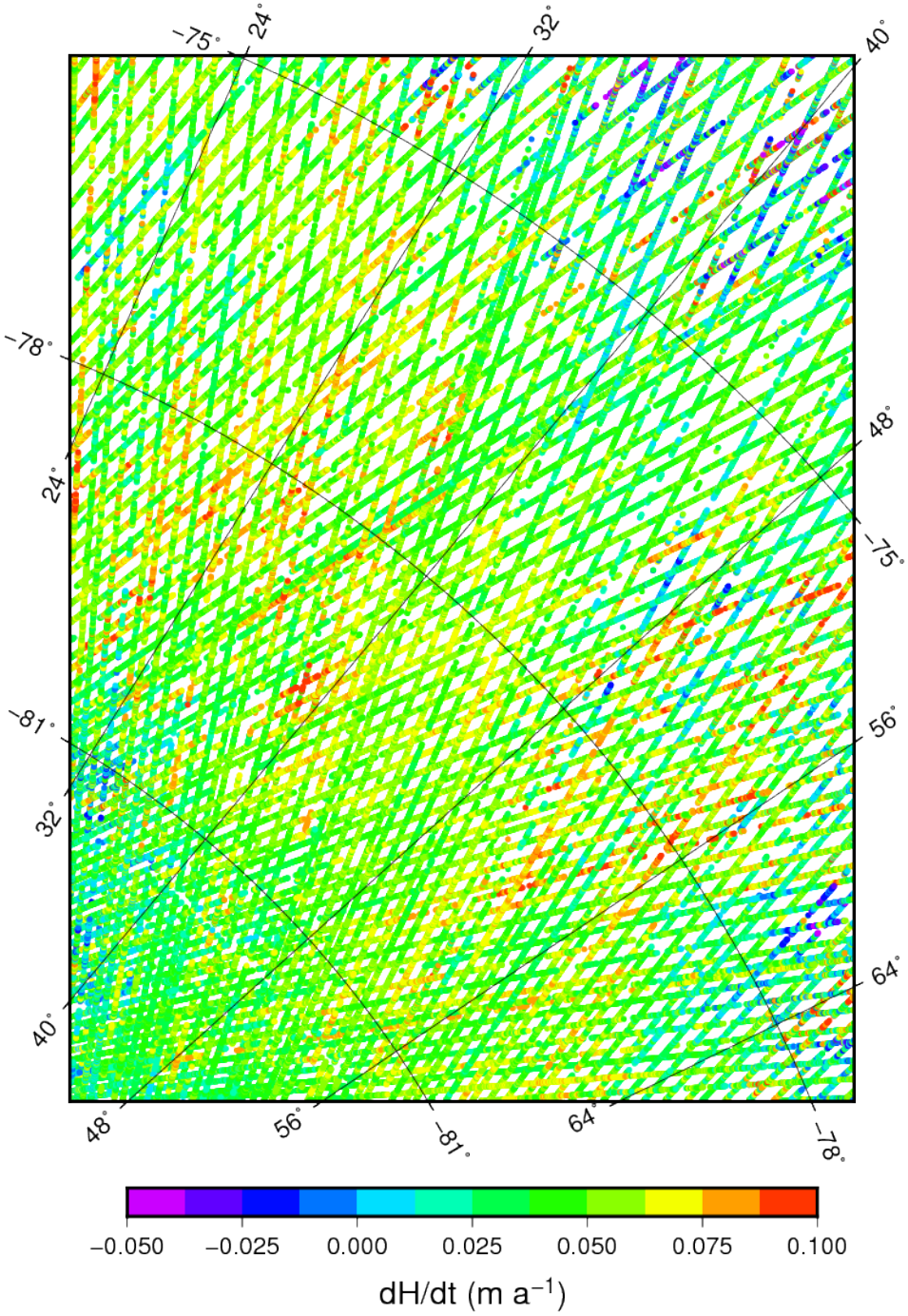

Figure 4.17: dH/dt estimated for the interior of my study site using the COMB-GFSI method. Filter applied after Pritchard et al. (2009). dH/dt estimates are generally smaller on the plateau and increase closer to the coast.

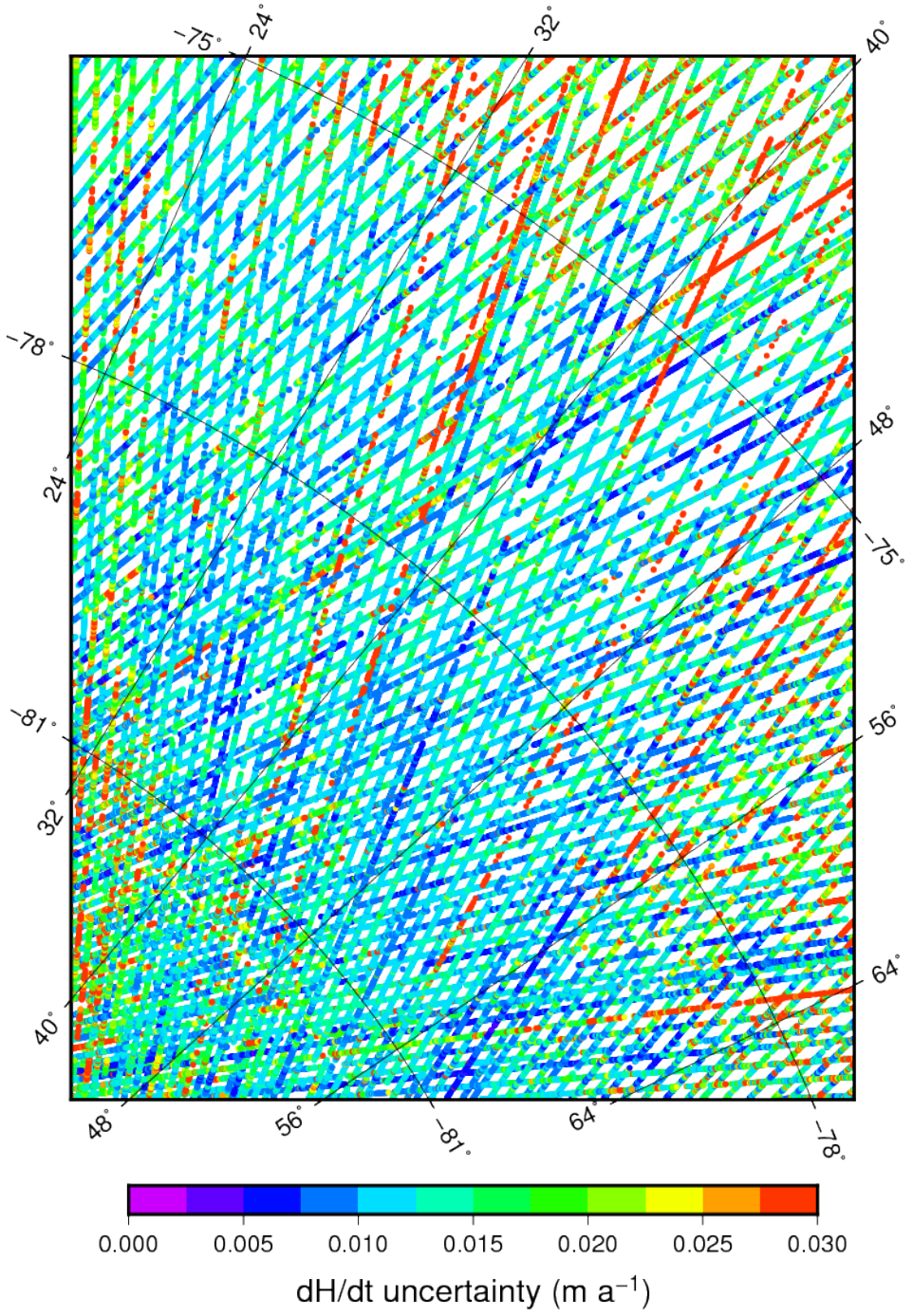

Figure 4.18: dH/dt uncertainty estimated for the interior of my study site using the COMB-GFSI. Filter applied after Pritchard et al. (2009). Some ground-tracks have larger uncertainties than close by ground-tracks. These ground-tracks have a higher than usual distance between the outermost repeat-tracks, which leads to higher uncertainties as points used in the interpolation are further away.

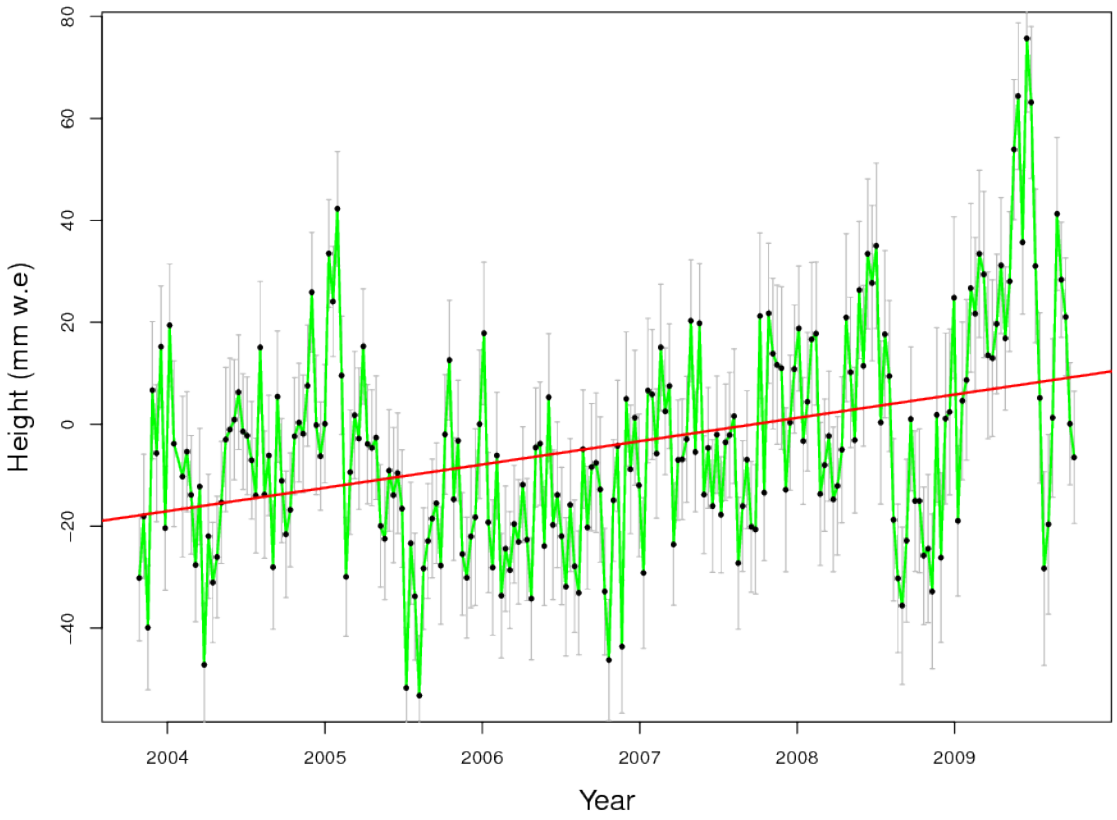

Figure 4.19: GRACE dH/dt in water equivalent mm for the region shown in Figure 4.17 over the ICESat operation period. Area: 750000 km^2, rate: 5.7 $\pm$ 0.74 mm w.e. a^{-1}. The largest increase happened in 2009 where there was a large precipitation anomaly over Dronning Maud Land and surrounds.

balance are occurring. Nonetheless it is also important to determine what is happening in the interior of East Antarctica as even small increases in height and mass over a large area can mitigate the losses in the west (Shepherd et al., 2012). Most recent regional atmospheric climate models, such as RACMO2 and RACMO2.1/ANT models predict low accumulation in the East Antarctic interior (Lenaerts et al., 2012; Shepherd et al., 2012). This is in direct contradiction to the GCMs, such as ECHAM5 and HadCM3 that predict a future increase in accumulation for the East Antarctic interior under a number of warming climate scenarios (Ligtenberg et al., 2013). Ligtenberg et al. (2013) found that, without the forcing of the RACMO2 model, the GCMs would over estimate SMB for the Antarctic interior. With the forcing in place, the SMB of the interior was expected to increase, however, at lower rates (Ligtenberg et al., 2013).

Using the COMB-GFSI method, I estimated a rate of 0.046 $\pm$ 0.022 m a^{-1} for the integrated interior. When I use the GRID-GFSI method, I obtain a rate of 0.046 $\pm$ 0.006 m a^{-1}. The distribution of these estimates can be seen in Figure 4.17. Most of the estimates range from 0.03 to 0.06 m a^{-1}, which also happen to be located in a region with the lowest surface slopes (Figure 4.21). In both cases the uncertainty is smaller than the rate estimate, so I can say with a 95% confidence level (2-sigma) that the interior is increasing in height.

The distribution of uncertainty in general follows the same pattern as that of the rate (Figure 4.18), where uncertainties are lowest in the regions with the smallest surface slopes. There are number of ground-tracks which have higher uncertainties. This is due to larger than usual distance between the outermost repeat-tracks, which leads to higher uncertainties as points used in the interpolation are further away. These points were not filtered out, as there were sufficient points to affect the mean used in the filtering process.

This positive inland signal is in general agreement with both the findings of Davis et al. (2005) who suggested that the increase in height in the interior was due to increased precipitation, and Boening et al. (2012), who found large increases in precipitation across Maud Drowning and Enderby Lands. To determine the mass

balance for the interior study site, I converted the dH/dt estimates into water equivalent (w.e.) rates using the method described earlier in Section 4.2.6. I obtained a rate of 12.2 ± 4.6 mm w.e. a^{-1} for the COMB-GFSI method and 10.9 ± 2.9 mm w.e. $a^{-1}$for the GRID-GFSI method.

Using data from the GRACE mission (Tapley et al., 2004), I calculate the rate of change of mass for that region and a rate of 5.7 ± 0.74 mm w.e. a^{-1} was obtained (Figure 4.19) (Darbeheshti et al., 2013). It should be noted that, similar to my results, the Darbeheshti et al. (2013) estimates are not corrected for GIA. The two estimates are both positive and they do fall within approximately two sigma of each other, nonetheless there is a difference. The difference in estimates may be attributed to GIA.

Whitehouse et al. (2012) compared two of their own models with the IJ05 (Ivins and James, 2005) and ICE-5G (Peltier, 2004) models. They found that for the region I am interested in, the uplift rates were slightly negative for three of the models (subsidence rate range from 0 to -2.5 mm a^{-1}). The exception being the ICE-5G model which predicts a slightly positive uplift signal (uplift between 0 and 2 mm a^{-1}).

If one assumes there is a slightly negative uplift signal and there is accumulation occurring in this region, this could account for the difference in estimates. The larger subsidence signal might be strong enough that the localised accumulation signal is overwhelmed, as the GRACE product is a low resolution product and is more susceptible to the GIA bias (Velicogna and Wahr, 2006; Sutterley et al., 2014). ICESat has a much higher resolution making it much more sensitive to such changes. For instance, for satellite altimetry there is a 1:1 relationship, in that 1 mm/yr of GIA equals 1 mm/yr height change, while for GRACE is is more like ∼3:1 ratio because the gravitational effect is larger then the uplift effect (Paul Tregoning, pers. comm., 2015).

Conversely, if one takes the positive uplift estimates from the ICE-5G model, this might be increasing both the mass and height estimates for the region and any difference between the GRACE and ICESat estimates could be due to differ-

ent instrumentation, the firn compaction model, differences in spatial footprint or processing methods used.

Nevertheless, both my estimate and the GRACE estimate are in agreement that, at least for the section of the interior I have used, the height of the ice is increasing due to accumulation.

This is in general agreement with regional atmospheric climate model simulations of Monaghan et al. (2006) (who use a combination of ice core, snow pit and snow stake data, as well as the ERA-40 model) and Lenaerts et al. (2012) (who use the RACMO2.1/ANT model). Both predicted positive accumulation rates for the interior study site region, ranging from 20 to 100 mm w.e. a^{-1} for the former and 0 to 50 mm w.e. a^{-1} for the latter. It should be noted that, although Monaghan et al. (2006) estimated positive accumulation rates for the interior study site region, they also suggest that there has been no significant change in snowfall since the 1950s for the whole of Antarctica.

4.3.7 Surface slope corrections

Using the method described in Section 4.2.5, I obtained surface slopes estimates for my study site (Figure 4.20a). Surface slopes were found to be smallest (less than 0.1 degrees) in the interior around Valkyrie Dome (or Dome Fuji) as well as due south, due north-west and directly east of the dome (Figure 4.21). The surface slopes increase from this region to the coast, where surface slopes are 1 degree or greater. Surface slopes were also found be large over rocky outcrops and mountain ranges, which is the case over the Princes Charles, Scott and Soer Rondane ranges (Figure 4.1).

I compared my surface slope estimates with those that I derived from the DEM of Bamber et al. (2009) (Figure 4.20b). Superficially they look similar, however my method tends to estimate larger surface slopes than those from the DEM. The difference in slope estimates of the two methods is presented in Figure 4.20c and the largest differences are along the coast and on rocky or mountainous terrain. In the interior the two methods are very similar, because the surface slopes here are small.

Closer to the coast, the DEM is often not in agreement with my crossover surface slope estimate. In such cases, I used the crossover estimate, which is generally steeper than its DEM counterpart. The creation of the Bamber et al. (2009) DEM required a number of filtering steps that may have had a moderating effect on the height estimates (Bamber et al., 2009).

Figure 4.23 shows the estimated uncertainty of the surface slope, as computed 100 metres away from the central position of the ground-track. In most cases, the repeat-tracks are closer than this distance. Consequently, this value is an upper bound of the maximum likely uncertainty. I chose to err on the side of caution, preferring to over-estimate the uncertainty than to under-estimate it. Surface slope uncertainties are generally smaller in the interior and larger along the coastline (Figures 4.22 & 4.23).

4.3.8 dM/dt estimates and associated uncertainties

Using the method described in Section 4.2.6, I calculated the dM/dt for four of the drainage basins (basins 6, 7, 8 and 9) using the COMB-GFSI and COMB-NNI interpolation methods (Table 4.3). I compared these results to those of Sasgen et al. (2013) and King et al. (2012), being the most recent studies to estimate dM/dt for separate drainage basin divides. Some of the Sasgen et al. (2013) drainage basin divides differ from those of Zwally et al. (2012), which I have used so far. The boundaries of the basins that I will compare are very similar, so direct comparisons are appropriate. I do not correct my estimates for GIA and therefore I am comparing my results with the uncorrected Sasgen et al. (2013) and King et al. (2012) results. I chose not to compare my results with those of Sasgen et al. (2013) and King et al. (2012) for the other basins as they are only partially in my study site and therefore do not lend themselves well to direct comparisons. In the case of basin 6, 83% of the basin is within my study site, so I compare values for this basin.

There is general agreement in the sign of each of the basins, however, my estimate of the overall dM/dt for all basins is smaller (Table 4.3). This difference is not statistically significant from the studies' estimates (this study, King et al. (2012)

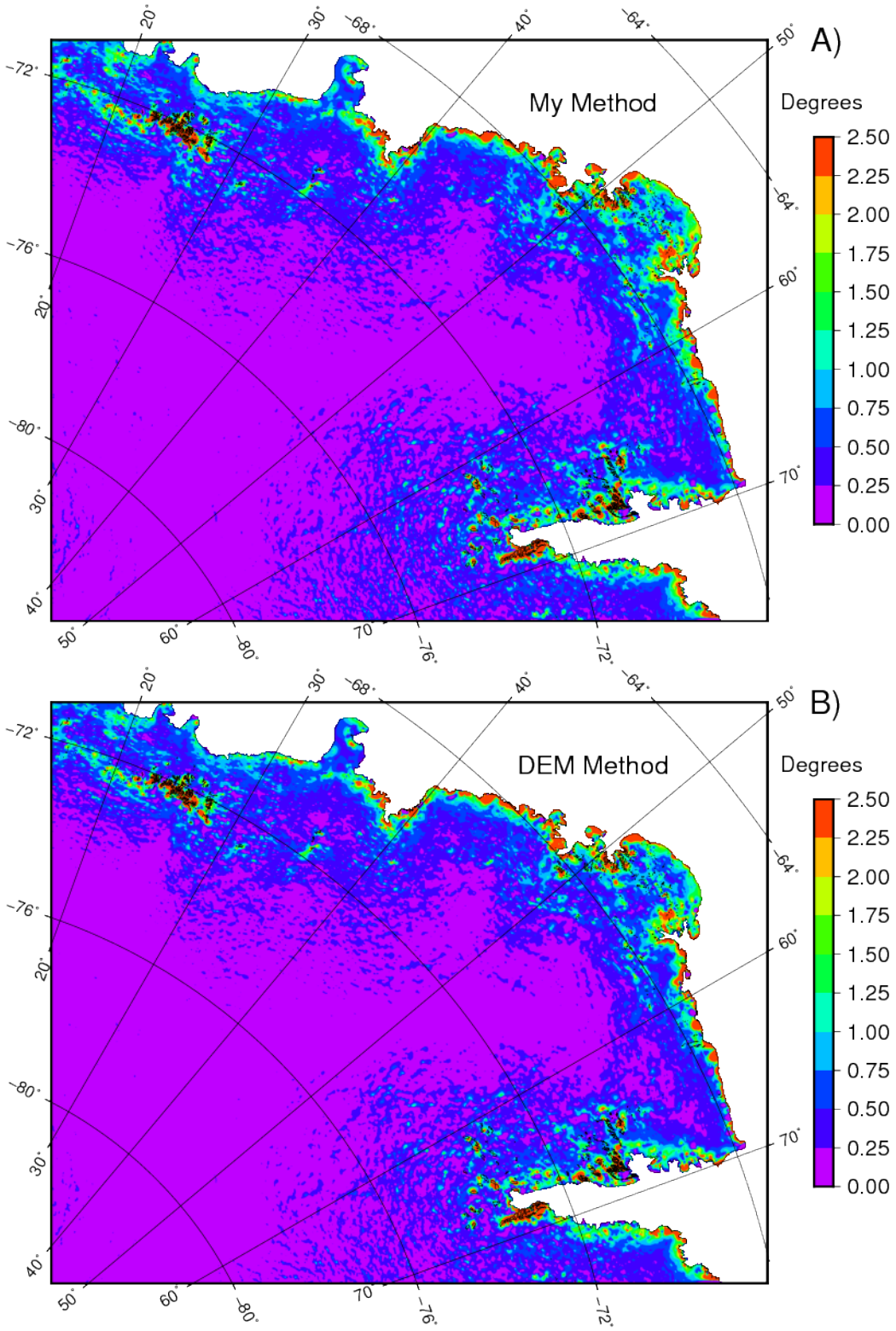
A)
My Method
Degrees
2.50
2.25
2.00
1.75
1.50
1.25
1.00
0.75
0.50
0.25
0.00
B)
DEM Method
Degrees
2.50
2.25
2.00
1.75
1.50
1.25
1.00
0.75
0.50
0.25
0.00

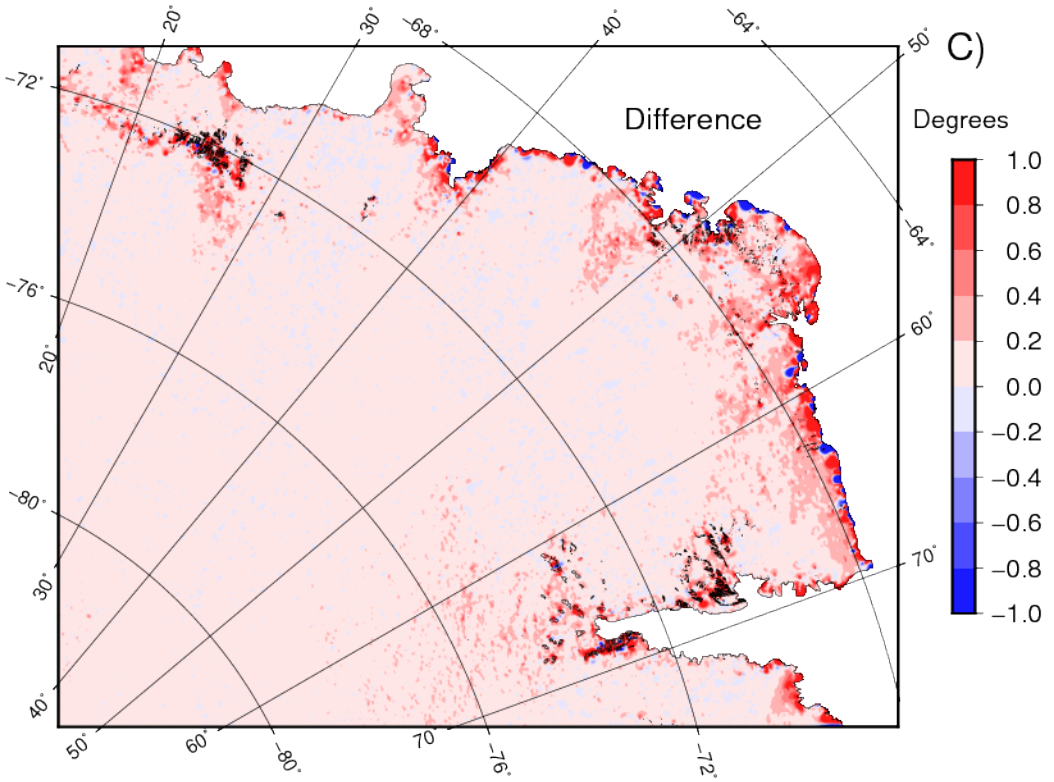

Figure 4.20: A) Surface slope magnitude estimates using a combination of surface slopes derived from the COMB-GFSI. Surface slopes are smallest in the interior around Valkyrie Dome and increase closer to the coastline. Surface slopes are also higher near rocky outcrops and mountain ranges. B) Surface slope estimates derived from the Bamber et al. (2009) DEM. All slope estimates are positive as the value shown is the magnitude. For plotting purpose the direction of the slope is not shown, however it is taken into account when the difference was calculated. The distribution of surface slope is similar to the combined method, however the surface slopes tend to be smaller overall. C) The difference in surface slope between the combined and DEM method. Positive values denote that this studies method estimates higher slopes then the DEM method and visa-versa for the negative values. The largest differences occur near the coast and on rocky/mountainous terrain.

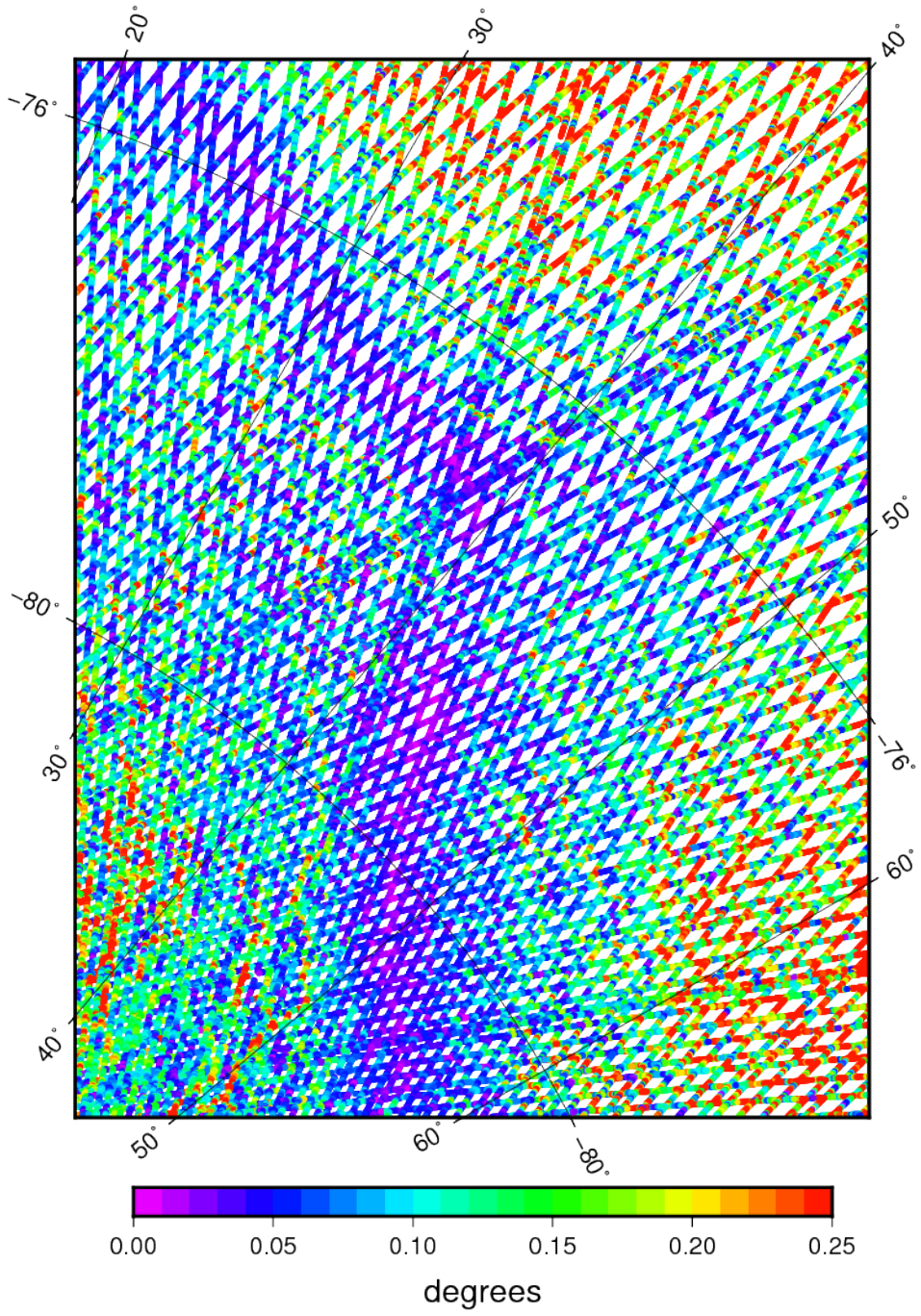

Figure 4.21: Surface slope estimates in the interior of the study site. Surface slopes are smallest on the plateau ranging from 0 - 0.25 degrees increasing towards the coastline and mountainous regions. All slope estimates are positive as the value shown is the magnitude. For plotting purpose the direction of the slope is not shown.

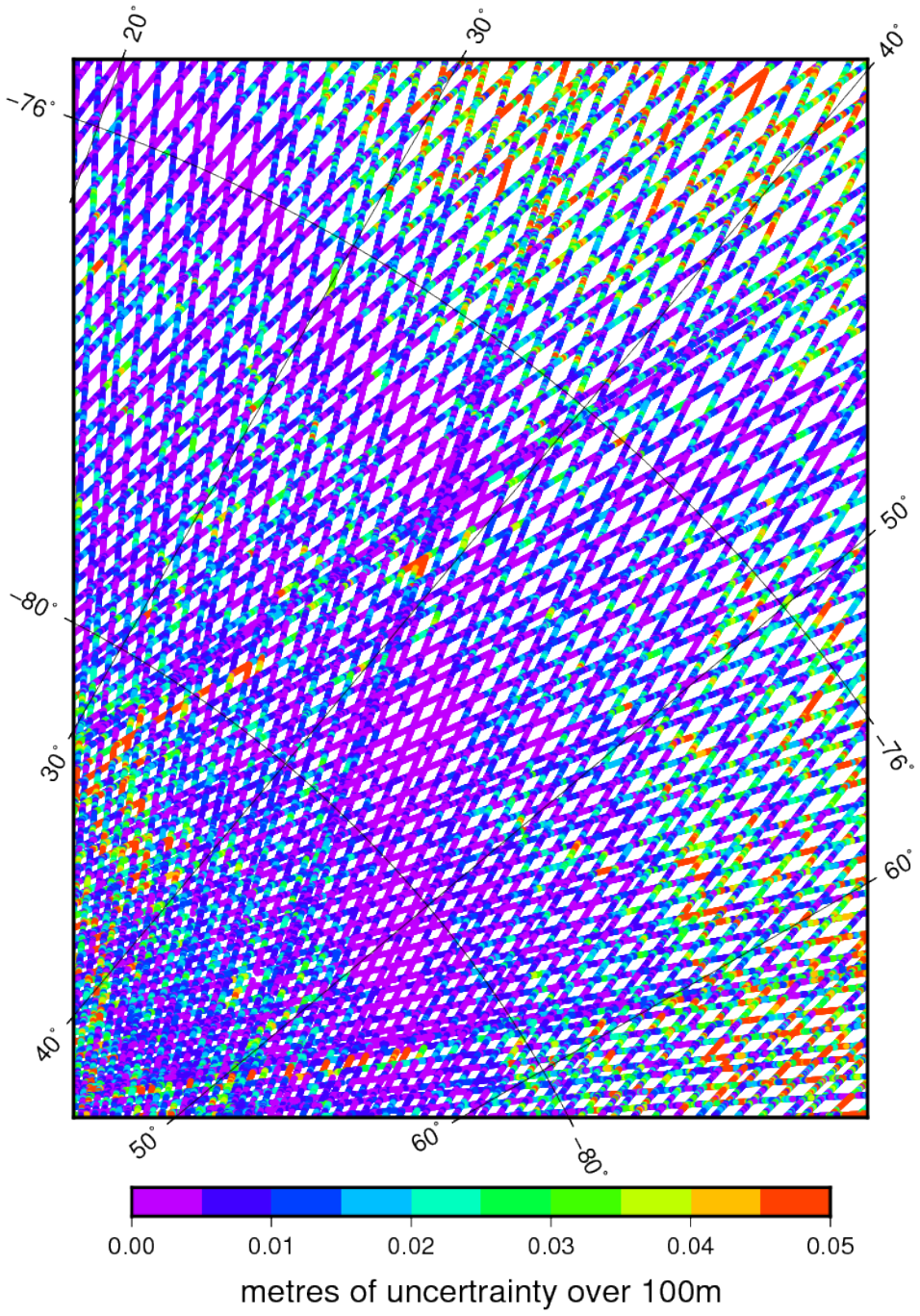

Figure 4.22: The height uncertainty introduced over 100 m because of surface slope uncertainty, in the interior of the study site. The surface slope uncertainty is calculated over 100 m, from the centre of all the repeat ground-tracks. Uncertainties are lowest on the plateau ranging from 0 to 0.02 m over 100 m, up to 0.05 m closer to the coast.

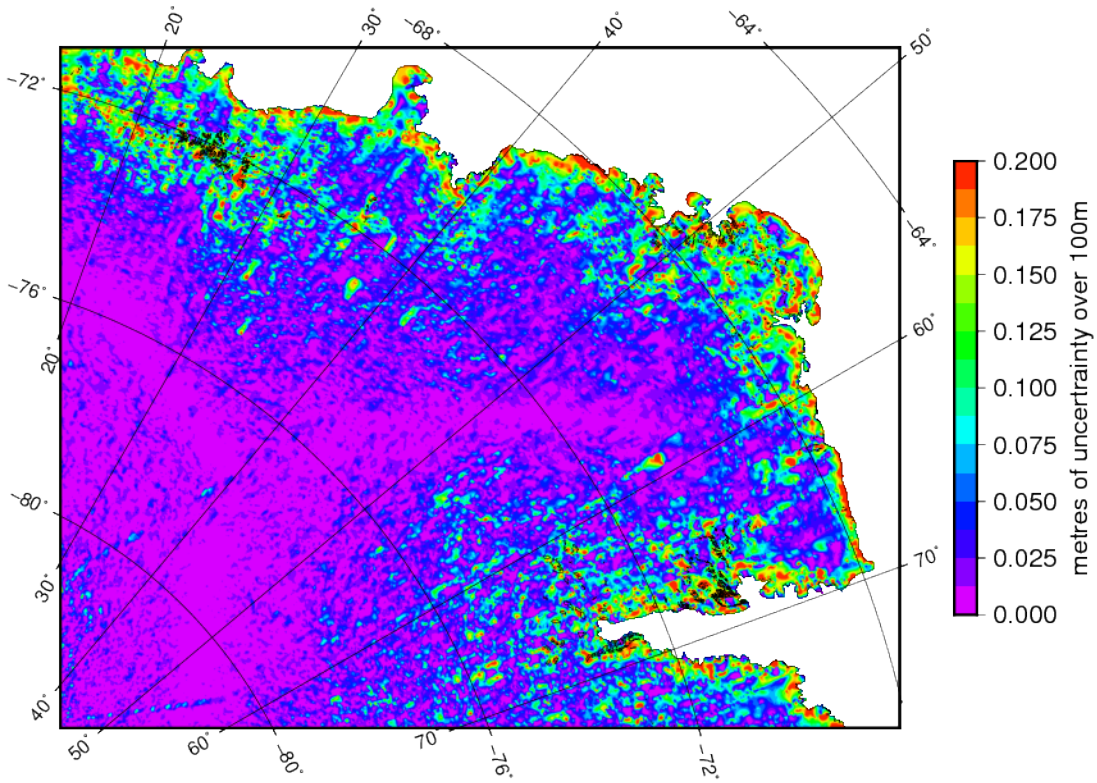

Figure 4.23: The height uncertainty introduced over 100 m because of surface slope uncertainty, from the centre of the all the repeat ground-tracks using my method.

and Sasgen et al. (2013)) being within approximately 1- to 2-sigma of each other (My estimate: 29.12 ± 3.91 Gt a^{-1}, King et al. (2012) estimate: 35.67 ± N/A Gt a^{-1} and Sasgen et al. (2013) estimate: 35.31 ± 7.78 Gt a^{-1}). On a drainage basin level the differences are more pronounced. The King et al. (2012) and Sasgen et al. (2013) dM/dt basin rates are generally larger than my dM/dt results. The exceptions are basin 8 and 9 where, for the former, my estimate is larger than the King et al. (2012) estimate and for the latter, my estimate is larger than the Sasgen et al. (2013) estimate (Table 4.3).

A possible reason why the GRACE mass rates are higher than my dM/dt estimates is the temporal range of the datasets. GRACE is currently still operational, while ICESat stopped collecting data in late 2009. Between mid 2009 and 2011, large accumulation anomalies occurred across much of coastal Maud Dronning and Enderby Lands (Shepherd et al., 2012; Sasgen et al., 2013). This was not observed by ICESat as it was no longer operational and it is therefore not surprising that my rates are lower than those recently derived from GRACE data.

Furthermore, the uncertainties estimated by this study are smaller than those of

Table 4.3: dM/dt results (along-track and crossover combined) for study site, using both the COMB-GFSI and COMB-NNI. Drainage basins by Sasgen et al. (2013). Drainage basins with * denote full coverage, while other basins only have partial data coverage. Note no uncertainties are provided in the King et al., 2012 study.

drainage basin	Modified Sasgen et al., 2013 Results (Gt a^{-1})		Modified King et al., 2012 Results (Gt a^{-1})	
	mean dM/dt	mean sigma	mean dM/dt	mean sigma
6	4.17	2.21	6.67	N/A
7*	17.00	2.00	18	N/A
8*	12.00	3.00	5	N/A
9*	2.14	0.57	6	N/A
All basins	35.31	7.78	35.67	N/A

drainage basin	Green's function spline interpolation (Gt a^{-1})		Nearest neighbour interpolation (Gt a^{-1})	
	mean dM/dt	mean sigma	mean dM/dt	mean sigma
6	3.71	1.77	2.50	1.79
7*	12.17	1.32	11.97	1.42
8*	8.23	0.47	7.82	0.50
9*	5.01	0.35	5.10	0.53
All basins	29.12	3.91	27.39	4.24

Sasgen et al. (2013). As the datasets and methodologies used were very different it is difficult to say exactly the reason for this. One large difference is the resolution of the two datasets which, given that the dM/dt are estimated on a basin level, may lead to higher uncertainties for the lower resolution GRACE data.

4.4 Summary and Conclusions

In this chapter I demonstrated that my crossover and along-track methods are able to obtain statistically significant results across much of the study site. It is clear that much of Enderby, Kemp, MacRobertson & Dronning Maud Lands are gaining height and mass. This can be attributed to the large positive anomalies which occurred along the coast of Maud Dronning and Enderby lands during 2005, 2007

and most strongly in 2009 (Shepherd et al., 2012; Sasgen et al., 2013). My results were in general agreement with the findings of Pritchard et al. (2009), who estimated height changes for the basins in my study site. The uncertainties I obtained were smaller than those of Pritchard et al. (2009), due to the different uncertainty contributors that are included in our respective uncertainty budgets. I obtained a mean uncertainty of 0.027 m a^{-1} for the whole study site, while Pritchard et al. (2009) estimated their "detection threshold" by combining a 0.07 m a^{-1} measurement uncertainty and the variability in height due to accumulation variation. The uncertainties due to interpolation and surface slope are smaller in comparison, however they are not insignificant and future studies should also include interpolation and slope uncertainties in total error budgets.

I found that the interior of my study site is gaining height at 12.2 ± 4.6 mm w.e. a^{-1}. This is in general agreement with regional atmospheric climate model simulations of Monaghan et al. (2006) and Lenaerts et al. (2012), who both predicted positive accumulation rates for the interior of the study site region. Although my results show that ice height is increasing in the interior, the GIA signal, regardless of the model used, is not sufficient to account for the increase in height, suggesting precipitation is the cause of this increase. There is some doubt over this assessment, as a combination of the uncertainties I obtained from interpolation and surface slope as well as the residual pointing and forward scattering errors, would lead to a statistically insignificant dH/dt estimate for the interior.

Nevertheless, I believe that for my study site, the interior is gaining mass due to accumulation and the GRACE results also confirm this, as the GRACE rate of 5.7 ± 0.74 mm w.e. a^{-1} is also larger than any GIA uplift or subsidence. The accumulation, however, is not increasing to the extent that might be expected by some global climate models for a warming climate, where the greater moisture-holding capacity of warmer air would offset losses along the margins of the ice sheets (Monaghan et al., 2006).

Chapter 5

Conclusions

The dH/dt estimates and uncertainties obtained using both the along-track and crossover data show that the choice of data geometry can have a substantial effect on the final results. For instance, the crossover method generally has estimates with lower uncertainties (0.04 ± 0.036 m a^{-1} for the whole study site, 0.046 ± 0.006 m a^{-1} for the interior) when applied to actual ICESat data, as seen in Chapter 4. I obtained similar mean uncertainty of 0.017 m a^{-1} for crossovers in my simulation study (Chapter 3).

This can be attributed to a number of factors. Firstly, the data density (both temporally and spatially) is always highest around crossovers, as this is the intersection between two repeat ground tracks. Consequently, there are more data points available for the interpolation step, which generally decreases the uncertainty of the height estimate and helps to constrain the rate estimate. Secondly, cross-track surface slope ambiguity is eliminated when the crossover geometry is such that the ascending and descending grounds tracks are not nearly parallel (Gunter et al., 2009).

Lastly, because the ICESat satellite is in a near polar orbit, the majority of crossovers occur in the interior of Antarctica closest to the geographic south pole. The density of crossovers decreases as the distance from the coast decreases. This relationship means that more points will be sampled in the interior than near the coast.

As most of the height change is occurring along the coastline, proportionally

fewer coastal rates will be estimated, in comparison to the more numerous inland rates. Lastly, as the interior is characterised with having lower slopes, these estimates will be more accurate. Consequently, when a mean rate is obtained, using uncertainties as a weighting, it will be skewed towards the inland estimates with a smaller uncertainty.

The upside of this is that more accurate dH/dt estimates are obtained in the interior. The downside is that less rates are estimated near the coast, which is where most of the change is occurring. In the worst case a regional signal near the coast may be incorrectly estimated or not estimated at all, due to the low density of crossovers. This is the case with site 4 (Section 4.3.5.4) where the rate estimated from a single crossover was slightly positive, while most of the along-track rates were negative. Consequently, the crossover analysis method was insensitive to this signal.

In order to calculate dV/dt, a dH/dt surface must be estimated from which the volume change can be determined. This conversion requires a further interpolation step, where dH/dt estimates are essentially extrapolated to regions where there are no height change estimates. This is problematic when using only crossovers, as the distance between them can be substantial, especially near the coast. Even though the crossover uncertainties are low, interpolating over these large distances negates the higher accuracy at the crossovers.

Consequently, crossover methods have fallen out of favour in recent years, in preference to along-track methods (Howat et al., 2008; Slobbe et al., 2008; Pritchard et al., 2009; Smith et al., 2009; Moholdt et al., 2010; Sørensen et al., 2011; Zwally et al., 2011a; Ewert et al., 2012, etc.). However they are still more accurate and Moholdt et al. (2010) states that they are extremely important in validating along-track height estimates and rates. Furthermore, my novel method takes advantage of the high accuracy and unique geometry of the crossover to independently estimate surface slope (see Section 3.2.2 for details) and remove surface slope bias from along-track rate estimates. This has not been attempted before and shows the enduring importance of crossover analysis methods.

Conversely, the along-track method uses all available data, leading to a much

higher spatial coverage. This is of great importance along the coast, where crossovers are rare. The disadvantage of this is that uncertainties are greater, and I estimated a dH/dt of 0.04 $\pm$ 0.036 m a^{-1} for the whole site using actual ICESat data (Chapter 4). Using simulated data I obtained an uncertainty of 0.083 m $a^{-1}$for the whole site (Chapter 3). I found that the uncertainties for the along-track method were generally an order of magnitude larger than the crossover estimates, for both the actual and simulated data.

These higher uncertainties are again due to a series of factors. Firstly, there is less data available temporally, and so estimates are less well constrained than at crossovers. This problem can be observed for all the case studies in Section 4.3.5 where due to the close proximity to the coast, large uncertainties are often obtained. Coastal regions generally have higher cloud cover, preventing laser pulses from reaching the ice surface, which in turn decreases the temporal resolution of ICESat over these areas.

Secondly, as the repeat ground track diverges from previous ground tracks, a surface slope bias is introduced if there is a slope perpendicular to the tracks. In this case any rate of change estimated using these diverging ground tracks must be corrected for surface slope. I have spoken about this correction in length in Chapter 3, and its impact on dH/dt estimates. As the "true" surface slope is not known it must be estimated which brings with it a level of uncertainty. This contributes to the overall increase in the along-track uncertainty budget, especially along the coast where surface slopes are greatest. Both methods have advantages and disadvantages and it is clear that, for the best results, a combination of both methods should be used.

Both the crossover and along-track method are reliant on interpolation, as ICESat height measurements vary spatially. Therefore, it is also important to determine whether the interpolation method affects the overall estimate and uncertainty. I have gone into much detail about this topic in my simulation study (Chapter 3) and found that the results using real ICESat data mirror the simulation results. The Green's function spline interpolation has the greatest accuracy and the lowest uncertain-

ties when using either the crossover or along-track method. Furthermore, the other interpolation methods, nearest neighbour interpolation or Delaunay triangulation with linear interpolation, were found to not only have larger uncertainties, but also present significantly different dH/dt estimates. This result highlights the need to test one's method with a variety of interpolation algorithms, to better understand the effect that they have on the final dH/dt or dM/dt result.

With these findings in mind, I looked at the actual results for my study site. I found that overall the region was gaining height, which was in good agreement with past studies, specifically Pritchard et al. (2009). My dH/dt results were with approximately 1-sigma of the Pritchard et al. (2009) estimates. In their study, they did not estimate uncertainty directly, whereas I obtained associated uncertainties for my estimates which were an order of magnitude smaller than their "detection threshold" estimates. Pritchard et al. (2009) include a 0.07 m a^{-1} measurement uncertainty and the variability in height due to accumulation variation (SMB). Consequently future studies should include uncertainties due to interpolation, surface slope and instrument bias.

The fact that the differences in the rates are so small, even though Pritchard et al. (2009) used nearly two years less data, is evidence that the positive anomalous precipitation events which occurred in 2005, 2007 and 2009 have kept the regional dH/dt relatively constant from 2003 to 2009. If these increases continue it would in part help in the mitigation of losses which are occurring in other parts of East and West Antarctica. In contrast, both my results and those of Pritchard et al. (2009) show that in areas where ice velocities are high (i.e. ice streams and glacial outlets), local ice height loss is occurring and, if the velocities were to increase, this could have a dampening effect on the positive regional signal (Rignot et al., 2008).

Currently, the largest regional rate signals were found along the coast as seen in Section 4.3. The larger positive signals were generally found in regions with low ice velocity (Table 4.1 and Section 4.3.5 for case studies), which Pritchard et al. (2009) also observed. Increases in the height of the firn column for these regions were generally attributable to increased seasonal precipitation, which led to higher SMB

estimates (Lenaerts et al., 2012). The large negative signals were found in areas with both high and low ice velocities (Table 4.1 and Section 4.3.5 for case studies). In the case of site 1, the SMB estimate was close to zero, suggesting that the losses in this region could be attributed to ice flow dynamics. Conversely, site 3, had a positive SMB, however the overall rate for the region was negative. This indicates that the height loss was occurring in the firn column and was due to ablation rather than ice flow dynamics.

All these case studies show that, even for a smaller section of East Antarctica, there are many different factors affecting the loss or gain of height along the coast. Although all these signals were large in magnitude, they were local in their distribution and consequently they only have a small impact on the overall signal of the study. Interestingly, it is the numerous smaller positive inland rates which shape the study site signal. This is also the case on a drainage basin level where, even though there were negative signals present along the coast, the mean rate was mostly positive (Table 4.1 & Figure 4.3).

There has been some debate in the scientific community about whether there has been an increase in precipitation in East Antarctica and whether it has led to an increase in the ice height in the interior (Davis et al., 2005; Monaghan et al., 2006; Boening et al., 2012). I investigated this for my study site in Section 4.3.6 and found that, at least for this region, the interior was gaining height and, importantly, the uncertainties were lower than the estimates. I converted estimates into water equivalent dH/dts and compared them to the GRACE estimates over the same region. The mean rate estimates derived from the ICESat and GRACE datasets were both positive (ICESat combined method: 12.2 ± 4.6 mm w.e. a^{-1}, GRACE: 5.7 ± 0.73 mm w.e. a^{-1}). The estimates were significantly different (2-sigma).

As these rate estimates in the interior are generally small, it could be argued that they are a consequence of GIA uplift. Whitehouse et al. (2012) assessed a number of GIA models for my region and, for most of the Antarctica interior, found a small GIA subsidence. The exception is the ICE-5G model which predicts a GIA uplift for my region. In either case, the GIA signal is smaller than either the ICESat

or GRACE rate estimates, which suggests that the positive rates are due to either accumulation. The rates obtained are similar to those predicted by the regional atmospheric climate model simulations of Monaghan et al. (2006) and Lenaerts et al. (2012).

Lastly, I converted my dH/dt rates into dM/dt rates using the method described in Section 4.3.8 and compared them to the GRACE derived dM/dt estimates from Sasgen et al. (2013) study. I found general agreement between the results (My estimate: 29.12 $\pm$ 3.91 Gt a^{-1}, King et al. (2012) estimate: 35.67 $\pm$ N/A Gt a^{-1} and Sasgen et al. (2013) estimate: 35.31 $\pm$ 7.78 Gt a^{-1}). My estimate was smaller, which was most likely due to the different in the temporal range between the two satellite datasets. As the ICESat mission ended in late 2009, it missed observing the increased accumulation which occurred in subsequent years. Nonetheless, all three studies are in agreement that ice mass for the study site is increasing significantly. These results give me confidence that my methods are sensitive to both local and larger regional ice height/mass changes, while improving our understanding of how interpolation and surface slope bias contribute to the uncertainty budget of those estimates.

Bibliography

Abshire, J. B., Sun, X., Riris, H., Sirota, J. M., McGarry, J. F., Palm, S., Yi, D., and Liiva, P. (2005). Geoscience Laser Altimeter System (GLAS) on the ICE-Sat Mission: On-orbit measurement performance. *Geophysical Research Letters*, 32(L21S02).

Alley, R. B., Clark, P. U., Huybrechts, P., and Joughin, I. (2005). Ice-Sheet and Sea-Level Changes. *Science*, 310(5747):456–460.

Allison, I., Alley, R., Fricker, H., Thomas, R., Warner, R., et al. (2009). Ice sheet mass balance and sea level. *Antarctic Science*, 21(5):413.

Arthern, R. J., Winebrenner, D. P., and Vaughan, D. G. (2006). Antarctic snow accumulation mapped using polarization of 4.3-cm wavelength microwave emission. *Journal of Geophysical Research: Atmospheres (1984–2012)*, 111(D06107).

Bamber, J., Gomez-Dans, J., and Griggs, J. (2009). A new 1 km digital elevation model of the Antarctic derived from combined satellite radar and laser data–part 1: Data and methods. *The Cryosphere*, 3(1):101–111.

Bamber, J. and Gomez-Dans, J. L. (2005). The accuracy of digital elevation models of the Antarctic continent. *Earth and Planetary Science Letters*, 237(3):516–523.

Bamber, J., Griggs, J., Hurkmans, R., Dowdeswell, J., Gogineni, S., Howat, I., Mouginot, J., Paden, J., Palmer, S., Rignot, E., et al. (2013). A new bed elevation dataset for Greenland. *The Cryosphere*, 7(2):499–510.

Bamber, J. L., Layberry, R. L., and Gogineni, S. (2001). A new ice thickness and

bed data set for the Greenland ice sheet 1. Measurement, data reduction, and errors. *Journal of Geophysical Research*, 106(D24):33773–33.

Bamber, J. L. and Payne, A. J. (2004). *Mass Balance of the Cryosphere*. Cambridge University Press Cambridge, UK.

Boening, C., Lebsock, M., Landerer, F., and Stephens, G. (2012). Snowfall-driven mass change on the East Antarctic ice sheet. *Geophysical Research Letters*, 39(L21501).

Borsa, A., Moholdt, G., Fricker, H., and Brunt, K. (2013). A range correction for ICESat and its potential impact on ice sheet mass balance studies. *The Cryosphere*, 7:4287–4319.

Brenner, A. C., DiMarzio, J. P., and Zwally, H. J. (2007). Precision and accuracy of satellite radar and laser altimeter data over the continental ice sheets. *Geoscience and Remote Sensing, IEEE Transactions on*, 45(2):321–331.

Burrough, P. A. (1986). *Principles of geographical information systems for land resources assessment*. Taylor & Francis.

Chen, J., Wilson, C., Blankenship, D., and Tapley, B. (2006). Antarctic mass rates from GRACE. *Geophysical Research Letters*, 33(L11502).

Church, J., Gregory, J., Huybrechts, P., Kuhn, M., Lambeck, K., Nhuan, M., Qin, D., and Woodworth, P. (2001). Changes in sea level. *, in: JT Houghton, Y. Ding, DJ Griggs, M. Noguer, PJ van der Linden, X. Dai, K. Maskell, and CA Johnson (eds.): Climate Change 2001: The Scientific Basis: Contribution of Working Group I to the Third Assessment Report of the Intergovernmental Panel*, pages 639–694.

Church, J. A. and White, N. J. (2006). A 20th century acceleration in global sea-level rise. *Geophysical Research Letters*, 33(L01602).

Church, J. A. and White, N. J. (2011). Sea-level rise from the late 19th to the early 21st century. *Surveys in Geophysics*, 32(4-5):585–602.

Church, J. A., White, N. J., Konikow, L. F., Domingues, C. M., Cogley, J. G., Rignot, E., Gregory, J. M., van den Broeke, M. R., Monaghan, A. J., and Velicogna, I. (2011). Revisiting the Earth's sea-level and energy budgets from 1961 to 2008. *Geophysical Research Letters*, 38(L18601).

Clark, I. and Harper, W. V. (2000). *Practical Geostatistics 2000*. Ecosse North America Columbus.

Cressie, N. (1992). Statistics for Spatial Data. *Terra Nova*, 4(5):613–617.

Csatho, B., Ahn, Y., Yoon, T., van der Veen, C., Vogel, S., Hamilton, G., Morse, D., Smith, B., and Spikes, V. (2005). ICESat measurements reveal complex pattern of elevation changes on Siple Coast ice streams, Antarctica. *Geophysical Research Letters*, 32(L23S04).

Darbeheshti, N., Zhou, L., Tregoning, P., McClusky, S., and Purcell, A. (2013). The ANU GRACE visualisation web portal. *Computers & Geosciences*, 52:227–233.

Davis, C. H., Li, Y., McConnell, J. R., Frey, M. M., and Hanna, E. (2005). Snowfall-driven growth in East Antarctic ice sheet mitigates recent sea-level rise. *Science*, 308(5730):1898–1901.

Davis, C. H. and Moore, R. K. (1993). A combined surface-and volume-scattering model for ice-sheet radar altimetry. *Journal of Glaciology*, 39:675–686.

De Berg, M., Cheong, O., van Kreveld, M., and Overmars, M. (2008). *Computational Geometry*. Springer.

Denton, G. H. and Hughes, T. J. (2002). Reconstructing the Antarctic ice sheet at the Last Glacial Maximum. *Quaternary Science Reviews*, 21(1):193–202.

DiMarzio, J., Brenner, A., Schutz, R., Shuman, C., and Zwally, H. (2007a). Glas/icesat 1 km laser altimetry digital elevation model of Greenland. *Digital media, National Snow and Ice Data Center, Boulder, CO*.

DiMarzio, J., Brenner, A., Schutz, R., Shuman, C., and Zwally, H. (2007b). GLAS/ICESat 500 m laser altimetry digital elevation model of Antarctica. *Boulder, Colorado USA: National Snow and Ice Data Center. Digital media.*

Ewert, H., Groh, A., and Dietrich, R. (2012). Volume and mass changes of the Greenland ice sheet inferred from ICESat and GRACE. *Journal of Geodynamics*, 59:111–123.

Fairbanks, R. G. (1989). A 17,000-year glacio-eustatic sea level record: influence of glacial melting rates on the Younger Dryas event and deep-ocean circulation. *Nature*, 342(6250):637–642.

Flament, T. and Rémy, F. (2012). Dynamic thinning of Antarctic glaciers from along-track repeat radar altimetry. *Journal of Glaciology*, 58(211):830–840.

Forsberg, R., Keller, K., Nielsen, C., Gundestrup, N., Tscherning, C. C., Madsen, S. N., and Dall, J. (2000). Elevation change measurements of the Greenland Ice Sheet. *Earth, Planets and Space*, 52(11):1049–1053.

Fortune, S. (1987). A sweepline algorithm for Voronoi diagrams. *Algorithmica*, 2(1-4):153–174.

Fretwell, P., Pritchard, H. D., Vaughan, D. G., Bamber, J., Barrand, N., Bell, R., Bianchi, C., Bingham, R., Blankenship, D., Casassa, G., et al. (2013). Bedmap2: improved ice bed, surface and thickness datasets for Antarctica. *The Cryosphere*, 7(1):375–393.

Fricker, H., Borsa, A., Minster, B., Carabajal, C., Quinn, K., and Bills, B. (2005). Assessment of ICESat performance at the Salar de Uyuni, Bolivia. *Geophysical Research Letters*, 32(L21501).

Gehrels, R. (2010). Sea-level changes since the Last Glacial Maximum: an appraisal of the IPCC Fourth Assessment Report. *Journal of Quaternary Science*, 25(1):26–38.

Gunter, B., Urban, T., Riva, R., Helsen, M., Harpold, R., Poole, S., Nagel, P., Schutz, B., and Tapley, B. (2009). A comparison of coincident GRACE and ICESat data over Antarctica. *Journal of Geodesy*, 83(11):1051–1060.

Helsen, M. M., van den Broeke, M. R., van de Wal, R. S., van de Berg, W. J., van Meijgaard, E., Davis, C. H., Li, Y., and Goodwin, I. (2008). Elevation changes in Antarctica mainly determined by accumulation variability. *Science*, 320(5883):1626–1629.

Herzfeld, U. C. (1992). Least-squares collocation, geophysical inverse theory and geostatistics: a bird's eye view. *Geophysical Journal International*, 111(2):237–249.

Herzfeld, U. C., McBride, P. J., Zwally, H. J., and Dimarzio, J. (2008). Elevation changes in Pine Island Glacier, Walgreen Coast, Antarctica, based on GLAS (2003) and ERS-1 (1995) altimeter data analyses and glaciological implications. *International Journal of Remote Sensing*, 29(19):5533–5553.

Hirasawa, N., Nakamura, H., and Yamanouchi, T. (2000). Abrupt changes in meteorological conditions observed at an inland Antarctic station in association with wintertime blocking. *Geophysical Research Letters*, 27(13):1911–1914.

Hock, R. and Jensen, H. (1999). Application of kriging interpolation for glacier mass balance computations. *Geografiska Annaler: Series A, Physical Geography*, 81(4):611–619.

Horwath, M., Legrésy, B., Rémy, F., Blarel, F., and Lemoine, J.-M. (2012). Consistent patterns of Antarctic ice sheet interannual variations from ENVISAT radar altimetry and GRACE satellite gravimetry. *Geophysical Journal International*, 189(2):863–876.

Howat, I. M., Smith, B. E., Joughin, I., and Scambos, T. A. (2008). Rates of southeast Greenland ice volume loss from combined ICESat and ASTER observations. *Geophysical Research Letters*, 35(L17505).

Hu, J. (1995). Methods of generating surfaces in environmental GIS applications. In *1995 ESRI User Conference Proceedings*.

Ivins, E. R. and James, T. S. (2005). Antarctic glacial isostatic adjustment: a new assessment. *Antarctic Science*, 17(04):541–553.

Jansen, E., Overpeck, J., Briffa, K., Duplessy, J., Joos, F., Masson-Delmotte, V., Olago, D., Otto-Bliesner, B., Peltier, W., Rahmstorf, S., et al. (2007). Chapter 6. palaeoclimate. *Climate Change 2007: The Physical Science Basis. Contribution of Working Group I to the Fourth Assessment Report of the Intergovernmental Panel on Climate Change*, pages 443–498.

Jezek, K. C. (2002). RADARSAT-1 Antarctic Mapping Project: change-detection and surface velocity campaign. *Annals of Glaciology*, 34(1):263–268.

Jones, K. H. (1998). A comparison of algorithms used to compute hill slope as a property of the DEM. *Computers & Geosciences*, 24(4):315–323.

Joughin, I., Smith, B. E., Howat, I. M., Scambos, T., and Moon, T. (2010). Greenland flow variability from ice-sheet-wide velocity mapping. *Journal of Glaciology*, 56(197):415–430.

Joughin, I., Smith, B. E., and Medley, B. (2014). Marine ice sheet collapse potentially under way for the thwaites glacier basin, west antarctica. *Science*, 344(6185):735–738.

Journel, A. G. and Huijbregts, C. J. (1978). *Mining Geostatistics*, volume 600. Academic press London.

Kedar, S., Hajj, G. A., Wilson, B. D., and Heflin, M. B. (2003). The effect of the second order GPS ionospheric correction on receiver positions. *Geophysical Research Letters*, 30(16):1829–.

Kim, J. and Tapley, B. D. (2002). Error analysis of a low-low satellite-to-satellite tracking mission. *Journal of Guidance, Control, and Dynamics*, 25(6):1100–1106.

King, M. A., Bingham, R. J., Moore, P., Whitehouse, P. L., Bentley, M. J., and Milne, G. A. (2012). Lower satellite-gravimetry estimates of Antarctic sea-level contribution. *Nature*, 491(7425):586–589.

Klees, R., Revtova, E., Gunter, B., Ditmar, P., Oudman, E., Winsemius, H., and Savenije, H. (2008). The design of an optimal filter for monthly GRACE gravity models. *Geophysical Journal International*, 175(2):417–432.

Kolensky, S. A. (2012). *A study of time-varying geopotential models for ICESat precision orbit determination*. PhD thesis, University of Texas.

Lacroix, P., Legrésy, B., Coleman, R., Dechambre, M., and Rémy, F. (2007). Dual-frequency altimeter signal from Envisat on the Amery ice-shelf. *Remote Sensing of Environment*, 109(3):285–294.

Lambeck, K. and Chappell, J. (2001). Sea level change through the last glacial cycle. *Science*, 292(5517):679–686.

Lambeck, K., Yokoyama, Y., and Purcell, T. (2002). Into and out of the Last Glacial Maximum: sea-level change during Oxygen Isotope Stages 3 and 2. *Quaternary Science Reviews*, 21(1):343–360.

Legresy, B., Papa, F., Remy, F., Vinay, G., van den Bosch, M., and Zanife, O.-Z. (2005). ENVISAT radar altimeter measurements over continental surfaces and ice caps using the ICE-2 retracking algorithm. *Remote Sensing of Environment*, 95(2):150–163.

Lenaerts, J., den Broeke, M., Berg, W., Meijgaard, E., and Kuipers Munneke, P. (2012). A new, high-resolution surface mass balance map of Antarctica (1979–2010) based on regional atmospheric climate modeling. *Geophysical Research Letters*, 39(L04501).

Ligtenberg, S., Helsen, M., and van den Broeke, M. (2011). An improved semi-empirical model for the densification of Antarctic firn. *The Cryosphere*, 5:809–819.

Ligtenberg, S., van de Berg, W., van den Broeke, M., Rae, J., and Van Meijgaard, E. (2013). Future surface mass balance of the Antarctic ice sheet and its influence on sea level change, simulated by a regional atmospheric climate model. *Climate Dynamics*, 41(3-4):867–884.

Lu, G. Y. and Wong, D. W. (2008). An adaptive inverse-distance weighting spatial interpolation technique. *Computers & Geosciences*, 34(9):1044–1055.

Luthcke, S., Rowlands, D., Williams, T., and Sirota, M. (2005). Reduction of ICESat systematic geolocation errors and the impact on ice sheet elevation change detection. *Geophysical Research Letters*, 32(L21S05).

Matheron, G. (1963). Principles of geostatistics. *Economic Geology*, 58(8):1246–1266.

Moholdt, G., Nuth, C., Hagen, J. O., and Kohler, J. (2010). Recent elevation changes of Svalbard glaciers derived from ICESat laser altimetry. *Remote Sensing of Environment*, 114(11):2756–2767.

Monaghan, A. J., Bromwich, D. H., Fogt, R. L., Wang, S.-H., Mayewski, P. A., Dixon, D. A., Ekaykin, A., Frezzotti, M., Goodwin, I., Isaksson, E., et al. (2006). Insignificant change in Antarctic snowfall since the International Geophysical Year. *Science*, 313(5788):827–831.

Nguyen, A. and Herring, T. (2005). Analysis of ICESat data using Kalman filter and kriging to study height changes in East Antarctica. *Geophysical Research Letters*, 32(L23S03).

Nguyen, A. T.-T. (2006). *Height change detection in Antarctica using satellite altimetry data and Kriging/Kalman filtering techniques*. PhD thesis, Massachusetts Institute of Technology.

NSIDC (2013). Correction to icesat data product surface elevations.

Olea, R. A. (1999). *Geostatistics for Engineers and Earth Scientists*. Kluwer Academic Boston.

Partington, K., Ridley, J., Rapley, C., and Zwally, H. (1989). Observations of the surface properties of the ice sheets by satellite radar altimetry. *Journal of Glaciology*, 35(120):267–275.

Peltier, W. (2001). Global glacial isostatic adjustment and modern instrumental records of relative sea level history. *International Geophysics*, 75:65–95.

Peltier, W. (2004). Global glacial isostasy and the surface of the ice-age earth: The ICE-5G (VM2) model and GRACE. *Annual Review of Earth and Planetary Sciences*, 32:111–149.

Pritchard, H., Ligtenberg, S., Fricker, H., Vaughan, D., van den Broeke, M., and Padman, L. (2012). Antarctic ice-sheet loss driven by basal melting of ice shelves. *Nature*, 484(7395):502–505.

Pritchard, H. D., Arthern, R. J., Vaughan, D. G., and Edwards, L. A. (2009). Extensive dynamic thinning on the margins of the Greenland and Antarctic ice sheets. *Nature*, 461(7266):971–975.

Pritchard, H. D., Luthcke, S., and Fleming, A. H. (2010). Understanding ice-sheet mass balance: progress in satellite altimetry and gravimetry. *Journal of Glaciology*, 56(200):1151–1161.

Ramillien, G., Lombard, A., Cazenave, A., Ivins, E., Llubes, M., Remy, F., and Biancale, R. (2006). Interannual variations of the mass balance of the Antarctica and Greenland ice sheets from GRACE. *Global and Planetary Change*, 53(3):198–208.

Rignot, E. (2006). Changes in ice dynamics and mass balance of the Antarctic ice sheet. *Philosophical Transactions of the Royal Society A: Mathematical, Physical and Engineering Sciences*, 364(1844):1637–1655.

Rignot, E., Bamber, J. L., van Den Broeke, M. R., Davis, C., Li, Y., Van De Berg, W. J., and Van Meijgaard, E. (2008). Recent Antarctic ice mass loss from radar interferometry and regional climate modelling. *Nature Geoscience*, 1(2):106–110.

Rignot, E., Mouginot, J., Morlighem, M., Seroussi, H., and Scheuchl, B. (2014). Widespread, rapid grounding line retreat of pine island, thwaites, smith, and kohler glaciers, west antarctica, from 1992 to 2011. *Geophysical Research Letters*, 41(10):3502–3509.

Rignot, E., Mouginot, J., and Scheuchl, B. (2011a). Ice flow of the Antarctic ice sheet. *Science*, 333(6048):1427–1430.

Rignot, E., Velicogna, I., van den Broeke, M., Monaghan, A., and Lenaerts, J. (2011b). Acceleration of the contribution of the Greenland and Antarctic ice sheets to sea level rise. *Geophysical Research Letters*, 38(L05503).

Rott, H., Rack, W., Skvarca, P., and De Angelis, H. (2002). Northern Larsen ice shelf, Antarctica: further retreat after collapse. *Annals of Glaciology*, 34(1):277–282.

Sandwell, D. T. (1987). Biharmonic spline interpolation of GEOS-3 and SEASAT altimeter data. *Geophysical Research Letters*, 14(2):139–142.

Sasgen, I., Konrad, H., Ivins, E., van den Broeke, M., Bamber, J., Martinec, Z., and Klemann, V. (2013). Antarctic ice-mass balance 2003 to 2012: regional reanalysis of GRACE satellite gravimetry measurements with improved estimate of glacial-isostatic adjustment based on GPS uplift rates. *The Cryosphere*, 7(5):1499–1512.

Sasgen, I., van den Broeke, M., Bamber, J. L., Rignot, E., Sørensen, L. S., Wouters, B., Martinec, Z., Velicogna, I., and Simonsen, S. B. (2012). Timing and origin of recent regional ice-mass loss in Greenland. *Earth and Planetary Science Letters*, 333:293–303.

Schenk, T. and Csatho, B. (2012). A new methodology for detecting ice sheet surface elevation changes from laser altimetry data. *Geoscience and Remote Sensing, IEEE Transactions on*, 50(9):3302–3316.

Schrama, E. J. and Wouters, B. (2011). Revisiting Greenland ice sheet mass loss observed by GRACE. *Journal of Geophysical Research: Solid Earth (1978–2012)*, 116(B02407).

Schutz, B. (2001). Laser altimetry and lidar from ICESat/GLAS. In *Geoscience and Remote Sensing Symposium, 2001. IGARSS'01. IEEE 2001 International*, volume 3, pages 1016–1019. IEEE.

Schutz, B. and Zwally, H. (2008). Overview of the Science Results from ICESat. In *16th International Workshop On Laser Ranging, Poznan Poland*.

Schutz, B., Zwally, H., Shuman, C., Hancock, D., and DiMarzio, J. (2005). Overview of the ICESat mission. *Geophysical Research Letters*, 32(L21S01).

Shepherd, A., Ivins, E. R., Geruo, A., Barletta, V. R., Bentley, M. J., Bettadpur, S., Briggs, K. H., Bromwich, D. H., Forsberg, R., Galin, N., et al. (2012). A reconciled estimate of ice-sheet mass balance. *Science*, 338(6111):1183–1189.

Shepherd, A. and Wingham, D. (2007). Recent sea-level contributions of the Antarctic and Greenland ice sheets. *Science*, 315(5818):1529–1532.

Shewchuk, J. R. (1996). Triangle: Engineering a 2D quality mesh generator and Delaunay triangulator. In Lin, M. and Manocha, D., editors, *Applied Computational Geometry Towards Geometric Engineering*, pages 203–222. Springer.

Shewchuk, J. R. (2002). Delaunay refinement algorithms for triangular mesh generation. *Computational Geometry*, 22(1):21–74.

Shi, H.-L., Lu, Y., Du, Z.-L., Jia, L.-L., Zhang, Z.-Z., and Zhou, C.-X. (2011). Mass change detection in Antarctic ice sheet using ICESat block analysis techniques from 2003˜ 2008. *Diqiu Wuli Xuebao*, 54(4):958–965.

Siegfried, M. R., Hawley, R. L., and Burkhart, J. F. (2011). High-resolution ground-based GPS measurements show intercampaign bias in ICESat elevation data near Summit, Greenland. *Geoscience and Remote Sensing, IEEE Transactions on*, 49(9):3393–3400.

Siemes, C., Ditmar, P., Riva, R., Slobbe, D., Liu, X., and Farahani, H. H. (2013). Estimation of mass change trends in the Earth's system on the basis of GRACE satellite data, with application to Greenland. *Journal of Geodesy*, 87(1):69–87.

Sinclair, D. (2010). S-hull: a fast radial sweep-hull routine for Delaunay triangulation. *S-hull.org*.

Sirota, J. M., Bae, S., Millar, P., Mostofi, D., Webb, C., Schutz, B., and Luthcke, S. (2005). The transmitter pointing determination in the geoscience laser altimeter system. *Geophysical Research Letters*, 32(L22S11).

Slobbe, D., Lindenbergh, R., and Ditmar, P. (2008). Estimation of volume change rates of Greenland's ice sheet from ICESat data using overlapping footprints. *Remote Sensing of Environment*, 112(12):4204–4213.

Smith, B. E., Bentley, C. R., and Raymond, C. F. (2005). Recent elevation changes on the ice streams and ridges of the Ross Embayment from ICESat crossovers. *Geophysical Research Letters*, 32(L21S09).

Smith, B. E., Fricker, H. A., Joughin, I. R., and Tulaczyk, S. (2009). An inventory of active subglacial lakes in Antarctica detected by ICESat (2003-2008). *Journal of Glaciology*, 55(192):573.

Solomon, S. (2007). *Climate change 2007-the physical science basis: Working group I contribution to the fourth assessment report of the IPCC*, volume 4. Cambridge University Press.

Sørensen, L. S., Simonsen, S. B., Nielsen, K., Lucas-Picher, P., Spada, G., Adalgeirsdottir, G., Forsberg, R., and Hvidberg, C. (2011). Mass balance of the Greenland ice sheet (2003-2008) from ICESat data-the impact of interpolation, sampling and firn density. *The Cryosphere*, 5(1):173–186.

Spinhirne, J. D., Palm, S. P., Hart, W. D., Hlavka, D. L., and Welton, E. J. (2005). Cloud and aerosol measurements from GLAS: Overview and initial results. *Geophysical Research Letters*, 32(L22S03).

Stern, N. N. H. (2007). *The Economics of Climate Change: The Stern Review*. Cambridge University Press.

Stocker, T., Qin, D., Plattner, G., Tignor, M., Allen, S., Boschung, J., Nauels, A., Xia, Y., Bex, V., and Midgley, P. (2013). Climate change 2013: The physical science basis. intergovernmental panel on climate change, working group i contribution to the ipcc fifth assessment report (ar5).

Sutterley, T. C., Velicogna, I., Csatho, B., van den Broeke, M., Rezvan-Behbahani, S., and Babonis, G. (2014). Evaluating Greenland glacial isostatic adjustment corrections using GRACE, altimetry and surface mass balance data. *Environmental Research Letters*, 9(1):014004.

Tapley, B., Ries, J., Bettadpur, S., Chambers, D., Cheng, M., Condi, F., Gunter, B., Kang, Z., Nagel, P., Pastor, R., et al. (2005). GGM02–an improved Earth gravity field model from GRACE. *Journal of Geodesy*, 79(8):467–478.

Tapley, B. D., Bettadpur, S., Watkins, M., and Reigber, C. (2004). The gravity recovery and climate experiment: Mission overview and early results. *Geophysical Research Letters*, 31(L09607).

Thomas, E. R., Marshall, G. J., and McConnell, J. R. (2008). A doubling in snow accumulation in the western Antarctic Peninsula since 1850. *Geophysical Research Letters*, 35(L01706).

Tomczak, M. (1998). Spatial interpolation and its uncertainty using automated anisotropic inverse distance weighting (IDW)-cross-validation/jackknife approach. *Journal of Geographic Information and Decision Analysis*, 2(2):18–30.

Truffer, M. and Fahnestock, M. (2007). Rethinking ice sheet time scales. *Science*, 315(5818):1508–1510.

Urban, T. J. and Schutz, B. E. (2005). ICESat sea level comparisons. *Geophysical Research Letters*, 32(L23S10).

van de Berg, W., van den Broeke, M., Reijmer, C., and van Meijgaard, E. (2006). Reassessment of the Antarctic surface mass balance using calibrated output of a regional atmospheric climate model. *Journal of Geophysical Research: Atmospheres (1984–2012)*, 111(D11104).

van den Broeke, M., Bamber, J., Ettema, J., Rignot, E., Schrama, E., van de Berg, W. J., van Meijgaard, E., Velicogna, I., and Wouters, B. (2009). Partitioning recent Greenland mass loss. *Science*, 326(5955):984–986.

van den Broeke, M. R., Bamber, J., Lenaerts, J., and Rignot, E. (2011). Ice sheets and sea level: thinking outside the box. *Surveys in Geophysics*, 32(4-5):495–505.

Van Der Veen, C. J., Ahn, Y., Csatho, B., Mosley-Thompson, E., and Krabill, W. (2009). Surface roughness over the northern half of the Greenland Ice Sheet from airborne laser altimetry. *Journal of Geophysical Research: Earth Surface (2003–2012)*, 114(F1).

Van Der Veen, C. J., Krabill, W., Csatho, B., and Bolzan, J. (1998). Surface roughness on the Greenland ice sheet from airborne laser altimetry. *Geophysical Research Letters*, 25(20):3887–3890.

van Ommen, T. D. and Morgan, V. (2010). Snowfall increase in coastal East Antarctica linked with southwest Western Australian drought. *Nature Geoscience*, 3(4):267–272.

Vaughan, D., Comiso, J., Allison, I., Carrasco, J., Kaser, G., Kwok, R., Mote, P., Murray, T., Paul, F., Ren, J., and Rignot, E. (2013). 2013: Observations: Cryosphere. In Stocker, T., Qin, D., Plattner, G., Tignor, M., Allen, S., Boschung, J., Nauels, A., Xia, Y., Bex, V., and Midgley, P., editors, *Climate Change 2013: The Physical Science Basis. Contribution of Working Group I to the Fifth Assessment Report of the Intergovernmental Panel on Climate Change*. Cambridge University Press, Cambridge, United Kingdom and New York, NY, USA.

Velicogna, I. and Wahr, J. (2006). Measurements of time-variable gravity show mass loss in Antarctica. *Science*, 311(5768):1754–1756.

Velicogna, I. and Wahr, J. (2013). Time-variable gravity observations of ice sheet mass balance: Precision and limitations of the GRACE satellite data. *Geophysical Research Letters*, 40(12):3055–3063.

Waelbroeck, C., Labeyrie, L., Michel, E., Duplessy, J. C., McManus, J., Lambeck, K., Balbon, E., and Labracherie, M. (2002). Sea-level and deep water temperature changes derived from benthic foraminifera isotopic records. *Quaternary Science Reviews*, 21(1):295–305.

Wahr, J., Swenson, S., and Velicogna, I. (2006). Accuracy of GRACE mass estimates. *Geophysical Research Letters*, 33(L06401).

Watson, D. (1982). ACORD: Automatic contouring of raw data. *Computers & Geosciences*, 8(1):97–101.

Wessel, P. (2009). A general-purpose Green's function-based interpolator. *Computers & Geosciences*, 35(6):1247–1254.

Wessel, P. and Bercovici, D. (1998). Interpolation with splines in tension: A Green's function approach. *Mathematical Geology*, 30(1):77–93.

Wessel, P. and Smith, W. (2013). *The Generic Mapping Tools (GMT) version 4.5.9, Technical Reference and Cookbook*. SOEST/NOAA.

Whitehouse, P. L., Bentley, M. J., Milne, G. A., King, M. A., and Thomas, I. D. (2012). A new glacial isostatic adjustment model for Antarctica: calibrated and tested using observations of relative sea-level change and present-day uplift rates. *Geophysical Journal International*, 190(3):1464–1482.

Wouters, B., Chambers, D., and Schrama, E. (2008). GRACE observes small-scale mass loss in Greenland. *Geophysical Research Letters*, 35(L20501).

Wu, X., Heflin, M. B., Schotman, H., Vermeersen, B. L., Dong, D., Gross, R. S., Ivins, E. R., Moore, A. W., and Owen, S. E. (2010). Simultaneous estimation of global present-day water transport and glacial isostatic adjustment. *Nature Geoscience*, 3(9):642–646.

Yi, D., Zwally, H. J., and Sun, X. (2005). ICESat measurement of Greenland ice sheet surface slope and roughness. *Annals of Glaciology*, 42(1):83–89.

Zhou, Q. and Liu, X. (2004). Analysis of errors of derived slope and aspect related to DEM data properties. *Computers & Geosciences*, 30(4):369–378.

Zwally, H. J. and Brenner, A. C. (2001). Ice sheet dynamics and mass balance. *International Geophysics*, 69:351–xxvi.

Zwally, H. J., Giovinetto, M. B., Beckley, M. A., and Saba, J. L. (2012). Antarctic and Greenland Drainage Systems, GSFC Cryospheric Sciences Laboratory. `http://icesat4.gsfc.nasa.gov/cryo_data/ant_grn_drainage_systems.php`.

Zwally, H. J., Giovinetto, M. B., Li, J., Cornejo, H. G., Beckley, M. A., Brenner, A. C., Saba, J. L., and Yi, D. (2005). Mass changes of the Greenland and Antarctic ice sheets and shelves and contributions to sea-level rise: 1992-2002. *Journal of Glaciology*, 51(175):509–527.

Zwally, H. J., Jun, L., Brenner, A. C., Beckley, M., Cornejo, H. G., Dimarzio, J., Giovinetto, M. B., Neumann, T. A., Robbins, J., Saba, J. L., et al. (2011a). Greenland ice sheet mass balance: distribution of increased mass loss with climate warming; 2003-07 versus 1992-2002. *Journal of Glaciology*, 57(201):88–102.

Zwally, H. J. and Schuman, C. (2002). ICESat Brochure. Technical report, NASA/GSFC.

Zwally, H. J., Schutz, B., Abdalati, W., Abshire, J., Bentley, C., Brenner, A., Bufton, J., Dezio, J., Hancock, D., and Harding, D. (2002). ICESat's laser measurements of polar ice, atmosphere, ocean, and land. *Journal of Geodynamics*, 34(3):405–445.

Zwally, H. J., Schutz, R., Bentley, C., Bufton, J., Herring, T., Minster, J., Spinhirne, J., and Thomas, R. (2011b). *GLAS/ICESat L2 Antarctic and Greenland Ice Sheet Altimetry Data. Version 33. GLA12.* National Snow and Ice Data Center, Boulder, Colorado USA.